Photophysical properties of Iridium-containing complexes – applications in cell imaging and sensing

Zainab Nafea Jaafar Zubaidi

A thesis submitted to the University of Sheffield in partial fulfilment of the requirements

for the Degree of Doctor of Philosophy

Department of Chemistry

University of Sheffield

United Kingdom

December 2018

Author’s Declaration

The work described in thesis was carried out between January 2015 and 2018 in the department of chemistry at the University of Sheffield. It is the individual work of the Author. Any views expressed in this thesis are those of the author, and in no way represent those of University of Sheffield. This thesis has not previously been submitted, in part or whole, for any other degree in this University or any other institution.

Zainab Nafea Jafaar Zubaidi

December 2018

Acknowledgements

First, I would like to thank my supervisor Professor Michael D. Ward for giving me this opportunity to join his research team, also his support, guidance and encouragement, to complete my PhD under his supervision. Mike, I learnt many things from you, not just chemistry, I learnt how to be patient and appreciate results when they happen (especially with purification). I also will apply your supervision style in the future as you displayed a different way of approaching situations (e.g. when students are in a bad mood).

A big thank you from the earth to the sky to my second supervisor Professor Julia Weinstein, who shared her knowledge and time (when Mike moved to Warwick). You advised me, and your positive energy when I was struggling allowed me to finish my thesis. Words cannot fully express how grateful I am that you were there for me; thank you so much.

I would also like to thank all of the members of the Ward group, past and present. A huge thank you to Alex and Craig for help with X-ray crystallography, and Callum for the cell imaging. Harry deserves a special mention for giving me an understanding of the theory behind solving and refining crystal structures.

I would also like to thank all of the technicians in the Chemistry department; Simon and Sharon for mass spectrometry; Stephen for elemental analysis; Dean and Tom for help with IT; Pete and Nick from stores, and Craig (again) for NMR assistance.

Thanks also go to the Iraqi Ministry of Higher Education and Scientific Research and Middle Technical University for giving me this opportunity to study in the UK, and for providing my funding.

Many thanks to my friends in the department and the GRC: Layla and Hanady (from Saudi Arabia), Fatema and Najwa (from Libya), Noor-Fatema (from Turkey), Zainab Murtadhawi (from Kuwait) and Tony (from Canada). You are all a fantastic bunch of people and I feel very fortunate to have had the opportunity to meet you in the UK. I wish everyone the best of luck in the future.

Finally, I would like to thank my family: my parents, brothers, sisters, my husband, my sons Hussein and Yaser and my daughter Noor. You are all the best!

List of Publication

1) **Zainab N. Zubaidi**, Alexander J. Metherell, Elizabeth Baggaley, Michael D. Ward, Ir(III) and Ir(III)/Re(I) complexes of a new bis(pyrazolyl-pyridine) bridging ligand containing a naphthalene-2,7-diyl spacer: Structural and photophysical properties, Polyhedron. 2017, **133**, 68-74

Abstract

This thesis describes the synthesis and photophysical studies of octahedral coordination complexes of Ir(III), and Ir(III)/Ln(III) dyads.

Chapter One: provides an introduction to the principles of luminescence, and a brief background to the photophysical properties of Ir(III) complexes, as well as Ir(III)/Ln(III) energy transfer processes.

Chapter Two: describes the synthesis and characterization series of a novel mononuclear-Ir(III) complexes with different substitution patterns on the cyclometalated ligands, and a pendant pyrene group: namely $^{F/F}$Ir•L^{pyrene}•NO$_3$, $^{F/H}$Ir•L^{pyrene}•NO$_3$ and $^{H/H}$Ir•L^{pyrene}•NO$_3$ complexes. The X-ray crystal structure of $^{F/F}$Ir•L^{pyrene}•NO$_3$ complex is briefly described. The dual emission of these complexes, and further photophysical properties have been studied.

Chapter Three: describes the synthesis, characterisation and X-ray structures of a series of mono-Ir(III) complexes based on the presence or absence of F atom substituents on the cyclometated phenylpyridine ligands, and different types of the ancillary ligand. The chapter also presents a systematic study of their excited states. Furthermore, the tunability of photophysical properties of Ir(III) complexes was observed because of position and number of electron-withdrawing groups in the cyclometalated ligands, and changes in the ancillary ligand.

Chapter Four: describes the synthesis, characterization and photophysical properties of novel Ir(III) complexes with an $^{+}$N-CH$_3$ substituent in the cyclometalated ligands, namely ^{22}IrCl$_2$•PF$_6$, ^{23}IrCl$_2$•PF$_6$, ^{24}IrCl$_2$•PF$_6$, ^{23}Ir•pypz•3PF$_6$, ^{24}Ir•pypz•3PF$_6$, ^{22}Ir•L$^{bi\text{-}ph}$•3PF$_6$, ^{23}Ir•L$^{bi\text{-}ph}$ •3PF$_6$ and ^{24}Ir•L$^{bi\text{-}ph}$•3PF$_6$. A strong luminescence was observed from all Ir(III) complexes. Moreover, sensitisation of emission from Ln, when Ln = Eu(III) and Tb(III), *via* an intermolecular energy transfer mechanism has been observed.

Chapter Five: describes the synthesis, characterization and X–ray crystal structures of a new bridging ligand which was used to prepare new mononuclear Ir(III) and dinuclear Ir(III)/Ir(III) and Ir(III)/Re(I) complexes. Luminescence measurements for all complexes have been performed. The effect of the role of the naphthyl group in the bridging ligand as a "stepping stone" in the energy transfer quenching of Ir(III) emission and on the energy transfer in the Ir(III)/Re(I) dyads has been established.

Chapter Six: describes an Ir(III)/ Eu(III) dyad as the basis of a ratiometric sensor for anions. Photoinduced energy-transfer occurs in Ir(III)/Eu(III) dyad resulting in partial quenching of the Ir(III) – based emission with concomitant sensitisation of the Eu(III)-based emission. This sensitised emission is quenched by a range of anions, which act as competing ligands for the Eu(III) centre and separate it from the dyad; therefore, excitation of Ir(III) only results in blue Ir(III)-based luminescence. Thus, the anions act as selective quenchers of the Eu(III) based luminescence in the Ir(III)/Eu(III) dyads, leading to the change in overall luminescence colour from red [from Eu(III)] to blue [from Ir(III)]. The hydrogen sulfate anion displays less efficient quenching of the Eu-based luminescence component in comparison with the acetate, dihydrogen phosphate and benzoate anions which show stronger quenching of the Eu(III)-based luminescence.

Chapter Seven: describes the synthetic procedures and characterisation data for the ligands and complexes that were reported in this thesis.

Abbreviations

PA	2,4,6-trinitrophenol
TNT	2,4,6-trinitrotoluene
A	absorbance
ATP	adenosine-5-triphosphate
AMP	adenosine monophosphate
ADP	adenosine diphosphate
BET	back energy-transfer
bi-ph	biphenyl
Bu_4NI	tetra butylammonium iodide
Cs_2CO_3	Caesium carbonate
DCM	Dichloromethane
DMSO	Dimethyl sulphoxide
d	doublet
dd	doublet of doublets
ddd	doublet of doublet of doublets
E.T	energy transfer
EJ	bladder epithelial cancer cell
ESMS	electrospray mass spectroscopy
equiv	equivalent
fac	Facial configuration
F	Fluorescence
FLIM	fluorescence lifetime imaging microscopy
G.S	ground state
HeLa cells	epithelial carcinoma cells
IC	internal conversion
IR	infrared spectrum
ISC	intersystem crossing

I	luminescence intensity with quencher
I_0	luminescence intensity without quencher
KNO_3	Potassium nitrate
KEnT	Rate constant energy transfer
kq	bimolecular quenching rate constant
Ln	Lanthanide
LC	Ligand centred transition
ILCT	Intra-ligand charge transfer transitions
LLCT	Ligand to ligand charge transfer transitions
LMCT	Ligand-to-metal charge transfer
LECs	light-emitting electrochemical cells
LUMO	Lowest Unoccupied Molecular Orbital
MeCN	acetonitrile
mer	Meridional configuration
MLCT	Metal to ligand charge transfer transition
MC	Metal–centered transition
MeOH	methanol
m	multiplets
naph	naphthalene
OFETs	organic field effect transistors
OLEDs	organic light emitting diodes
OPVs	organic photovoltaic devices
PFA	paraformaldehyde
ppt.	precipitate
P	Phosphorescence
PBS	Phosphate buffered saline
PDT	photodynamic therapy
PET	photo-induced electron transfer mechanism
PEnT	Photoinduced Energy Transfer

PS	Photosensitiser
pypz	pyridyl pyrazol
[Q]	molar concentration of the quencher
ref.	reference
S_1	lowest singlet excited state
S_0	singlet ground state
TGLI	time-gated luminescence imaging
T	triplet excited state
td	triplet of doublets
Vis.	Visible
τ	lifetime
τ_{uq}	Unquenched Ir-based lifetime of Ir(III)/Gd(III) dyad
Φ, QY	quantum yield
τ_q	Quenched Ir-based lifetime of Ir(III)/Eu(III) dyad

Table of Contents

CHAPTER ONE

Luminescence of coordination Ir(III) complexes: Luminescence processes, cyclometalated Ir(III) complexes properties and applications.

1 Luminescence of coordination Ir(III) complexes: Luminescence processes, cyclometalated Ir(III) complexes properties and applications.

1.1 Luminescence phenomena

Photoluminescence is an emission of light from any emitting species, and occurs from electronically excited states after direct photoexcitation. Luminescence phenomena are formally divided into two types: fluorescence and phosphorescence. These are called ‘cold light’ as they do not require a high temperature for excitation, and generate no noticeable heat during emission.[1] The main criterion to distinguish between fluorescence and phosphorescence is the spin multiplicity of the excited state compared to the ground state. In fluorescence processes, there is no change in electron spin during the transition: usually the electron relaxes from the lowest singlet excited state (S_1), to the singlet ground state (S_0). In contrast, phosphorescence processes are spin forbidden, and typically the electron relaxes from a triplet excited state (T) to S_0. Fluorescence is spin-allowed and therefore has a short lifetime, typically 10^8 s^{-1} for emission of a photon, whereas in the phosphorescence process the relaxation of the electron from a triplet to the singlet ground state is forbidden (needs change in spin orientation to become opposite to the electron spin orientation in the ground state) with typically long lifetime (~10^{-3} – 10^0 s).[2]

1.1.1 Luminescence phenomena process

The electronic transitions involved in absorption and emission of light are usually indicated in a Jablonski diagram.[2] The Jablonski diagram[3] (**Figure** 1-1) is used to illustrate the electronic and vibrational energy levels and the electronic transitions in molecular process that can occur in singlet excited states or between singlet and triplet excited states. When the molecule absorbs the energy of the photons, excitations from the ground state S_0 to the higher excited singlet states are symbolized by S_1, S_2, …etc. Each electronic energy level has a number of the sublevels which are vibrational energy levels, symbolized by 0, 1, 2…. etc. The difference in energy between S_0 and S_1 excited states is too large to be reached by thermal population of S_1 energy level, for this reason the light is used instead of heat to induce the electronic excitation.[2] The molecule in its excited state is unstable, so it must undergo some relaxation or deactivation process using several of the different available pathways for loss of electronic excitation.[4,5] All these deactivation process are physical deactivation with no chemical change involved.

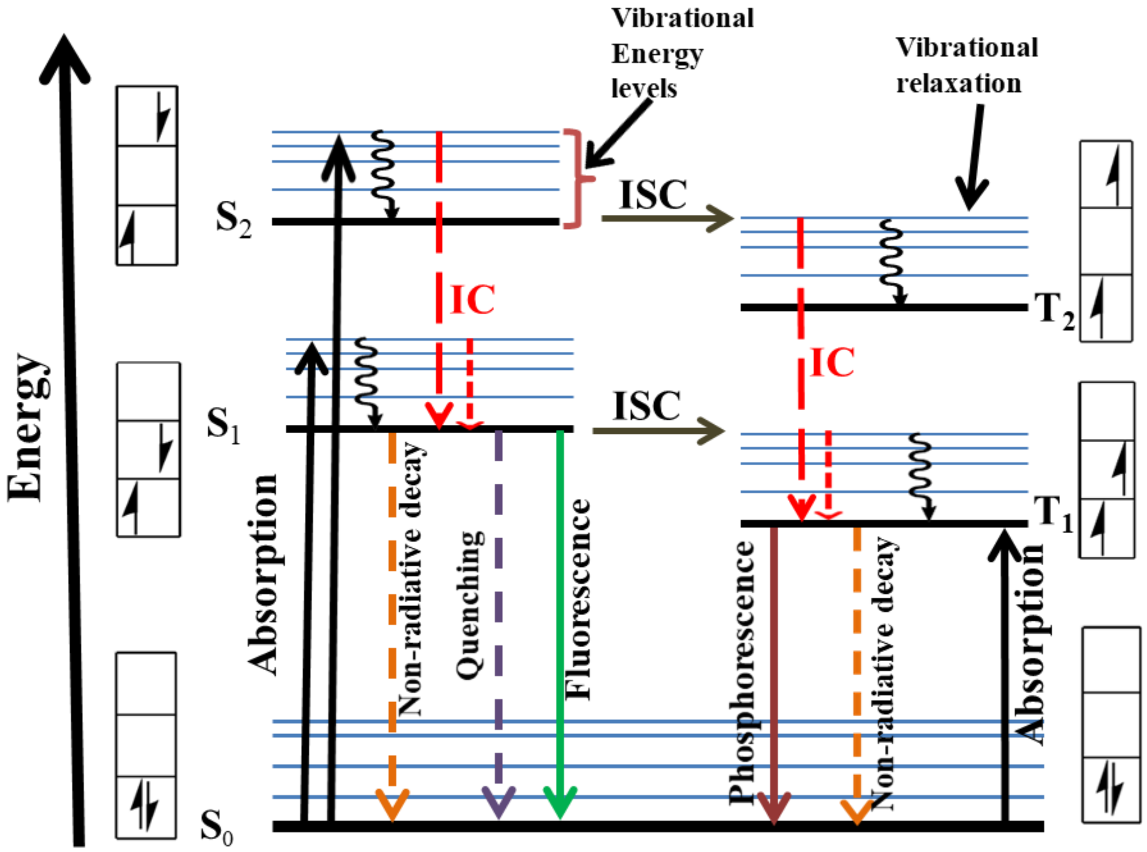

Figure 1-1 Traditional Jablonski energy diagram showing possible electronic transitions associated with absorption and emission of light (IC is internal conversion and ISC is intersystem crossing).

1.1.1.1 Radiative and non-radiative decays from singlet excited states (S_1):

An internal conversion (IC) (allowed process) is observed when a molecule relaxes from a high-lying singlet excited state S_n, when $n > 1$, to the lowest singlet excited state S_1. This transition happens due to a good overlap between two different wavefunctions of the same spin multiplicity on a time scale of 10^{-12} s. This radiationless transition is usually accompanied by heat loss.[6,7]

Fluorescence (F): is the emission of a photon from the lowest excited state S_1 to S_0. In other words, this is a radiative transition between states of the same multiplicity on the time scale 10^{-8} s. This process is a spin-allowed process.[6]

Quenching or collisional decay excited states: can also lose energy to another molecule through energy transfer process either over a distance (intermolecular electronic energy transfer), or within the same molecule (intramolecular energy transfer) or by collisions with quenching species (collisional quenching).[4,5,6]

Non-radiative decay: can be described this process as dissipation of energy from an excited state to the ground state without emission of light.

Intersystem crossing: is a transition from S_1 state to the lower energy T_1 state in a spin-forbidden process. This non-radiative transition between states of the different multiplicities is facilitated by the spin-orbit coupling effect of heavy atoms.

1.1.1.2 Radiative and non-radiative decays from triplet excited states (T_n):

An internal conversion (IC) (allowed process): this transition occurs from a high-lying triplet excited state T_n, when n>1, to the lowest triplet excited state T_1.[7,8]

Phosphorescence (P): is when an electron relaxes from lowest the energy state of T_1 to S_0 accompanied by emission of a photon. This radiative decay is spin-forbidden with a time scale 10^{-3} to 10^{2} s in organic molecules,[6] but can be greatly enhanced by spin-orbit coupling in transition metal complexes, leading to phosphorescence lifetimes of several hundreds of nanoseconds.

In metal coordination and organometallic complexes, the electronic transitions are related to the light absorption from S_0 to S_n energy levels of different nature and electronic localization.[9] The mainly types of transitions are as following:

Ligand centred transition (^{1}LC = π-π*): occurs between ligand-centred orbitals or to other ligand orbitals (ligand to ligand charge transfer transitions or intra-ligand, LLCT, ILCT).

Metal–centred transition (^{1}MC = d-d): occurs between d- orbitals, means electronic transitions are localised on the metal ion.

Metal to ligand charge transfer transition (^{1}MLCT = d-π*): occurs from a d-orbital of the metal to the lowest energy empty π* orbital of the ligand. **Ligand-to-metal charge transfer (^{1}LMCT):** occurs from a filled π orbital of a ligand to an empty metal d orbital.

It should be noted that there are two important selection rules for electronic transitions: the **spin selection rule** and the **Laporte rule** which decide whether particular transitions are allowed or forbidden.[10, 9]

Spin selection rules: requires no change in the total spin multiplicity (singlet to singlet or triplet to triplet) during the electronic transition. In contrast, transitions between different multiplicities (singlet to triplet or triplet to singlet) are forbidden. In some cases, spin-forbidden transitions are observed when the spin selection rule is relaxed by spin-orbit coupling effects, but such transitions are of low intensity.

Laporte rule: applies to centrosymmetric molecules. All electronic transitions which conserve parity ($\Delta l = 0$) are Laporte-forbidden, for example s-s, p-p, d-d and f-f transitions. While electronic transitions that produce a different parity (implying $\Delta l = \pm 1$) are Laporte allowed. This means that pure d-d transitions in octahedral complexes are very weak, but in tetrahedral complexes (which are not centrosymmetric) they are much more intense. In addition, there are some processes able to turn some forbidden transitions into allowed ones through mixing different orbitals or states, like p and d orbitals (d/p mixing) or singlet and triplet states (spin-orbit coupling).

Spin-orbit coupling process: mixes different spin multiplicity states leading to apparently spin-forbidden transitions becoming allowed. Electronic transitions that occur between different spin multiplicity states display what is called intersystem crossing (ISC) and it becomes possible in metal complexes. Ir(III) has the highest spin orbit coupling constant in the transition metals. The spin orbit coupling constant ζ 4430 for the Ir metal is higher than the other metals, like Os, Fe and Ru, which are ζ 3381, 431 and 1042 cm^{-1}, respectively.[11]

The rate at which a process occurs depends on the selection rules. Typically, spin-forbidden transitions tend to be several orders of magnitude slower than spin-allowed transitions. Moreover, another important excited state property is the **lifetime (τ)**, which can be defined as the time it takes for the number of excited molecules to decay to 1/e of the original population, the **quantum yield (ϕ)** is the ratio between number of photons emitted and number of photons absorbed and is therefore a measure of how much excited-state energy is lost to non-radiative processes. The **Stokes shift** is the difference between maximum wavelengths of absorption and emission, providing the same pair of states is involved in the absorption and emission processes (**Figure** 1-2).[2,4,6,12]

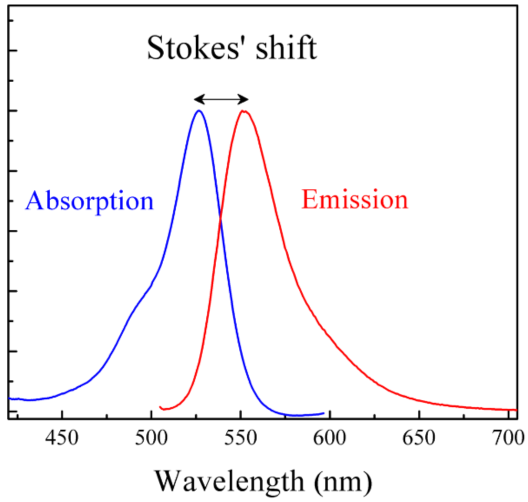

Figure 1-2 The illustration of the difference between maximum wavelength of absorption and maximum wavelength of emission, the so-called Stokes shift, spectrum image was taken from website http://www.snipview.com/q/Raman spectroscopy.[13]

This thesis will focus mainly on the photophysical properties of a new series of Ir(III) complexes as phosphorescent emitters, and the possible use Ir(III) unit as energy donor to sensitise Ln(III) luminescence in mixed d-f dyads.

1.2 Part One: Iridium complexes

1.2.1 Ir(III) complexes of bidentate ligands

Luminescent Ir(III) complexes based on phenylpyridine ligands have unique luminescence properties which make them of great interest. They are very kinetically and thermodynamically stable due to strong Ir-ligand bonds,[14,15] they have long luminescence lifetimes,[16,17] high quantum yields,[14, 18, 19] large Stokes' shifts,[20] and emission colour which is readily tunable by changing ligand substituents. Their colour can be easily tuned the emission from red to green and then blue by using different substituents on the cyclometallating phenyl ring of the (C^N) donor covering the visible region of the electromagnetic spectrum. Because of these properties, Ir(III) complexes are promising for different applications such as photocatalysis,[21] biological imaging[22] and as emitters in the active luminescent layers of a light-emitting electrochemical cells LECs and organic light-emitting diode OLEDs.[23–25]

Cyclometalated Ir(III) complexes are octahedral, in most cases bearing three bidentate ligands, usually with two (the C^N donor) being the same. These complexes may be homoleptic or heteroleptic. Heteroleptic Ir(III) complexes generally have two identical cyclometalated ligands that coordinate to Ir(III) in a five-membered chelate ring, with very strong Ir-C and Ir-N covalent bonds. The third ligand is different, *i.e.* the complex is of the form $[Ir(C^\wedge N)_2(L^\wedge X)]$ (in some cases L=X). In such complexes, there are three possible isomers as shown in **Figure** 1-3.

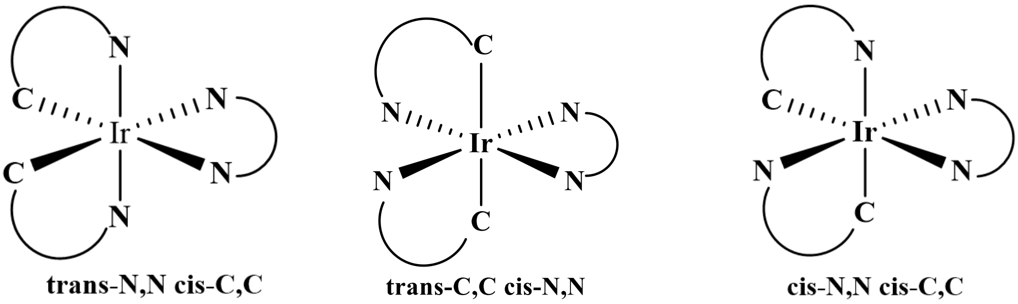

Figure 1-3 Geometric configuration isomers for $Ir(C^\wedge N)_2(N^\wedge N)$ complex.

The most favoured isomer has the trans-*N,N* cis-*C,C* arrangement of the two phenylpyridine ligands.[26] This is due to strong trans effect of the carbon ligands in the Ir-C bonds which means that they end up *cis* to one another. That results in the Ir-N bonds from the C^N donors generally located in a trans position one to another.[26–28] In contrast, homoleptic Ir(III) complexes have three equal cyclometalated ligands $[Ir(C^\wedge N)_3]$ which can exist in two possible isomers having a facial (*fac*) configuration or meridional (*mer*) configuration (**Figure** 1-4).[29]

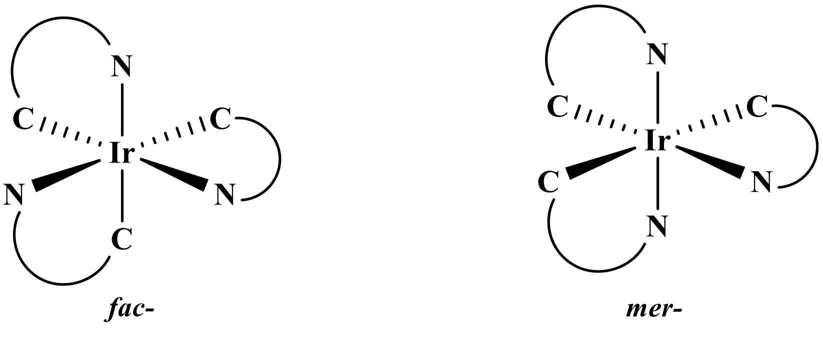

Figure 1-4 Geometrical *fac*- and *mer*- configuration isomers for homoleptic $Ir(C^\wedge N)_3$ complex.

The *fac* isomer is thermodynamically more stable than the *mer* isomer, moreover the *mer* isomer can be converted easily into more stable *fac* isomer either thermally or photochemically.[17, 18, 30] Ir-C and Ir-N bonds are slightly different lengths in the two isomers. In the *fac* isomer both Ir-C and Ir-N bond lengths are approximately identical while in the *mer* isomer the Ir-N bonds length are slightly shorter than bonds length of Ir-C. This difference may affect the electrochemical and spectroscopic properties of the *fac* and *mer* isomers.[31] Both these types of homoleptic and heteroleptic complex can be synthesised from reacted dichloro-bridged cyclometalated Ir(III) dimers with an excess of either (N^N) or (C^N) ligands but with different conditions like temperature or type of solvent.[31, 32]

1.2.2 The Ir(III) intrinsic and the octahedral coordination properties

The Ir(III) trication has a $5d^6$ electronic configuration.[33] In an octahedral Ir(III) complex, the *d* orbitals are split into two degenerate sets: t_{2g}, which is a fully occupied set of three orbitals, and $e_{g,}$ which is a fully unoccupied set of two orbitals. These two orbital sets are separated by an amount $\Delta_{oct.}$ which depends on many important features of the complexes:

(1) The cyclometallated phenylpyridine ligands C^N, as well as commonly-used diamine ligands N^N such as bipyridines, are amongst the strongest field ligands known and therefore strongly stabilise the t_{2g} electronic configuration of Ir(III).[14]
(2) The Ir(III) metal ion generates a higher crystal field splitting than (for example) Ru(III) or Rh(III) because it is a third-row ion with 5d orbitals that overlap with ligands better than do 4d or 3d orbitals as they are larger.[14]
(3) High oxidation state of Ir(III) metal.

The very large $\Delta_{oct.}$ of Ir(III) is large enough to push the MC (d-d) excited state up in energy close to, or higher than, emissive MLCT and LC states. The luminescence from Ir(III) complexes of this type always comes from a triplet excited state which can be a ^{3}MLCT state or ^{3}LC or sometimes an admixture of the two ^{3}MLCT and ^{3}LC.[34–37]

There are ways to analyse the emission spectral features of the Ir(III) complexes to see whether the excited state is ^{3}MLCT or ^{3}LC in nature:

1) The typical feature profile for ^{3}MLCT is an unstructured and broad band, with the MLCT state involving π^* orbitals of the ancillary ligands. In contrast, a ^{3}LC excited state generates more structured emission with separate vibronic features, and the excited state is localised on the cyclometalated ligand.[19,38,39]

2) Blue or red- shifting at 77K (rigidochromism) is diagnostic of the type of excited state. Charge-transfer transitions such as MLCT tend to be substantially blue-shifted (higher in

energy) in a frozen polar solvent at 77K. On the contrary, luminescence from ^{3}LC transitions is almost unaffected by environmental changes in frozen polar solvent.[4]

It is important to know localisation and nature of the excited state to be able to understand photophysical properties. Some simple descriptions for localisation of Highest Occupied Molecular Orbital (HOMO) and Lowest Unoccupied Molecular Orbital (LUMO) levels in chloride bridged Ir(III) dimer and mono-Ir(III) (homoleptic and heteroleptic) complexes.

Homoleptic Ir(III) complexes: HOMO level is mainly centred at the Ir(III) and π orbital of phenyl ring of the cyclometetated ligand, whereas the LUMO is mostly localised on at the π^* orbital of pyridine ring of the same ligand.[30, 40]

Heteroleptic Ir(III) complexes: The HOMO is localised in the same places mentioned for homoleptic complexes, but the LUMO is localised on the ancillary ligand.[40,41]

1.2.3 Tuning the emission colour of Ir(III) complexes

The colour variation of the Ir(III) complexes depends on the energy gap between HOMO and LUMO levels. There are many approaches to Ir(III)-based tuning emission to give blue, green or red emission.[38, 42, 43] These approaches are grouped according to Thompson, Forrest *et.al.*[44, 45] strategies by using electron- donating or electron-withdrawing substituents at: (i) the phenyl rings of the cyclometalating C^N ligand, where the HOMO is localised;[31,43, 46] (ii) the ancillary N^N ligand, where the LUMO level is localised for MLCT emission;[47] (iii) the pyridine rings of the cyclometalating C^N ligand, where LUMO level is localised for LC emission; (iv) changing pyridyl ring in the C^N ligand to another donor such as an N-heterocyclic carbene, triazolyl or N-pyrazolyl groups (**Figure** 1-5), which have a high-lying LUMO level which raises both the MLCT and LC energy levels.[31, 43, 48–51]

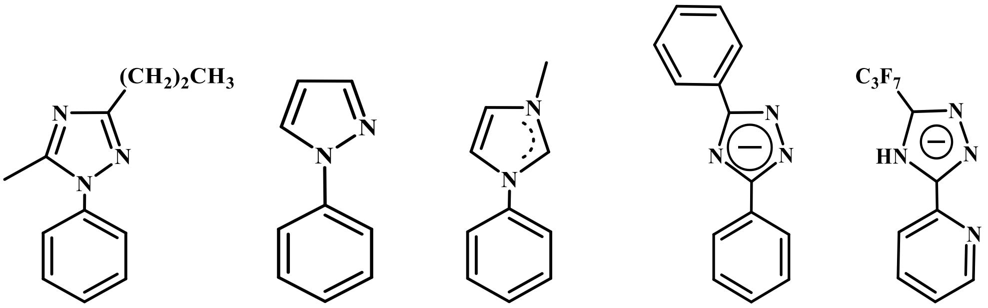

Figure 1-5 Chemical structures of some ligands leading to blue shifted emission.

We can conclude that type and position of the substitutions on the C^N rings or ancillary ligands have a strong effect on the luminescence colour. It is convenient here to mention some groups and how they affect tuning colour.

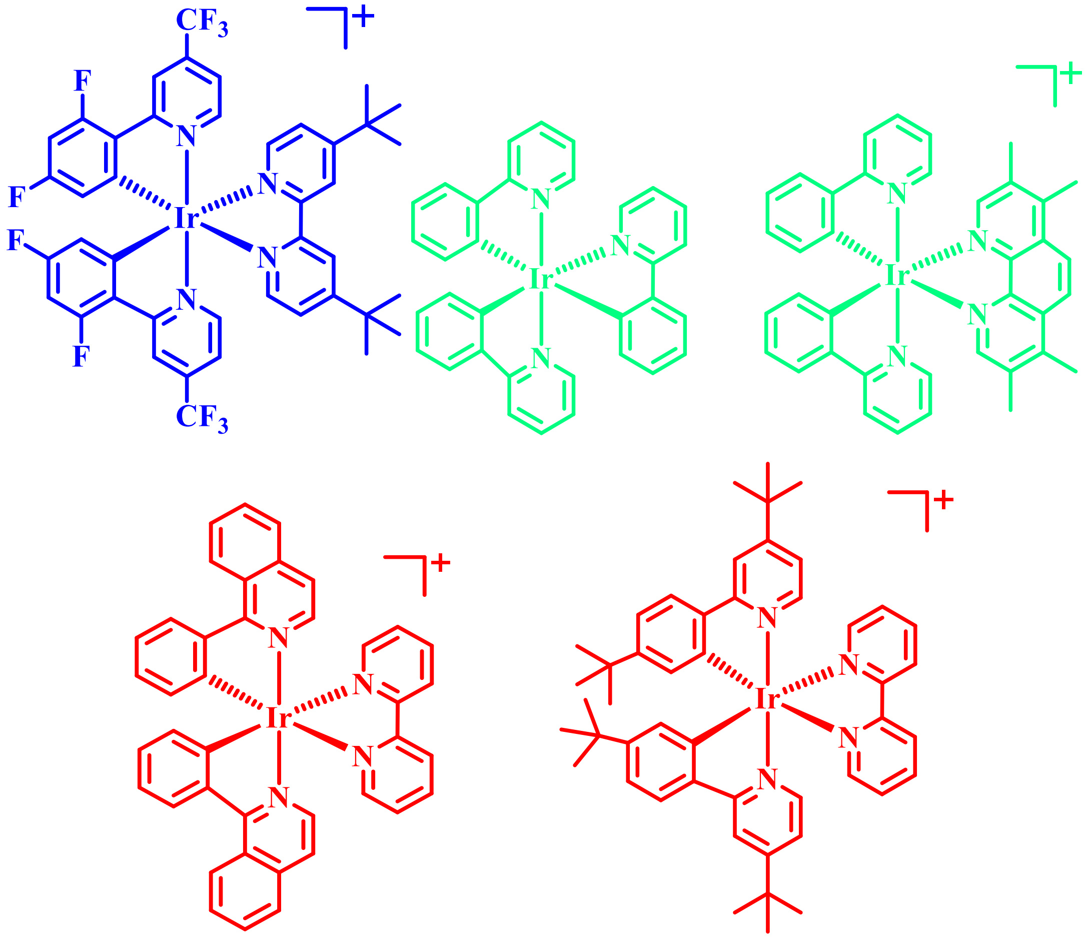

Figure 1-6 Examples of cyclometalated Ir(III) complexes with tunable emission in the visible region.[19, 30] The colour of the complex indicates the colour of emission.

The $Ir(ppy)_3$ (ppy=2-phenylpyridine) exhibits green emission,[52] (**Figure** 1-6). Substitution with electron-withdrawing groups, such as $-CF_3$, -F groups at the cyclometalating phenyl ring leads to MLCT and LC transitions being blue-shifted (**Figure** 1-6). The increased energy gap between HOMO and LUMO levels is because the HOMO is stabilised by increased strength of the σ-bond between Ir-C, and reduced electron density on the Ir(III) ion.[19, 26, 53] When the electron-withdrawing groups are attached to the pyridyl ring or ancillary ligand, a shift to lower energies (red-shift) of the emission is observed due to stabilisation of the LUMO level.[54]

Huang *et al.* [55] reported examples in which emission could be tuned through expansion of the π-conjugated system of the N^N chelating ligand, in 1-phenylisoquinoline iridium(III) complexes [Iridium(piq)$_2$(N^N)]PF_6 (where piq = 1-phenylisoquinoline) (**Figure** 1-6): these showed a great effect of changing ligands on the photoluminescence properties of Ir(III) complexes.[55] Likewise, using electron donating substituents such as $–C(CH_3)_3$[56] instead of electron-withdrawing ones will also cause change in emission energy.

1.3 Part Two: Lanthanides

This section is firstly concerned with the fundamental physical properties of lanthanide (Ln) elements and how Ln-based luminescence can be sensitised by indirect excitation processes, including excitation using d-block complexes as antennae units which then energy transfer to Ln(III) unit. The second part focuses on selected d-f complexes which display sensitised luminescence from Eu(III) and Tb(III) ions following sensitisation from a d-block antenna unit.

The lanthanide metals are the 15 elements starting with lanthanum, (atomic number 57), and ending with lutetium, (atomic number 71). These metals have very similar chemistry due to their general electron configuration, [Xe] $4f^n$ $5d^x$ $6s^2$. The fourth ionization energy for lanthanide ions is higher than the sum of the first three ionization energies, therefore, most lanthanide coordination chemistry is confined to trivalent oxidation state as [Xe]$4f^n$, where n= 0-14.[57] The decrease in size of ionic radii, which known as lanthanide contraction, may lead to a decrease in coordination numbers.[57, 58] The 4f-block lanthanide metals are only weakly affected by the coordinating ligands displaying weak ligand field effects when compared to the d-block transition metals. The weakness of the coupling is due to the shielding of the 4f orbitals by the overlying filled orbitals $5s^2$ and $5p^6$. In addition, the 4f orbitals act as core electrons and lie close to the nucleus, so the overlap between 4f orbitals and ligand orbitals is poor.[57] Lanthanide ions have high charge densities, therefore; the nature of the Ln(III)–ligand bond is predominantly electrostatic. Lanthanide(III) ions are hard Lewis acids and coordinate well to hard Lewis bases like amines and carboxylic ligands.[59] The coordination numbers and geometries of Ln(III) complexes are determined by inter-ligand steric effects. Because of the weak effect of the environments, the magnetic properties and the spectroscopic properties of the Ln(III) ions in their complexes are similar to the free Ln(III) ions.[57]

1.3.1 Physical properties and Luminescence of Lanthanides

The interest in Ln luminescence has been substantial over past few years because of its potential in applications such as optical imaging of cells,[58, 59] biological probes, medical diagnostics, analytical assays[60, 61] and for sensing of anions.[62] The popularity of lanthanides for such luminescence-based applications is due to their unique photophysical properties and long lifetimes, with different Ln(III) ions emitting in the visible or near-infrared regions.[63,64]

Ln(III) ions exhibit luminescence based on *f-f* transitions. These transitions are formally Laporte–forbidden according to electronic dipole selection rules, resulting in very low extinction coefficients of $\varepsilon < 1$ mol^{-1}.dm^{3}.cm^{-1}.[65] Moreover, the *4f* orbitals behave as a subshell due to shielding from the filled 5s and 5p shells. The spectroscopic properties (electronic absorption and emission spectra) arising from the *f-f* transitions are narrow and sharp because f-orbital energies are not affected much by ligand vibrations.[57] Furthermore, the luminescence properties of each lanthanide metal are determined by the energy gap between the emissive excited state and the ground state. The most well-known luminescent Ln(III) ions in the visible (Vis.) region are Eu(III) and Tb(III) which have energy gaps ΔE_{Eu} = 12 300 cm^{-1}($^5D_0 \rightarrow {}^7F_6$), ΔE_{Tb} = 14 800 cm^{-1} ($^5D_4 \rightarrow {}^7F_0$). For Gd(III) ΔE_{Gd} = 32 200 cm^{-1}, ($^5P_{7/2} \rightarrow {}^8S_{7/2}$) which is in the UV region. Eu(III) emissions occur between 550 - 750 nm while Tb(III) emits between 450 - 650 nm.[66] The f-f electronic transition can occur either with no change of spin (fluorescence) as in Nd^{+3}, Ho^{+3}, Er^{+3}, Pt^{+3} and Yb^{+3}: or with a change in spin (phosphorescence) as happens in Eu^{+3} (red), Gd^{+3} (emit in the UV region), Tb^{+3} (green), Dy^{+3} (yellow) and Tm^{+3} (blue).[58] La^{+3} and Lu^{+3} are not luminescent ions as they have no f-f transitions.

As mentioned above, direct excitation of Ln(III) ions is very difficult due to the f-f excitations being Laporte-forbidden and therefore having very low intensity. Luminescence can be generated from Ln(III) using direct excitation either by using a laser or at high Ln ions concentrations. Direct excitation by a laser is not practical in biological applications, however the indirect excitation of Ln(III) ions by energy-transfer (E.T) from an antenna group can generate luminescence from Ln(III) ions following an intramolecular energy transfer process.[34, 67, 68–71]

The mechanism of luminescence of a lanthanide complex containing transition antenna can be described as follows according to Jablonski diagram: An electron in S_0 of an antenna ligand is promoted to the singlet excited state after absorption of light. The fate of this photon can then follow two paths: i) relax to S_0 as fluorescence, which occurs with no change of spin like

$S_1 \rightarrow S_0$,[72] ii) conversion (non-radiative process) to the triplet excited state of an antenna ligand via ISC. From the T_1 state the photon can relax to S_0 via phosphorescence, ($T_1 \rightarrow S_0$),[72] or further transfer of energy to the excited of a Ln(III) ion can occur. Finally, E.T. to the Ln(III) ion is followed by the characteristic luminescence of the Ln(III) metal. This process is summarized in.**Figure** 1-7.

In this thesis, to facilitate E.T between components in d/f complexes the bridging ligand needs to be designed to coordinate completely to a Ln(III) ion at one site and an Ir(III) complex, which is easily excited by light, as sensitizer at the other site. When designing d-f complexes there are many factors should be considered to ensure successful sensitisation of luminescence from the Ln(III) centre via d-f energy-transfer. The nature of the lanthanide which needs to be excited dictates the type of d-block antenna which should have an excited state higher in energy than the Ln(III) excited state (**Figure** 1-7).

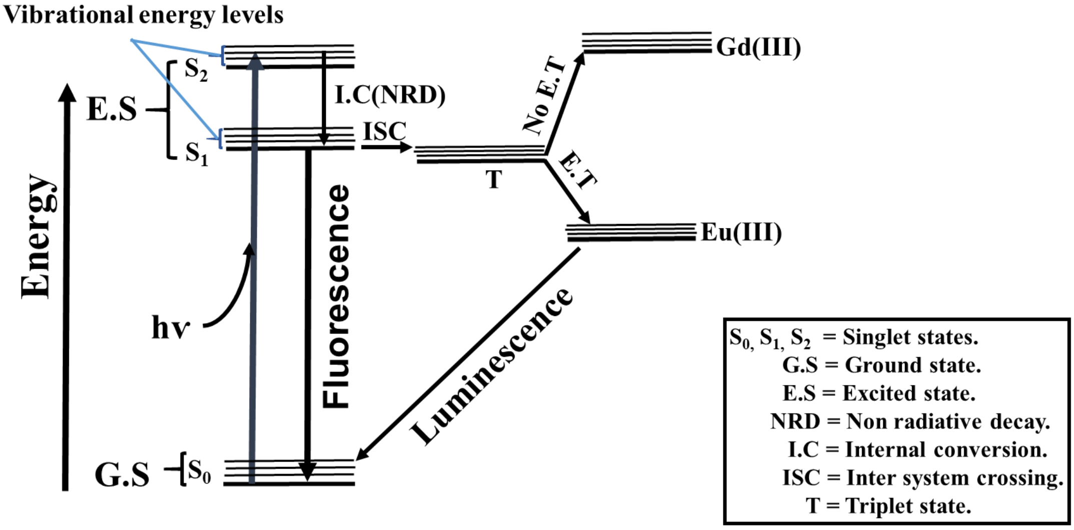

Figure 1-7 Jablonski energy level diagram for d-block complex and Ln emissive states.

Emission from Ln(III) ions occurs over a wide energy range depending on the ion. For example, Gd(III) emission appears in the UV region because of the largest energy gap while Nd(III) and Yb(III) emissions appear in the NIR region because of the smaller energies gaps.[35,73] A common cause of luminescence quenching for Ln(III) ions is non-radiative quenching due to energy transfer to vibrations of N-H, O-H and C-H bonds that lie close to the Ln(III).[73] Non-radiative decay is an important process to determine the Ln(III) luminescence quantum yield QY.[74] The direct coordination of H_2O or a molecule containing an N-H bond to the Ln(III) metal has a large effect on the emission intensity and lifetime of the Ln(III) by increasing the non-radiative decay pathways. The efficient way to minimise such non-radiative decay processes is to use a highly multidentate ligand (such as a macrocycle) which protects the Ln(III) ion from interactions with the solvent.[74]

1.3.2 Type of Antenna Units

The important factor restricting the choice of an antenna unit is that its emissive excited state energy must lie above the energy of the emissive Ln(III) state to achieve successful sensitisation emission from Ln(III).[71,75] Recently, Ir(III) complexes have become of great interest as antenna groups to sensitise Ln(III) because the emissive triplet excited state of the Ir(III) chromophore can be higher than the excited state of Eu(III) and Tb(III). This permits the d-complex fragment to act as the antenna group.[75] Usually an antenna triplet excited state needs to be at least 17500 cm^{-1} higher than the lowest excited state of 17200 cm^{-1} for Eu(III) and 20500 cm^{-1} for Tb(III) for efficient sensitisation of Ln(III) without thermally activated back energy-transfer (BET) at room temperature, that would result in a loss of luminescence. The sensitization of the Ln(III) ion occurs from the d-block chromophore excited state *via* the aromatic bridging ligand such as naphthyl group,[76] terpyridines[77] and bipyridines.[78]

1.3.3 *d*-block complexes and their emission properties

Complexes of 3rd row transition metals, such as Ir(III) and Re(I), which display luminescence at room temperature, have received at great deal of attention over the past 40 years, having potential applications in lighting, imaging and bio-sensing. The design strategies for d-block luminescent complexes are related to covalent bond, σ-donating interaction between L and metal centre.[36] A good example of a room temperature luminescent d-block complex is $[Ru(bpy)_3]^{2+}$, shown in **Figure** 1-8, where bpy is a 2,2′-bipyridyl ligand. The emissive state in this complex is a triplet metal to ligand charge transfer (^{3}MLCT) from the Ru(II) metal ion to a bpy ligand (d-π^*), which gives rise to a broad structure luminescence spectrum as shown in **Figure** 1-9.[79]

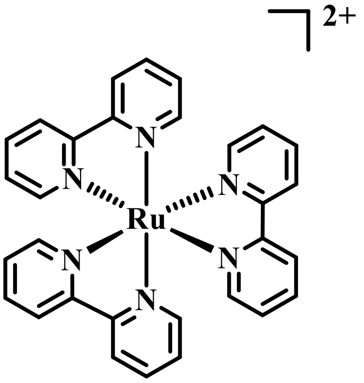

Figure 1-8 Chemical structure of $[Ru(bpy)_3]^{2+}$ complex.

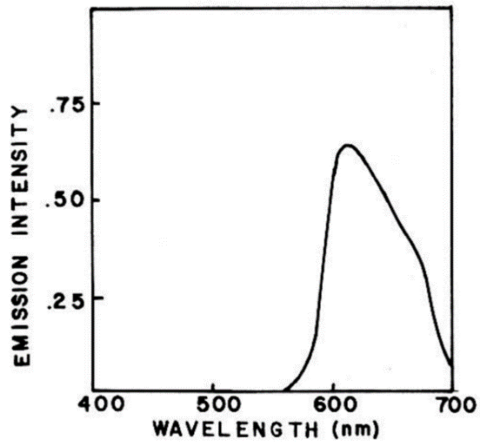

Figure 1-9 Emission spectrum of $Ru(bpy)_3^{2+}$ in aqueous solution at room temperature, taken with permission from ref. 79.

Pt(II) complexes with cyclometallated aromatic ligands can also have strong luminescence properties, which are exploited in cell imaging applications. Pt(II) is a d^8 metal ion and adopts a square planar geometry. The ligand 1,3-di(2-pyridyl)benzene(bpyb) (**Figure** 1-10) is based on N^C^N- coordination to make a complex employed in cell imaging because of its desirable photophysical properties, most notably a high quantum yield, long emission lifetime (µs timescale) and high photostability. This type of compound has a rigid and strong ligand field based on a tridentate cyclometalled ligand. These factors allow this class of complexes to have high d-d energy states relative to the emissive excited states, which means that quenching by d-d states is minimised and the luminescence is strong.[80]

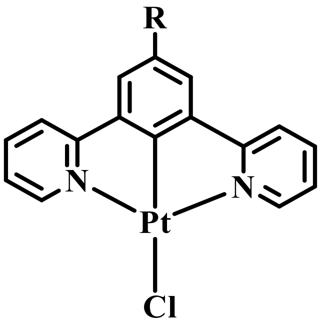

Figure 1-10 Chemical structure of [PtLCl] complexes, R=H, C(O)CH_3, CH_3 and $C_6H_4N(CH_4)_2$.[80]

1.4 Photoinduced energy transfer using d-f dyads.

Many researchers are interested to sensitise Ln(III) luminescence by using d-block metal ions in d/f dyads. Many d-block complexes can have strong MLCT absorption bands which can act as photophysical antennae in many polynuclear assemblies such as coordination networks.[81,82] Consequently the study of d-f dyad complexes has developed rapidly.[83] An ideal d-block antenna complex needs to have the following properties: i) stability during photoexcitation; ii) high absorption coefficents in the UV-Vis to NIR region; iii) a vacant externally-directed co-ordination site to enable co-ordination of the Ln (III) ion (**Figure** 1-11); iv) a long-lived excited state, to increase the probability of photoinduced energy transfer to the Ln(III) ions. A sample type of d/f dyad from the Ward group[84,85] is shown in **Figure** 1-11.

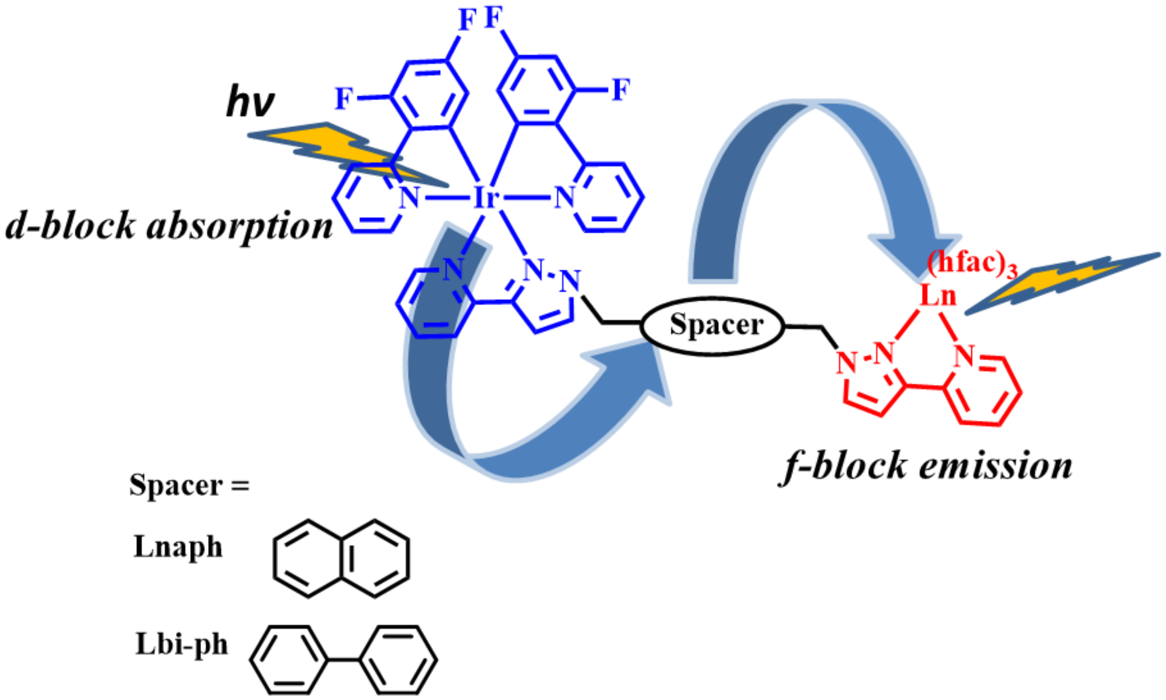

Figure 1-11 The basic design of d→f complex for photosensitisation of Ln(III) ion.[85]

With the aim of achieving the d→f E.T process, when d-block is as an energy donor and Ln(III) is as an energy acceptor. Good overlap between the absorption spectrum of the Ln(III) acceptor and the emission spectrum of the d-block donor unit is required to ensure E.T to the Ln (III) ion.[86, 87] It is worth to mention, that there are many factors that could reduce the efficiency of the transfers energy process, such as short lifetime and long separating distance between the partners.[64]

There are two mechanisms that describe the process of energy transfer from the donor (chromophore) excited state to the acceptor: these are the Förster and Dexter mechanisms.

1.4.1 Förster mechanism

This process is based on a dipole–dipole interaction (or Columbic interaction) through space, between the electronic transition dipole moments of the donor and acceptor transitions. The rate of E.T. occurring via this mechanism is proportional to r^{-6}. For a successful Förster energy transfer, there should be good overlap between the absorption spectrum of the donor and the emission spectrum of the acceptor. **Figure** 1-12 shows the Förster mechanism of energy transfer. This commonly occurs between singlet states on the donor and acceptor components.[88, 89]

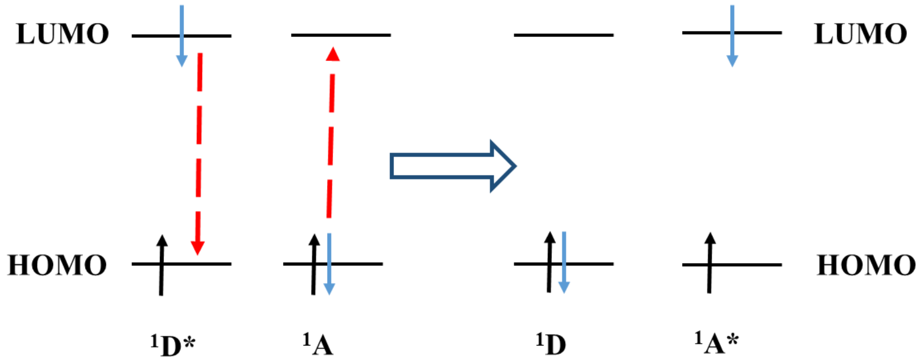

Figure 1-12 Singlet-singlet Förster energy transfer mechanism. D= donor, A= acceptor, 1=singlet and *=excited state.

1.4.2 Dexter mechanism

The process relies on the simultaneous exchange of two electrons between donor and acceptor. It occurs through orbital overlap, *i.e.* close donor/acceptor contact or through the bonds of a bridging group. The rate of E.T occurring via this mechanism is proportional to e^{-r} as exponential functions decay more quickly than r^{-6}, then the effect of distance is more important than for the Förster energy-transfer and it requires a distance between donor and acceptor of typically less than 10 Å. Also, the energy transfer by this mechanism are not limited to singlet states, and in fact commonly involves energy transfer between triplet states on the donor and acceptor components (**Figure** 1-13).[90–92]

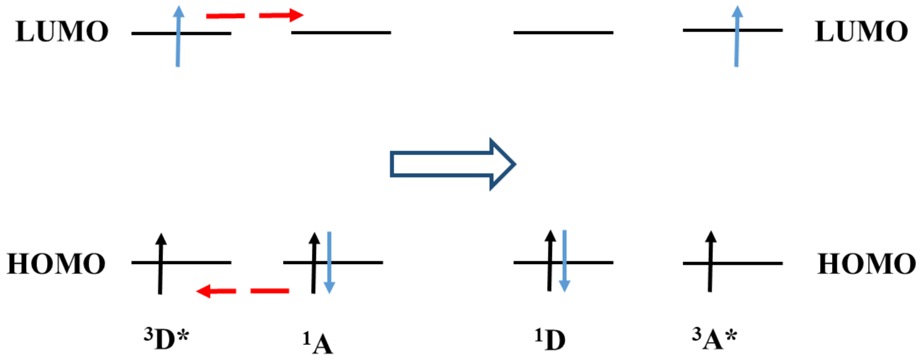

Figure 1-13 Triplet-triplet Dexter energy transfer mechanism. D= donor, A= acceptor, 1=singlet and *=excited state.

1.5 Work from other groups

Other groups have also investigated energy transfer to Ln(III) ions in mixed d-f dyads, often in order to achieve NIR luminescence from lanthanides such as Yb(III) or Nd(III).[93] For example in one of the earliest examples, Beeby *et.al.*[94] used a of Pd(II)-porphyrin chromophore to sensitise luminescence from a Yb(III) macrocyclic complex (**Figure** 1-14).[94]

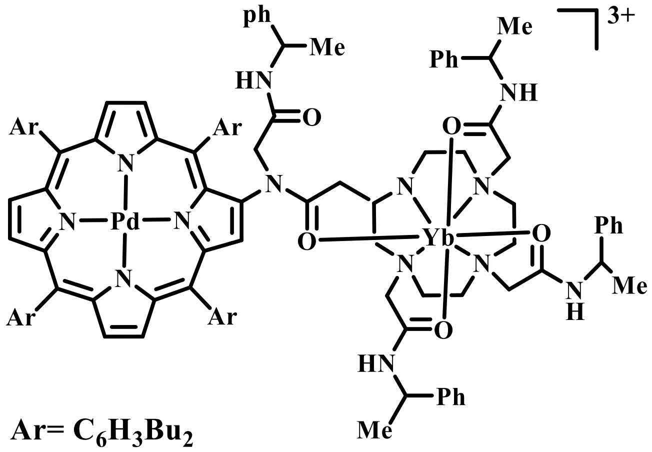

Figure 1-14 Chemical structure of Pd(II)-Yb(III) dyads.[94]

Van Veggel *et.al.*[81] showed that the energy transfer happens from the $[Ru(bpy)_3]^{2+}$ to a Yb(III) and Nd(III) centre (**Figure** 1-15) because of the high spectral overlap between energy levels of the donating $[Ru(bpy)_3]^{2+}$ and receiving Ln(III) centre. The sensitized NIR luminescence emission of Ln(III) units was enabled by excitation with Vis. light. The E.T rate in Ru-Nd_2 complex was faster than the E.T rate in Ru-Yb_2 complex due to the energy gap between ^{3}antenna level and Nd(III) excited state being higher than ^{3}antenna level and Yb(III) excited state (approximately at 17100 cm^{-1} and 10240 cm^{-1}, respectively).[81]

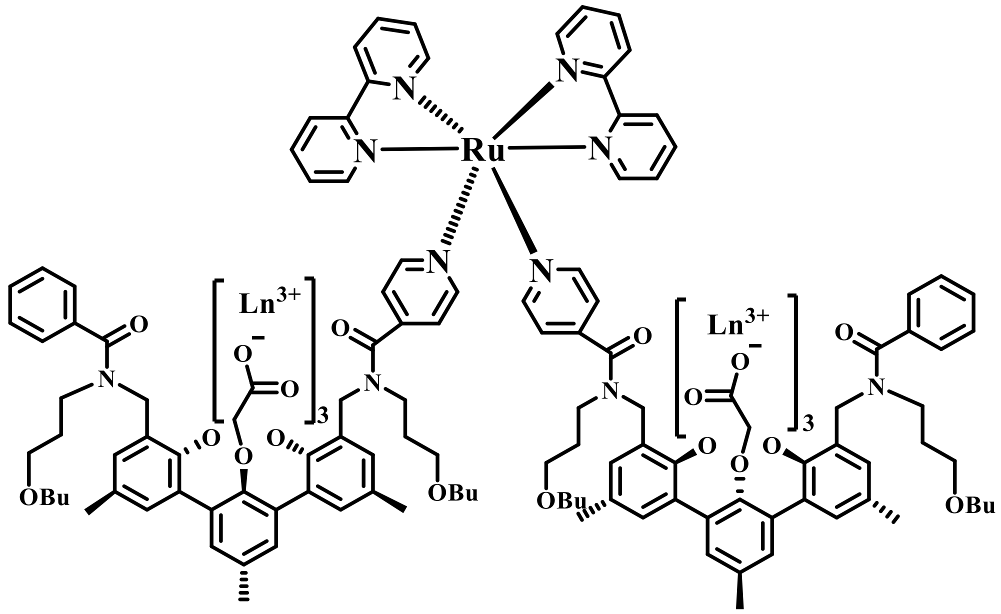

Figure 1-15 Chemical structures of sensitizers $[Ru(bpy)_3]^{2+}$ for Ln, (when Ln=Nd^{+3} and Yb^{+3}).[81]

De Cola and co-workers[95] in 2005 used a cyclometalled blue-emitting Ir(III) complex connected to a Eu(III) terpyridine complex through a triazole-based spacer ligand to study d→f photoinduced energy transfer (PEnT) in Ir/Eu dyads (**Figure** 1-16). The complex showed a ^{3}MLCT transition in the visible region for the Ir(III) unit, and π-π* transitions in the UV. On excitation of the Ir(III) unit, Eu(III)-based emission from the $^5D_0 \rightarrow ^7F_2$ transition was observed. The two components were linked via the terminal carboxylate units of the Ir(III) unit which coordinated to the Eu(III) centre. An interesting white light emission was observed due to a balance between Ir(III)-based blue emission and Eu(III)-based red emission. The resulting white light emission property was exploited in white-emitting electrophosphorescent devices.[95]

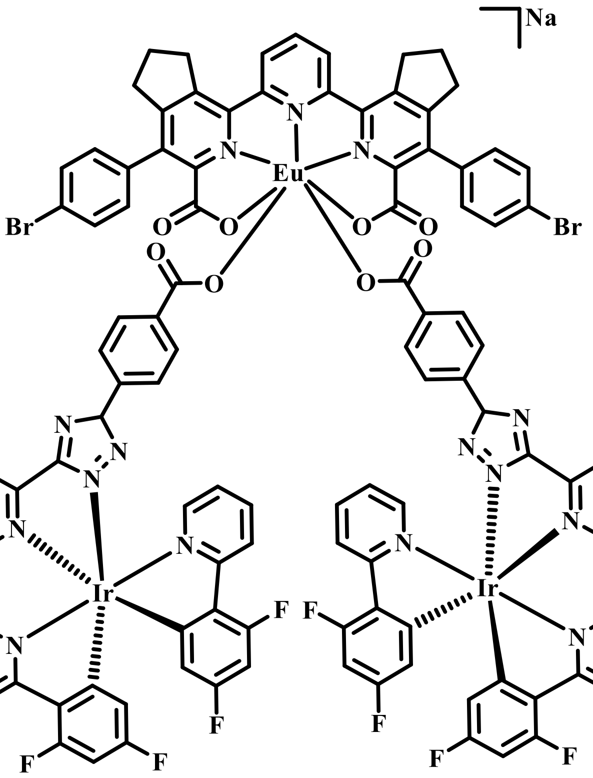

Figure 1-16 The chemical structures of (1) cyclometalated Ir(III) complex and (2) Eu(III) terpyridine complex.[95]

Huang *et.al.*[96] reported a series of Ir(III)/Eu(III) dyads in which the Ln(III) ion is bound to a bridging N^N ligand **Figure** 1-17 that has a vacant O,O-donor site to bind a lanthanide(III) ion. The emissive energy level of Eu(III) is $^5D_0$ which has an energy of *ca.* 17500 cm^{-1}, and the excited-state energy level of the donor Ir(III) chromophore should lie at least 2000 cm^{-1} (as mentioned before) higher than this to prevent BET. The result of the study was that E.T from the Ir(III) complex to Eu(III) complex occurs *via* the bridging ligand. The triplet energy level of ligand is higher than Eu(III) energy level and lower than the ^{3}MLCT Ir(III) energy level.[96]

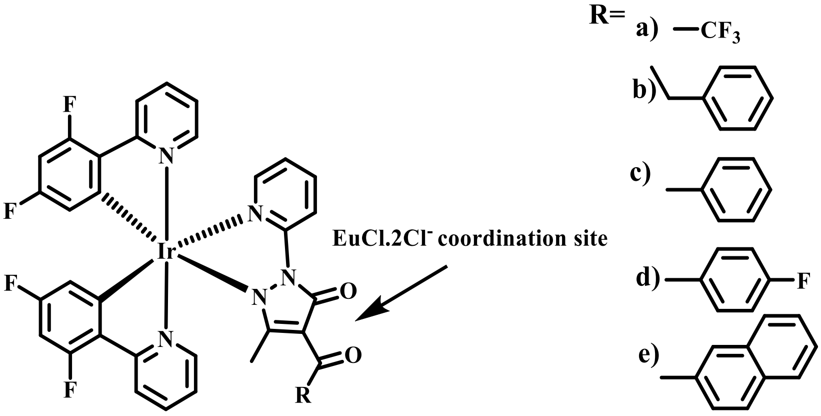

Figure 1-17 Ir(III) N^N bridge ligand.[96]

1.6 Previous work by the Ward group

The Ward group and co-workers have been interested in the using transition metals as energy donor (chromophores) to make d-f energy transfer dyads, where the two metals are joined through an organic spacer. The photophysical properties of a series of d/f systems have been studied.[85,97] The first series of complexes that the Ward group investigated as the basis of d-f dyads was a simple Ln(diketone)$_3$.2H$_2$O with a bidentate di-imine ligand (as organic chromophore),[98] for example phenanthroline or bipyridine (**Figure** 1-18). These complexes are best formed in DCM, as more polar solvents break up the di-imine adduct.[84]

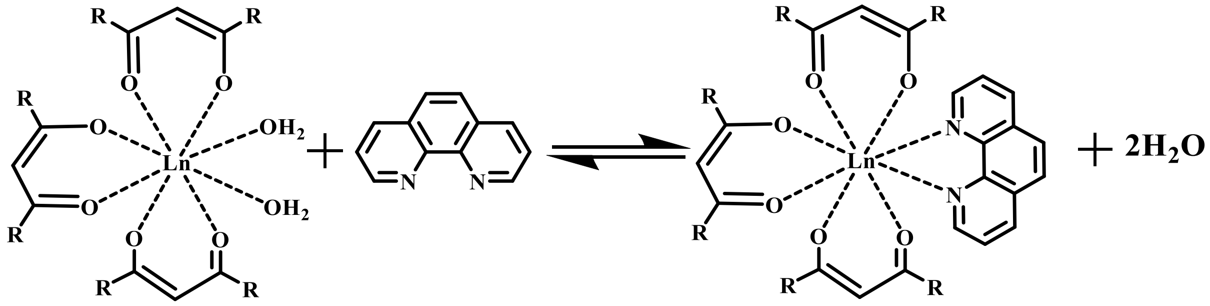

Figure 1-18 Ln(diketonate)$_3$(diimine) complex structure.[84]

The first example of a simple d-f dyad in this family based on this type of lanthanide component was a Re(I)/Ln(III) system. The complexes [Re(bpym)(CO)$_3$Cl] (bpym=2,2′-bipyrimidine) and [Re(bppz)(CO)$_3$Cl] (bppz=2,3-bis(2-pyridyl)pyrazine) each contain a di-imine ligand with a vacant bidentate site, which is able to bind the Ln(diketonate)$_3$ unit (**Figure** 1-19).[99]

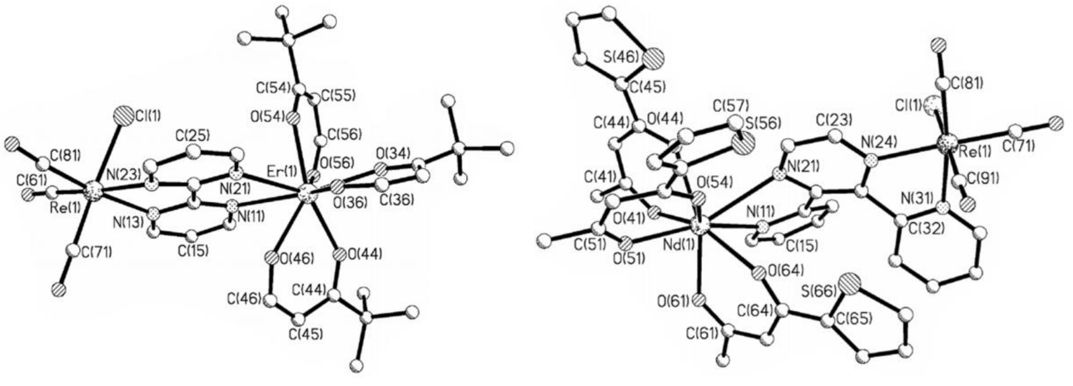

(a) **(b)**

Figure 1-19 X-ray structure of (a) [Re(bpym)(CO)$_3$Cl] and (b) [Re(bppz)(CO)$_3$Cl], taken permission from ref. 99.

Also a [Re(CO$_3$)ClL](L=bis-bidentate ligand Py-CH=N-N=CH=Py) with two iminopyridine binding sites (when Py=2-pyridyl) was used to prepare d/f dyads, as shown in **Figure** 1-20.[100]

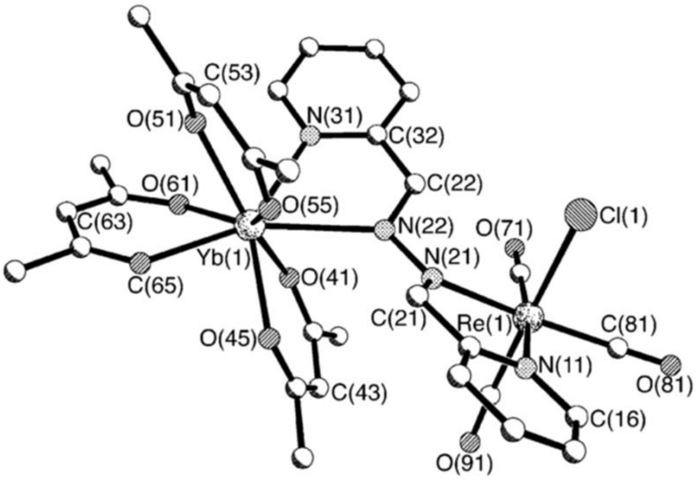

Figure 1-20 Crystal structure of [Re(CO$_3$)Cl(µ- Py-CH=N-N=CH=Py)Yb(hfac)$_3$] with F atoms on the (hfac) ligands for clarity). Permission was taken from ref. 100.

These complexes reacted with Ln(diketonate)$_3$.2H$_2$O to form the dinuclear Re/Ln dyads. Binding constants were determined by UV/Vis spectroscopy titrations in DCM and were *ca.* 10^5 M^{-1}. The mechanism of d→f energy transfer in [Cl$_2$Pt(µ-dppz)Nd(btfa)$_3$] (dppz= 2,3-bis(2-pyridyl)pyrazine), (btfa= benzoyltrifluoroacetone) (**Figure** 1-21) and [(PPh$_3$)$_2$Pt(µpdo)Gd(tta)$_3$](pdo=5,6dihydroxy1,10phenanthroline),(tta=thenoyltrifluoroacetone) complexes (**Figure** 1-22) was studied. The conjugated bridging ligands provides electronic coupling which will facilitate Dexter energy-transfer mechanism and these complexes show sensitized NIR luminescence of Ln(III) following excitation of the d-block chromophore.[99,101]

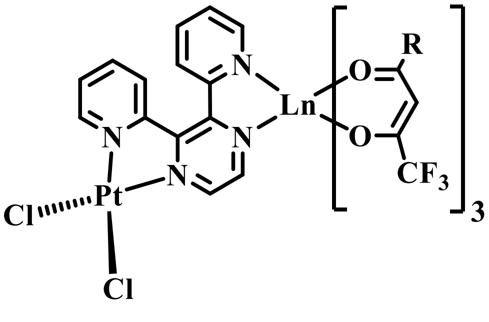

Figure 1-21 Chemical structure of [(Cl)$_2$Pt(µ-dppz)Nd(btfa)$_3$], When Ln = Nd(III), R = 2-thienyl.[101]

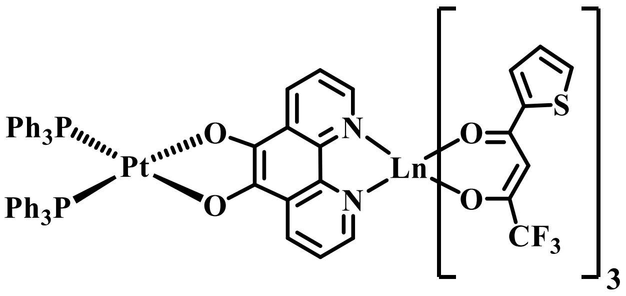

Figure 1-22 Chemical structure of [$(PPh_3)_2$Pt(μ-pdo)Gd$(tta)_3$], When Ln = Gd(III).[102]

Other studies have looked at Pt(II) complexes as energy donors such as, [Pt(dppe)(pdo)] (pdo coordinated as an O,O′-donor chelate), $PtCl_2$(bppz),[101, 102] and [Pt(bpym)$(CC\text{-}C_6H_4CF_3)_2$] units as shown in **Figure** 1-23,[103] as chromophores for Ln centres.

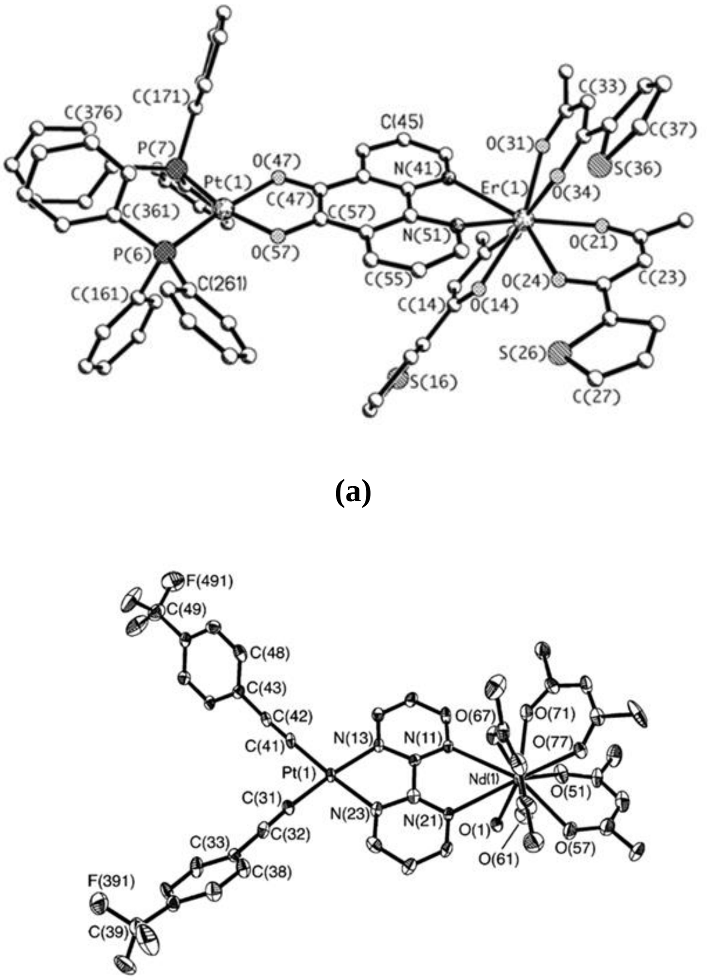

(a)

(b)

Figure 1-23 (a) X-ray structure of [Pt$(dppe)_2$(μ-pdo)Gd$(tta)_3$], taken with permission from ref. 102. (b) Crystal structure of [Pt(μ-bpym)$(CC\text{-}C_6H_4CF_3)_2$Nd$(hfac)_3$], taken with permission from ref. 103.

Recently, the Ward group[104] has studied the photophysical properties of a series of blue-luminescent Ir(III) complexes ^{24}Ir.L^{pph} (^{24}Ir= 2-(2,4-difluorophenyl)pyridine, L^{pph} = bis(pyrazolylpyridine) bridging ligand with a phenyl spacer) and ^{24}Ir.L^{pBiph} (L^{pBiph} = biphenyl spacer) as shown in **Figure** 1-24. The organic ligand on the Ir(III) centre has a vacant pyrazolyl-pyridine binding site, which can bind strongly with Ln(III) fragments to give dinuclear d/f complexes which show E.T. from the d-block unit to the lanthanide(III) ion.[104]

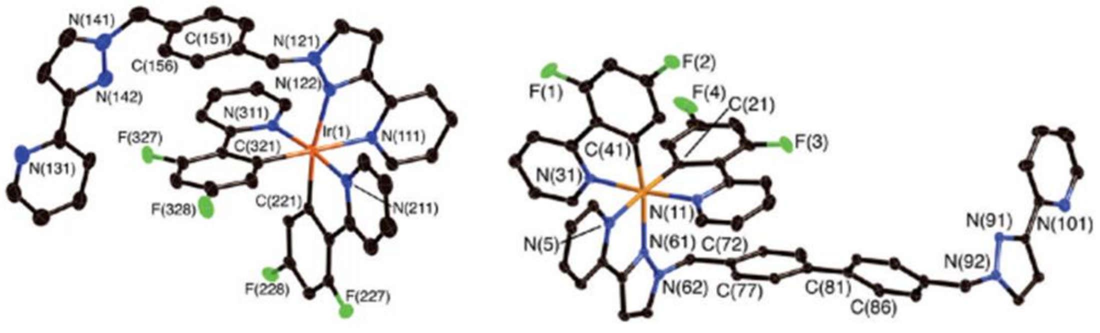

(a) **(b)**

Figure 1-24 X-ray structure of complex (a) ^{24}Ir.L^{pph} and (b) ^{24}Ir.L^{pBiph}, taken with permission from ref. 104.

Energy transfer from the Ir.L^{pytz} chromophore (pytz=3,2-di-(2-pyridyl)-4H-1,2,4-triazole), (**Figure** 1-25), to Eu(III) in an Ir/Eu dyad results in significant quenching of the Ir-based luminescence and the appearance of sensitised Eu-based luminescence, as shown in **Figure** 1-26. Emission from the Tb(III) analogue was weak in comparison, due to the large amount of Tb----Ir back energy transfer (**Figure** 1-27).[97]

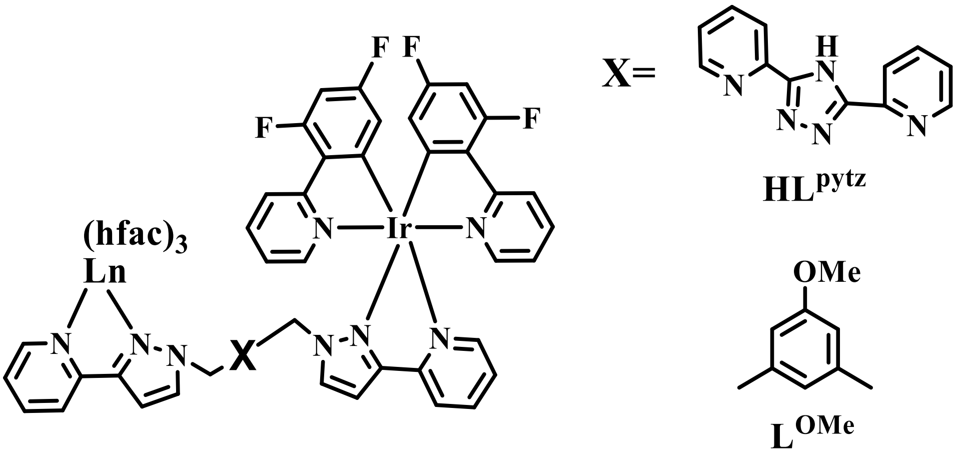

Figure 1-25 Chemical structures of Ir/Ln dayds with L^{pytz} and L^{OMe} spacers, when Ln=Eu(III), Tb(III).[97]

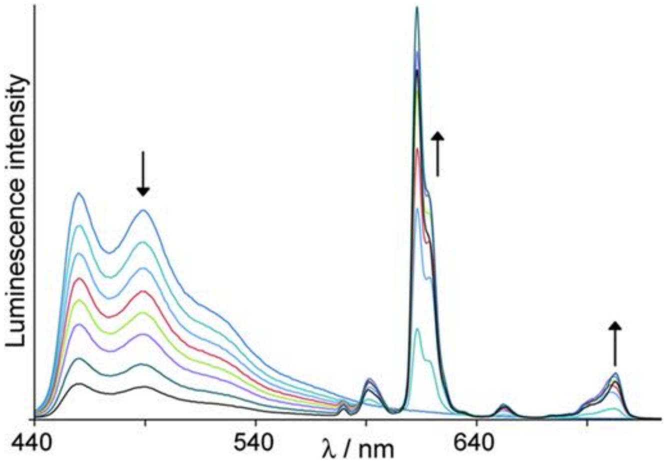

Figure 1-26 Luminescence titration in which portions of Eu(hfac)$_3$.2H$_2$O are added to Ir.L^{pytz} in CH$_2$Cl$_2$, taken permission from ref. 97.

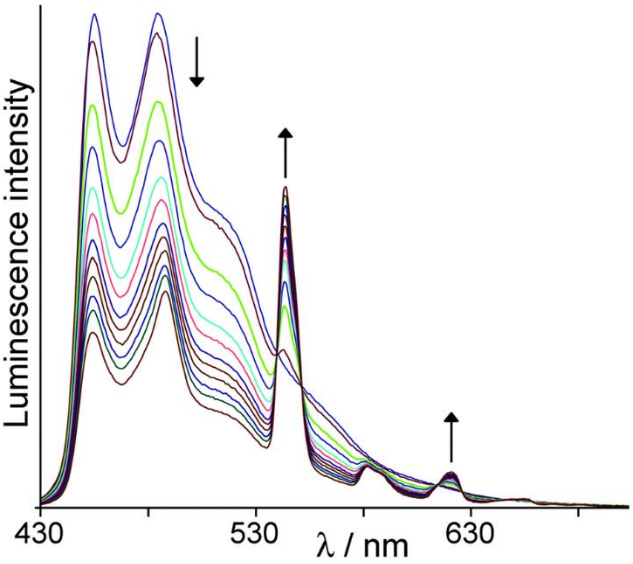

Figure 1-27 Luminescence titration in which portions of Tb(hfac)$_3$.2H$_2$O are added to Ir.L^{OMe} in CH$_2$Cl$_2$, taken permission from ref. 97.

1.7 Application of cyclometalated Ir(III) complexes

Cyclometalated Ir(III) complexes are used in a variety of applications. Some examples are given below:

i) Ir(III) complexes have been used as luminescent chemosensors for cations or anions,[112, 113] and also volatile organic compounds – anything that can interact with the Ir(III) complex and affect the emission wavelength properties.[106, 107] Also, many Ir(III) polypyridine complexes have been reported as pH probes.[106, 108] Moreover,

ii) the properties of Ir(III) complexes such as high ϕ, high sensitivity and long emission lifetime, can be exploited for oxygen detection through energy transfer from the

^{3}Ir(III) complex excited state to $^3O_2$ to generate $^1O_2$. As well, Ir(III) complexes have been used as luminescent probes for biomolecules such as proteins,[106] amino acids[109] or DNA[110] detection of these can be observed through quenching of Ir(III) emission.[53,106,111] Furthermore, interesting research has been published on the use of Ir(III) emission for detection of explosive materials such as 2,4,6-trinitrophenol (PA) or 2,4,6-trinitrotoluene (TNT).[112, 113]

iii) The photophysical properties of Ir(III) complexes, like large Stokes' shifts (which prevent self-quenching due to re-absorption of light), high emission quantum yield, tunable emission colour and long lifetimes, combine to make Ir(III) complexes suitable for applications in cell imaging.[30,114]

iv) Non-toxic Ir(III) complexes, with affinity for tumour cells over healthy cells, can be used in photodynamic therapy (PDT) for tumour treatment with a high degree of spatial precision. The mechanism of Ir(III) photodynamic therapy involves the excitation of the Ir(III) unit as photosensitiser (PS) in the normal way to generate the triplet excited state ^{3}PS*, which can then undergo a subsequent type 1 or type 2 process. A type 1 process is when ^{3}PS* participates in proton or electron transfer reactions which generates ultimately reactive oxygen species. In contrast, type 2 processes are initiated by ^{3}PS* and can form $^1O_2$ through energy-transfer to ground-state $^3O_2$: $^1O_2$ is highly reactive and is an excellent oxidizing agent which can kill tumour cells in a biological environment.[115] Both types of process (type 1, which is proton or electron transfer; and type 2, which is energy transfer) are summarised in the **Figure** 1-28.

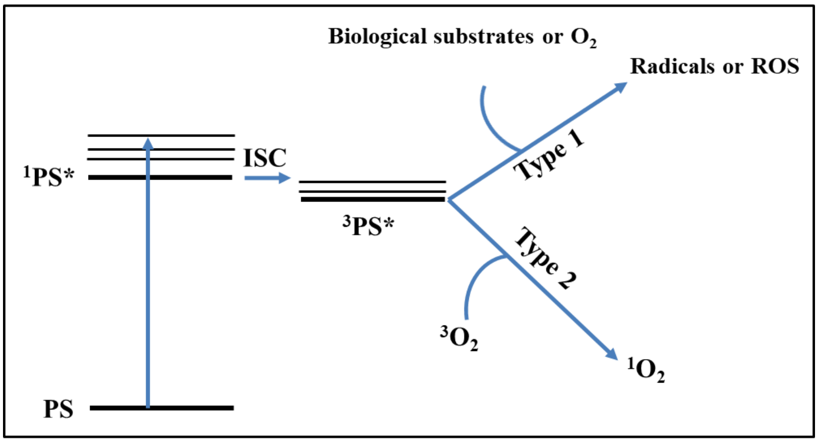

Figure 1-28 Mechanisms of the processes of PDT action.

v) Cyclometalated Ir(III) complexes can be used in photoredox catalysis for many redox reactions such as H_2 production via proton reduction[116,117] or CO_2 reduction.[19] The cyclometalated Ir(III) complexes are coordinatively saturated with octahedral coordination spheres around Ir core which prevents direct interaction of substrates with the Ir centre, but outer-sphere electron transfer can occur easily.

vi) Recently, an interesting development is the use of phosphorescent Ir(III) complexes for security protection. An Ir(III) complex $[ppy_2IrNH]^+PF_6^-$ was used for data encryption and decryption (read-out). The strategy of that depends on two techniques: fluorescence lifetime imaging microscopy (FLIM) and time-gated luminescence imaging (TGLI). On security paper which is impregnated with, for example, the $[ppy_2IrNH]^+PF_6^-$ is an encouraging alternative to fluorescent organic dyes due to its tuneable emission colour that can be used as “invisible ink”.[107]

vii) Neutral and cationic Ir(III) complexes have been used in solid-state lighting devices such as OLEDs and LECs.[118]

1.8 Ir(III) complexes as imaging agents and biomolecular probes

The luminescence energy of Ir(III) complexes are readily tuned either by changing the nature of C^N and N^N ligands, or by adding electron withdrawing groups on C^N ligands to facilitate emission in the visible region.[119] The family of Ir(III) complexes in form $[Ir(ppy)_2(N^\wedge N)]^+$ and their derivatives are attractive for various biochemical applications, and utilized as labels in cell imaging and as active components in therapeutic treatments.[120] An Ir(III) complexes have many features which allow these complexes to be used as labels: excited by visible light which prevents damage to cells (which occurs if UV light is used), highly absorption in the visible region, tuning the emission properties over a wide region of wavelengths because of the presence of multiple emissive excited states for instance MLCT, LLCT and ILCT.[22,120,121,122]

The first study to use Ir(III) complexes in the cell imaging was reported by Li *et.al.*[123] who prepared low-cytotoxicity monocationic Ir(III) complexes with different N^N ligands (**Figure** 1-29). The luminescence properties of these complexes occur in the region from $\lambda_{max.}$ 623 nm (red luminescence) to $\lambda_{max.}$ 517 nm (green luminescence), which is a good region to visualize the epithelioid carcinoma cells HeLa cells. These Ir(III) complexes have fluorinated cyclometalating ligands and a positive charge that help permeability across the membrane and localisation in the cytoplasm (**Figure** 1-30).

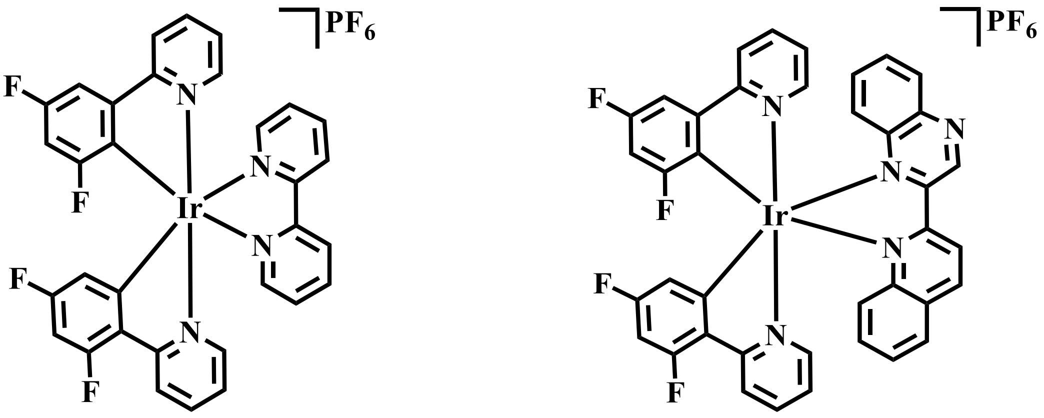

(1) **(2)**

Figure 1-29 Chemical structure of the (1) $[Ir(dfppy)_2(bipy)]^+$and (2) $[Ir(dfppy)_2(quqo)]^+$complexes.

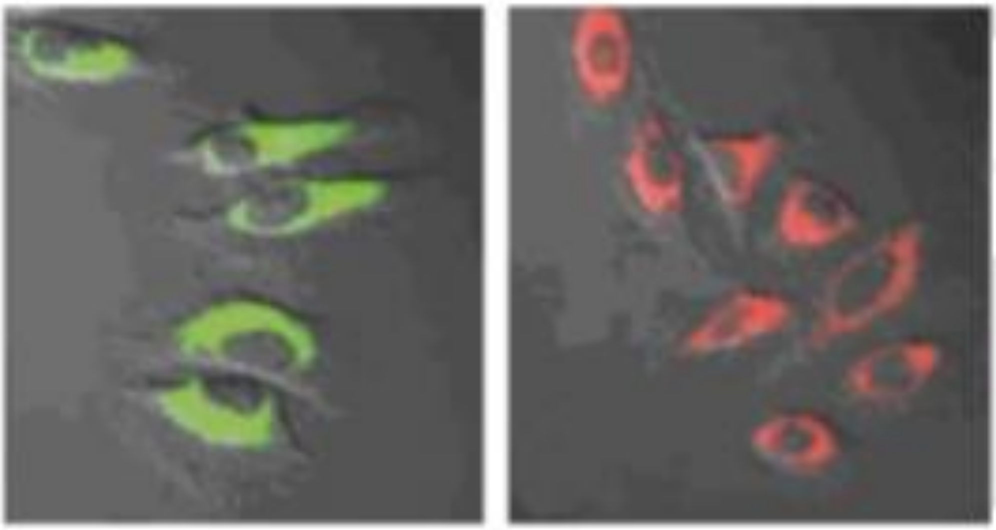

Figure 1-30 Luminescence images of incubated (1) and (2) complexes with HeLa cells. Reproduced with permission from ref. 123.

Li *et.al.*[124] have investigated cis-$[Ir(ppy)_2(DMSO)_2]PF_6$ (**Figure** 1-31) for labelling of biomolecules. This complex is not emitting at room temperature but is a good emitter in the presence of histidine-rich proteins like BSA which replace DMSO molecules with histidine. This bis-cyclometalated Ir(III) complex was investigated by confocal microscopy on two cell lines (HeLa and HeLa derivative (KB)) and on primary cells (mesenchymal stem cells (MSCs)) and fibroblast synoviocyte cells (FLS). The result of the study indicated that the uptake of 10 μM of the complex happens via an energy- dependent pathway, with the complex being localized in the nuclei rather than cytoplasm of live cell (**Figure** 1-32); cellular emission was observed after 6 min. incubation.

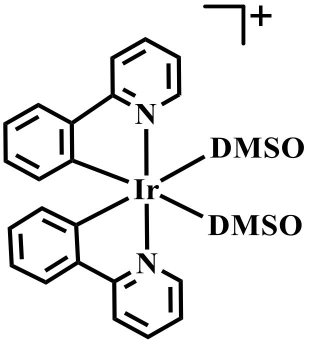

Figure 1-31 Chemical structure of Ir(ppy)$_2$(DMSO)$_2$$^+$.

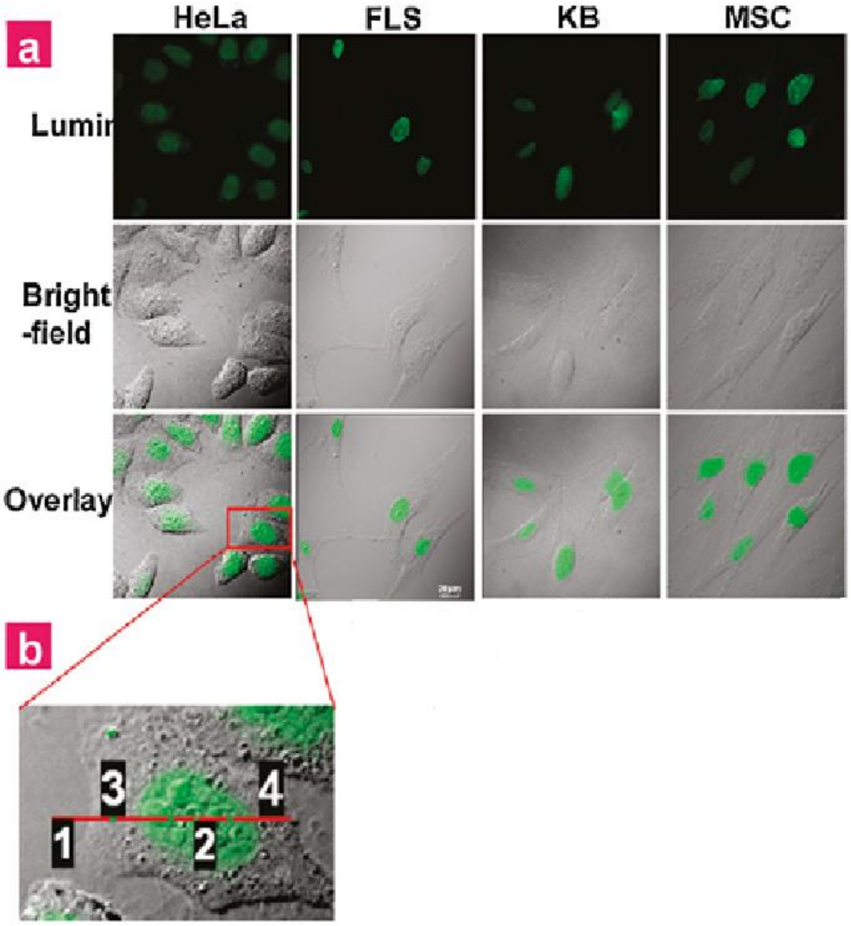

Figure 1-32 (a) Confocal images of incubation of [Ir(dfppy)$_2$(bipy)]$^+$with HeLa, FLS, KBr and MSC cells for 10 min. (b) Zoom –in to the (1) extracellular region, (2) nuclear region and both (3) and (4) cytoplasm region. Permission was obtained from ref. 124.

Murphy *et.al.*[125] have examined cell imaging of two closely related neutral Ir(III) complexes; *fac*-Ir(ppy)$_3$ and Ir(ppy)$_2$(pybz), where pybzH is pyridylbenzimidazole (**Figure** 1-33). In spite of *fac*-Ir(ppy)$_3$ being highly luminescent with close to unity quantum yield, only weak images could be obtained from cells at high concentrations. However, Ir(ppy)$_2$(pybz) complex showed successful imaging with localization in lysosomes and weak localization in cytoplasm. The reason for this difference in the behavior of complexes was attributed to the benzimidazole nitrogen atom in $Ir(ppy)_2(pybz)$, that could form H-bonding or could form protonated $Ir(ppy)_2(pybz)$ complex during uptake and localization processes (**Figure** 1-34).

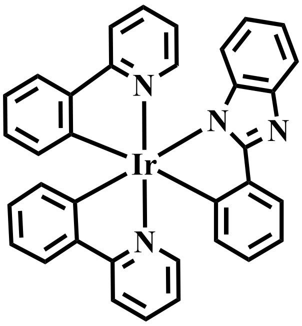

Figure 1-33 Chemical structure of $Ir(ppy)_2(pybz)$ complex.

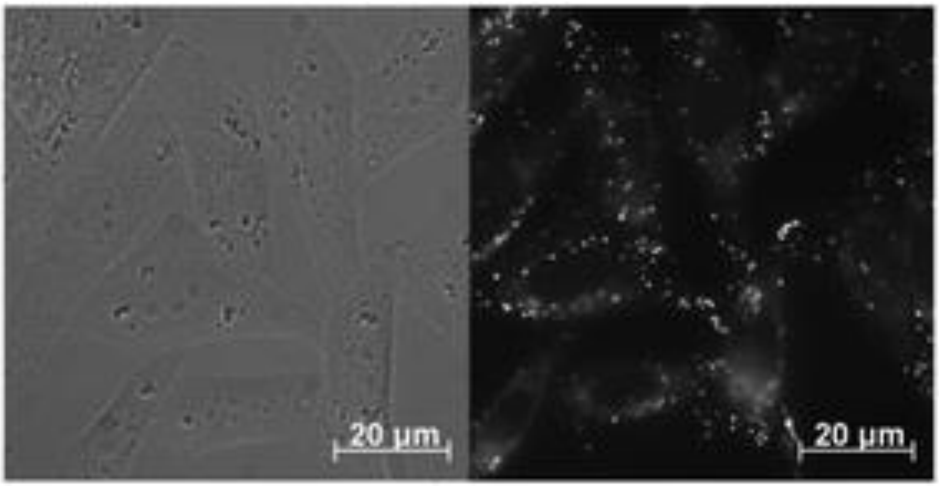

Figure 1-34 Bright- field and fluororescencemicroscopy images of CHO cells after incubation with $Ir(ppy)_2(DMSO)_2^{+,}$ Permission was taken from ref. 125.

Liu *et.al.*[126] have designed two NIR-emitting Ir(III) complexes $[Ir(pbq\text{-}g)_2(N^\wedge N)]^+Cl^-$ (*pbq-g* = phenylbenzo[*g*]-quinoline; N^N = 2-(1-benzyl-1*H*-pyrazol-3-yl) pyridine (**Ir-a**) (**Figure** 1-35), and 2-(1-(naphthalen-1-ylmethyl)-1*H*-pyrazol-3-yl) pyridine (**Ir-b**) (**Figure** 1-35) with excellent photophysical and imaging properties. In spite of (**Ir-a**) and (**Ir-b**) complexes having different N^N ligands, interestingly both of them showed similar NIR emission bands with λ_{max} at 751 nm and 750 nm, respectively in PBS solution. Cellular imaging studies of these two complexes revealed that uptake happens by an energy-dependent rather than the endocytosis pathway.

This study concluded that (**Ir-a**) and (**Ir-b**) complexes have high mitochondrial specificity (in HeLa cells), low cytotoxicity, are stable at different pH and highly photostable (**Figure** 1-36). All these properties encourage the use of these complexes in bioimaging applications.

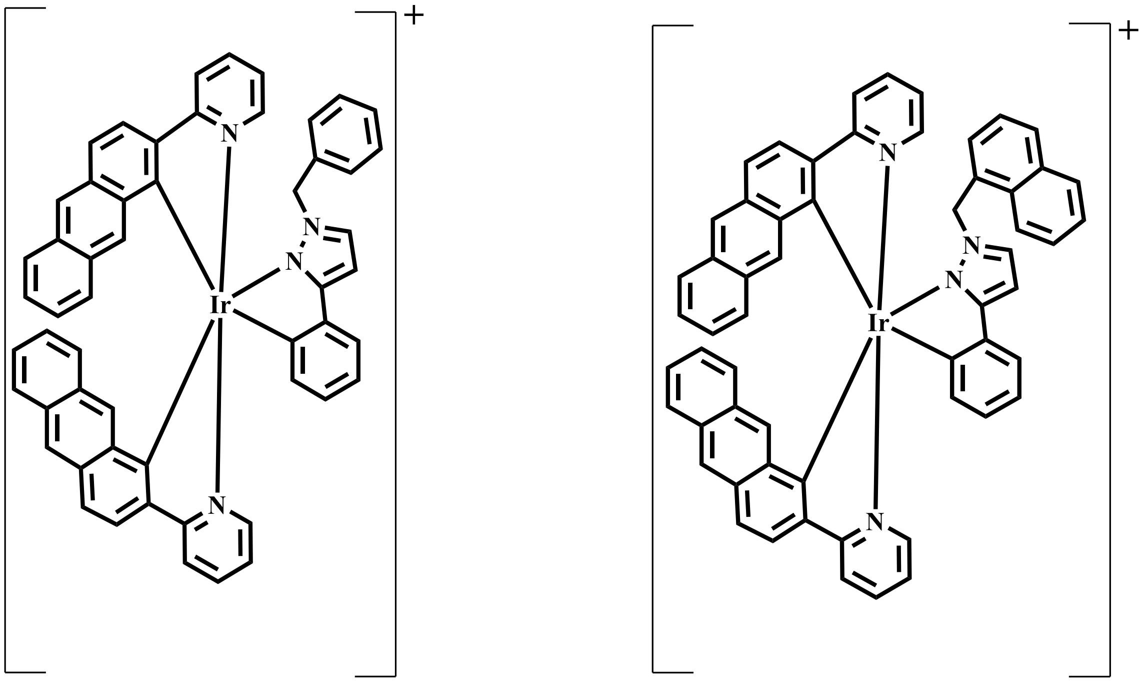

(**Ir-a**) (**Ir-b**)

Figure 1-35 Chemical structure of (a) $[Ir(\textit{pbq-g})_2(N\hat{}N)]^{+}Cl^{-}$ (*pbq-g* = phenylbenzo[*g*]-quinoline; N^N = 2-(1-benzyl-1*H*-pyrazol-3-yl) pyridine (Ir-a) and (b) 2-(1-(naphthalen-1-ylmethyl)-1*H*-pyrazol-3-yl) pyridine (Ir-b).

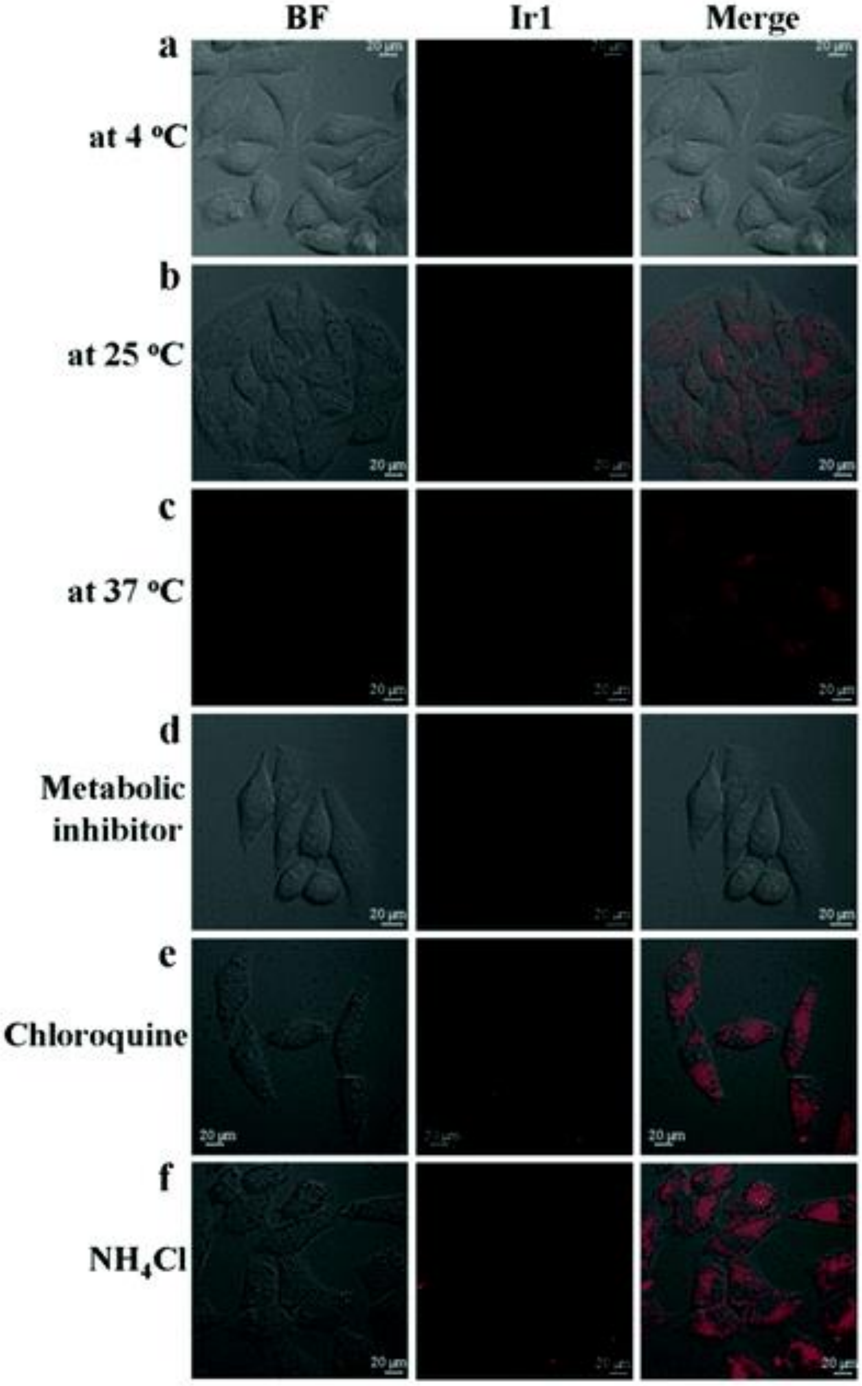

Figure 1-36 Confocal and bright-field images of incubated (a) with HeLa cells at different temperatures in PBS and different inhibitors. Permission was taken from ref. 126.

1.9 References

1 B. Valeur and M. N. B. Santos, *J. Chem. Educ.*, 2011, **88**, 731–738.

2 L. R. Joseph, *Principles of Fluorescence Spectroscopy*, Springer Science+Business Media, LLC, USA, University of Maryland School of Medicine, Baitimore, Maryland, USA, Third., 2010.

3 A. Jabłoński, *Zeitschrift für Phys.*, 1935, **94**, 38–46.

4 A. Juris, A.; Banlzani, V.; Barigelletti, F.; Campagna, S.; Belser, P.; von Zelewsky, *Coord. Chem. Rev.*, 1988, **84**, 85–277.

5 P. Schwille and J. Ries, *Principles and Applications of Fluorescence Correlation Spectroscopy (FCS)*, Blackwell, 2011.

6 C. E. Wayne and R. P. Wayne, *photochemistry*, New York, Oxford., 1996.

7 P. Seybold, M. Gouterman, P. Seybold and M. Gouterman, *Chem. Rev.*, 1965, **65**, 413–433.

8 P. S. Wagenknecht and P. C. Ford, *Coord. Chem. Rev.*, 2011, **255**, 591–616.

9 C. J. Jones, *d- and f- block chemistry*, Royal Society of Chemistry, Cambridge, 2001.

10 A. E. Housecroft, C. E.; Sharpe, *Inorganic chemistry*, Fourth Edition, Pearson., 2012.

11 G. M. Montalti M, Credi A, Prodi L, *Handbook of Photochemistry*, Taylor & Francis, Boca Raton, 2006.

12 V. B.-K. J. Michl, *Electronic aspects of organic photochemistry*, Wiley Interscience, New York, 1990.

13 Taken image from website, http://www.snipview.com/q/Raman spectroscopy, (accessed 6 December 2018).

14 S. Ladouceur and E. Zysman-colman, *Eur. J. Inorg. Chem.*, 2013, **2013**, 2985–3007.

15 A. R. G. Smith, P. L. Burn and B. J. Powell, *ChemPhysChem*, 2011, **12**, 2429–2438.

16 V. F. Moreira, F. L. T. Greenwood and M. P. Coogan, *Chem. Commun*, 2010, **46**, 186–202.

17 M. S. Lowry, W. R. Hudson, R. A. Pascal and S. Bernhard, *J. Am. Chem. Soc.*, 2004, **126**, 14129–14135.

18 K. P. S. Zanoni, R. L. Coppo, R. C. Amaral and N. Y. M. Iha, *Dalton. Trans.*, 2015, **44**, 14559–14573.

19 M. S. Lowry and S. Bernhard, *Chem. Eur. J.*, 2006, **12**, 7970–7977.

20 E. Baggaley, J. A. Weinstein and J. A. G. Williams, *Coord. Chem. Rev.*, 2012, **256**, 1762–1785.

21 J. Lalevøe, M. Peter, F. Dumur, D. Gigmes, N. Blanchard, M. Tehfe and F. Morlet-savary, *Chem. Eur. J.*, 2011, **17**, 15027–15031.

22 K. K. Lo, *Acc. Chem. Res.*, 2015, **48**, 2985–2995.

23 M. A. Baldo, M. E. Thompson and S. R. Forrest, *Nature*, 2000, **403**, 750–753.

24 C. Adachi, M. A. Baldo, S. T. Forrest and M. E. Thompson, *Appl. Phys. Lett.*, 2000, **77**, 904–906.

25 M. S. Lowry and S. Bernhard, *Chem. Eur. J.*, 2006, **12**, 7970–7977.

26 V. Balzani and A. Credi, *Coord. Chem. Rev.*, 1998, **171**, 3–16.

27 S. Sprouse, K. A. King, P. J. Spellane and R. J. Watts, *J. Am. Chem. Soc.*, 1984, **106**, 6647–6653.

28 K. Dedeian, P. Djurovich, F. Garces, G. Carlson and R. Watts, *Inorg. Chem.*, 1991, **30**, 1685–1687.

29 H. Amouri and M. Gruselle, *Chiralty in Transition Metal Chemistry: Molecules, Supramolecular Assemblies and Materials*, John Wiley & Sons, Ltd, 2008.

30 C. Fan and C. Yang, *Chem. Soc. Rev.*, 2014, **43**, 6439–6469.

31 A. B. Tamayo, B. D. Alleyne, P. I. Djurovich, S. Lamansky, I. Tsyba, N. N. Ho, R. Bau and M. E. Thompson, *J. Am. Chem. Soc.*, 2003, **125**, 7377–7387.

32 F. O. Graces, K. A. King and R. J. Watts, *Inorg. Chem.*, 1988, **27**, 3464–3471.

33 R. C. Evans, P. Douglas and C. J. Winscom, *Coord. Chem. Rev.*, 2006, **250**, 2093–2126.

34 N. Sabbatini and M. Guardigli, *Coord. Chem. Rev.*, 1993, **123**, 201–228.

35 A. Beeby, I. M. Clarkson, R. S. Dickins, S. Faulkner, D. Parker, L. Royle, A. S. de Sousa, J. A. G. Williams and M. Woods, *J. Chem. Soc., Perkin Trans.*, 1999, **2**, 493–503.

36 E. Orselli, G. S. Kottas, A. E. Konradsson, P. Coppo, R. Fröhlich, L. De Cola, A. Van Dijken, M. Büchel and H. Börner, *Inorg. Chem.*, 2007, **46**, 11082–11093.

37 H. Yersin, *Transition Metal and Rare Earth Compounds III (Topics in Current Chemistry) 241:1-26*, Springer, Berlin, 2004.

38 A. Tsuboyama, H. Iwawaki, M. Furugori, T. Mukaide, J. Kamatani, S. Igawa, T. Moriyama, S. Miura, T. Takiguchi, S. Okada, M. Hoshino and K. Ueno, *J. Am. Chem. Soc.*, 2003, **125**, 12971–12979.

39 I. Anorganische, P. Chemie and U. Bern, *Inorg. Chem.*, 1993, **32**, 3081–3087.

40 Y. You and W. Nam, *Chem. Soc. Rev.*, 2012, **41**, 7061–7084.

41 K. P. S. Zanoni, B. K. Kariyazaki, A. Ito, M. K. Brennaman, T. J. Meyer and N. Y. Murakami Iha, *Inorg. Chem.*, 2014, **53**, 4089–4099.

42 S. Adachi, M. A. Baldo, S. R. Forrest, S. Lamansky and M. E. Thompson, *Appl. Phys. Lett.*, 2001, **78**, 1622–1624.

43 T. Sajoto, P. I. Djurovich, A. Tamayo, M. Yousufuddin, R. Bau, M. E. Thompson, R. J. Holmes and S. R. Forrest, *Inorg. Chem.*, 2005, **44**, 7992–8003.

44 S. Lamansky, P. Djurovich, D. Murphy, F. Abdel-razzaq, R. Kwong, I. Tsyba, M. Bortz, B. Mui, R. Bau and Thompson, *Inorg. Chem.*, 2001, **40**, 1704–1711.

45 S. Lamansky, P. Djurovich, D. Murphy, F. Abdel-razzaq, H. Lee, C. Adachi, P. E. Burrows, S. R. Forrest and M. E. Thompson, *J. Am. Chem. Soc.*, 2001, **123**, 4304–4312.

46 V. V Grushin, N. Herron, D. D. Lecloux, W. J. Marshall, A. Viacheslav and Y. Wang, *Chem. Commun*, 2001, 1494–1495.

47 J. Li, P. I. Djurovich, B. D. Alleyne, M. Yousufuddin, N. N. Ho, J. C. Thomas, J. C. Peters, R. Bau and M. E. Thompson, *Inorg. Chem.*, 2005, **44**, 1713–1727.

48 K. Dedeian, J. Shi, N. Shepherd, E. Forsythe and D. C. Morton, *Inorg. Chem.*, 2005, **44**, 4445–4447.

49 P. Coppo, E. a Plummer and L. De Cola, *Chem. Commun.*, 2004, 1774–1775.

50 C. Yang, S. Li, Y. Chi, C. Wang, C. Shu, A. Chemistry, N. Chiao and T. Uni, *Inorg. Chem.*, 2005, **44**, 7770–7780.

51 C. S. K. Mak, A. Hayer, S. I. Pascu, S. E. Watkins, A. B. Holmes and A. Ko, *Chem. Commun*, 2005, 4708–4710.

52 W. J. Finkenzeller and H. Yersin, *Chem. Phys. Lett.*, 2003, **377**, 299–305.

53 X. Jiang, J. Peng, J. Wang, X. Guo and D. Zhao, *ACS Appl. Mater. Interfaces*, 2016, **8**, 3591–3600.

54 C. Chang, C. Yang, K. Chen, Y. Chi, C. Shu and M. Ho, *Dalton. Trans.*, 2007, **2**, 1881–1890.

55 Q. Zhao, S. Liu, M. Shi, C. Wang, M. Yu, L. Li, F. Li, T. Yi and C. Huang, *Inorg.Chem.*, 2006, **45**, 6152–6160.

56 K. Hasan, A. K. Bansal, I. D. W. Samuel, C. Roldán-Carmona, H. J. Bolink and E. Zysman-Colman, *Sci. Rep.*, 2015, **5**, 1–16.

57 N. Kaltsoyannis and P. Scott, *The f elements*, Oxford; New York: Oxford university Press, 1999.

58 A. Sigel and H. Sigel, *The Lanthanides and their interrelations with biosystems. Metal ions in biological systems*, Maecel Dekker, New York, 2003.

59 S. Petoud, S. M. Cohen, J.-C. Bunzli and K. N. Raymond, *J. Am. Chem. Soc.*, 2003, **125**, 13324–13325.

60 G. Stochel, A. Wanat and E. Kuli, *Coord. Chem. Rev.*, 1998, **171**, 203–220.

61 C. Piguet and J. G. Bünzli, *Chem. Soc. Rev.*, 1999, **28**, 347–358.

62 L. Flamigni, A. Barbieri, C. Sabatini, B. Ventura and F. Barigelletti, in *Topic in current chemistry 281, Photochemistry and Photophysics of coordination compounds: Lanthanides.*, 2007, pp. 1–43.

63 T. Gunnlaugsson and F. Stomeo, *Org. Biomol. Chem.*, 2007, **5**, 1999–2009.

64 B. Alpha, J.-M. Lehn, R. Ballardini, V. Balzani, S. Perathoner and N. Sabbatini, *Photochem Photobiol*, 1990, **52**, 299–306.

65 G. R. Copping and J.-C. G. Bunzli, *Lanthanide probes in life, chemical and earth sciences; theory and practice.*, Elsevier, New York, 1989.

66 I. Hemmilá, V. Mukkala, I. Hemmilá and V. Mukkala, *Crit. Rev. Clin. Lab. Sci.*, 2001, **38**, 441–519.

67 D. Parker and J. A. G. Williams, *J. Chem. Soc., Perkin Trans.*, 1996, **2**, 1581–1586.

68 D. Parker, *Coord. Chem. Rev.*, 2000, **205**, 109–130.

69 M. P. O. Wolbers, F. C. J. M. Van Veggel, B. H. M. Snellink-ruël, J. W. Hofstraat, A. J. Geurts and D. N. Reinhoudt, *J. Chem. Soc., Perkin Trans.*, 1998, **2**, 2141–2150.

70 S. Petoud, G. Muller, E. G. Moore, J. Xu, J. Sokolnicki, J. P. Riehl, U. N. Le, S. M. Cohen and K. N. Raymond, *J. Am Chem. Soc.*, 2007, **129**, 77–83.

71 M. Woods and A. D. Sherry, *Inorg. Chem.*, 2003, **42**, 4401–4408.

72 J.-C. G. Bunzli and C. Piguet, *Chem. Soc. Rev.*, 2005, **34**, 1048–1077.

73 S. Aime, M. Botta, D. Parker and J. A. G. Williamsb, *J. Chem. Soc. Dalton. Trans.*, 1996, 17–23.

74 M. P. Lowe, D. Parker, O. Reany, S. Aime, M. Botta, G. Castellano, E. Gianolio and R. Pagliarin, *J. Am. Chem. Soc.*, 2001, **123**, 7601–7609.

75 M. S. Tremblay, Q. Zhu, A. A. Martı, J. Dyer, M. Halim, S. Jockusch, N. J. Turro and D. Sames, *Org Lett*, 2006, **8**, 2723–2726.

76 A. Beeby, D. Parker and J. A. G. Williams, *J. Chem. Soc. Dalton. Trans.*, 1996, **2**, 1565–1579.

77 A. P. de Silva, H. Q. N. Gunaratne and T. E. Rice, *Angew. Chem. Int. Ed. Engl.*, 1996, **35**, 2116–2118.

78 J.-M. Lehn, *Angew. Chem. Int. Ed. Engl.*, 1990, **29**, 1304–1319.

79 R. J. Watts, *J. Chem. Educ.*, 1983, **60**, 834.

80 S. W. Botchway, M. Charnley, J. W. Haycock, A. W. Parker, D. L. Rochester, J. Weinstein and J. A. G. Williams, *Proc. Natl. Acad. Sci. U. S. A.*, 2008, **105**, 16071–16076.

81 S. I. Klink, H. Keizer and F. C. J. M. van Veggel, *Angew. Chem. Int. Ed.*, 2000, **39**, 4319–4321.

82 P. D. Beer, F. Szemes, P. Passaniti, M. Maestri, U. K. Ox, C. G. Ciamician, V. Uni, V. Selmi and I.- Bologna, *Inorg.Chem.*, 2004, **43**, 3965–3975.

83 T. Gunnlaugsson, J. P. Leonard, S. Katell and A. J. Harte, *Chem. Commun*, 2004, 782–783.

84 M. D. Ward, *Coord. Chem. Rev.*, 2007, **251**, 1663–1677.

85 D. Sykes, S. C. Parker, I. V Sazanovich, A. Stephenson, J. A. Weinstein and M. D. Ward, *Inorg. Chem.*, 2013, **52**, 10500–10511.

86 N. Sabbatini, N. Guardigli and J. M. Lehn, *Coord. Chem. Rev.*, 1993, **123**, 201–228.

87 S. Faulkner, L. S. Natrajan, W. S. Perry and D. Sykes, *Dalton. Trans.,* 2009, 3971–3979.

88 T. Nelson, S. Fernandez-Alberti, A. E. Roitberg and S. Tretiak, *Phys. Chem. Chem. Phy.*, 2013, **15**, 9245–9256.

89 A. Nielsen, G. Kuzmanich and M. A. Garcia-garibay, *J. Phys. Chem. A*, 2014, **118**, 1858–1863.

90 L. C. Courrol, F. R. O. Silva, L. Gomes and N. D. V Junior, *J. Lumin.*, 2007, **122–123**, 288–290.

91 S. Faure, C. Stern, R. Guilard and P. D. Harvey, *J. Am. Chem. Soc.*, 2004, **126**, 1253–1261.

92 T. A. Masters, R. J. Marsh, D. A. Armoogum, N. Nicolaou, B. Larijani and A. J. Bain, *J. Am Chem. Soc.*, 2013, **135**, 7883–7890.

93 S. I. Klink, H. Keizer and F. C. J. M. van Veggel, *Angew. Chem. Int*, 2000, **39**, 4319–4321.

94 A. Beeby, R. S. Dickins, S. FitzGerald, L. J. Govenlock, D. Parker, J. a. G. Williams, C. L. Maupin, J. P. Riehl and G. Siligardi, *Chem. Commun.*, 2000, **1**, 1183–1184.

95 P. Coppo, M. Duati, V. N. Kozhevnikov, J. W. Hofstraat and L. De Cola, *Angew. Chemie*, 2005, **117**, 1840–1844.

96 W. Jiang, B. Lou, J. Wang, H. Lv, Z. Bian and C. Huang, *Dalton. Trans.*, 2011, **40**, 11410.

97 D. Sykes, A. J. Cankut, N. M. Ali, A. Stephenson, S. J. P. Spall, S. C. Parker, J. a Weinstein and M. D. Ward, *Dalton Trans.*, 2014, **43**, 6414–6428.

98 K. Iftikhar, M. Sayeed and N. Ahmad, *Inorg. Chem.*, 1982, **21**, 80–84.

99 N. M. Shavaleev, Z. R. Bell and M. D. Ward, *J. Chem. Soc. Dalton. Trans.*, 2002, 3925–3927.

100 N. M. Shavaleev, Z. R. Bell, G. Accorsi and M. D. Ward, *Inorganica Chim. Acta*, 2003, **351**, 159–166.

101 N. M. Shavaleev, L. P. Moorcraft, S. J. A. Pope, Z. R. Bell, S. Faulkner and M. D. Ward, *Chem. Eur. J.*, 2003, **9**, 5283–5291.

102 N. M. Shavaleev, L. P. Moorcraft, S. J. a Pope, Z. R. Bell, S. Faulkner and M. D. Ward, *Chem.commun.*, 2003, 1134–1135.

103 N. M. Shavaleev, G. Accorsi, D. Virgili, R. Bell, T. Lazarides, G. Calogero, N. Armaroli and M. D. Ward, *Inorg. Chem.*, 2005, **44**, 61–72.

104 D. Sykes, I. S. Tidmarsh, A. Barbieri, I. V. S, J. A. Weinstein and M. D. Ward, *Inorg. Chem.*, 2011, **50**, 11323–11339.

105 Y. Liu, M. Li, Q. Zhao, H. Wu, K. Huang and F. Li, *Inorg. Chem.* 2011, **50**, 5969–5977.

106 K. K. Lo, S. P. Li and K. Y. Zhang, *New J. Chem.*, 2011, **35**, 265–287.

107 H. Sun, S. Liu, W. Lin, K. Y. Zhang, W. Lv, X. Huang, F. Huo, H. Yang, G. Jenkins, Q. Zhao and W. Huang, *Nat. Commun.*, 2014, **5**, 1–9.

108 A. Nakagawa, Y. Hisamatsu, S. Moromizato, M. Kohno and S. Aoki, *Inorg. Chem.*, 2014, **3**, 409–422.

109 K. Kam and W. Lo, *Luminescent and Photoactive Transition Metal Complexes as Biomolecular Probes and Cellular Reagents*, Springer, Berlin, Heidelberg, 2015.

110 M. P. Coogan and V. F. Moreira, *Chem. Commun.*, 2014, **50**, 384–399.

111 M. K. Kuimova, G. Yahioglu and P. R. Ogilby, *J. Am Chem. Soc.*, 2009, **131**, 332–340.

112 G. G. Shan, H. B. Li, H. Z. Sun, D. X. Zhu, H. T. Cao, Z. M. Su, *J. Mater. Chem. C*, 2013, **1**, 1440–1449.

113 K. S. Bejoymohandas, T. M. George, S. Bhattacharya, S. Natarajanb and M. L. P. Reddy, *J. Mater. Chem. C*, 2014, **2**, 515–523.

114 Q. Zhao, C. Huanga and F. Li, *Chem. Soc. Rev.*, 2011, **40**, 2508–2524.

115 M. M. Alonso, N. Busto, L. D. Aguirre, L. Berlanga, M. C. Carrión, J. V Vicente, A. M. Rodríguez, A. Carbayo, B. R. Manzano, E. Ortí, F. A. Jalón, B. García and G. Espino, *Chem. Eur. J.*, 2018, **24**, 1–19.

116 B. C. Ulbricht, B. Beyer, C. Friebe, A. Winter and U. S. Schubert, *Adv. Mater.*, 2009, **21**, 4418–4441.

117 T. Stoll, C. E. Castillo, M. Kayanuma, M. Sandroni, C. Daniel, F. Odobel, J. Fortage and M. Collomb, *Coord. Chem. Rev.*, 2015, **304**–**305**, 20–37.

118 Y. Jeon, C. Damodharan, R. Kumar, J. Jang and Y. Choe, *Electrochim. Acta*, 2016, **195**, 112–123.

119 B. Aranda, P. Aguirre, S. A. Moya, M. Bonneau, G. W. J. A, L. Toupet, M.

Escadeillas, H. Le Bozec and V. Guerchais, *Polyhedron*, 2015, **86**, 120–124.

120 F. L. Thorp-Greenwood, R. G. Balasingham and M. P. Coogan, *J. Organomet. Chem.*, 2012, **714**, 12–21.

121 R. G. Balasingham, C. F. Williams, H. J. Mottram, M. P. Coogan and S. J. A. Pope, *Organometallics*, 2012, **31**, 5835–5843.

122 M. Rajendran, E. Yapici and L. W. Miller, *Inorg. Chem.*, 2014, **53**, 1839–1853.

123 M. Yu, Q. Zhao, L. Shi, F. Li, Z. Zhou, H. Yang, T. Yi, C. Huang, *Chem. Commun.*, 2008, 2115-2117.

124 C. Li, M. Yu, Y. Sun, Y. Wu, C. Huang and F. Li, *J. Am. Chem. Soc.*, 2011, **133**, 11231–11239.

125 L. Murphy, A. Congreve, L. O. Pålsson and J. A. G. Williams, *Chem. Commun.*, 2010, **46**, 8743–8745.

126 Y. Liu, P. Zhang, X. Fang, G. Wu, S. Chen, Z. Zhang, H. Chao, W. Tan and L. Xu, *Dalton. Trans.*, 2017, **46**, 4777–4785.

CHAPTER TWO

Luminescence studies of Ir-Pyrene complexes

2 Luminescence studies of Ir-Pyrene complexes

2.1 Overview of pyrene

In 1837, Auguste Laurent, a French Chemist, discovered pyrene in the extract from coal tar. The correct chemical formula was calculated by Gräbe, in 1871 and the correct chemical structure was reported by Philip and Bamberger in 1887.[1, 2] The molecule consists of 16 carbon atoms within four six-membered rings forming a planar structure. This structure can be described, using Clar's sextet rules, as having two double bonds and two aromatic rings. **Figure** 2-1 explains its decreased stability and increased reactivity compared to systems in which all rings are aromatic.[3]

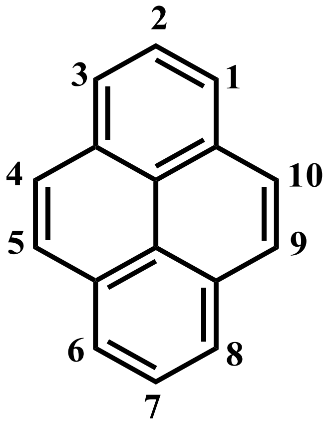

Figure 2-1: Pyrene structure according to Clar's sextet rules.[4]

In recent years, pyrene and its derivatives have received extensive attention due to their photophysical properties, chemical stability and thermal stability.[5]

Pyrene-based complexes have also been exploited in applications, such as chemosensors,[6] intercalators in biological systems, organic field effect transistors (OFETs), organic light emitting diodes (OLEDs), organic photovoltaic devices (OPVs) and in materials for photodynamic therapy.[5–8] For these versatile photophysical properties, pyrene is called "fruitfly of photochemistry".[4] Pyrene derivatives can participate in charge transfer assemblies as either an electron donor or an electron acceptor, depending on the nature of the attached substituent.[9] Due to pyrene's planar aromatic nature, it easily engages in π-π stacking interactions and can form an excimer in which an excited-state pyrene moiety stacks with another pyrene in the ground state.[10]

The easy way to distinguish between an excimer and a monomer of pyrene is the emission profile. Excimer-based pyrene emission appears as a broad, structureless band in the region of 480 nm, at concentrations ca.10^{-5} M and higher (as will be mentioned later).[3] However, emission from monomeric pyrene occurs in the blue region, between 370 nm and 420 nm and displays a pronounced vibrational structure.[10–12] This chapter reports the photophysical properties of a novel series of Ir-pyrene coordination complexes. The study focuses on the effect of variation of the substituent atom (F/F, F/H, and H/H) on the cyclometalating ligands attached to Ir(III) unit, in order to develop systematic tuning of excited state emission properties. It has been accepted that the emission maximum from the Ir (III) metal complex unit changes in accordance with the substitution of electron donating or electron withdrawing groups on the cyclometalating ppy ligands. This affects the energy gap between the HOMO and LUMO energy levels.[13]

The photophysical study presented in this chapter is divided into two parts. Firstly, excitation of the pyrene unit was performed, leading to emission from both pyrene itself and the Ir (III) metal complex unit. Secondly, selective excitation of the Ir(III) unit was performed, leading to emission from Ir(III) unit. These studies assisted the understanding of the nature and emissive properties of the excited states and any inter-component energy-transfer events.

2.1.1 Pyrene Chemistry

Pyrene has three types of position for chemical reactivity due to its three mirror planes. The first plane is vertical, second plane is horizontal and the third plane is that of the molecule, as shown in **Figure** 2-2.

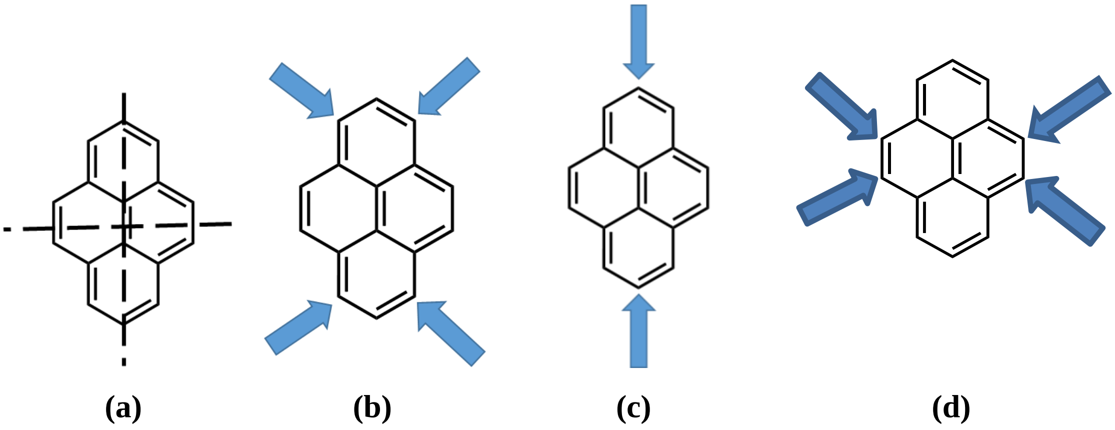
(a) (b) (c) (d)

Figure 2-2: (a) Vertical and horizontal mirror plane. (b) 1, 3, 6, 8 substitution sites. (c) 2, 7 substitution sites. (d) 4, 5, 9, 10 substitution sites.

1-(Bromomethyl)pyrene compound is formed as a result of an electrophilic aromatic substitution in the C1 position. This pyrene derivative is more easily obtained rather than that with the substitution in C2 and C7 positions because of the high contributions of the HOMO and LUMO at the C1 carbon atom, whereas in the C2 and C7 positions the HOMO and LUMO have a nodal plane and lie perpendicular to the axis of C2 and C7, leading to harder substitution in these positions (**Figure** 2-3).[4,14–16]


(a) **(b)**

Figure 2-3: (a) The HOMO orbital, (b) The LUMO orbital of pyrene.[3]

Many investigations into the design and synthesis of pyrene-based complexes have been based on the substitution in positions C1, C3, C6 and C8. These positions are the most electron rich ones in the structure. Complexes of such pyrene derivatives with Ir, Ru and Pd have also been extensively studied.[3, 8, 17]

2.2 Summary of previous work on photophysical properties of Ir-pyrene complexes

In light of their numerous and diverse applications, the photophysical properties of complexes resulting from coordination of pyrene-based ligands to metal centres have been the subject of extensive analysis. The electronic and structural properties of the pyrene moiety can enhance many photophysical properties of these complexes, leading to versatile applications. For example:

1- As fluorescent probes in sensing.[18]
2- Elongation of the emission lifetime of the coordination complexes via π-π^* emission or the “triplet reservoir” effect.[19]
3- Inter/intra-molecular π-π^* stacking interactions which can also be explored in sensing, or in construction of new materials.[20]

Orti and co-workers[7] have designed suitable chemical multichromophoric pyrene-Ir(III) complexes incorporating pyrenes as functional groups attached to the 5,5′ positions of a 2,2′-bipyridine ancillary ligand (**Figure** 2-4). The theoretically predicted and experimentally observed emission properties at room temperature show that the ^{3}ILCT emission corresponding to the (pyrene)$_2$bpy ancillary ligand is much weaker than the emission from the ^{3}MLCT state, which is centred on the Ir(III) complex. The excited state has been engineered with and without substitution of electron withdrawing (F) atoms on the cyclometalated Ir(III) moiety. It has also been demonstrated that fluorination of Ir(III)-based cyclometalated moiety influences luminescence properties.[7]

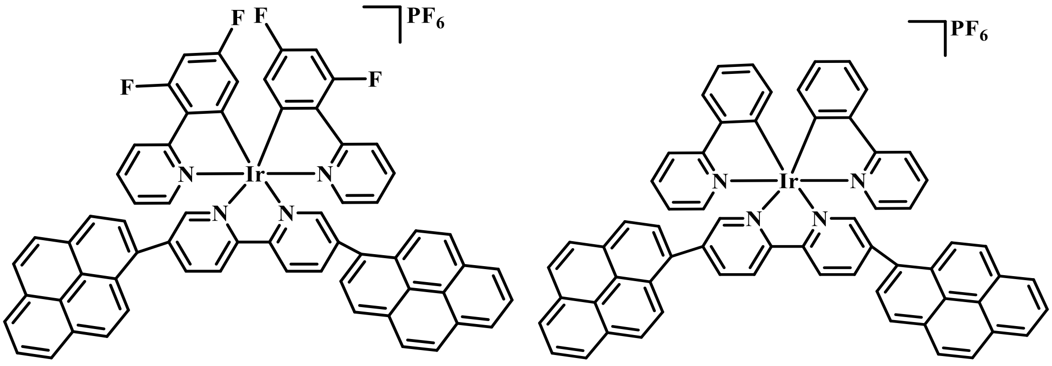

(a) **(b)**

Figure 2-4: Orti's group Ir(III) complexes (a) with, (b) without fluorine substitution.[7]

Mc Clenaghan *et. al.*[21] modified a cyclometalated Ir(III) core with a pendant pyrene moiety through an aliphatic spacer in order to study the photophysical properties of the resulting bichromophoric complex, (**Figure** 2-5). A non-conjugated aliphatic spacer is the key to achieving a long luminescence lifetime in this complex (τ = 225 μs) through reversible electronic energy transfer between Ir(III) and pyrene excited states (the 'reservoir effect'). These properties have a wide application in multicomponent artificial photoactive arrays.[21]

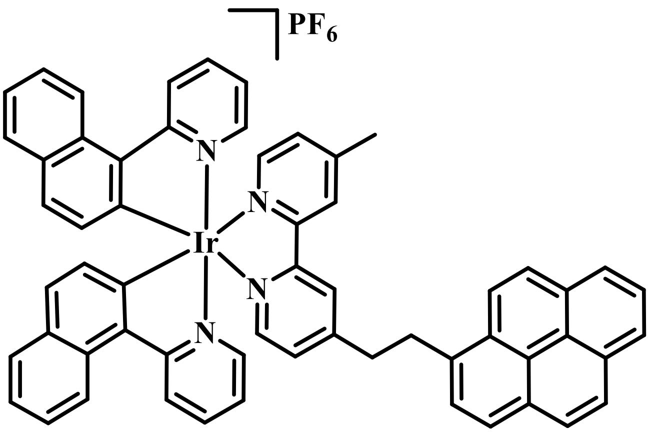

Figure 2-5: Mc-Clenaghan's group Ir(III) complex with a pyrene unit attached via an aliphatic spacer.[21]

Patrick *et. al.*[19] reported two Ir-pyrene complexes of the structure Ir(CN)$_2$(NN)pyrene (**Figure** 2-6) which shows dual emissions, originating from radiative decay of ^{3}pyrene ($^3\pi$-π*) states with a long lifetime, and from a ^{3}Ir(III) (^{3}MLCT) state with a short lifetime. A difference between the two models is that complex (1) in **Figure** 2-6 has a longer linker and shows extended excited-state lifetimes, because the two excited states ($^3\pi$-π* and ^{3}MLCT) lie close in energy allowing delocalisation of excited-state energy between these two states. In complex (2), (**Figure** 2-6), without the methylene linker between Ir(III) unit and the pyrene unit, the difference in energy between these two states appears to be larger.[19]

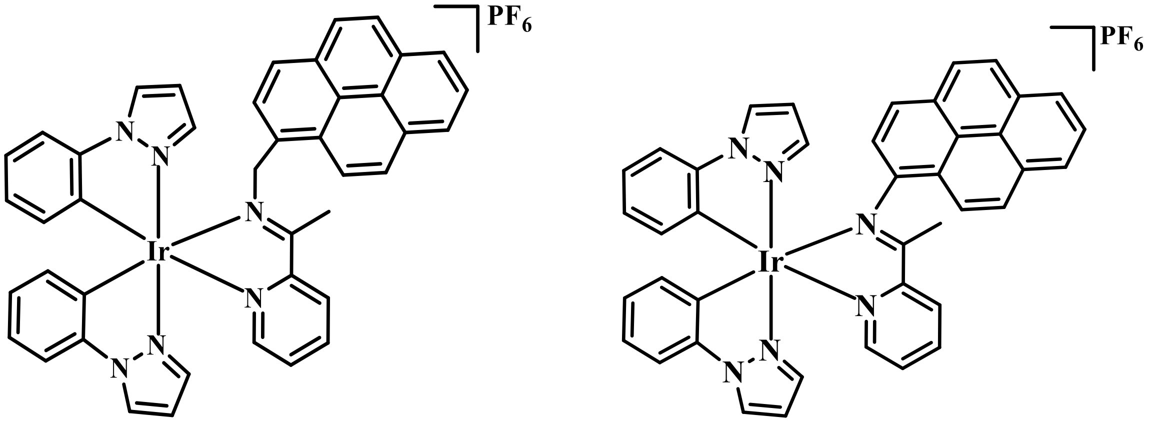

(1) **(2)**

Figure 2-6: Ir(III) pyrene complexes: (1) with a methylene linker, and (2) with a direct attachment of the pyrene unit to the Ir(III) (CN)$_2$(NN) unit.[19]

2.3 The aims of this study

This chapter reports synthesis and the structural, UV-Vis and photophysical characterization of a series of bis-heteroleptic Ir(III) complexes, linked via a CH$_2$-group to a pyrene unit. We chose the methylene linker because direct attachment of the pyrene to the pypz ligand has been shown to result in the quenching of optical properties of the Ir(III) excited state.[21]

The aim of this study is twofold:

1- To investigate systematic relationships between the structure of a series of Ir-pyrene complexes and their photophysical properties: namely, to study the effect of functionalisation of ppy ligands by fluorine atoms on the HOMO-LUMO energy gap, and consequently on the photophysical properties of the complexes.

2- To evaluate excited-state energy transfer between the pyrene and Ir(III) moieties.

2.4 Results and Discussion

A series of $^{F/F,\ F/H,\ H/H}$ Ir•L^{pyrene}•NO_3 complexes were synthesised in order to investigate the interactions between the two chromophore components: free pyrene which is strongly fluorescent, and $^{F/F,\ F/H,H/H}$ Ir• CH_3•NO_3 which is strongly phosphorescent.

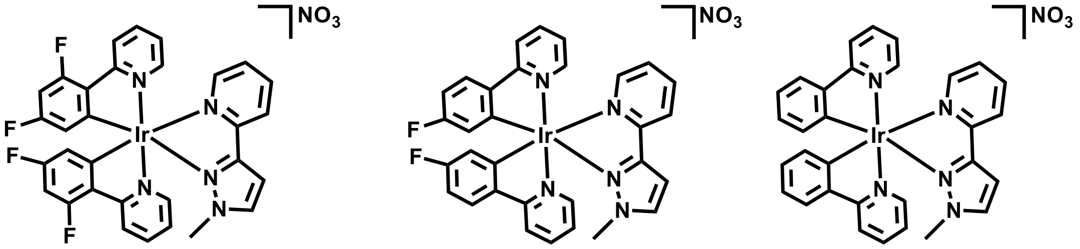

$^{F/F}$Ir•CH_3•NO_3 **$^{F/H}$Ir•CH_3•NO_3** **$^{H/H}$Ir•CH_3•NO_3**

Figure 2-7 Chemical structure of mono- $^{F/F,\ F/H\ and\ H/H}$ Ir• CH_3•NO_3 complexes.

2.4.1 Synthesis

The $^{(F/F,\ F/H,\ H/H)}$ Ir•L^{pyrene}•NO_3 complexes can be synthesised in several ways. The first synthetic procedure involves two steps. The first step is to synthesise the ligand pyrene•pypz by refluxing starting material 1-Bromomethylpyrene with pypz (1:1 ratio) in dry tetrahydrofuran (THF) solution, in presence of sodium hydride (NaH), at 75° C, under nitrogen, for 20 hrs (**Figure** 2-8, route 1). Isolation of a yellow pyrene•pypz ligand was achieved via multiple purification steps, including a neutral alumina column eluted with DCM:MeOH (95:5), and a silica-gel column with MeCN as eluent. This was followed by MeCN:$KNO_{3(aq.)}$:H_2O (100:5:5) as eluent (unusual for a neutral organic molecule). However, impurities were still present as seen in the electrospray mass spectra and ^{1}H NMR spectra even after many columns. It was, therefore, decided to use the ligand in the next step without further purification. Accordingly, the crude pyrene•pypz ligand was reacted with the chloride-bridged dimer $[(C^\wedge N)_2Ir(\mu\text{-}Cl)_2Ir(C^\wedge N)_2]$ (2:1) equivalents whilst being protected from light. The desired Ir•L^{pyrene}•NO_3 complexes were obtained, albeit with a low yield.

The second synthetic procedure (route 2) is a direct reaction of 1-bromomethylpyrene with pre-prepared $^{F/F,\ F/H.\ H/H}$Ir•L^{pyrene}•NO_3 in THF in presence of NaH, tetrabutylammonium iodide (Bu_4NI) as catalyst, at 75° C, under nitrogen, for 24 hrs, as shown in **Figure** 2-8. This reaction occurs through a S_N2 mechanism. This is an easier procedure than the 1st method and also resulted in a good yield of the product. The $^{F/F,\ F/H.\ H/H}$Ir•L^{pyrene}•NO_3 complex obtained was purified by silica column chromatography, eluted by DCM only, then DCM:MeOH (95:5), then MeCN only until all unwanted bands were removed, and finally eluted with MeCN:$KNO_{3(aq.)}$:H_2O to collect the band which showed no emission under a UV lamp. The solvent was evaporated under reduced pressure and the complex characterized by mass spectroscopy, ^{1}H NMR spectroscopy and X-ray crystallography. The photophysical properties of all $^{F/F,\ F/H,\ H/H}$Ir•L^{pyrene}•NO_3 complexes were investigated by absorption and emission spectroscopy.

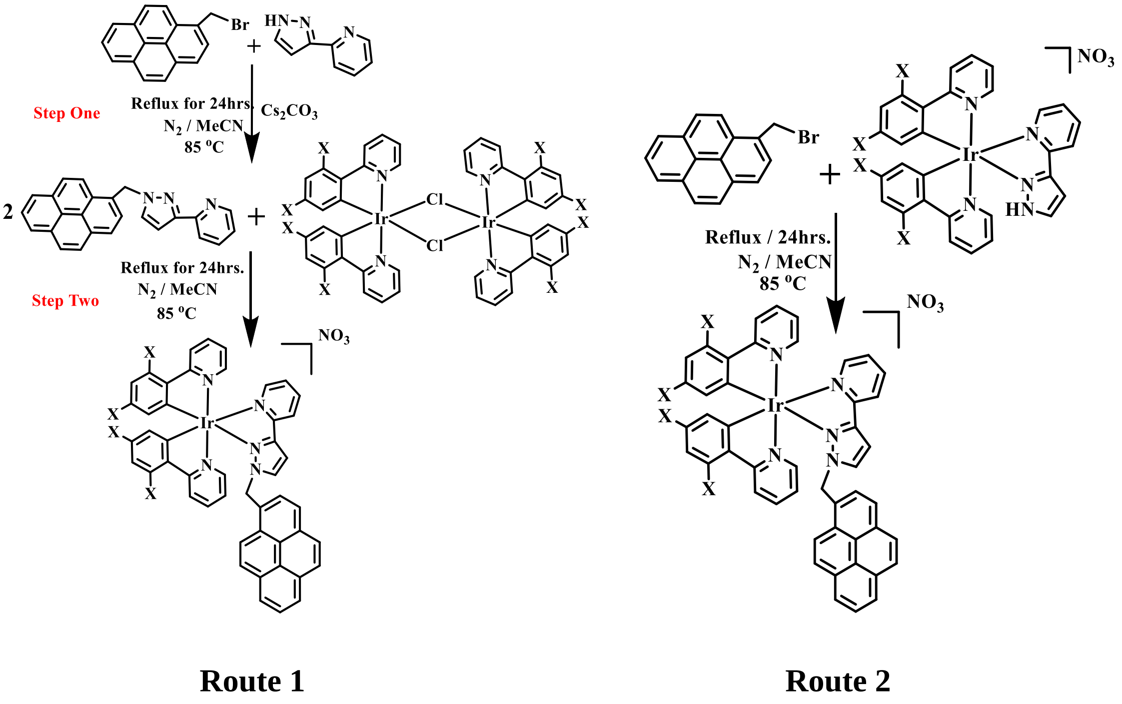

Figure 2-8: Two synthetic routes followed in the synthesis of $^{X/X}$Ir•L^{pyrene}•NO_3 complex, when X,X= F/F, F/H, H/H substitution.

2.5 X-ray Crystallography of $^{F/F}Ir \bullet L^{pyrene} \bullet NO_3$ complex

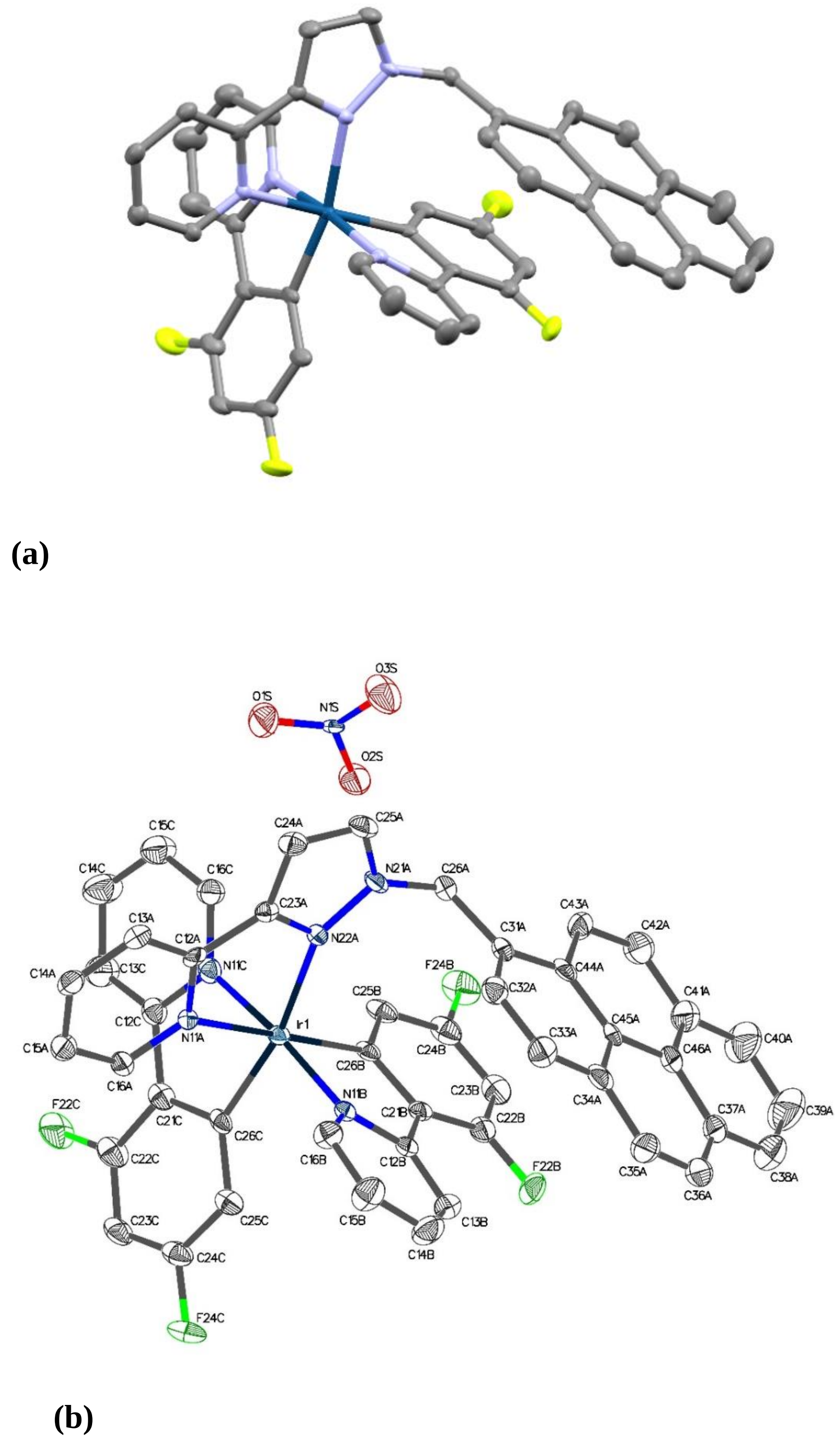

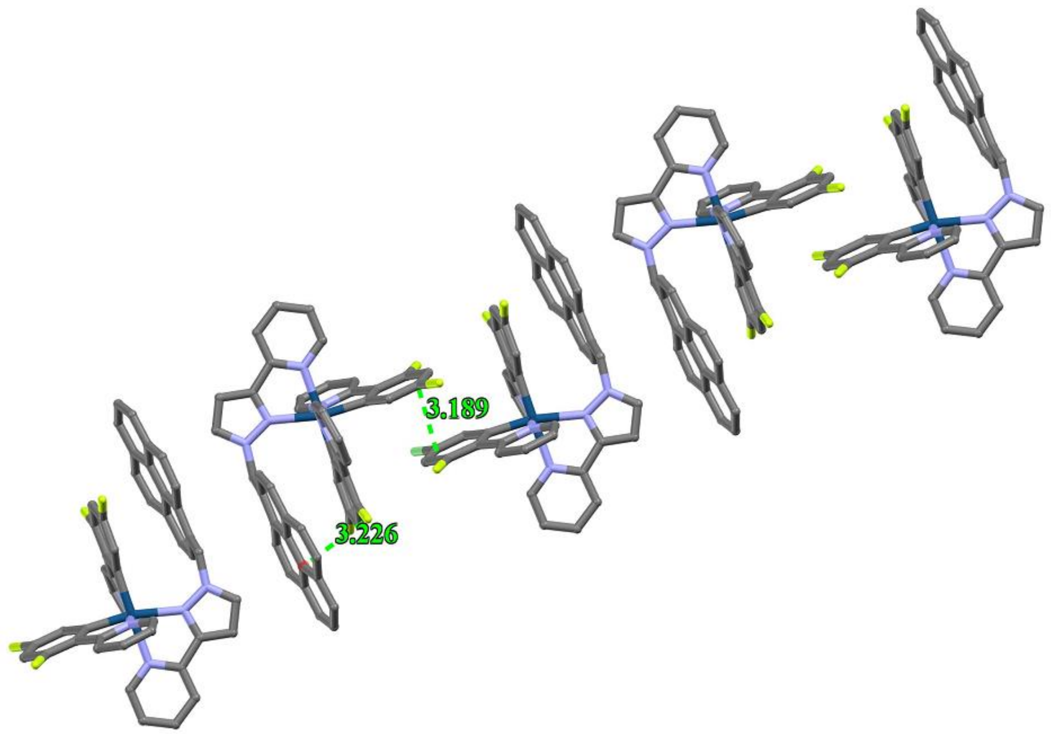

(c)

Figure 2-9: (a) Crystal structure of $^{F/F}$Ir•L^{pyrene}•NO_3 complex molecule. (b) View of the $^{F/F}$Ir•L^{pyrene}•NO_3 complex molecule. (c) Intermolecular *π*-*π* stacking interactions between 2,4-difluoro-phenyl rings and intramolecular *π*-*π* stacking interactions between pyrene ring and 2,4-difluoro-phenyl ring are noted, with the distances stated (in a).

An X-ray quality crystal of $^{F/F}$Ir•L^{pyrene}•NO_3 was grown from MeCN and diethyl ether using the slow solvent diffusion method over 4 days. The compound crystallised in the monoclinic space group P2_1/c. The octahedral geometry of the Ir(III) ion involves the trans-arrangement of the N-donors of the two cyclometalated ppy ligands. The CH_2Cl_2 solvent and NO_3-anion have been modelled in the structure (**Figure** 2-9-**b**). Moreover, the methylene group gives the pendant pyrene more flexibility to adjust itself to optimise the π-π stacking interactions with one of the coordinated ppy ligands: the stacking distance is approximately 3.2 Å, as shown in **Figure** 2-9-**c**. The bond lengths are summarised in **Table 2-1**.

Table 2-1: Selected bond length / Å for $^{F/F}Ir \bullet L^{pyrene} \bullet NO_3$.

Ir-C/-N Bonds	Bond length / Å
Ir(1)-C(26C)	1.957 (8)
Ir(1)-C(26B)	1.964 (7)
Ir(1)-N(11B)	1.985 (7)
Ir(1)-N(11C)	1.993 (7)
Ir(1)-N(11A)	2.102 (6)
Ir(1)-N(22A)	2.131 (6)

These bond lengths are typical of other Ir-cyclometalated complexes with similar ligands.[22]

2.6 Photophysical study of a series of $Ir \bullet L^{pyrene} \bullet NO_3$ complexes

2.6.1 UV-Visible Absorption spectroscopy

Absorption spectra of a dilute solution of the complexes $^{H/H,\ F/H,\ F/F}Ir \bullet L^{pyrene} \bullet NO_3$ (ca. 10^{-6} M) were measured in MeCN at room temperature. All absorption spectra are depicted in **Figure** 2-10.

The absorption spectra in **Figure** 2-10 are composed of ppy π-π* transitions below 300 nm and pyrene π-π* transitions below 360 nm. The low energy absorptions above 360 nm are assigned to MLCT transitions. The pyrene-based transitions are clearly distinct from the MLCT transitions in all Ir-pyrene complexes and retain a strong vibronic progression, characteristic of pyrene. MLCT transitions appear as a weak broad absorption band. Extinction coefficient data are provided in **Table 2-2** and are typical for the π–π* transitions (close to 10^5 $M^{-1}cm^{-1}$) and charge transfer transitions (of the order of 10^3 $M^{-1}cm^{-1}$).

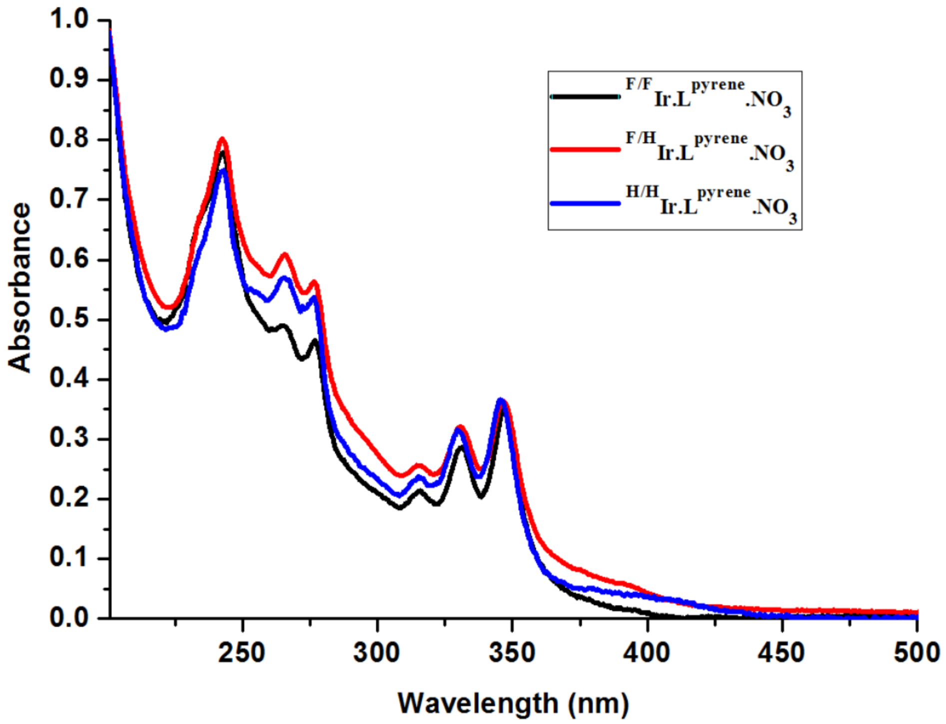

Figure 2-10: Electronic absorption spectra of Ir•L^{pyrene}•NO$_3$ complexes in MeCN solution (~10^{-6} M) at 298 K.

Table 2-2: Absorption maxima and extinction coefficients for the series of Ir•L^{pyrene}•NO$_3$ complexes in MeCN solvent at 298 K.

Complexes	$\lambda_{max.}$ (nm), ε (L.mol^{-1}.cm^{-1})							
$^{F/F}$Ir•L^{pyrene}•NO$_3$	242 (68800)	265 (5000)	277 (46700)	315 (22300)	330 (28500)	347 (34400)	386 (2700)	
$^{F/H}$Ir•L^{pyrene}•NO$_3$	242 (80300)	265 (58000)	276 (55100)	315 (23000)	330 (31500)	347 (33500)	391 (4800)	
$^{H/H}$Ir•L^{pyrene}•NO$_3$	242 (82500)	265 (63000)	276 (58500)	315 (26000)	330 (34400)	346 (33500)	375 (5900)	396 (3800)

2.6.2 Photophysical Study

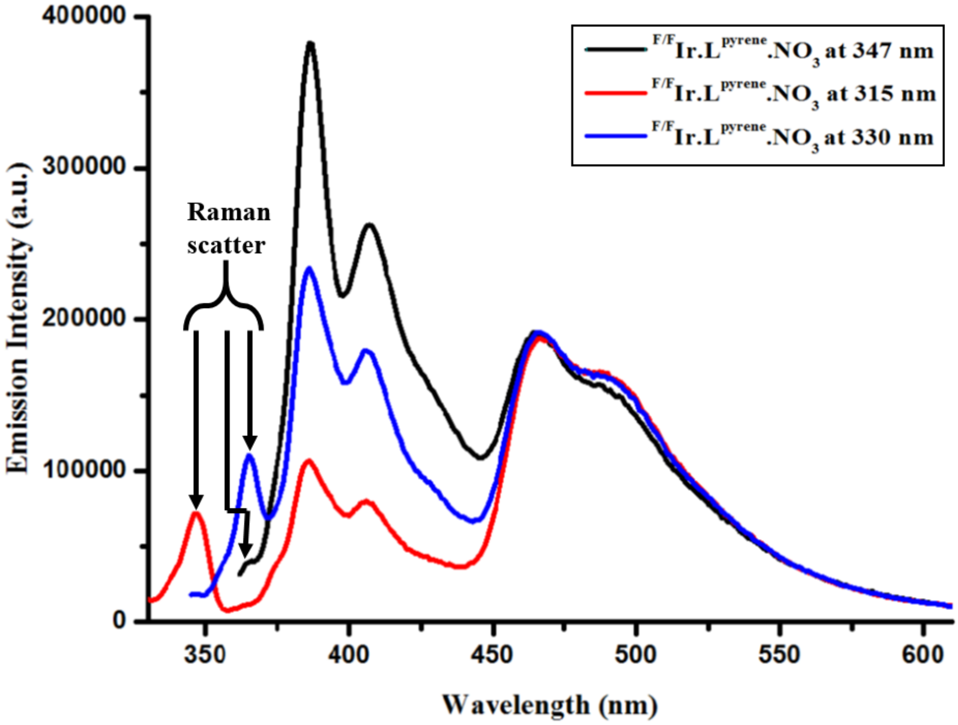

Figure 2-11: Emission spectra of $^{F/F}Ir\bullet L^{pyrene}\bullet NO_3$ complex in aerated MeCN at different excitation wavelengths at 298 K. The structured band at 360-440 nm is ^{1}pyr. features while the abroad band ~ 450-550 nm feature of ^{3}Ir moiety.

Figure 2-11 shows the emission spectra of a dilute solution of $^{F/F}Ir\bullet L^{pyrene}\bullet NO_3$ recorded using excitation wavelengths at 315, 330 and 347 nm, in MeCN at 298 K, which represents the excitation of the pyrene moiety in $^{F/F}Ir\bullet L^{pyrene}\bullet NO_3$ complex as shown in the absorption spectra in **Figure** 2-10. The peaks on the left between 330 nm and 370 nm in **Figure** 2-11 are due to the Raman scattering from the solvent.

As depicted in **Figure** 2-11, all emission spectra of $^{F/F}Ir\bullet L^{pyrene}\bullet NO_3$ have the same spectral features independent of the excitation wavelengths. However, the relative intensity of the pyrene-localised fluorescence and emission from the Ir-based MLCT excited state changes with the excitation wavelength.[23] This means that photons are emitted from both excited states, the pyrene-based one and the Ir-based one.

The emission spectra of all series of Ir•L^{pyrene}•NO$_3$ complexes in MeCN solvent, along with that of the free pyrene are shown in **Figure** 2-12. The excitation wavelength was 315 nm for all complexes, the concentration used was ~10^{-6} M and all spectra were recorded at 298 K.

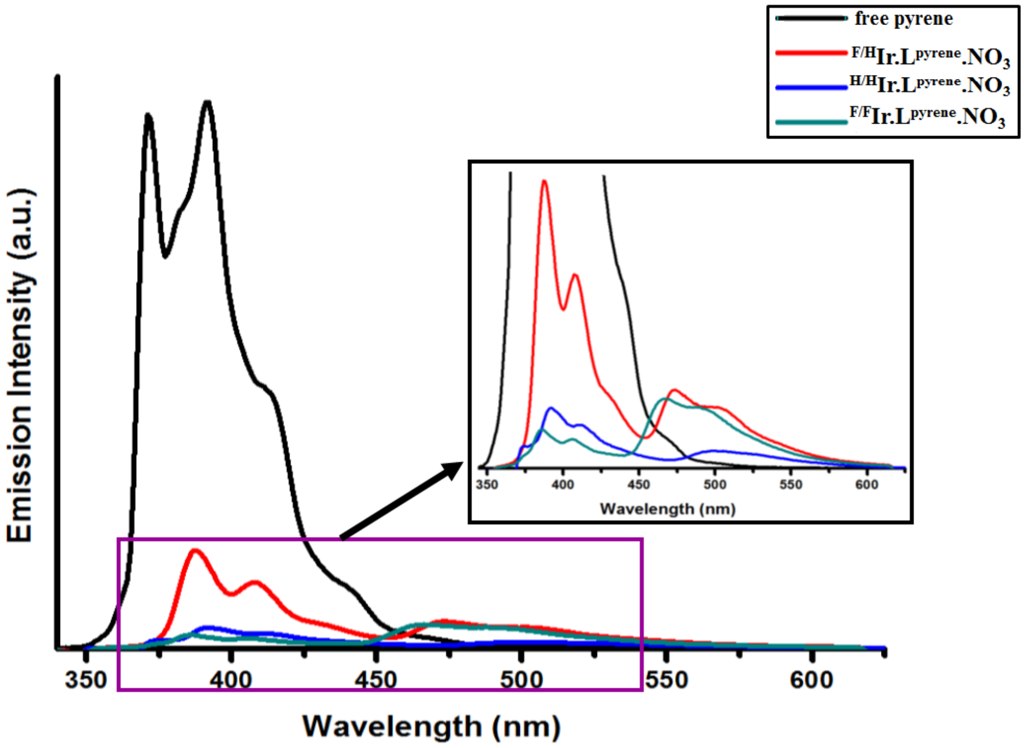

Figure 2-12: Emission spectra of all $^{F/F,\ F/H,\ H/H}$Ir•L^{pyrene}•NO$_3$ complexes and free pyrene under direct excitation into the pyrene unit at 315 nm; data in CH$_3$CN at 298 K.

Upon excitation at 315 nm (**Figure** 2-12), the spectrum showed dual emissions from both pyrene unit (^{1}LC) and Ir(III) unit (^{3}MLCT) excited states. Energy transfer from ^{1}pyr excited state acting as a donor to an ^{1}Ir excited state acting as an acceptor, (**Figure** 2-16), is possible. However, due to the absorption spectra of Ir(III) units and emission of free pyrene overlap, both units are populated when the $^{F/F,\ F/H,\ H/H}$Ir•L^{pyrene}•NO$_3$ complexes are excited as illustrated in **Figure** 2-13. Therefore, it is difficult to investigate whether energy transfer from ^{1}Py takes place.

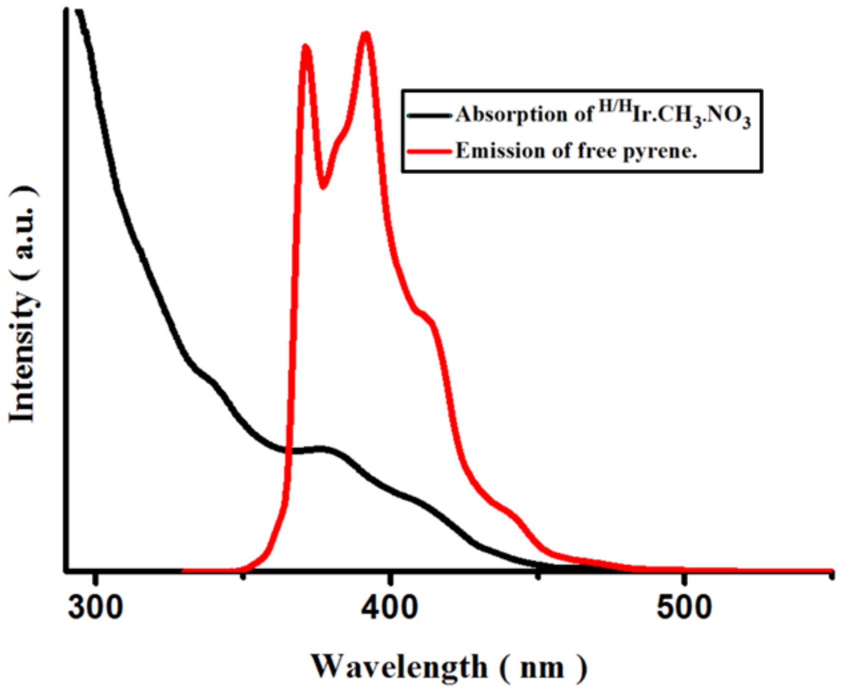

Figure 2-13: Absorption of $^{H/H}Ir\bullet CH_3\bullet NO_3$ complex and luminescence emission spectra of free pyrene in MeCN at 298 K, shows the probability to have energy transfer from pyrene unit to Ir(III) unit.

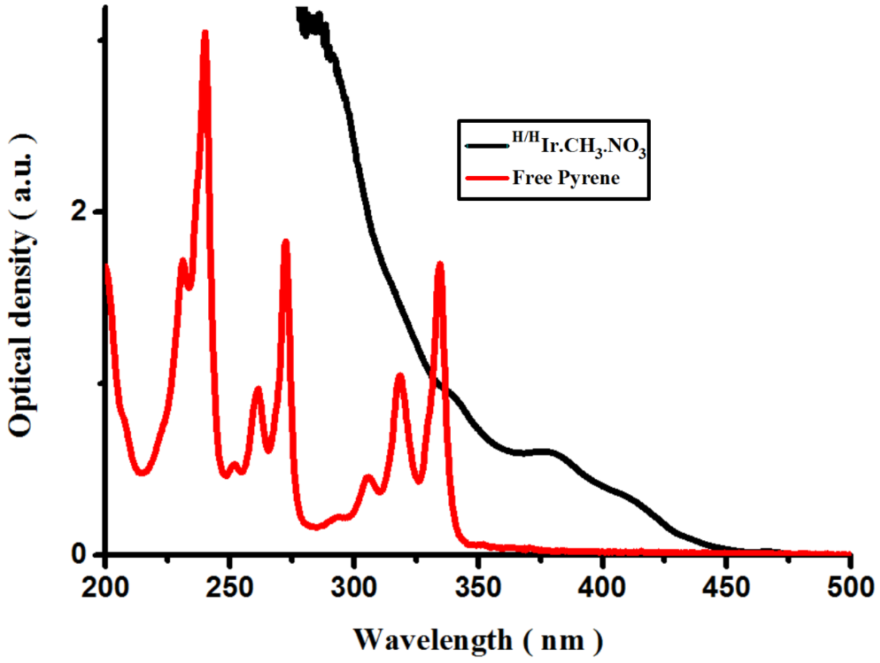

Figure 2-14: Absorption spectra of free pyrene and $^{H/H}Ir\bullet CH_3\bullet NO_3$ complex in MeCN at 298 K, which shows that at all wavelengths where pyrene absorbs, the Ir(III) complex also absorbes; thus it is not possible to excite pyrene unit selectively.

However, if ET from ^{1}pyr. to MLCT was complete (efficient), no ^{1}pyr* emission would be observed. The fact that a ^{1}pyr-based emission was observed at the wavelength below 450 nm, (**Figure** 2-19**)**, suggests that the energy transfer is not complete (if occuring at all) so pyrene fluorescence is not quenched. Whilst it is energetically favourable, the reason for the incomplete energy transfer could be due to the pyrene unit being at a considerable distance from the cyclometalating Ir(III) unit. This could potentially occur due to the presence of the CH_2-linker, which gives good flexibility to the pyrene unit to localise in an another conformation compared to that being observed in the solid state by X-ray crystallography (**Figure** 2-9-**a**).

There is a possibility of ET from ^{3}MLCT excited state, acting as a donor, to the lower-lying ^{3}pyr excited state, acting as acceptor, with the energy difference ~4420 cm^{-1} as illustrated in **Figure** 2-16. However, no difference was observed in the lifetime of ^{3}MLCT state between Ir•L^{pyrene}•NO_3 and Ir•CH_3•NO_3 complexes. Therefore, this implies that there is no ET, otherwise a reduction of the Ir-based ^{3}MLCT lifetime would have been observed. The lack of ET between the triplet states may again be ascribed to conformational flexibility which distances pyrene from the Ir(III) unit. The lack of ^{1}pyr.*→^{1}MLCT energy transfer can be explained in the same way. It is important to note that the solutions of $^{F/F,\ F/H,\ H/H}$Ir•L^{pyrene}•NO_3 complexes and free pyrene used for these studies were isoabsorbing at 315 nm (A = 0.08).

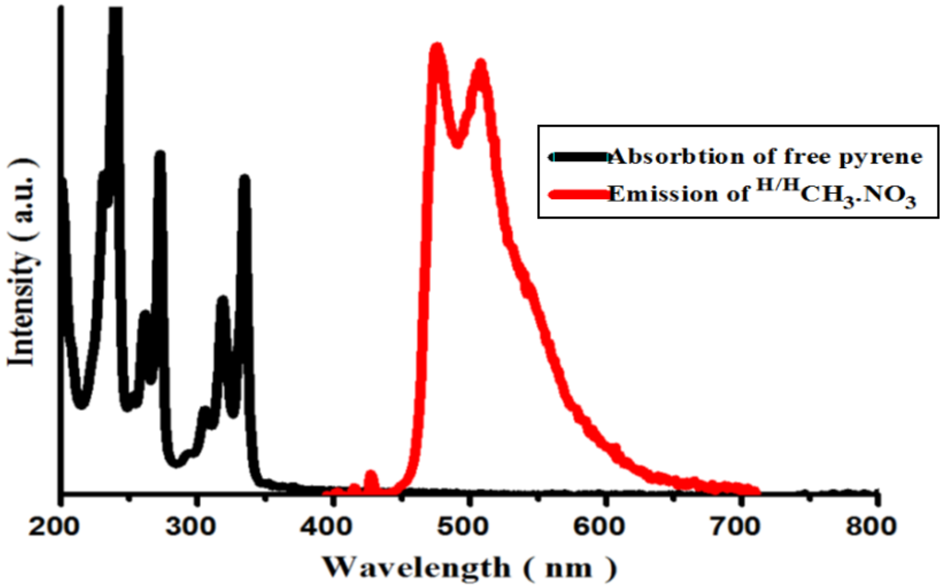

Figure 2-15: Absorption of free pyrene and luminescence emission spectra of $^{H/H}$Ir•L^{pyrene}•NO_3 complex in MeCN at 298 K, shows no energy transfer from ^{1}pyrene(donor) to Ir-MLCT (acceptor).

It should be noted that all three Ir-pyrene complexes, each with different substituents on the ppy rings, show poor E.T to the pyrene unit for the same reason, which is unfavourable conformation.

In the first scenario, excitation of the pyrene moiety at 315, 330 and 347 nm occurs to the singlet excited state (^{1}pyr). This can also be called ligand-centred (^{1}LC). The ^{1}pyr state can experience partial energy-transfer to the Ir-based ^{3}MLCT state. However, as the pyrene fluorescence is not completely quenched, this means that this energy-transfer is only partial, also allowing some direct fluorescence from ^{1}pyr to the ground state (GS) to occur. Thus the emission is seen from both emissive levels ^{3}MLCT and ^{1}pyr together.

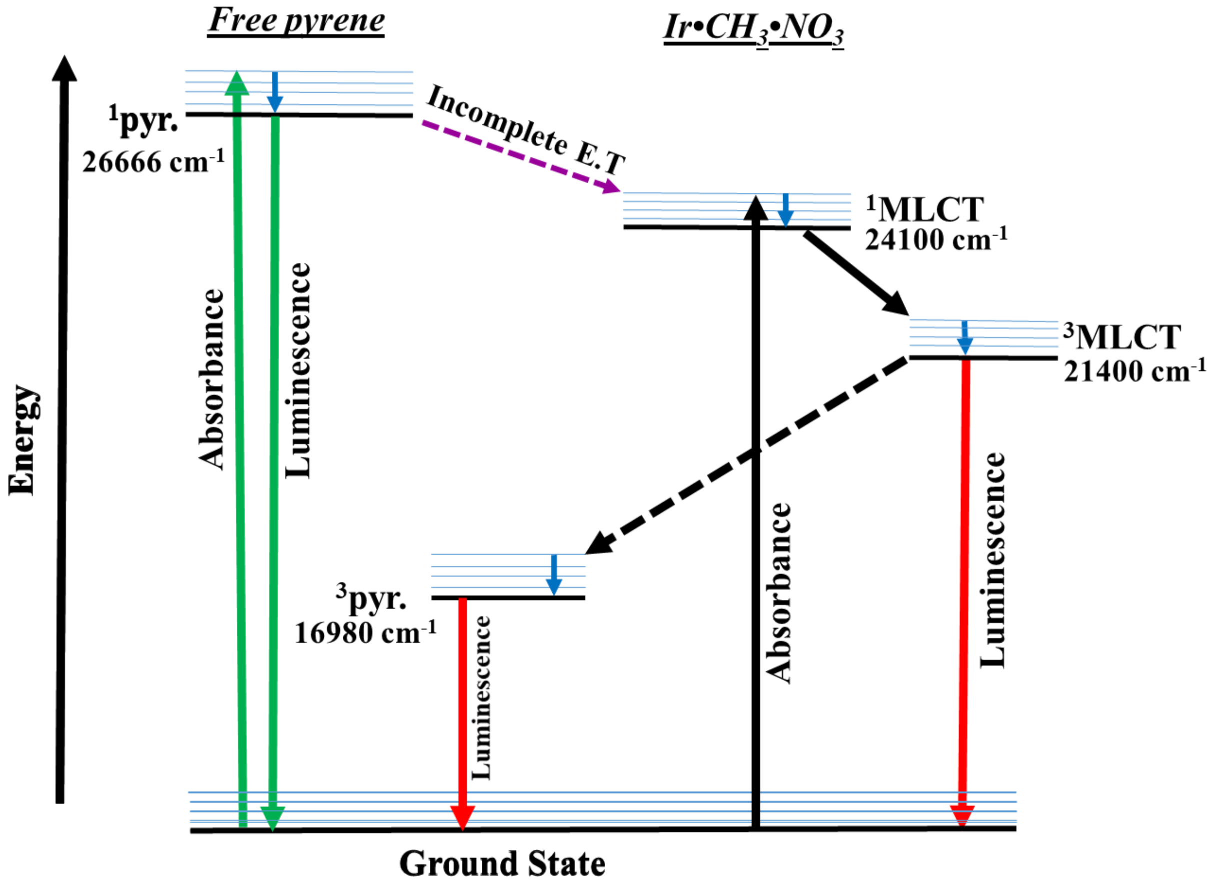

Figure 2-16: Jablonski diagram showing energy levels and luminescence of bichromophore $^{F/F, F/H, H/H}$Ir•L^{pyrene}•NO$_3$ in two cases of excitations.(→ up) represents excitation of pyrene moiety, (→ down) represents emission from pyrene moiety, (→) represents excitation of the Ir(III) moiety, (→) represents internal conversion, and (→), (→) represents partial energy transfer.

Table 2-3: Emission lifetime of a series $^{F/F,\ F/H,\ H/H}Ir{\bullet}L^{pyrene}{\bullet}NO_3$, free pyrene and series $^{F/F,\ F/H,\ H/H}Ir{\bullet}CH_3{\bullet}NO_3$ in MeCN; recorded in the 475-525 nm window, of wavelengths at 298 K.

Complexes/Lifetime	In Air/ns	In Argon/ns
$^{F\text{-}F}Ir{\bullet}L^{pyrene}{\bullet}NO_3$	24 (23%), 200 (15%), 2 (likely instrument response, the rest)	1008
$^{F\text{-}H}Ir{\bullet}L^{pyrene}{\bullet}NO_3$	40, 166	740
$^{H\text{-}H}Ir{\bullet}L^{pyrene}{\bullet}NO_3$	180	220
Free Pyrene	144	
$^{F\text{-}F}Ir{\bullet}CH_3{\bullet}NO_3$	182	490
$^{F\text{-}H}Ir{\bullet}CH_3{\bullet}NO_3$	91 (90%), 260 (10%)	470
$^{H\text{-}H}Ir{\bullet}CH_3{\bullet}NO_3$	57 and 200	370

Luminescence lifetime measurements of the $^{F\text{-}F/F\text{-}H}Ir{\bullet}L^{pyrene}{\bullet}NO_3$ and $^{F\text{-}H/H\text{-}H}Ir{\bullet}CH_3{\bullet}NO_3$ complexes gave biexponential decays in aerated MeCN at high dilution, with τ_1 ~ 200 ns and τ_2 ~ 60 ns. This may potentially have arisen from the presence of a mixture of conformers of the flexible molecule via the (CH_2) group. In contrast $^{H\text{-}H}Ir{\bullet}L^{pyrene}{\bullet}NO_3$ demonstrated a mono-exponential luminescence decay. The lifetimes measured, in the wavelength window 475-525 nm, in deoxygenated solutions are longer than the luminescence lifetime in air for all complexes. This is due to the prevention of the quenching of the emissive excited state by collision with oxygen molecules.

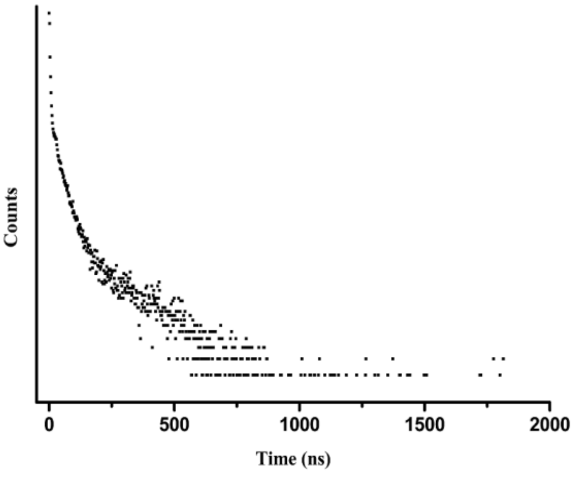

Figure 2-17: Emission intensity decay of $^{F/F}Ir{\bullet}L^{pyrene}{\bullet}NO_3$ in air in MeCN at 298 k, excitation at 405 nm (registration at 475-525 nm).

The other photophysical measurement performed for the entire series of $Ir{\bullet}L^{pyrene}{\bullet}NO_3$ and series of $Ir{\bullet}CH_3{\bullet}NO_3$ complexes was determination of quantum yield (ϕ) in aerated MeCN. All these complexes were calibrated against a known Pt(NCN)Cl (NCN = 2,6-dipyrido-phenyl) complex as a standard (ϕ =0.039)[24]. The quantum yield data for all the complexes were recorded in **Table** 2-4 and show that these are weak emitters. The quantum yield values were calculated by using equation (1):

$$\phi_{comp.} = \phi_{ref.} \times \frac{I_{comp.}}{I_{ref.}} \times \frac{A_{ref.}}{A_{comp.}} \times \frac{\eta^2_{comp.}}{\eta^2_{ref.}} \quad \text{..........} \textbf{ eq. (2-1)}$$

ϕ = quantum yield.

$I_{comp.\ or\ ref.}$ = integrated area under emission peak of interest.

A = optical density.

η = refractive index of the solvent.

comp. = complex.

ref. = reference.

Table 2-4: Quantum yield data of $^{F/F,\ F/H,\ H/H}Ir{\bullet}L^{pyrene}{\bullet}NO_3$ and $^{F/F,\ F/H,\ H/H}Ir{\bullet}CH_3{\bullet}NO_3$ complexes.

Complexes	ϕ (aerated)
$^{F\text{-}F}Ir{\bullet}L^{pyrene}{\bullet}NO_3$	0.02
$^{F\text{-}H}Ir{\bullet}L^{pyrene}{\bullet}NO_3$	0.03
$^{H\text{-}H}Ir{\bullet}L^{pyrene}{\bullet}NO_3$	0.02
$^{F\text{-}F}Ir{\bullet}CH_3{\bullet}NO_3$	0.10
$^{F\text{-}H}Ir{\bullet}CH_3{\bullet}NO_3$	0.05
$^{H\text{-}H}Ir{\bullet}CH_3{\bullet}NO_3$	0.10

2.7 Systematic investigation of the MLCT excited states of $\mathrm{Ir{\bullet}L^{pyrene}{\bullet}NO_3}$ complexes

All $\mathrm{^{F/F,\ F/H,\ H/H}Ir{\bullet}L^{pyrene}{\bullet}NO_3}$ complexes have the same ancillary ligand (pypz-pyrene) as shown in **Figure** 2-18 .However, they are different in the functionalisation of the phenyl rings on the C^N ligands with either one electron-withdrawing fluorine atom, in the F/H complex, or two, as in the complex called "F/F".

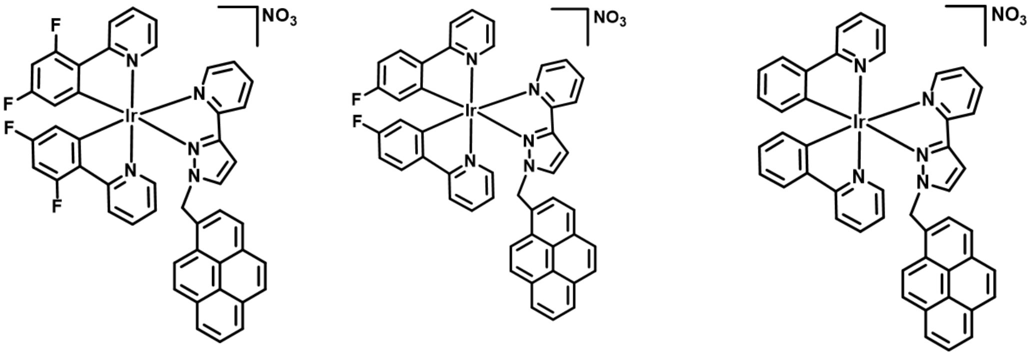

$\mathrm{^{F/F}Ir{\bullet}L^{pyrene}{\bullet}NO_3}$ $\mathrm{^{F/H}Ir{\bullet}L^{pyrene}{\bullet}NO_3}$ $\mathrm{^{H/H}Ir{\bullet}L^{pyrene}{\bullet}NO_3}$

Figure 2-18: Series complexes of $\mathrm{^{F/F,\ F/H,\ H/H}Ir{\bullet}L^{pyrene}{\bullet}NO_3}$ with different functionalisation groups.

The different functionalisation on the phenyl rings of the C^N ligand could lead to shifting of the emission bands to the higher or lower energy depending on the stabilisation of the LUMO and the energy gap between the HOMO and the LUMO.[25] The HOMO of the $\mathrm{Ir{\bullet}L^{pyrene}{\bullet}NO_3}$ complexes is delocalized on the phenyl-π ring of C^N ligand and the Ir-d orbitals. The LUMO is located primarily on the pyridine ring (π* orbital) of C^N ligand. A combination of having a third row transition metal ion with a cyclometallating ppy ligand, leads to a strong ligand field, causing a large splitting between the metal t_{2g} and e_g orbitals. The lowest π* orbital is the LUMO of the aromatic system due to the delocalisation from two aromatic rings together in ppy and the prescence of electronegative N-atoms in the rings. These π* orbitals lie in energy below the Ir-based (e_g) orbitals. The lowest-energy excited state responsible for the emission is, therefore, an MLCT state, from dπ(Ir) to the π* orbitals.[24, 26, 27] The luminescence energy increases when changing from H/H to F/H to F/F substitution on the phenyl ring of C^N ligands because the HOMO energy decreases when F atom is added to phenyl rings. The highest energy emission bands are observed at 466, 474 and 500 nm for F/F, F/H, and H/H substitution, respectively, as shown in **Figure** 2-12 and illustrated clearly in **Figure** 2-20-**a**. These band positions allowed us to estimate ^{3}MLCT energy in the $^{F/F}$Ir•L^{pyrene}•NO_3 complex as 21400 cm^{-1}, in the $^{H/H}$Ir-pyrene complex as 20000 cm^{-1}, and in $^{F/H}$Ir•L^{pyrene}•NO_3 as 21100 cm^{-1}.[28] These values may be compared to 16980 cm^{-1} for the triplet energy excited state for free pyrene. Interestingly, as illustrated in **Figure** 2-19, when exciting the Ir(III) unit, a weak ET process from ^{3}MLCT to the ^{3}pyrene energy level is observed.

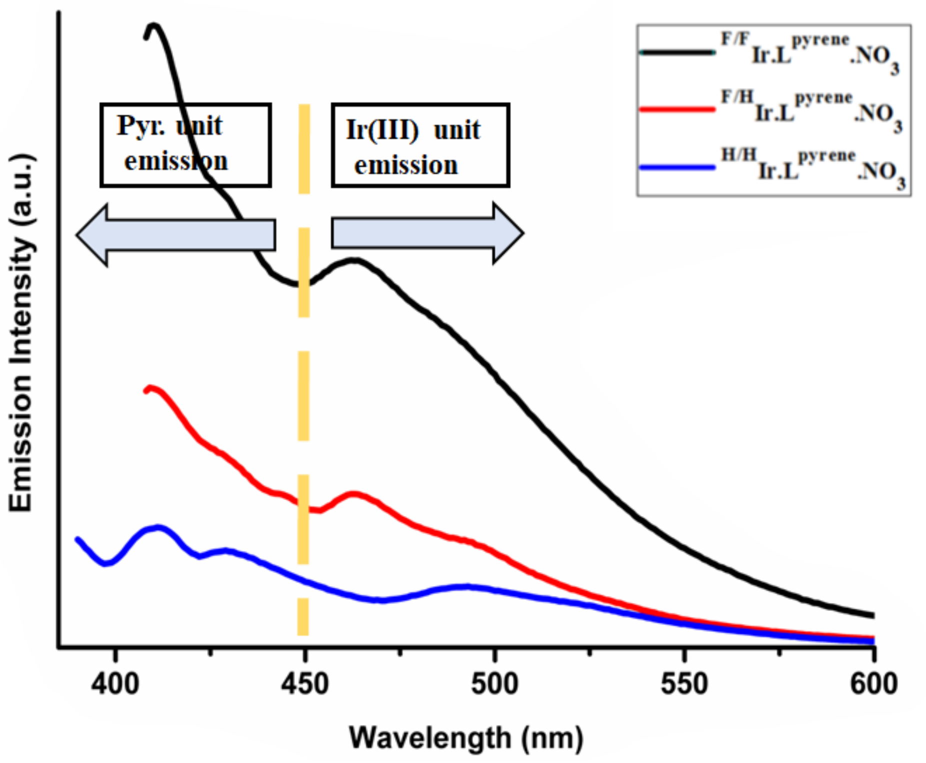

Figure 2-19: Emission spectrum of all Ir•L^{pyrene}•NO_3 complexes in case of excitation Ir(III) unit at 393 nm.

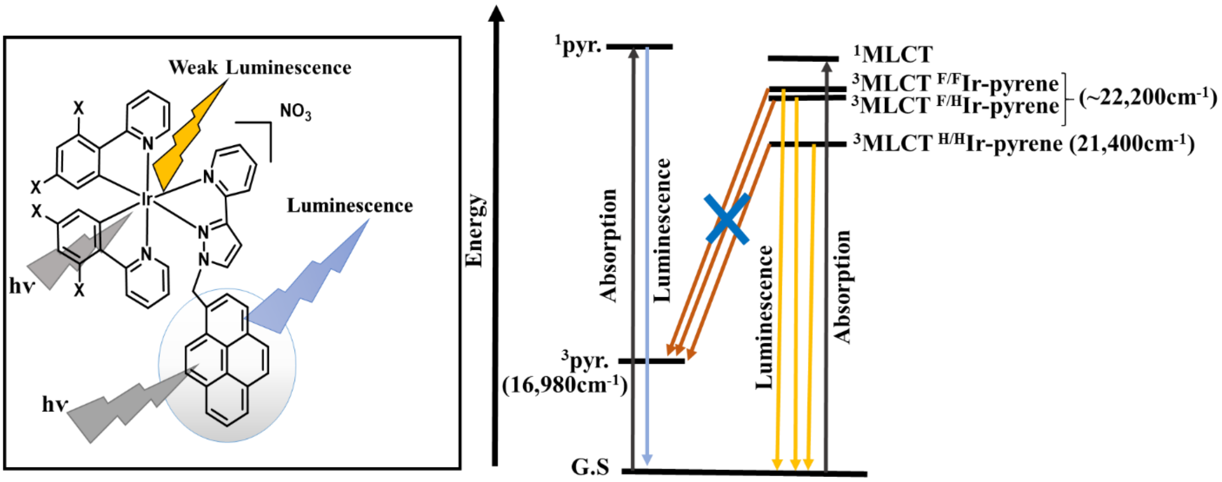

(a) **b)**

Figure 2-20: Outline luminescence scheme summarizing how the different energy levels of the ^{3}MLCT states between $^{F/F}$Ir•L^{pyrene}•NO$_3$, $^{F/H}$Ir•L^{pyrene}•NO$_3$ and $^{H/H}$Ir•L^{pyrene}•NO$_3$ complexes results in different luminescence pathways to the ground state through different excitation wavelengths.

2.8 Concentration Dependence and Excimer Formation

In order to obtain more insight into the photophysical properties of $^{F/F}$Ir•L^{pyrene}•NO$_3$ in MeCN, the effect of the concentrations of the complexes on the fluorescence emission have been examined. This is to establish whether the presence of free pyrene in an Ir-pyrene complex was leading to excimer formation in the excited state in solution. Upon increasing the concentration from 2.5×10^{-7} M to 1×10^{-4} M, the intensity of the emission band was observed to increase gradually and no growing of a new emission band at longer wavelength was observed. Both pyrene and Ir•L^{pyrene}•NO$_3$ emission corresponded to the monomer, with λ_{max} 386 nm as illustrated in **Figure** 2-21.

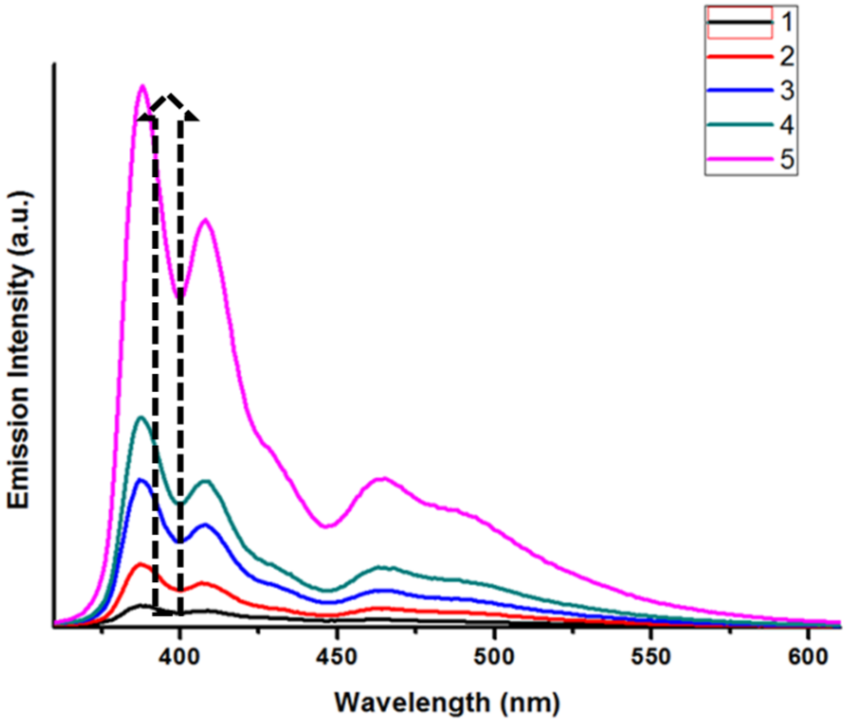

(a)

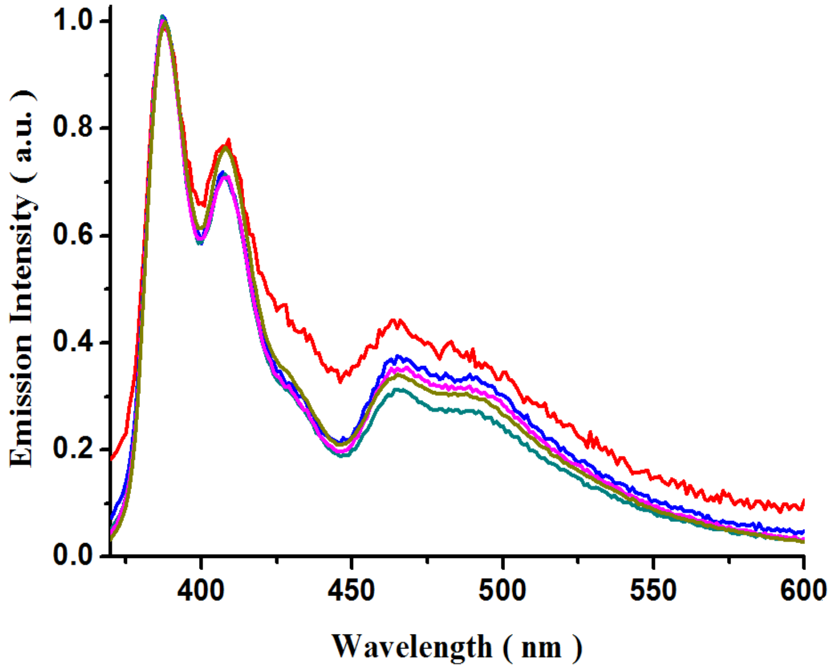

(b)

Figure 2-21: Emission spectra of pyrene in the $^{F/F}$Ir•L^{pyrene}•NO$_3$ in MeCN at 298 K at different concentrations: (1) 2.5×10^{-7} M, (2) 1×10^{-6} M, (3) 2.5×10^{-6} M, (4) 5×10^{-6} M, (5) 5×10^{-4} M. $\lambda_{ex.}$= 315 nm.(b) Normalised intensity emission showing no effect on increase concentration.

2.9 Conclusions

By reacting 1-bromomethyl pyrene with different Ir-cyclometalated complexes containing a pypz ligand, a new series of bichromophoric complexes was obtained. The new compounds were fully characterised by mass spectrometry, NMR spectroscopy, and X-ray crystallography (for $^{F/F}$Ir•L^{pyrene}•NO_3). The photophysical properties were investigated by UV-Vis absorption spectroscopy, emission spectroscopy, and emission lifetime measurements. Quenching of the ^{1}pyrene emission by the Ir(III) MLCT state *via* an energy-transfer mechanism was expected but, interestingly, energy transfer turned out to be relatively weak with incomplete quenching of the pyrene-based emission due to only partial energy-transfer. Likewise, there was no quenching of the ^{3}MLCT state of the Ir-based emission by the ^{3}pyrene state, indicating the absence of energy transfer, despite this process being energetically favourable. We suggest that lack of energy transfer is probably due to conformational flexibility provided by the –CH_2-spacer between the Ir(III) and pyrene. This leads to excessive distance between the two parts of the molecule or an orientation that is unfavourable for energy-transfer. The emission spectra of Ir(III) complexes are sensitive to the presence of fluorine substituents in the phenyl ring of the cyclometallating phenyl-pyridine ligand.

The results presented in this chapter show an interesting outcome: lack of energy transfer in Ir(III)-pyrene bichromophoric systems, which results in dual emission from these compounds.

2.10 References

1 C. Gräbe, *Justus Liebigs Ann. Chem.*, 1871, **158**, 285–299.

2 G. Goldschmied, *Justus Liebigs Ann. Chem.*, 1907, **351**, 218–232.

3 L. J. Zöphel, PhD Thesis, der Johannes Gutenberg-Universität Mainz, 2012.

4 T. M. Figueira-Duarte and K. Müllen, *Chem. Rev.*, 2011, **111**, 7260–7314.

5 R. Zhang, T. Zhang, L. Xu, F. Han, Y. Zhao and Z. Ni, *J. Mol. Struct.*, 2017, **1127**, 237–246.

6 Y. Niko, S. Sasaki, K. Narushima, D. K. Sharma, M. Vacha and G. I. Konishi, *J. Org. Chem.*, 2015, **80**, 10794–10805.

7 E. C. Constable, M. Neuburger, P. Rösel, G. E. Schneider, J. A. Zampese, C. E. Housecroft, F. Monti, N. Armaroli, R. D. Costa and E. Ortí, *Inorg. Chem.*, 2013, **52**, 885–897.

8 R. M. Edkins, K. Fucke, M. J. G. Peach, A. G. Crawford, T. B. Marder and A. Beeby, *Inorg. Chem.*, 2013, **52**, 9842–9860.

9 A. G. Crawford, PhD Thesis, University of Durham, 2011.

10 A. J. Howarth, M. B. Majewski and M. O. Wolf, *Coord. Chem. Rev.*, 2015, **282–283**, 139–149.

11 C. Bohne, E. B. Abuin and J. C. Scaiano, *J. Am. Chem. Soc.*, 1990, **112**, 4226–4231.

12 F. Hauke, A. Hirsch, S. Atalick and D. Guldi, *Eur. J. Org. Chem.*, 2005, 1741–1751.

13 K. P. S. Zanoni, B. K. Kariyazaki, A. Ito, M. K. Brennaman, T. J. Meyer and N. Y. Murakami Iha, *Inorg. Chem.*, 2014, **53**, 4089–4099.

14 A. C. Hazell and J. G. Lomborg, *Acta Cryst.*, 1972, **28**, 1059–1064.

15 Y. Miura, E. Yamano, A. Tanaka and J. Yamauchi, *J. Org. Chem.*, 1994, **59**, 3294–3300.

16 Y. Qiao, J. Zhang, W. Xu and D. Zhu, *Tetrahedron*, 2011, **67**, 3395–3405.

17 J. M. Casas-Solvas, J. D. Howgego and A. P. Davis, *Org. Biomol. Chem.*, 2014, **12**, 212–232.

18 S. Nagatoishi, T. Nojima, B. Juskowiak and S. Takenaka, *Angew. Chemie - Int. Ed.*, 2005, **44**, 5067–5070.

19 A. J. Howarth, D. L. Davies, F. Lelj, M. O. Wolf and B. O. Patrick, *Inorg. Chem.*, 2014, **53**, 11882–11889.

20 S. Nishizawa, Y. Kato and N. Teramae, *J. Am. Chem. Soc.*, 1999, **121**, 9463–9464.

21 J. Fernando, E. Barano and N. D. Mcclenaghan, *Inorg. Chem.*, 2014, **53**, 2677–2682.

22 D. Sykes, I. S. Tidmarsh, A. Barbieri, I. V. S, J. A. Weinstein and M. D. Ward, *Inorg. Chem.*, 2011, **50**, 11323–11339.

23 T. Vo-Dinh, *Anal. Chem.*, 1978, **50**, 396–401.

24 J. A. G. Williams, A. Beeby, E. . S. Davies, J. A. Weinstein and C. Wilson, *Inorg. Chem. Commun.*, 2003, **42**, 8609–8611.

25 J. Du, Y. Luo, X. Xie, W. Hu and W. Shen, *Mol. Simul.*, 2016, **42**, 1036–1042.

26 J. Li, P. I. Djurovich, B. D. Alleyne, M. Yousufuddin, N. N. Ho, J. C. Thomas, J. C. Peters, R. Bau and M. E. Thompson, *Inorg. Chem.*, 2005, **44**, 1713–1727.

27 K. Hasan, A. K. Bansal, I. D. W. Samuel, C. Roldán-carmona, H. J. Bolink and E. Zysman-Colman, *Sci. Rep.*, 2015, **5**, 1–16.

28 D. Sykes, S. C. Parker, I. V Sazanovich, A. Stephenson, J. A. Weinstein and M. D. Ward, *Inorg. Chem.*, 2013, **52**, 10500–10511.

CHAPTER THREE

Systematic Studies of Excited States of Ir(III) Complexes.

3 Systematic Studies of Excited States of Ir(III) Complexes

3.1 Interplay of HOMO –LUMO in a single Ir(III) complexes

Of special interest for Ir(III) complexes of bidentate cyclometalating ligands are the colour tunability of the emission across the visible emission spectrum, to use in many applications like OLEDs due to resulting white light.[1–3] The emission colour of Ir(III) complexes results from the triplet excited state, either ^{3}MLCT, or an admixture states of ^{3}MLCT and ^{3}LC character.[4–7] Basically, from the type of the coordinating ligands, and their σ-donating and π-accepting abilities, can be predicted the luminescence properties of the Ir(III) complexes.[4] For the common case of green-emitting *fac*-Ir(ppy)$_3$, the emission level is believed to be from ^{3}MLCT state due to promotion of an electron from d-orbital of metal centre, which is the HOMO orbital, to an empty π* orbital of the pyridine ring, which is the LUMO orbital.[8, 9] There are several strategies which can be used to control the HOMO-LUMO energy gap and allow color variation of the emission from green to yellow to red[10, 11] and to blue[4].

a) Changing the type and size of the ligand: more extended electronic delocalisation lowers the LUMO level in energy and leads to lower-lying both ^{3}MLCT and ^{3}LC excited states. For example, in general formula of Ir(C^N)$_2$(LX), the complex Ir(ppy)$_2$(acac) (where ppy is phenyl pyridine and acac is acetyl acetonate (**Figure** 3-1), emits from ^{3}MLCT with wavelength emission $\lambda_{em.}$516 nm, whereas Ir(thpy)$_2$(acac) complex, where thpy is thionyl-pyridine (**Figure** 3-1), emits from a ^{3}LC excited state with $\lambda_{em.}$562 nm.[12]

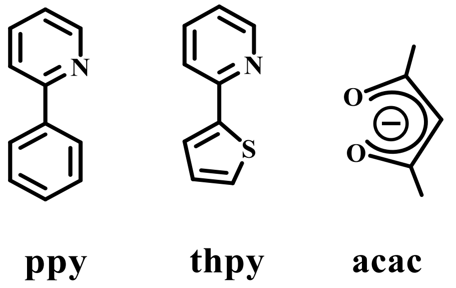

Figure 3-1. Ancillary ligands of neutral Ir(C^N)$_2$(LX) complex, when C^N is ppy, thpy and LX is acac.

b) Addition of electron withdrawing substituents (like F atoms) on the phenyl ring of the cyclometalating ligand will stabilise the HOMO level from both Ir(III) ion and the phenyl ring, whereas the LUMO level is almost not affected.[13–15] Addition of electron-donating substituents on the pyridine ring of cyclometalating ligands will destabilise the LUMO level.[16–18] As a consequence, this has the effect to increase energy gap between HOMO and LUMO levels and move both MLCT and LC electronic transitions to higher energy.

c) Changing the pyridyl ring of cyclometalating ligand by other heterocyclic moieties (**Figure** 3-2) can lead to a rise in the LUMO level above that of the pyridine ring. This pushes electronic transitions of both MLCT and LC states to higher energy: use of carbenes as strong σ-donating ligands has the same effect.[4,19]

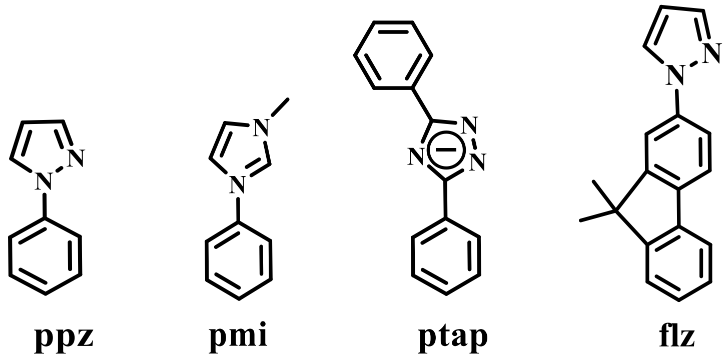

Figure 3-2 Heterocyclic ligands.

d) Changing the ancillary ligand that is attached to the Ir(III) ion, for example from aromatic ligands (e.g. bipyridine) to stronger electron withdrawing groups such as isocyanide and cyano derivatives, perturbs the HOMO-LUMO levels by increasing the energy gap between them.[20–22]

Recently, Martinez-Alonso *et.al*.[23] reported that in complex (1) (**Figure** 3-3**)** the HOMO orbitals are delocalised over Ir(III) d_π orbitals and the π-orbitals of the (N^O) ancillary ligand; whereas the LUMO is localised on the C^N cyclometalating ligands. In complex (2), on the other hand (**Figure** 3-3) the HOMO and the LUMO are both localised on the N^O ancillary ligand. The strong stabilisation of the LUMO compared to complex (1) is attributed to the weaker electron donor ability into the aromatic system of benzothiazole compared to benzimidazole due to poor overlapping of 3p orbital from the S atom compared to the 2p orbital of the N atom with the rest of the aromatic ring. This result contrasts with the HOMO and LUMO orbital localisation on the common cyclometalating Ir(III) complex with the formula $[\mathrm{Ir(C^\wedge N)_2(N^\wedge N)}]^+$, when C^N is ppy and N^N is diamine.[23]

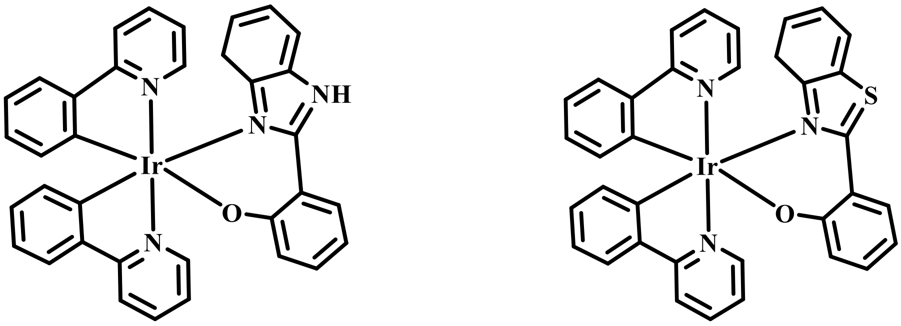

Complex (1) **Complex (2)**

Figure 3-3 Molecular structure of nutral Ir(III) complexes (1) labled with NH and (2) labled with S atom.

Ir, as the third row metal, complexes with cyclometalated ligands, such as ppy and analogues, have very strong ligand field of the cyclometalated C atom, which lead to large splitting between t_{2g} and e_g orbitals. The low energy LUMO of ppy ligands is localised on the π* of an aromatic system and due to the delocalisation from two aromatic rings in ppy, and the presence of the N atoms in the pyrine rings, these π* orbitals become more stable and lie below the Ir e_g orbitals. The HOMO is localised on both the metal and the phenyl ring. Thus, the substitution into the phenyl ring of the cyclometalated ligand (withdrawing or donating groups) will affect the stabilisation of the HOMO level.

3.2 The aims of this chapter

In order to control the HOMO-LUMO energy gap on a range of Ir(III) complexes, we can design Ir(III) complexes in two parts. The absence or presence of electron-withdrawing F atoms on the phenyl ring of the cyclometalating ligand has a strong effect on excited-state luminescence properties. In addition, the nature of the ancillary ligand has a substantial effect, and variation of these two parameters is the basis of this chapter. This chapter principally aims to study the control of the HOMO-LUMO energy gap through study the photophysical properties of a series of mono-Ir(III) complexes and how their excited states can be tuned through structure modification. This is assessed through synthesis and characterisation of Ir(III) complexes and the study of their photophysical properties.

3.3 The sets of mono-Ir(III) complexes used in this chapter

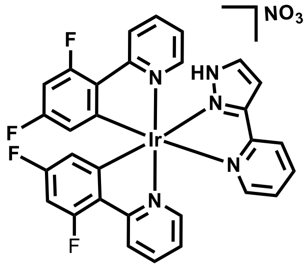

$^{F/F}$Ir•pypz•NO$_3$

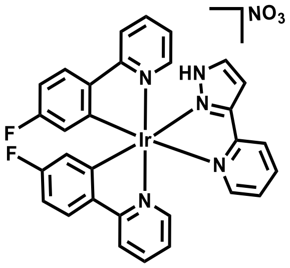

$^{F/H}$Ir•pypz•NO$_3$

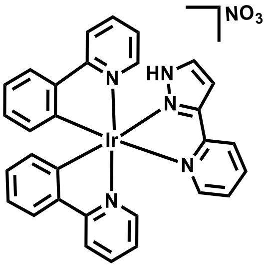

$^{H/H}$Ir•pypz•NO$_3$

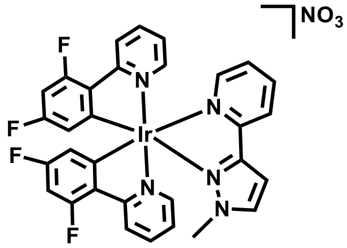

$^{F/F}$Ir•CH$_3$•NO$_3$

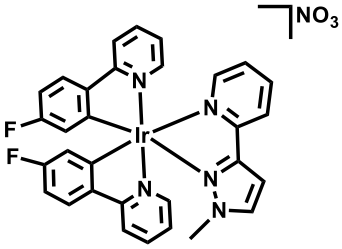

$^{F/H}$Ir•CH$_3$•NO$_3$

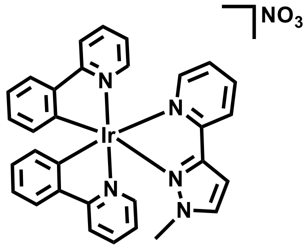

$^{H/H}$Ir•CH$_3$•NO$_3$

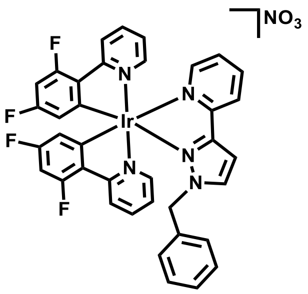

$^{F/F}$Ir•L^{phenyl}•NO$_3$

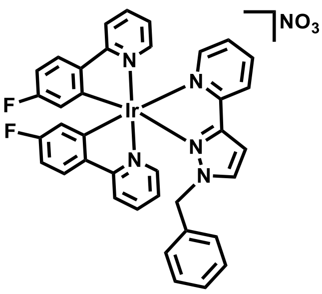

$^{F/H}$Ir•L^{phenyl}•NO$_3$

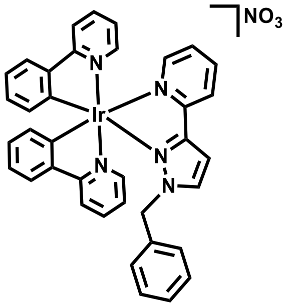

$^{H/H}$Ir•L^{phenyl}•NO$_3$

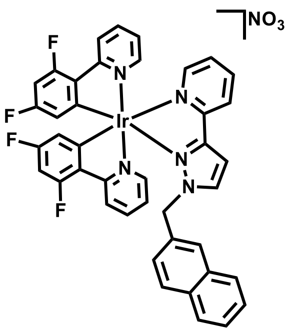

$^{F/F}$Ir•L^{2naph}•NO$_3$

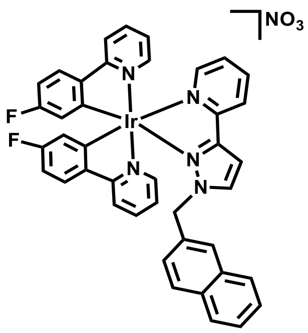

$^{F/H}$Ir•L^{2naph}•NO$_3$

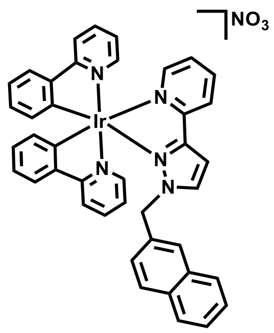

$^{H/H}$Ir•L^{2naph}•NO$_3$

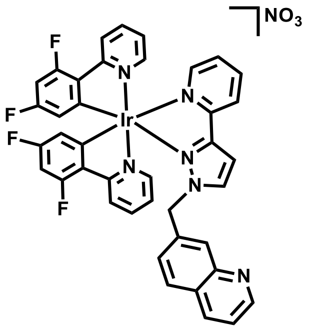

${}^{F/F}\mathrm{Ir}\bullet\mathrm{L}^{quinoline}\bullet\mathrm{NO}_3$

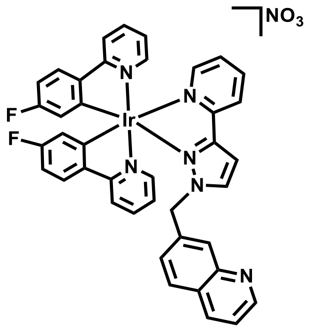

${}^{F/H}\mathrm{Ir}\bullet\mathrm{L}^{quinoline}\bullet\mathrm{NO}_3$

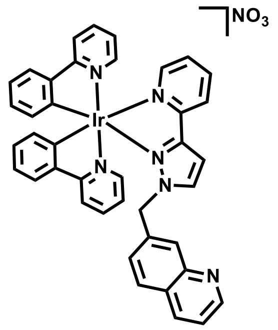

${}^{H/H}\mathrm{Ir}\bullet\mathrm{L}^{quinoline}\bullet\mathrm{NO}_3$

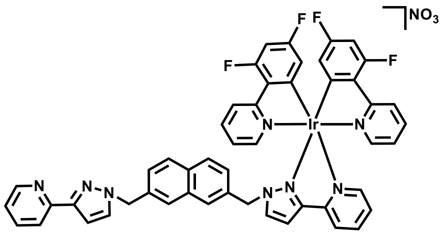

${}^{F/F}\mathrm{Ir}\bullet\mathrm{L}^{naph}\bullet\mathrm{NO}_3$

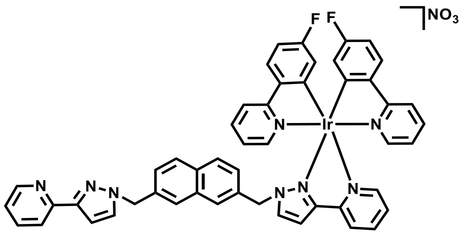

${}^{F/H}\mathrm{Ir}\bullet\mathrm{L}^{naph}\bullet\mathrm{NO}_3$

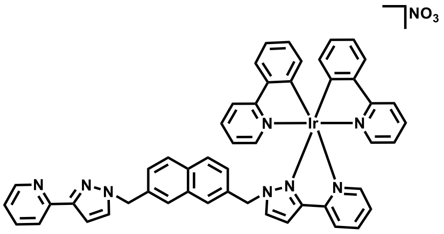

${}^{H/H}\mathrm{Ir}\bullet\mathrm{L}^{naph}\bullet\mathrm{NO}_3$

Figure 3-4 Chemical structures of mono- ${}^{F/F,\ F/H\ \mathrm{and}\ H/H}$Ir(III) complexes studied in this chapter.

3.4 Results and Discussion

3.4.1 Syntheses and characterization

Five different series of mononuclear Ir(III) complexes have been synthesized (**Figure** 3-5) with variations in the type of ancillary ligand, and the absence or presence F atoms on the phenyl rings of the cyclometalating ligands.

To synthesise these types of complexes, two routes have been followed. Route 1 involves synthesis of the ancillary ligand, purification, and then attachment to the Ir-dimer to give the final complex. This procedure can take a long time in purification as some ligands require many columns with different eluents for purification.

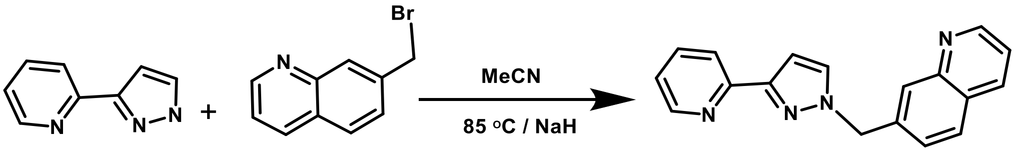

(First step)

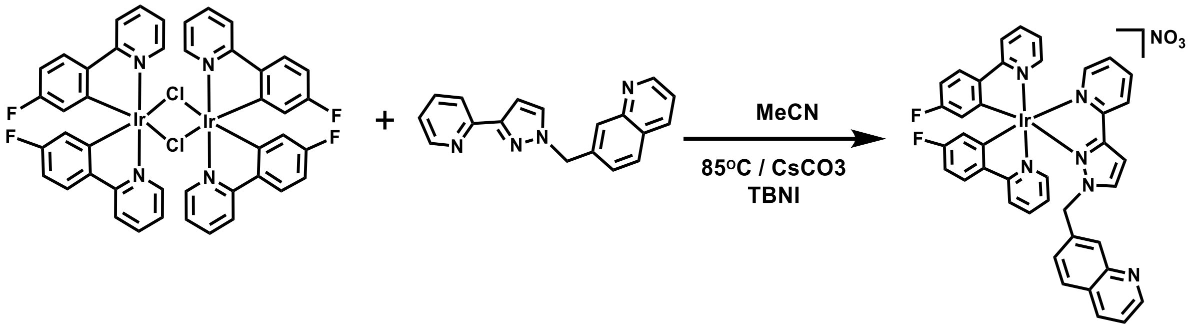

(Second step)

Figure 3-5 Synthesis of Ir(III) complexes by following route one in two steps.

Route 2 is functinoalisation of a pre-prepared complex core with a reactive pyrazolyl site. All complexes prepared in this way followed the same method in two steps. Step 1 is the reaction of the Ir(III) dimer with pypz to give the $^{x/x}$Ir•pypz•NO_3 complex (when X/X is F/F or F/H or H/H). In step 2, the complex obtained in step 1 is then alkylated at the pyrazolyl NH site by reaction with [substituent–CH_2Br] in a S_N2 mechanism in a ratio 1:1 in presence of $CsCO_3$ as a base and iodide as a catalyst, as shown in **Figure** 3-6. The crude reaction mixture is then cooled to room temperature, the solvent evaporated to dryness, and the resulting solid containing the desired product purified by silica gel chromatography. Purification conditions for each complex are mentioned briefly in the experimental section and are summarised in **Table** 3-1.

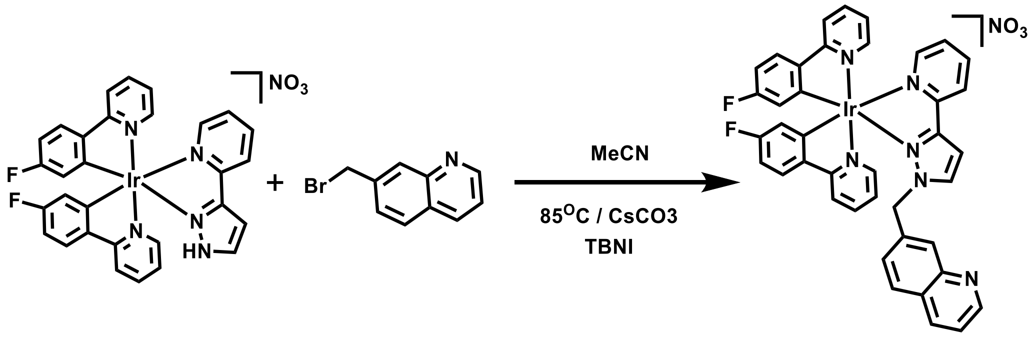

Figure 3-6 Synthesis of complexes by following route two in one step.

Table 3-1 Summary of the chromatographic purification methods of Ir(III) complexes.

Ir(III) complexes	Conditions of purification
$^{F/F}$Ir•pypz•NO_3 $^{F/H}$ Ir•pypz•NO_3 $^{H/H}$ Ir•pypz•NO_3	Silica gel (200-300 mesh) eluted with MeCN:$KNO_{3(aq)}$ (96:4).
$^{F/F}$ Ir•CH_3•NO_3 $^{F/H}$ Ir•CH_3•NO_3 $^{H/H}$ Ir•CH_3•NO_3	Silica gel (200-300 mesh) eluted with MeCN:$KNO_{3(aq)}$ (96:4).
$^{F/F}$ Ir•L^{phenyl}•NO_3 $^{F/H}$ Ir•L^{phenyl}•NO_3 $^{H/H}$ Ir•L^{phenyl}•NO_3	Silica gel (200-300 mesh) eluted with MeCN:$KNO_{3(aq)}$ (96:4).
$^{F/F}$ Ir•$L^{2\text{-}naph}$•NO_3 $^{F/H}$ Ir•$L^{2\text{-}naph}$•NO_3 $^{H/H}$ Ir•$L^{2\text{-}naph}$•NO_3	Silica gel (200-300 mesh) eluted with: 1 - 1000 mL MeCN. 2 - DCM/MeOH (95:5).
$^{F/F}$ Ir•$L^{quinoline}$•NO_3 $^{F/H}$ Ir•$L^{quinoline}$•NO_3 $^{H/H}$ Ir•$L^{quinoline}$•NO_3	Silica gel (200-300 mesh) eluted with: 1- 1000 mL MeCN; 2 - MeCN:$KNO_{3(aq)}$:H_2O (100:5:10).
$^{F/F}$ Ir•L^{pyrene}•NO_3 $^{F/H}$ Ir•L^{pyrene}•NO_3 $^{H/H}$ Ir•L^{pyrene}•NO_3	Silica gel (200-300 mesh) eluted with: 1 - 1000 mL Toluene. 2 - Toluene:MeOH (95:5). 3 - MeCN:H_2O:$KNO_{3(aq)}$(100:10:5).

3.4.2 ^{1}H NMR spectra of some of the Ir(III) complexes.

In this chapter, the successful synthesis of all of the mononuclear Ir(III) complexes was confirmed by mass spectrometry, ^{1}H NMR spectroscopy and in some cases by X-ray crystallography. All ^{1}H NMR spectroscopy was done in deuterated MeCN at room temperature. We have chosen a set of complexes with the ancillary substituent quinoline to show how the presence and absence of F groups on the complex core affects the splitting and shifting the ^{1}H peaks of the protons. ^{1}H-NMR spectra of $^{F/F}$Ir•L^{quinoline}•NO$_3$ and $^{H/H}$Ir•L^{quinoline}•NO$_3$ are shown in **Figure** 3-7 and **Figure** 3-8. ^{1}H NMR spectroscopy was used to check the absolute position of proton of diastereotopic CH$_2$ group. All complexes gave the exact number of the protons required (26H, 28H and 30H) for $^{F/F}$Ir•L^{quinoline}•NO$_3$, $^{F/H}$Ir•L^{quinoline}•NO$_3$ and $^{H/H}$Ir•L^{quinoline}•NO$_3$ complexes respectively.

The diastereotopic CH$_2$ protons appear as dd signals in $^{F/F}$Ir•L^{quinoline}•NO$_3$ with high *J* -coupling constants at 5.92 ppm and at 5.80 ppm (*J* = 18.5 Hz). The signal at 5.80 ppm overlaps with adjacent peaks at 5.80 ppm as shown in expanded part of **Figure** 3-7.

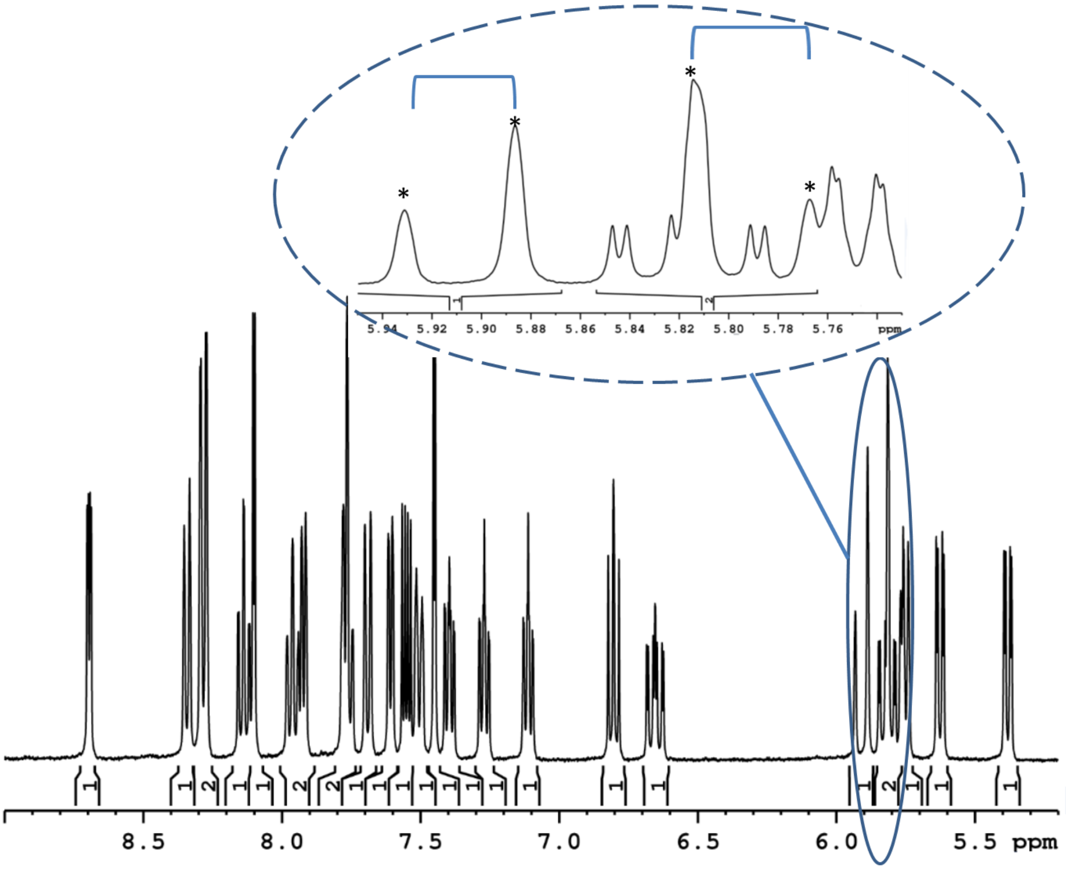

Figure 3-7 ^{1}H NMR $^{F/F}$Ir•L^{quinoline}•NO$_3$ in deuterated MeCN at 298 K. Zoom-in showing splitting of diastereotopic CH$_2$ group protons at 5.80 ppm the signal clearly overlap with adjacent peak.

The ^{1}H NMR spectrum of $^{H/H}$Ir•L^{quinoline}•NO$_3$ the diastereotopic CH$_2$ protons at 5.62 and 5.87 ppm which again have a large *J* -coupling of about 17 Hz (**Figure** 3-8).

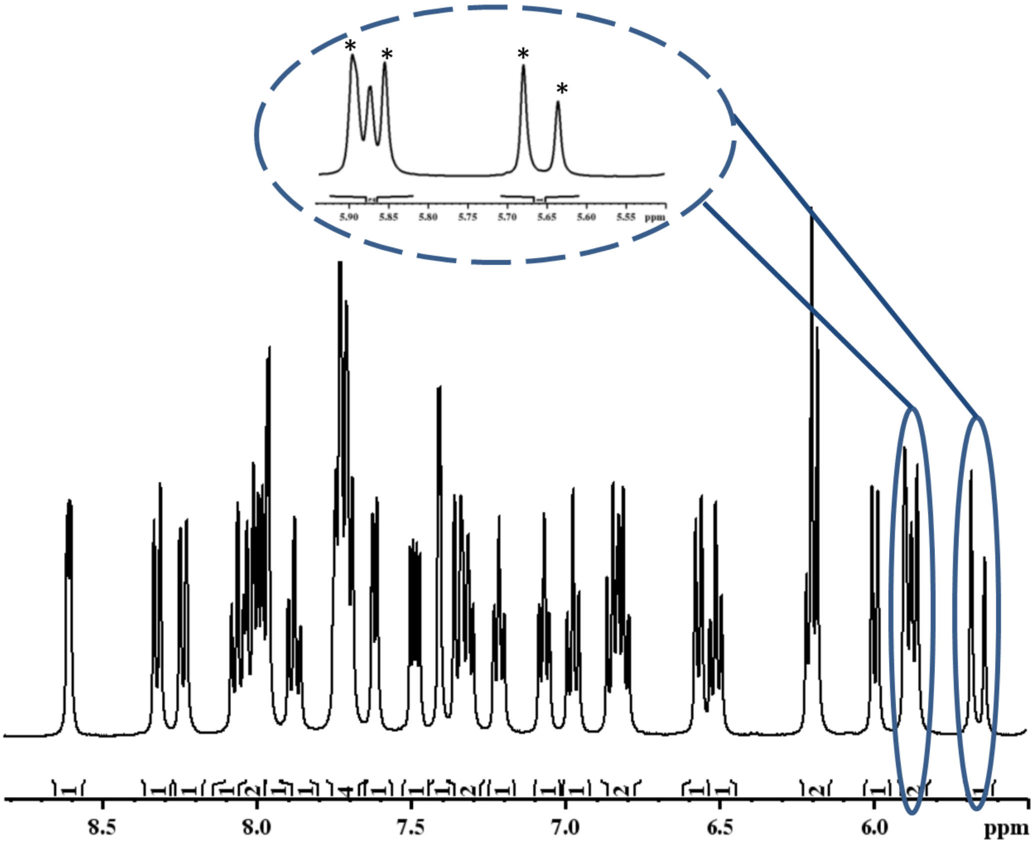

Figure 3-8 ^{1}H NMR $^{H/H}$Ir•L^{quinoline}•NO$_3$ in deuterated MeCN at 298 K, showing CH$_2$ group proton splitting.

3.4.3 X-ray crystallography of some Ir(III) complexes.

X-ray crystal structures were obtained from crystals grown by slow diffusion of diethyl ether into a solution of complex in MeCN, in the dark at 298 K. The main feature for all mononuclear Ir(III) complexes is Ir(III) centre in a pseudo-octahedral geometry with the arrangment of two ppy rings in expected *trans*-N_2, *cis*-C_2 positions.[24] In addition, the Ir-C and Ir-N bond lengths of cyclometalated ligands lie around the expected values of *ca.* 2 Å.[25–27] In all crystal cases the Ir-N(ancillary ligand) bond distance are considerably longer because of the strong *trans* effect of electron-donating cyclometalated Ir-C atoms,[28, 29] as listed on each complex crystal table.

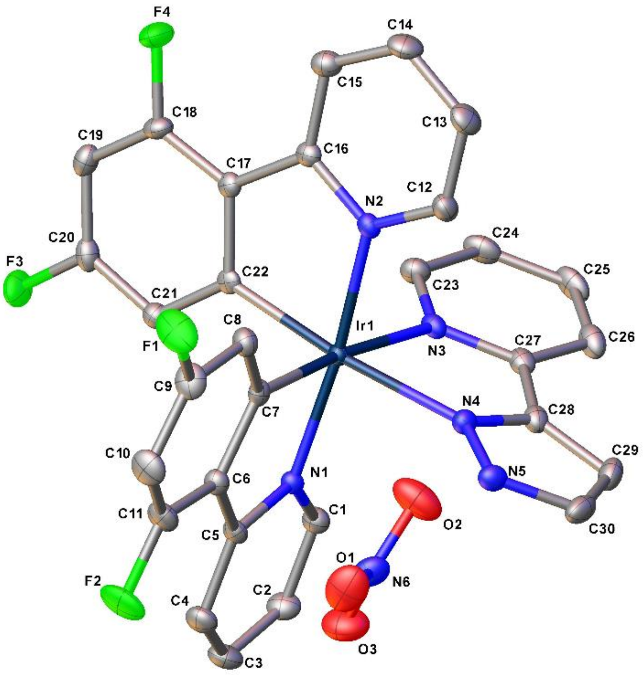

(a)

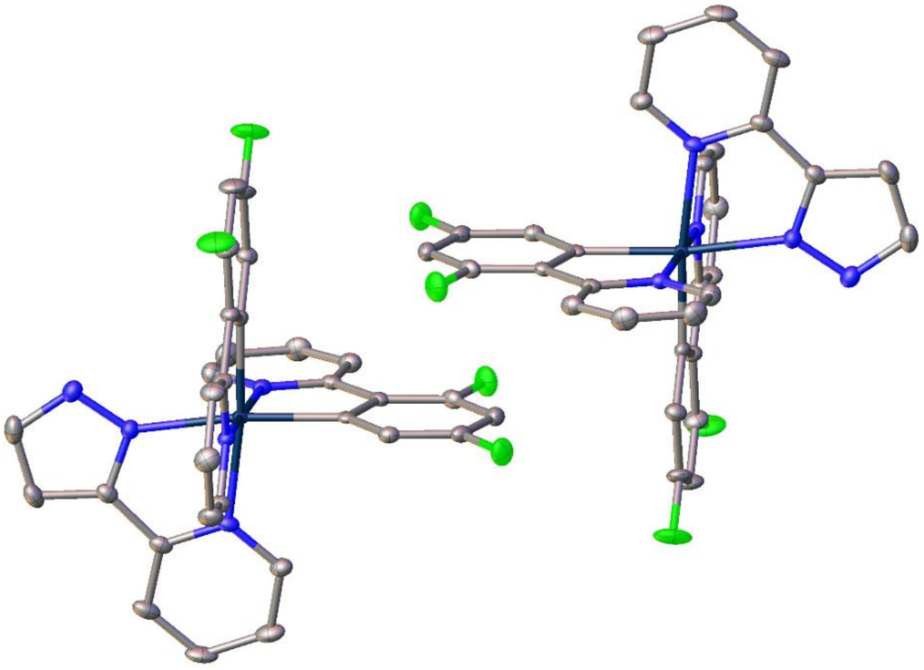

(b)

Figure 3-9 Two views of the structure of $^{F/F}$Ir•pypz•NO_3 with thermal ellipsoids at 50% probability level with intermolecular *π-π* stacking between F_2-phenyl rings of cyclometalated ligands.

Figure 3-9 shows the crystal structure of $^{F/F}$Ir•pypz•NO_3 which crystallizes in the triclinic space group P-1. The pypz ligand coordinates trans to the two cyclometalated C atoms of the phenyl rings. The NO_3 anion is present. The crystal structure is stabilised by aromatic π-stacking between the F_2-phenyl rings with a centroid-centroid distance of 3.67 Å. The crystallographic data are listed in **Table 3-2**.

Table 3-2 Selected distances parameters for solvate $^{F/F}$Ir•pypz•NO_3 complex.

$^{F/F}$Ir•pypz•NO_3- Bonds	**Distances [Å]**
Ir-C_7	2.007 (2)
Ir-C_{22}	2.010 (2)
Ir-$N_{1(C\text{^}N)}$	2.044 (18)
Ir-$N_{2(C\text{^}N)}$	2.038 (19)
Ir-$N_{3(N\text{^}N)}$	2.165 (18)
Ir-$N_{4(N\text{^}N)}$	2.123 (18)

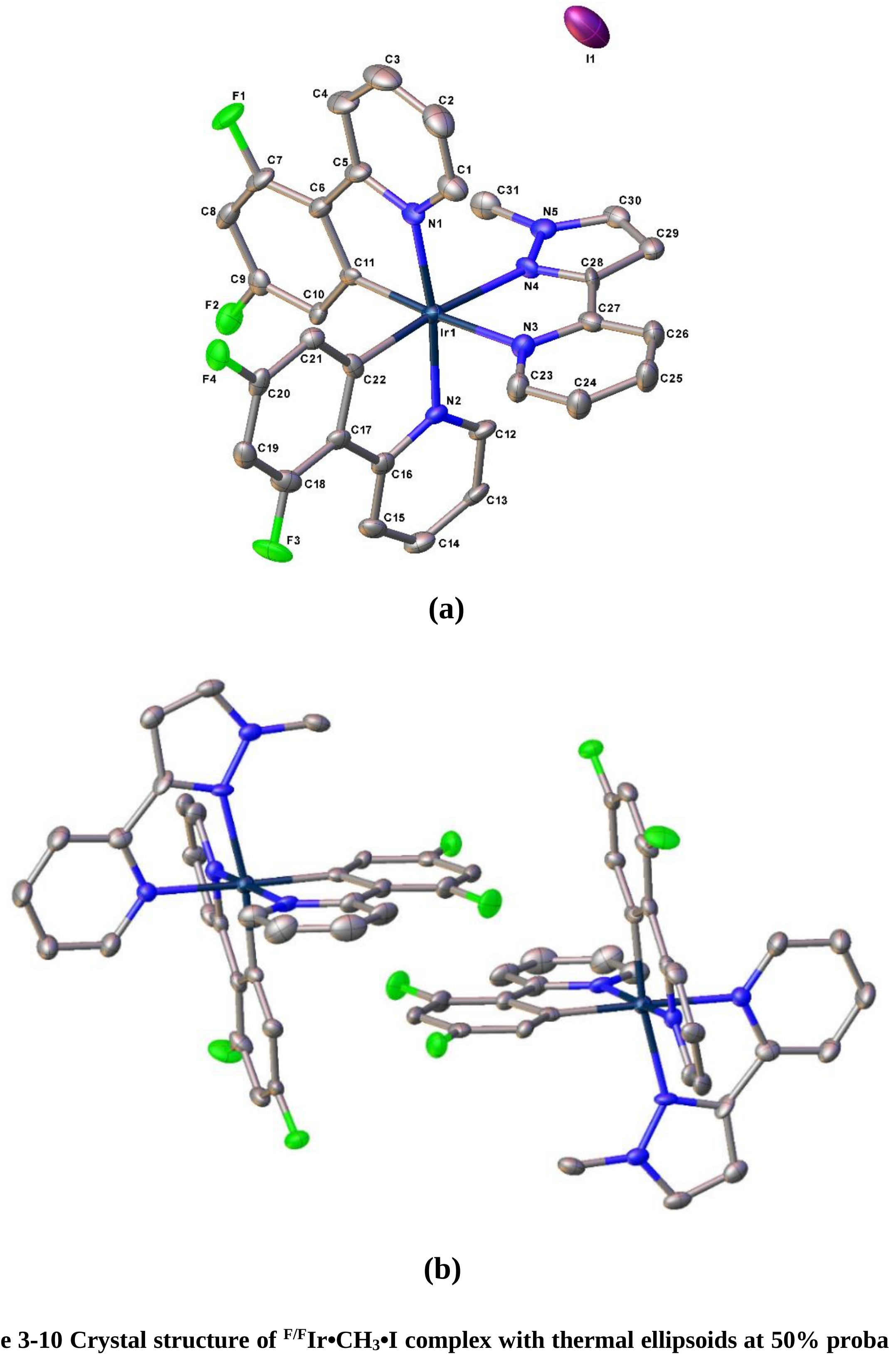

Figure 3-10 Crystal structure of $^{F/F}$Ir•CH$_3$•I complex with thermal ellipsoids at 50% probability level.

The crystal structure of the $^{F/F}$Ir•CH$_3$ complex cation has been published.[30] However, there is a slight difference between published complex ^{F}Ir•L^{Me}•CH$_2$Cl$_2$, and what we found in $^{F/F}$Ir•CH$_3$•I complex in space group, crystal system and bond lengths. The core structure of

$^{F/F}$Ir•CH$_3$•I complex is the same as the previously-reported nitrate salt: we have got iodide as anion due to use of CH$_3$I in the synthesis. The difference in crystallographic refinement data between $^{F/F}$Ir•CH$_3$•I and $^{F/F}$Ir•L^{Me}•CH$_2$Cl$_2$ are sumarised in **Table 3-3**. The $^{F/F}$Ir•CH$_3$•I complex shows intermolecular π-stacking with centroid-centroid separations *ca.* 3.848 Å between aromatic cyclometalated ligands,[31] with a shift of *ca.* 2.032. The crystal structure is depicted in **Figure** 3-10. The difference are likely due to difference in the concentration (I$^-$ vs NO$_3^-$) and inclusion of a CH$_2$Cl$_2$ molecules in the crystal in the published structure.

Table 3-3 Selected distances parameters for solvate $^{F/F}$Ir•CH$_3$•I complex compare to the published ^{F}Ir•L^{Me}•CH$_2$Cl$_2$ complex.

$^{F/F}$Ir•CH$_3$•I - Bonds	Distances [Å]	^{F}Ir•L^{Me}•CH$_2$Cl$_2$ - Bonds	Distances [Å]
Ir-C$_{11(C\^N)}$	2.006 (11)	**Ir-C$_{121(C\^N)}$**	2.007 (6)
Ir-C$_{22(C\^N)}$	2.007 (10)	**Ir-C$_{141(C\^N)}$**	2.021 (6)
Ir-N$_{1(C\^N)}$	2.053 (9)	**Ir-N$_{111(C\^N)}$**	2.047 (5)
Ir-N$_{2(C\^N)}$	2.054 (9)	**Ir-N$_{131(C\^N)}$**	2.042 (5)
Ir-N$_{3(N\^N)}$	2.158 (9)	**Ir-N$_{151(N\^N)}$**	2.155 (6)
Ir-N$_{4(N\^N)}$	2.141 (8)	**Ir-N$_{162(N\^N)}$**	2.152 (6)

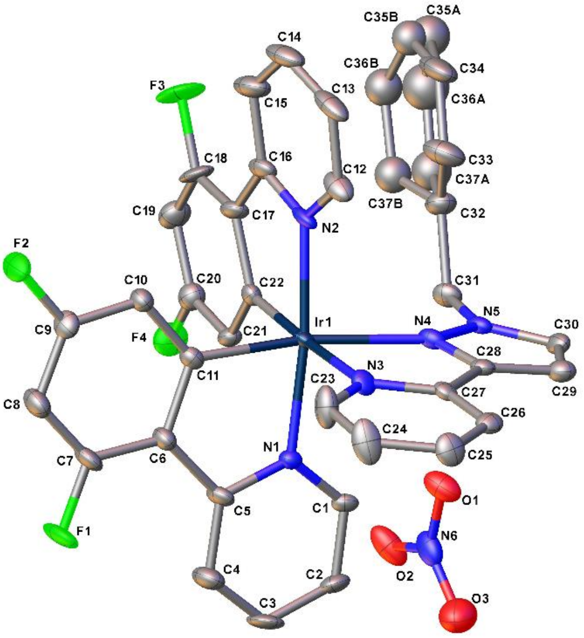

Figure 3-11 Molecular structure of the $^{F/F}$Ir•L^{phenyl}•NO$_3$ complex cation of NO$_3$ anion with displacement ellipsoids at 50% probability level, showing the disorder of the pendant phenyl ring.

The crystal structure of $^{F/F}$Ir•L^{phenyl}•NO$_3$ complex is depicted in **Figure** 3-11. The main feature is disordered ancillary phenyl group in a ratio 54% and 46% over the two sites. This is stacked with one phenyl ring of the cyclometalated ligands with a distance about *ca.* >4 Å with the parallel aromatic sections.[31] The crystallographic parameters are listed in **Table 3-4**.

Table 3-4 Selected distances parameters for solvate $^{F/F}$Ir•L^{phenyl}•NO$_3$ complex.

$^{F/F}$Ir•L^{phenyl}•NO$_3$ - Bonds	**Distances [Å]**
Ir-C$_{11(C\wedge N)}$	2.009 (5)
Ir-C$_{22(C\wedge N)}$	2.008 (5)
Ir-N$_{3(N\wedge N)}$	2.162 (4)
Ir-N$_{4(N\wedge N)}$	2.152 (4)
Ir-N$_{1(C\wedge N)}$	2.051 (4)
Ir-N$_{2(C\wedge N)}$	2.054 (4)

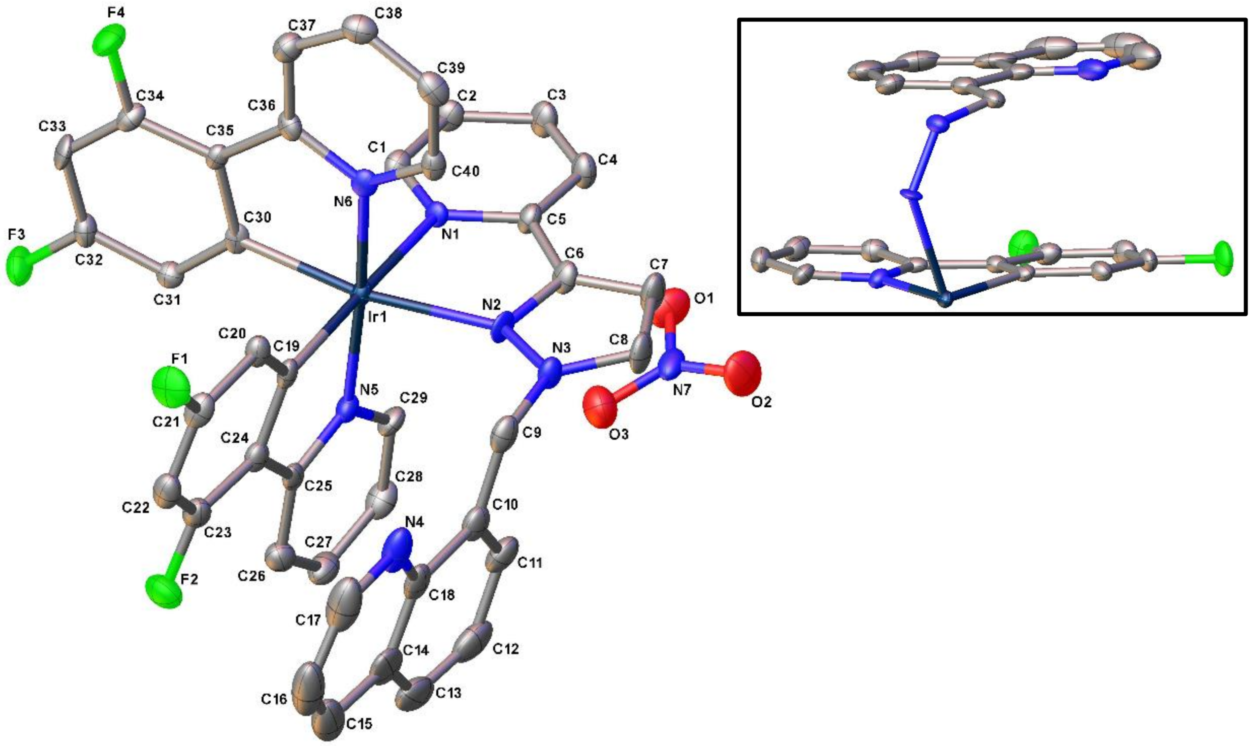

Figure 3-12 Molecular structure of the $^{F/F}$Ir•L^{quinoline}•NO$_3$ complex cation with NO$_3$ anion and MeCN solvent with displacement ellipsoids at 50%probability level with expanded to the shifting between quinoline ring and F$_2$ppy rings of the cyclometalating ligands.

The crystal structutre of $^{F/F}\text{Ir}\bullet\text{L}^{quinoline}\bullet\text{NO}_3$, which crystallizes in space group C2/c, shows the same core structure as other complexes. One of the F_2ppy cyclometalating ligands stacks with the pendant quinoline group with an average inter-plane distance of 3.551 Å. A centroid – centroid between pyridine of pypz of one molecule and pyridine of pypz of another molecule can be seen with a separation >4 Å, which is not pi-stacks.[31] The crystallographic bond lengths of $^{F/F}\text{Ir}\bullet\text{L}^{quinoline}\bullet\text{NO}_3$ complex are listed in **Table 3-5**.

Table 3-5 Selected distances parameters for solvate $^{F/F}\text{Ir}\bullet\text{L}^{quinoline}\bullet\text{NO}_3$ complex.

$^{F/F}\text{Ir}\bullet\text{L}^{quinoline}\bullet\text{NO}_3$ -Bonds	**Distances [Å]**
Ir-$\text{C}_{19(C\wedge N)}$	**2.017 (5)**
Ir-$\text{C}_{30(C\wedge N)}$	**2.012 (5)**
Ir-$\text{N}_{1(C\wedge N)}$	**2.157 (4)**
Ir-$\text{N}_{2(C\wedge N)}$	**2.147 (4)**
Ir-$\text{N}_{5(N\wedge N)}$	**2.042 (4)**
Ir-$\text{N}_{6(N\wedge N)}$	**2.041 (4)**

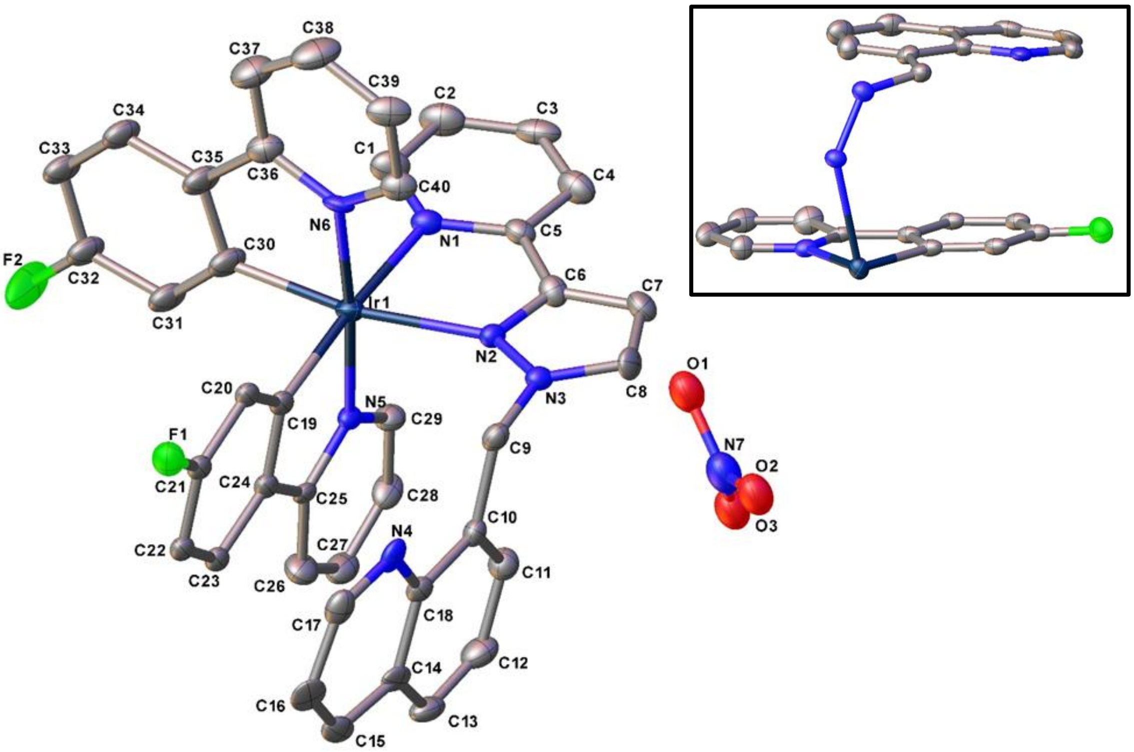

(a)

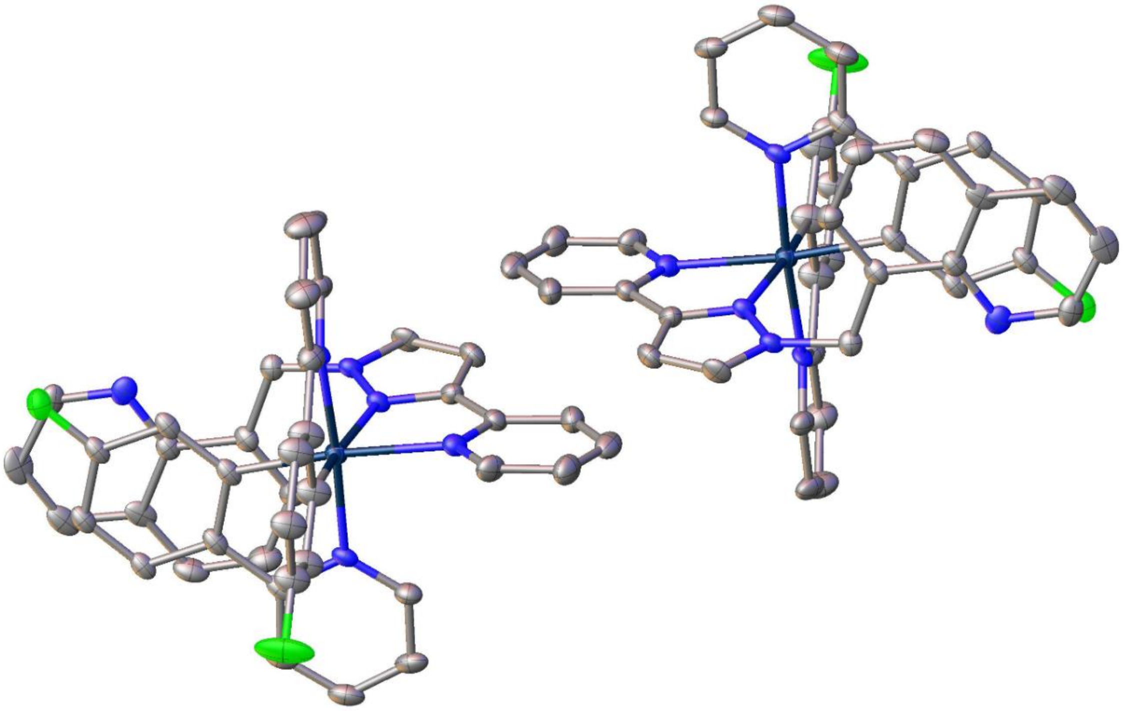

(b)

Figure 3-13 (a) Molecular structure of the $^{F/H}$Ir•L^{quinoline}•NO_3 complex with displacement ellipsoids at 50% probability with expanded to the shifting between quinoline ring and F_2ppy rings of the cyclometalating ligands. (b) shows pi-stacks between pyridine units.

The crystal structure of $^{F/H}$Ir•L^{quinoline}•NO_3, which crystallizes in space group $P2_1/c$, shows the same core structure as $^{F/F}$Ir•L^{quinoline}•NO_3. The F_2ppy cyclometalating ligands plane stacks with the pendant quinoline group plane with an intra-ring separation of 3.730Å. Average intermolecular plane distance between pyridine of pypz is ca. 3.532 Å. The crystallographic bond lengths of $^{F/H}$Ir•L^{quinoline}•NO_3 complex are summarised in **Table 3-6**.

Table 3-6 Selected bond distances parameters for $^{F/H}$Ir•L^{quinoline}•NO_3 complex

$^{F/H}$Ir•L^{quinoline}•NO_3 -Bonds	Distances [Å]
Ir-$C_{19(C\wedge N)}$	2.014 (12)
Ir-$C_{30(C\wedge N)}$	2.001 (13)
Ir-$N_{1(C\wedge N)}$	2.170 (10)
Ir-$N_{2(C\wedge N)}$	2.168 (9)
Ir-$N_{5(N\wedge N)}$	2.058 (9)
Ir-$N_{6(N\wedge N)}$	2.061 (9)

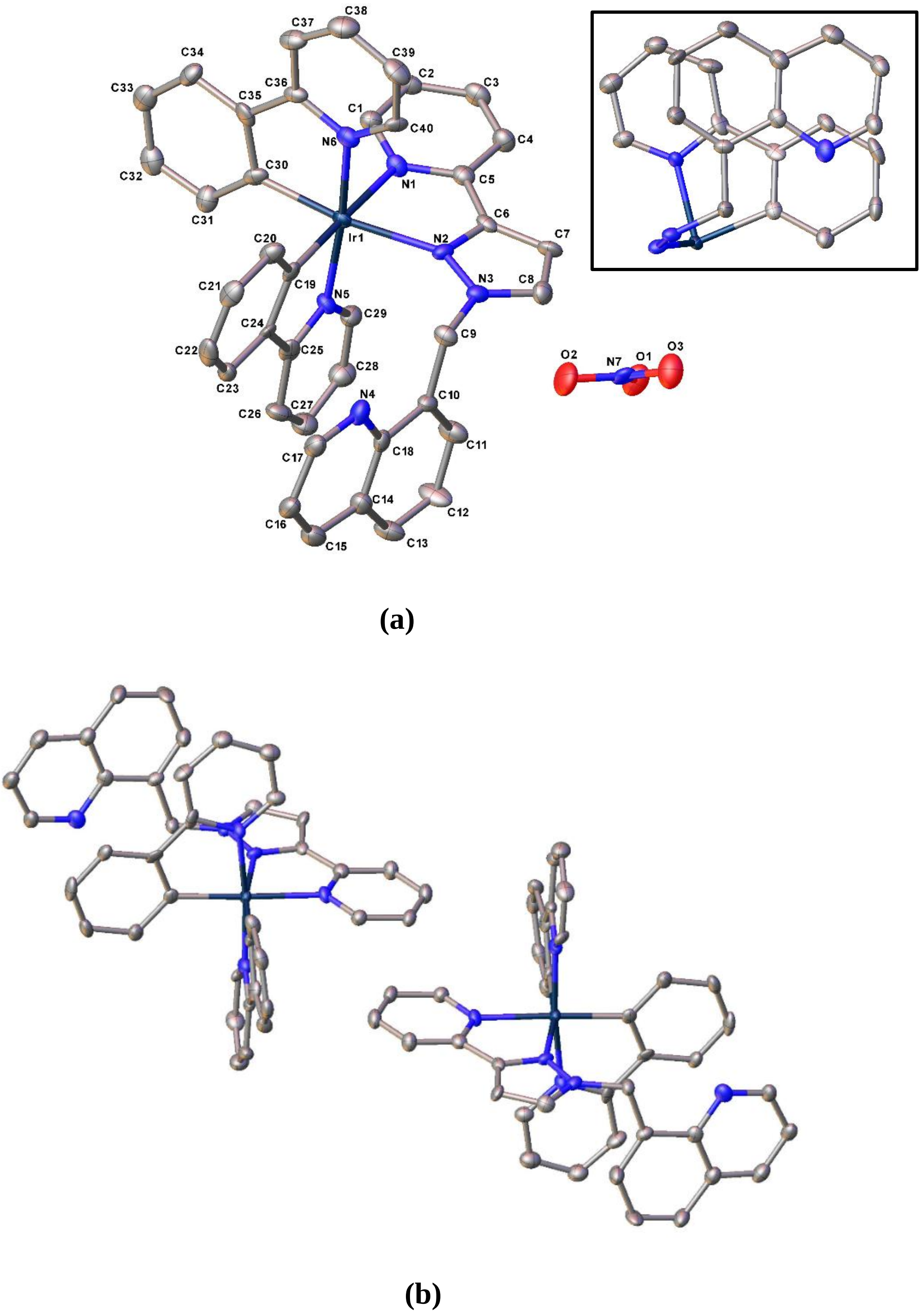

Figure 3-14 (a) Molecular structure of the $^{H/H}$Ir•L^{quinoline}•NO_3 complex cation of NO_3 anion and MeCN solvent with displacement ellipsoids at 50%probability level with the expanded the shifting between quinoline ring and ppy rings of the cyclometalating ligands (Top-right side in the box). (b) shows pi-stacks between pyridine rings.

The structure of $^{H/H}$Ir•L^{quinoline}•NO_3 is shown in **Figure** 3-14-**a**; it crystallizes in the triclinic space group P-1. Similar intra-ligand pi-stacks are observed as were seen in $^{F/F}$Ir•L^{quinoline}•NO_3 but with slightly longer separation between the quinoline and F_2-ppy planes ca. 3.730Å. The average intermolecular plane distance between pyridine of pypz is ca. 3.730 Å**. Table 3-7** shows the crystallographic bond lengths of $^{H/H}$Ir•L^{quinoline}•NO_3 complex.

Table 3-7 Selected distances parameters for solvate $^{H/H}$Ir•L^{quinoline}•NO_3 complex.

$^{H/H}$Ir•L^{quinoline}•NO_3 -Bonds	**Distances [Å]**
Ir-$C_{19(C\wedge N)}$	2.017 (7)
Ir-$C_{30(C\wedge N)}$	1.998 (8)
Ir-$N_{1(N\wedge N)}$	2.161(6)
Ir-$N_{2(N\wedge N)}$	2.163 (6)
Ir-$N_{5(C\wedge N)}$	2.042 (6)
Ir-$N_{6(C\wedge N)}$	2.049 (6)

3.5 Photophysical Studies

3.5.1 UV absorption spectroscopy

UV-Vis absorption spectra for all complexes have been measured in MeCN at 298 K. All the UV-Vis and photophysical properties are listed in **Table 3-8**.

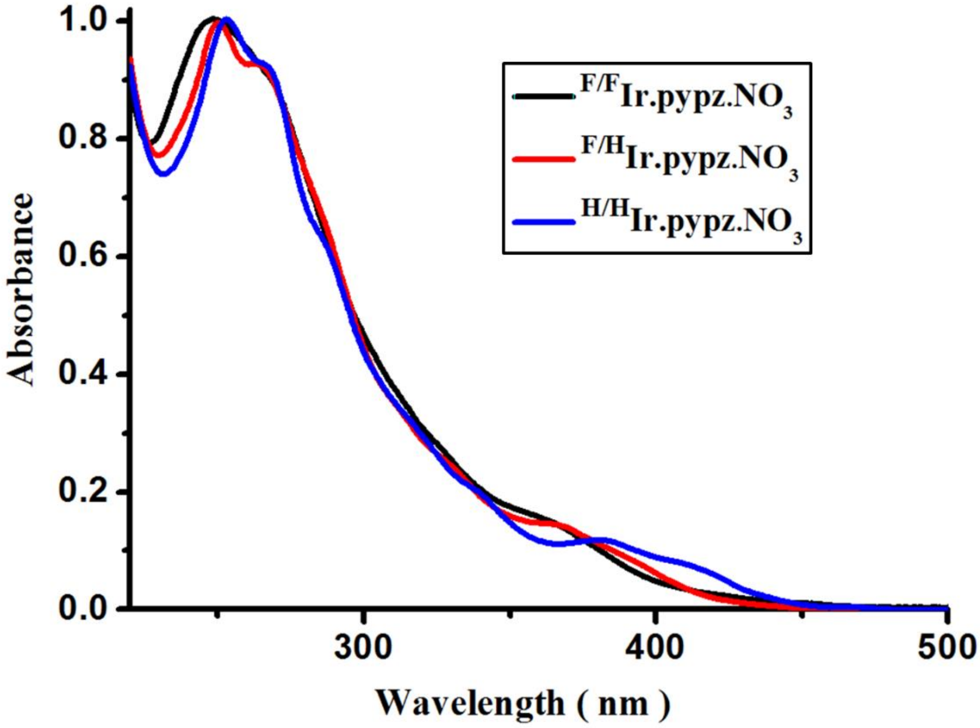

Figure 3-15 Normalised absorption spectra of complexes $^{F/F,\ F/H,\ H/H}$Ir•pypz•NO_3 in MeCN solvent at 298 K.

Figure 3-15 displays overlapping UV/Vis spectra of the 3 complexes in CH_3CN. Absorption bands below 300 nm can be attributed to $^1\pi$-π^* transitions of the ligand.[32] The bands that feature below 300 nm are resolved in all complexes. The lower energy bands between 350 – 450 nm can be assigned to the mixtures of the LC and MLCT transitions[32] with the transitions for $^{H/H}$Ir•pypz•NO_3 being better resolved than in $^{F/H}$Ir•pypz•NO_3 and $^{F/F}$Ir•pypz•NO_3. These bands in the low energy region are affected by electron withdrawing / electron donating groups through the substituents on the phenyl rings of the C^N ligands.[33]

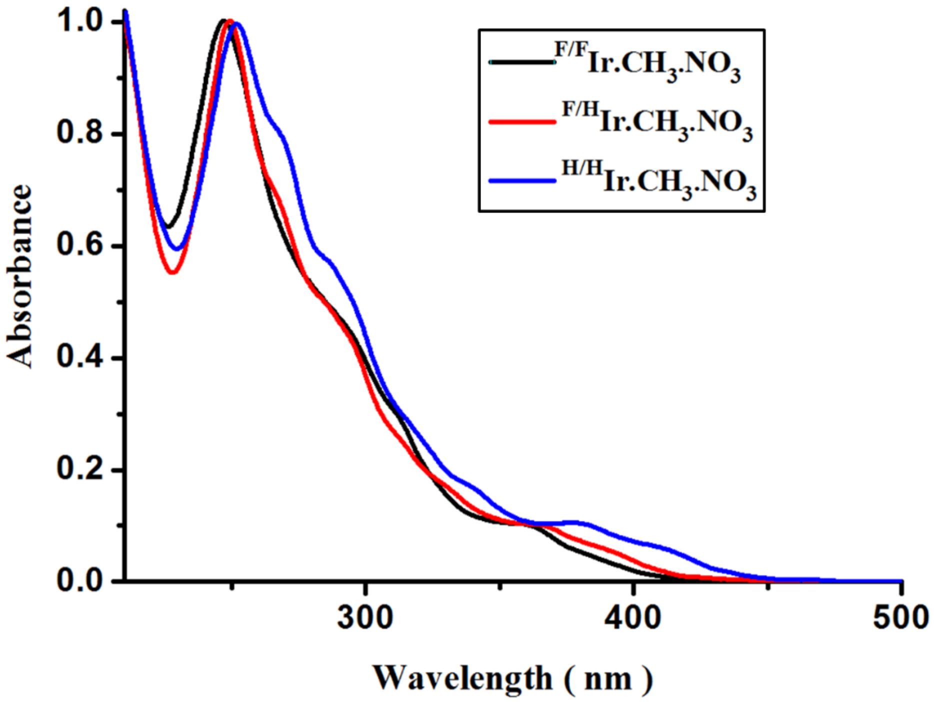

Figure 3-16 Normalised absorption spectra of complexes $^{F/F,\ F/H,\ H/H}Ir{\bullet}CH_3{\bullet}NO_3$ in MeCN solvent at 298 K. Zoom-in region between 380-500 nm shown seperately.

Figure 3-16 displays UV/Vis spectra of $^{F/F,F/H,H/H}Ir{\bullet}CH_3{\bullet}NO_3$. The spectra of $^{F/F,\ F/H,\ H/H}Ir{\bullet}CH_3{\bullet}NO_3$ complexes are similar in the region below 300 nm as it is mainly intraligand transitions that occur in this region In the Vis. region, between 380 – 480 nm, abosption bands for $^{H/H}Ir{\bullet}CH_3{\bullet}NO_3$ the MLCT/LC transitions are at lower energy than for other two $^{F/F}Ir{\bullet}CH_3{\bullet}NO_3$ and $^{F/H}Ir{\bullet}CH_3{\bullet}NO_3$ complexes, which is obvious from expanded spectrum (**Figure** 3-16). Interestingly, at 480 nm a weak absorption band in $^{H/H}Ir{\bullet}CH_3{\bullet}NO_3$ complex is observed, which might correspond to direct population of $^3\pi$-π^* level states because of high spin orbit coupling of Ir(III) metal.[32] In general, it is clear that the presence of two F atoms as withdrawing groups on the phenyl rings of the C^N cyclometalated ligands shift the lowest-energy bands to the high energy relative to that in $^{H/H}Ir{\bullet}CH_3{\bullet}NO_3$ complex, and in $^{F/H}Ir{\bullet}CH_3{\bullet}NO_3$ the absorptions are between the H,H- and F,F- derivatives.[33] These shifts of absorption bands in $^{F/F,\ F/H,\ H/H}Ir{\bullet}CH_3{\bullet}NO_3$ complexes are clearer than in the spectra of the $^{F/F,\ F/H,\ H/H}Ir{\bullet}pypz{\bullet}NO_3$ complexes.

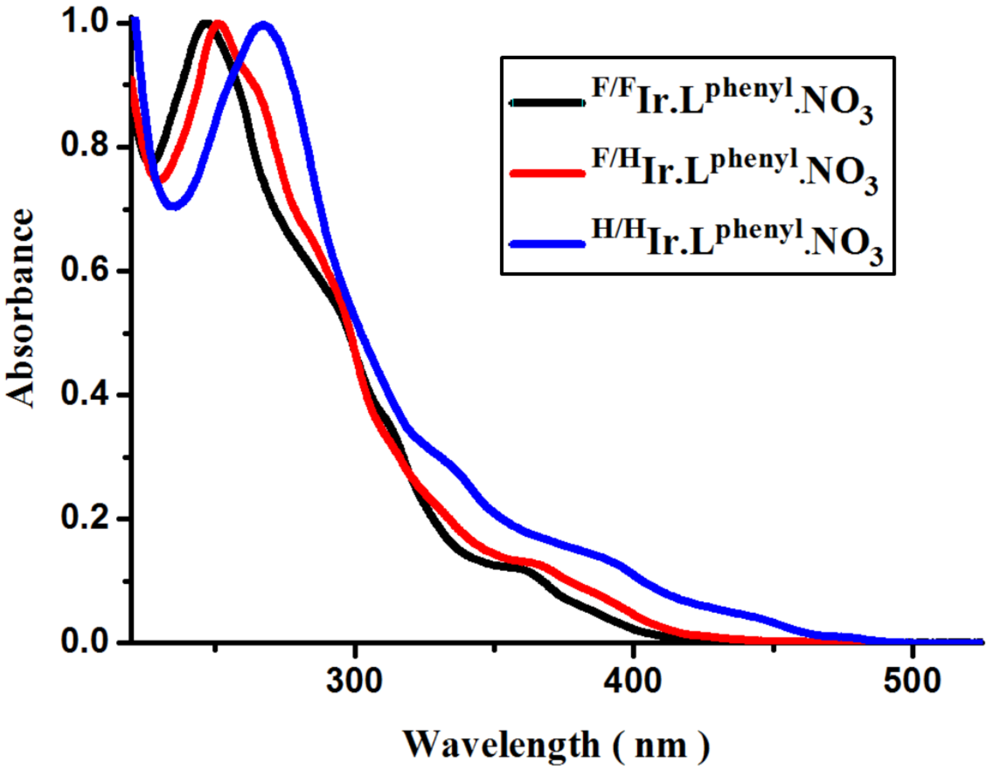

Figure 3-17 Normalised absorption spectra of complexes $^{F/F, F/H, H/H}$Ir•L^{phenyl}•NO$_3$ in MeCN solvent at 298 K.

Similar considerations apply to the UV/Vis spectra of $^{F/F, F/H, H/H}$Ir•L^{phenyl}•NO$_3$ which show similar variations in UV/Vis absorption spectra with F/F, F/H or H/H substituents. **Figure** 3-18 and **Figure** 3-19 show normalised absorption spectra of series substitution of F/F, F/H and H/H complexes with L^{quinoline} and L$^{2\text{-}naph}$, respectively.

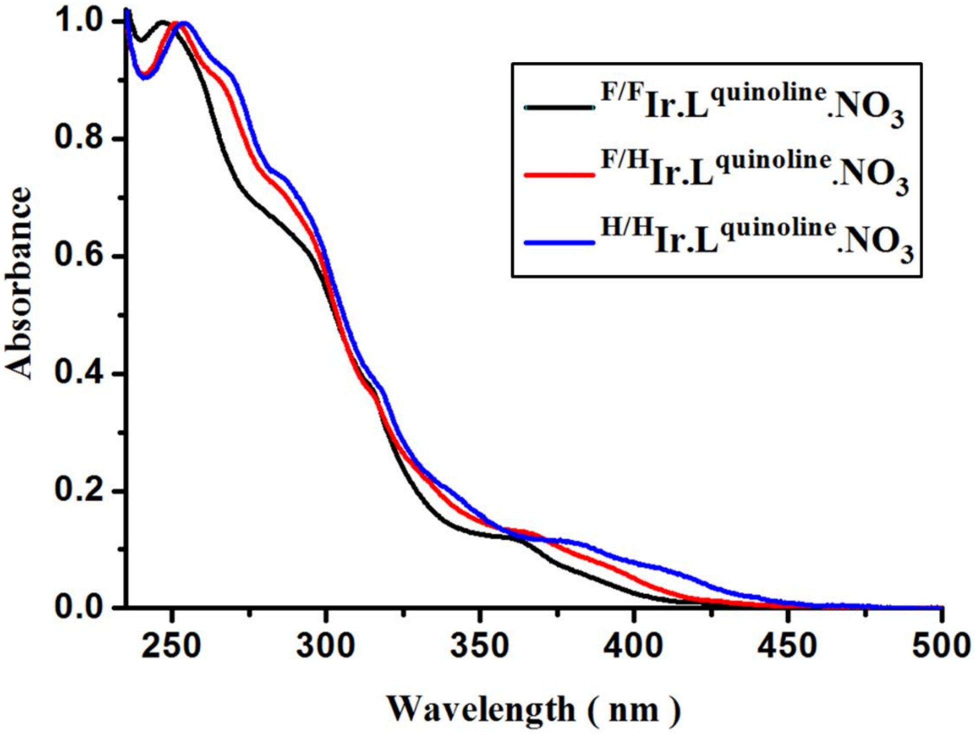

Figure 3-18 Normalised absorption spectra of complexes $^{F/F,\ F/H,\ H/H}$Ir•L^{quinoline}•NO$_3$ in MeCN solvent at 298 K.

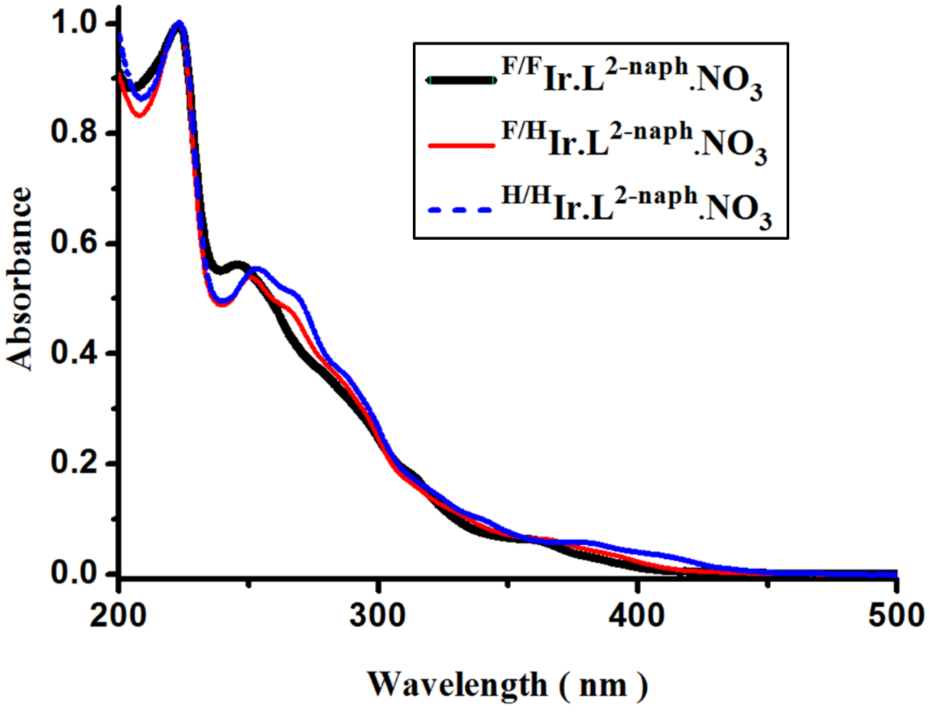

Figure 3-19 Normalised absorption spectra of complexes $^{F/F,\ F/H,\ H/H}$Ir•L^{2naph}•NO$_3$ in MeCN solvent at 298 K.

Table 3-8 UV-Vis and photophysical data for mono-Ir(III) complexes.

	Absorption		Emission			
	λ_{abs} nm	λ_{abs} ε (10^{-3} $M^{-1}.cm^{-1}$)	$\lambda_{em. max}$ nm	ϕ	τ (in air) ± 20 ns	τ (in argon) ± 20 μs
$^{H/H}$Ir•L^{Pyrene}•NO$_3$	375	242 (82500), 265 (63000), 276 (58540), 315 (26000), 330 (34430), 346 (33500), 375 (5960), 396 (3790)	493	0.02	τ_1 =112, τ_2=36.5	0.13
$^{F/H}$Ir•L^{Pyrene}•NO$_3$	393	242 (80300), 265 (57990), 276 (55090), 315 (23000), 330 (31500), 347 (33550), 391 (4780)	462	0.03	τ_1 =156, τ =35.6	0.64
$^{F/F}$Ir•L^{Pyrene}•NO$_3$	393	242 (68800), 265 (50040), 277 (46700), 315 (22300), 330 (28500), 347 (34400), 386 (2700)	463	0.02	τ_1=24 (23%), τ_2=200 (15%), τ_3=2 (instrument response)	1.01
$^{H/H}$Ir•L^{quinoline}•NO$_3$	380	253 (49790), 269 (44940), 288 (34350), 380 (4870), 410 (2930)	476	0.04	τ_1=220, τ_2=60	1.53
$^{F/H}$Ir•L^{quinoline}•NO$_3$	360	250 (47230), 368 (41080), 290 (31520), 360 (5520)	464/476	0.09	τ_1=242, τ_2=25	2.10
$^{F/F}$Ir•L^{quinoline}•NO$_3$	360	247(46300), 290 (29100), 314 (17430), 360 (5240)	450	0.08	τ_1=750, τ_2=30	1.40
$^{H/H}$Ir•L^{phenyl}•NO$_3$	380	266 (56500), 332 (11640), 380 (5480), 436 (970), 476 (110)	476/455		τ_1=194, τ_2=64	
$^{F/H}$Ir•L^{phenyl}•NO$_3$	360	250 (49800), 266 (43730), 287 (31030), 313 (15660), 332 (9860), 360 (6040), 390 (3300)	462	0.04	τ_1=130, τ_2=80	2.30
$^{F/F}$Ir•L^{phenyl}•NO$_3$	380	247 (50300), 289 (26900), 312 (16800), 360 (5730), 413 (460)	453	0.2	τ_1=220, τ_2=50	3.33
$^{H/H}$Ir•L$^{2\text{-}naph}$•NO$_3$	380	223 (79230), 253 (42900), 268 (38680), 289 (26800), 380 (4430), 410 (2730)	475	0.03	τ_1=160, τ_2=50	2.86
$^{F/H}$Ir•L$^{2\text{-}naph}$•NO$_3$	360	223 (95170), 250 (48890), 266 (42660), 285 (31230), 360 (5710)	463/493	0.0002	τ_1=320, τ_2=30	1.61
$^{F/F}$Ir•L$^{2\text{-}naphl}$•NO$_3$	360	223 (97670), 245 (45800), 280 (34600), 314 (15770), 360 (5620), 417 (440)	466/455	0.02	τ_1=300 ±40, τ_2 = 40±5	2.00
$^{H/H}$Ir•L^{naph}•NO$_3$	380	-	475/506		τ_1=200 , τ_2 = 40	-
$^{F/H}$Ir•L^{naph}•NO$_3$	365	-	464	0.007	0.4 (400ns)	2.00

$^{F/F}$Ir•L^{naph}•NO$_3$	360	226 (88), 246 (64), 279 (43), 315 (15), 360 (5.5)	455	0.004	τ_1 = 36, τ_2 = 365	no significant change
$^{H/H}$Ir•CH$_3$•NO$_3$	380	250 (47140), 269 (36920), 286 (26710), 318 (11850), 380 (4830), 409 (2790)	475	0.1	τ_1 = 57, τ_2 = 200	0.45
$^{F/H}$Ir•CH$_3$•NO$_3$	360	249 (56910), 268 (38820), 290 (26410), 314 (13470), 331 (8940), 360 (5640), 390 (3150)	463	0.05	120 ns	0.46
$^{F/F}$Ir•CH$_3$•NO$_3$	360	247 (61950), 290 (29170), 311 (15570), 357 (5457)	453	0.1	180 ns	0.65
$^{H/H}$Ir•pypz•NO$_3$	380	-	493	-	45 ns	0.33
$^{F/H}$Ir•pypz•NO$_3$	375	-	465	-	40 ns	
$^{F/F}$Ir•pypz•NO$_3$	375	-	468		70 ns	

3.5.2 Emission spectroscopy

The principal point that will be discussed in this part is the effect of the presence or absence of the substitution (F) atom, in the phenyl rings of the cyclometalating ligands, on the emission spectra of the complexes. The steady state emission spectra for all complexes were measured in air, MeCN solvent, at 298 K and using an optical density of less than 0.1 at the excitation wavelength. All the details of luminescence measurements and further measurements like lifetime are summarised in **Table 3-8**.

Part One

3.5.2.1 Photophysical properties of $^{F/F,\ F/H\ and\ H/H}Ir{\bullet}CH_3{\bullet}NO_3$

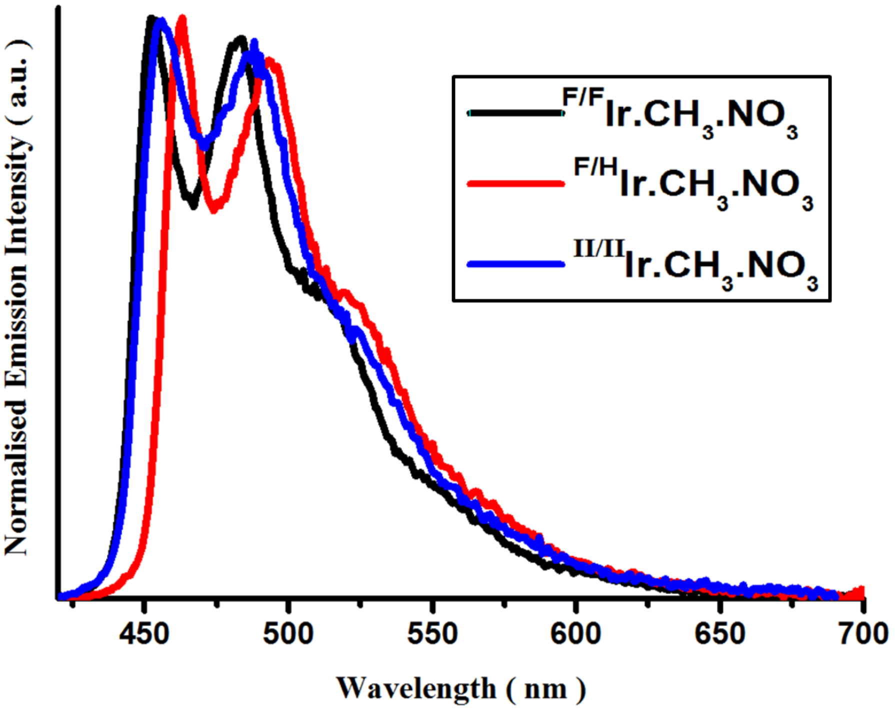

Figure 3-20 Normalised emission spectra of $^{F/F,\ F/H\ and\ H/H}$ $Ir{\bullet}CH_3{\bullet}NO_3$ complexes in MeCN solvent at 298 K with the $\lambda_{exc.}$ = 360 nm.

As is clear in **Figure** 3-20, the emission spectra of the $^{F/F,\ F/H\ and\ H/H}Ir{\bullet}CH_3{\bullet}NO_3$ complexes exhibited structured and relatively weak emission, between 450 and 650 nm, which are assigned mainly to LC electronic transition probably overlapping with MLCT emission. Interestingly, the emission of $^{F/H}Ir{\bullet}CH_3{\bullet}NO_3$ is at the lowest energy for these three complexes, due to stabilisation of the LUMO level on the pyridine ring and decreasing in the energy gap between HOMO and LUMO levels.

3.5.2.2 Photophysical properties of $^{F/F,\ F/H\ and\ H/H}Ir{\bullet}L^{phenyl}{\bullet}NO_3$

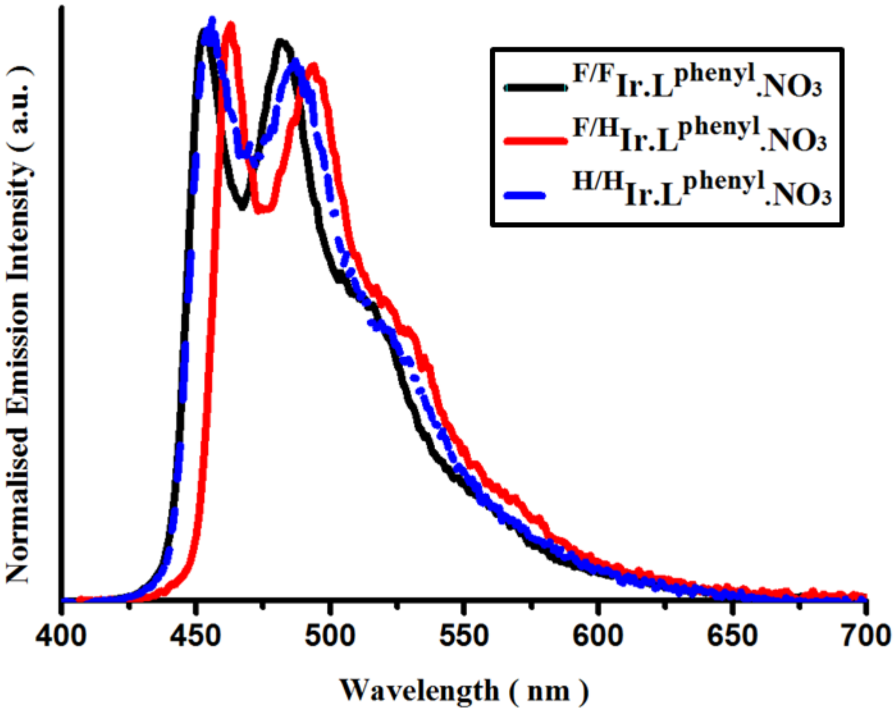

Figure 3-21 Normalised emission spectra of $^{F/F,F/H\ and\ H/H}Ir{\bullet}L^{phenyl}{\bullet}NO_3$ complexes in MeCN solvent at 298 K with the $\lambda_{exc.}$ = 360 nm.

The normalised emission spectra of $^{F/F,\ F/H\ and\ H/H}Ir{\bullet}L^{phenyl}{\bullet}NO_3$ complexes (**Figure** 3-21) are similar to those of $^{F/F,\ F/H\ and\ H/H}Ir{\bullet}CH_3{\bullet}NO_3$ as they are based on the same electronic transitions. Again, the emission from $^{F/H}Ir{\bullet}L^{phenyl}{\bullet}NO_3$ was clearly at the lowest energy compared to the $^{F/F}$ and $^{H/H}Ir{\bullet}L^{phenyl}{\bullet}NO_3$ complexes.

3.5.2.3 Photophysical properties of $^{F/F,\ F/H\ and\ H/H}$Ir•L$^{2\text{-naph}}$•NO$_3$

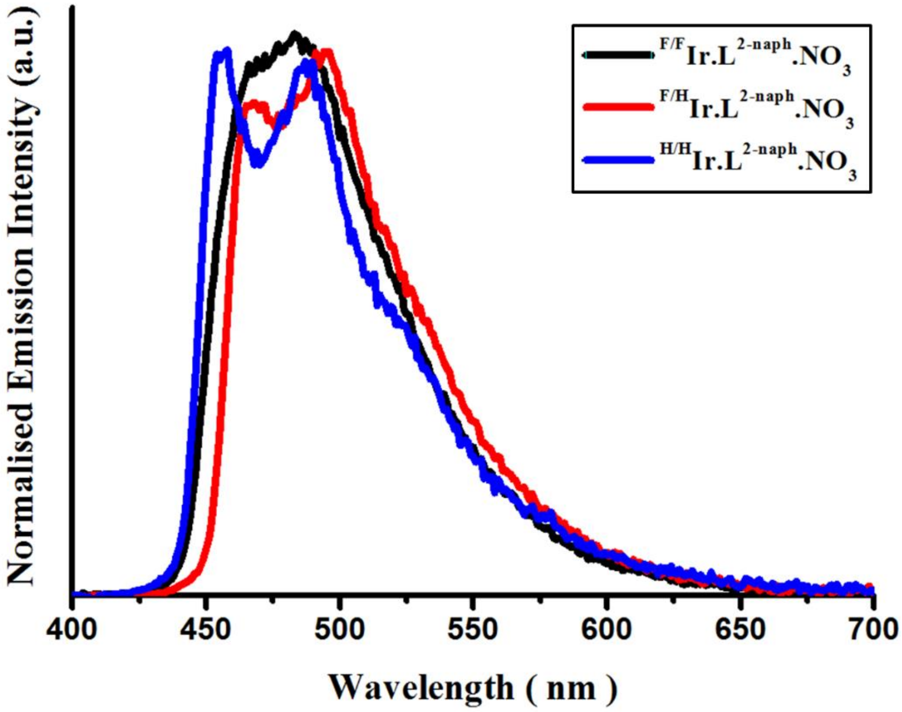

Figure 3-22 Normalised emission spectra of $^{F/F,\ F/H\ and\ H/H}$ Ir•L$^{2\text{-naph}}$•NO$_3$ complexes in MeCN solvent at 298 K with λ_{exc} = 360 nm.

The normalised emission spectra of $^{F/F,\ F/H\ and\ H/H}$Ir•L$^{2\text{-naph}}$•NO$_3$ showed weak, structured emission between 430-650 nm, with the same assignments as before. Interestingly, the emission of $^{F/F}$Ir•L$^{2\text{-naph}}$•NO$_3$ complex was observed to be very weak compared to the other two complexes. The $^{F/F}$Ir•L$^{2\text{-naph}}$•NO$_3$ has lower ϕ of emission because ^{3}Ir state has highest energy than ^{3}naph state, then the energy transfers from ^{3}Ir state to the ^{3}naph state. In contrast, $^{F/H}$Ir•L$^{2\text{-naph}}$•NO$_3$ and $^{H/H}$Ir•L$^{2\text{-naph}}$•NO$_3$ complexes are lower in energy and less well quenched by the ^{3}naph state (**Figure** 3-22).

3.5.2.4 Photophysical properties of ${}^{F/F,\ F/H\ \mathrm{and}\ H/H}$Ir•L^{quinoline}•NO$_3$

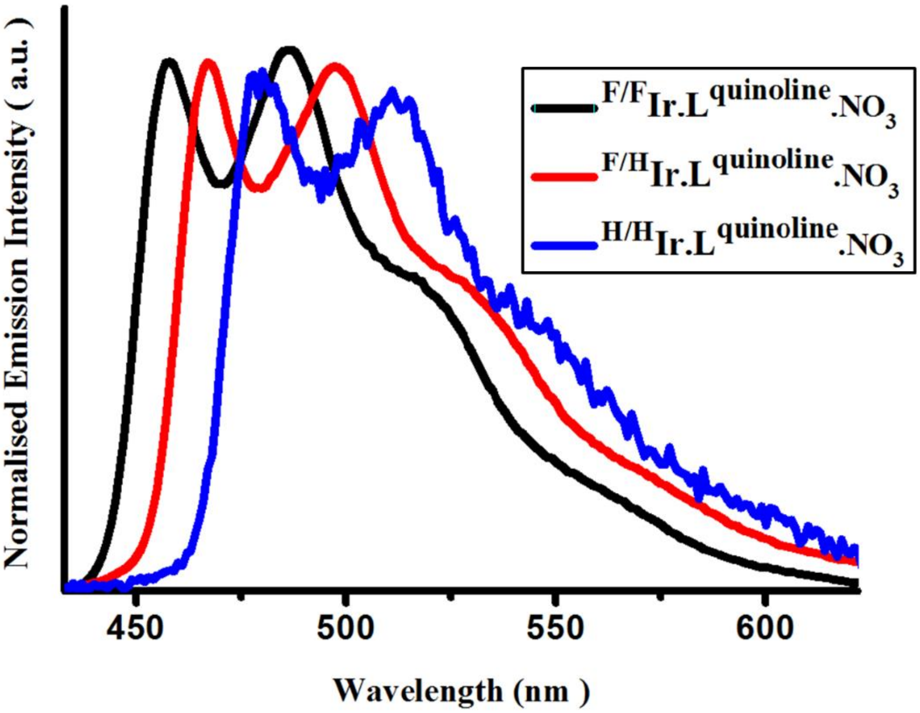

Figure 3-23 Normalised emission spectra of ${}^{F/F,F/H\ \mathrm{and}\ H/H}$Ir•L^{quinoline}•NO$_3$ complexes in MeCN solvent at 298 K with λ_{exc} = 360 nm.

Figure 3-23 shows the normalised emission spectra of the complexes ${}^{F/F,F/H\ \mathrm{and}\ H/H}$Ir•L^{quinoline}•NO$_3$ complexes. There is a much bigger difference here between ${}^{F/F,F/H\ \mathrm{and}\ H/H}$Ir•L^{quinoline}•NO$_3$ complexes, than that was observed with the other complexes ${}^{F/F,F/H\ \mathrm{and}\ H/H}$Ir•L^{Phenyl}•NO$_{3,}$ ${}^{F/F,F/H\ \mathrm{and}\ H/H}$Ir•L${}^{2\text{-}naph}$•NO$_{3,}$ ${}^{F/F,F/H\ \mathrm{and}\ H/H}$Ir•CH$_3$•NO$_3$. The ${}^{F/F,F/H\ \mathrm{and}\ H/H}$Ir•L^{Phenyl}•NO$_{3,}$ ${}^{F/F,F/H\ \mathrm{and}\ H/H}$Ir•L${}^{2\text{-}naph}$•NO$_{3,}$ ${}^{F/F,F/H\ \mathrm{and}\ H/H}$Ir•CH$_3$•NO$_3$ spectra were nearly superimposed with only small differences. In general, the emission exhibited structured profile with the broad band above 525 nm, which could be attributed to ILCT electronic transitions. ${}^{F/F\ \mathrm{and}\ F/H}$Ir•L^{quinoline}•NO$_3$ complexes showed strong luminescence but ${}^{H/H}$Ir•L^{quinoline}•NO$_3$ emits very weakly, with low ϕ = 0.04. These complexes show that F/F substitution moves the luminescence in the blue region whereas the H/H substitution is much lower in energy, and the F/H substitution falls between them.

Because the same ancillary ligand was used, this result could be attributed to the effect of F/F, F/H and H/H substituents on the C^N ligands. This substitution also changed the localization and order of the lowest triplet excited states. Admixture of charge transfer character, which depends on the energy gap between MLCT and LC orbitals can also be varied by the electronic structure of C^N ligands pattern.[34]

There is a much bigger difference in the photophysical properties of Ir(III) complexes when the ancillary ligand used is quinoline. The reason for that could be the effect of the stabilisation or destabilisation of the MLCT state, which effects the contribution of MLCT character in the lowest excited state. Moreover, the lesser contribution of MLCT character means more LC electronic transitions contribution within lowest excited state, and vice versa.[35]

Part Two

3.5.2.5 Photophysical properties of $^{F/F}$Ir(III) complexes with different ancillary ligands

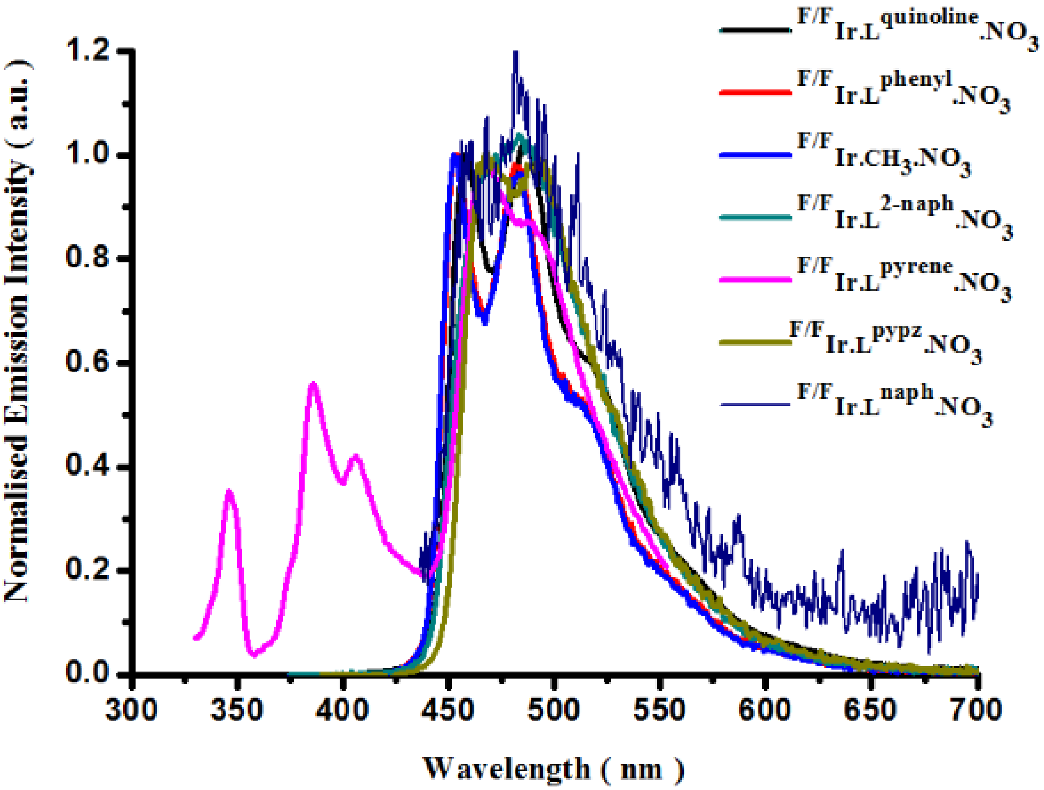

Figure 3-24 Normalised emission spectra of a series of $^{F/F}$Ir(III) complexes in MeCN at 298 K. The peak between 325-425 nm is due to emission of pyrene unit.

In the region between 430 – 600 nm, all of Ir(III) complexes show bright luminescence; just $^{F/F}$Ir•L^{naph}•NO$_3$ gave weak emission because the naph group could cause quenching and reduce emission intensity (**Figure** 3-24). Some spectra showed clear vibronic structure while the others showed less structure in their emission profile, but mainly all emission can be attributed to the admixture of the ^{3}MLCT and ^{3}LC states.[12, 36] The shift in emission wavelength across the series is controlled by the electronic properties of the ancillary ligand.[15,35] The

$^{F/F}$Ir•L^{pyrene}•NO$_3$ complex shows, in addition to Ir(III) unit emission similar to the other Ir(III) complexes in the region between 430 – 600 additional pyrene-based fluorescence emission in the region 330 – 440 nm for the same reason as mentioned in the previous **chapter 2** on the pyrene-substituted complexes.

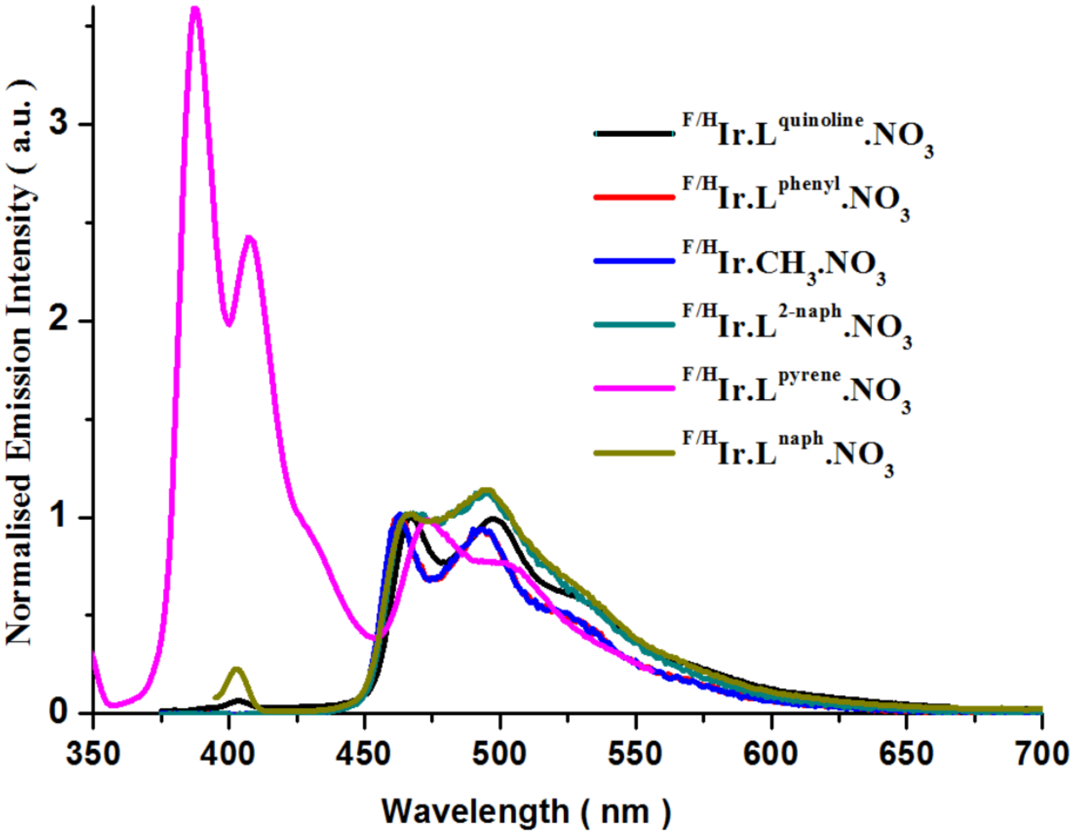

Figure 3-25 Normalised emission spectra of series of $^{F/H}$Ir(III) complexes in MeCN at 298 K. The peak between 325-425 nm is due to emission of pyrene unit.

Likewise, all $^{F/H}$Ir(III) complexes display approximately the same emission profile between 450 – 600 nm **Figure** 3-25. The structured luminescence emissions could be attributed to the $^{F/H}$Ir•pypz•NO$_3$ fragment which are attributed to the mixture ^{3}MLCT and ^{3}LC electronic transitions. $^{F/H}$Ir•L^{pyrene}•NO$_3$ complex shows in addition a high intensity pyrene-based fluorescence component.

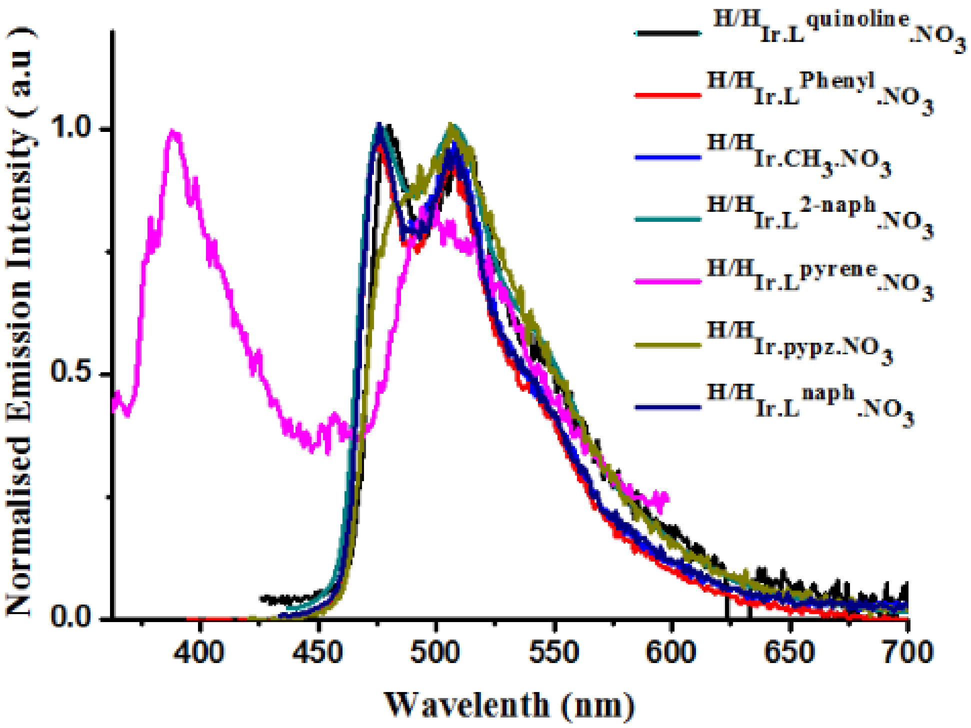

Figure 3-26 Normalised emission spectra of series of $^{H/H}$Ir(III) complexes in MeCN at 298 K. The peak between 325-425 nm is due to emission of pyrene unit.

Luminescence spectra of the $^{H/H}$Ir(III) complexes are depicted in **Figure** 3-26, It is clear there is no effect of the ancillary ligands in the emission of Ir(III) complexes. All Ir(III) complexes were emitted in the range between 450 – 600 nm. Again the emission arises from a mixture of ^{3}MLCT and ^{3}LC states.

3.6 Evaluating the potential of Ir(III) complex as bioimaging agents.

3.6.1 Luminescence Cell Imaging Studies

Several of the mononuclear Ir(III) complexes were tested for their cell imaging capabilities by PhD student Callum Jones in the Medical School, the University of Sheffield. The complexes $^{F\text{-}F}Ir{\bullet}L^{2naph}{\bullet}NO_3$, $^{F\text{-}H}Ir{\bullet}L^{2naph}{\bullet}NO_3$, $^{H/H}Ir{\bullet}L^{2naph}{\bullet}NO_3$ and $^{F\text{-}H}Ir{\bullet}L^{Phenyl}{\bullet}NO_3$ are partially soluble in water. The cellular uptake of $^{F\text{-}F}Ir{\bullet}L^{2naph}{\bullet}NO_3$, $^{F\text{-}H}Ir{\bullet}L^{2naph}{\bullet}NO_3$, $^{H/H}Ir{\bullet}L^{2naph}{\bullet}NO_3$ and $^{F\text{-}H}Ir{\bullet}L^{Phenyl}{\bullet}NO_3$ by live EJ cells (bladder epithelial cancer cells) was investigated.

In these studies, the stock solutions of Ir-complexes were prepared in dimethylsulphoxide (DMSO) at 10 mM. 2 μL of the stock solution was then diluted in the media, to make a 10 μM working solution of the compound for imaging. The overall concentration of DMSO was 0.1%.

The cells were incubated in 10 μM solution of the compound (0.1 % DMSO in media) for 2 hours, washed 3 times with PBS, fixed for 10 minutes with 1% paraformaldehyde PFA in phosphate buffered saline (PBS), washed again with PBS, and then coverslip mounted with IMMU-Mount on a glass slide.

The fixed and mounted cells were then imaged using a widefield Nikon eclipse TE200 microscope using irradiation with a Prior Lumen 200 at 50% light output (λ_{exc} 358 nm, unfiltered emission) and images captured with a Hamamatsu digital camera C4742-95. The emission images were captured without a filter, collecting light across visible region.

All complexes absorb at 358 nm excitation. Control experiments on unlabelled cells have been undertaken under identical conditions. **Figure** 3-27, **Figure** 3-28, **Figure** 3-29 and **Figure** 3-30 show the cell images labelled with each mono Ir(III) complexes.

All the compounds showed cellular uptake. Cellular accumulation was found to be mainly cytoplasmic, and to a much smaller extent nuclear. The accumulation in the cells is confirmed by the emission observed coinciding with the position of the cells in the bright field images.

The punctuate-like staining of the cytoplasm is typical for Ir(III) complexes that have been previously reported in cell imaging studies.[37, 38] The punctuate staining is usually attributed to the localisation in the lysosomes (more lipophilic organelles, which also have a relatively acidic environment compared to the rest of the cytoplasm, with a pH of about 4.5 – 5).

Different regions of each sample were captured, labelled (1), (2), (3), and/or (4), to ensure that the images give an accurate representation of the cellular uptake of the compounds.

3.6.1.1 Cell imaging of EJ cells incubated with the $^{F/F}$Ir•L^{2naph}•NO$_3$

(a) **(b)**

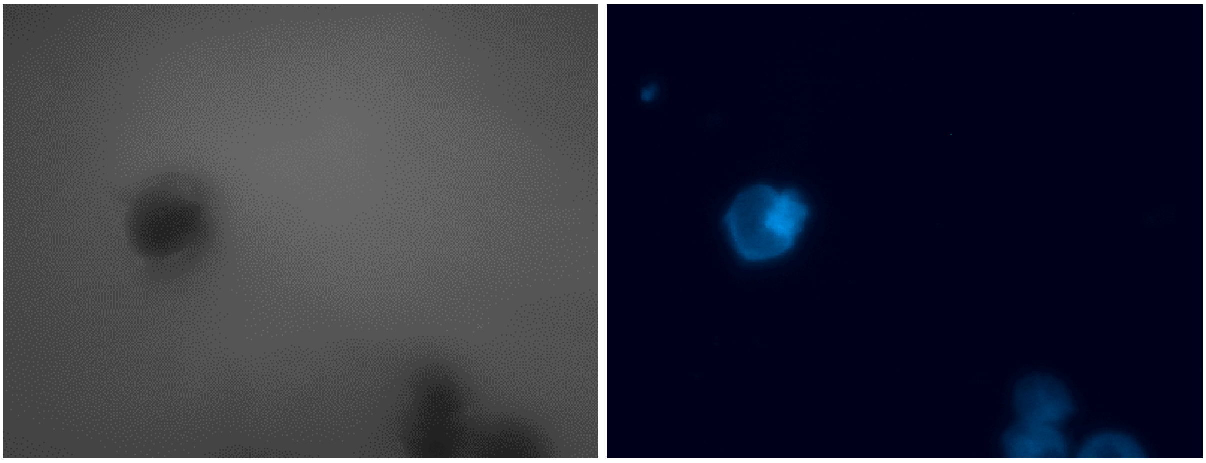

$^{F/F}$Ir•L^{2naph}•NO$_3$ brightfield (1) **$^{F/F}$Ir•L^{2naph}•NO$_3$ 10 µM 2hr (1)**

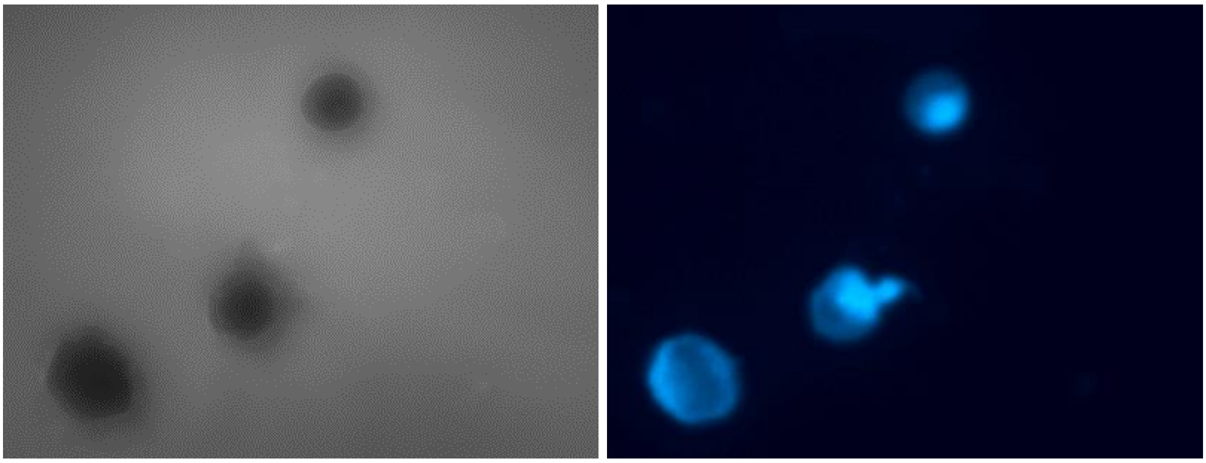

$^{F/F}$Ir•L^{2naph}•NO$_3$ brightfield (2) **$^{F/F}$Ir•L^{2naph}•NO$_3$ 10 µM 2hr (2)**

Figure 3-27 Cell imaging of EJ cells incubated with the $^{F/F}$Ir•L^{2naph}•NO$_3$10 µM (0.1% DMSO in PBS), for 2 hrs. Images recorded at 298 K, under $\lambda_{exc.}$ 358 nm, on Nikon eclipse TE200 microscope. (a) $^{F/F}$Ir•L^{2naph}.NO$_3$ brightfield image; (b) $^{F/F}$Ir•L^{2naph} .NO$_3$ emission image of the same area as in (a). There is a much smaller number of cells captured in the field of view that would be anticipated, indicating that cells were probably killed and washed off.

3.6.1.2 Cell imaging of EJ cells incubated with ${}^{\mathrm{H/H}}\mathrm{Ir}{\bullet}\mathrm{L}^{\mathrm{2naph}}{\bullet}\mathrm{NO_3}$

(a) **(b)**

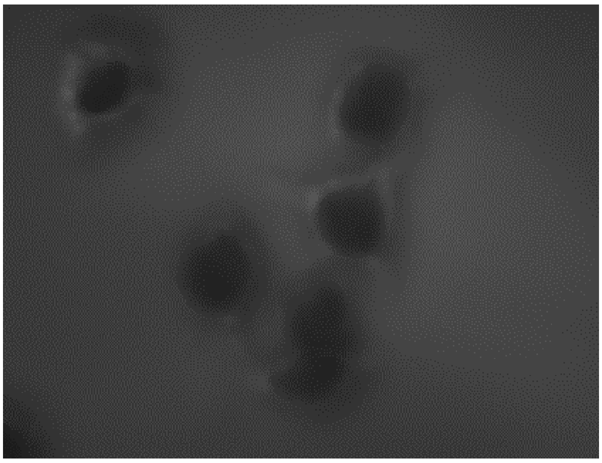

${}^{\mathrm{H/H}}\mathrm{Ir}{\bullet}\mathrm{L}^{\mathrm{2naph}}{\bullet}\mathrm{NO_3}$ brightfield (1)

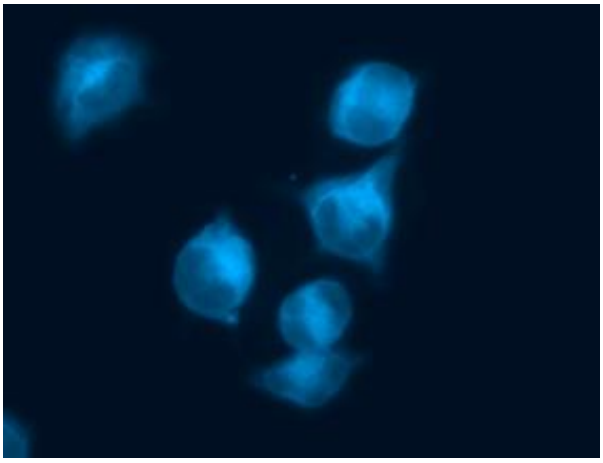

${}^{\mathrm{H/H}}\mathrm{Ir}{\bullet}\mathrm{L}^{\mathrm{2naph}}{\bullet}\mathrm{NO_3}$ 10 µM 2hr (1)

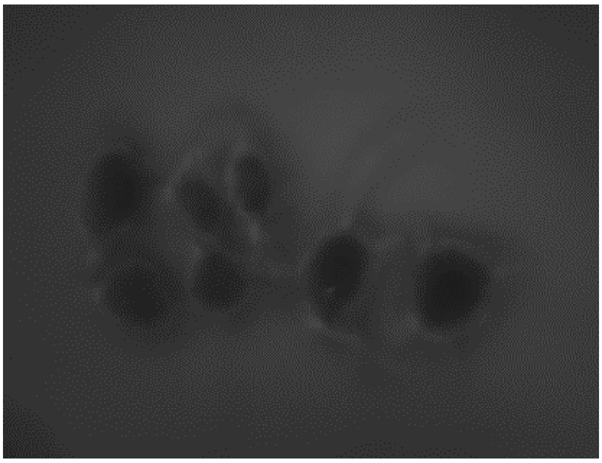

${}^{\mathrm{H/H}}\mathrm{Ir}{\bullet}\mathrm{L}^{\mathrm{2naph}}{\bullet}\mathrm{NO_3}$ brightfield (2)

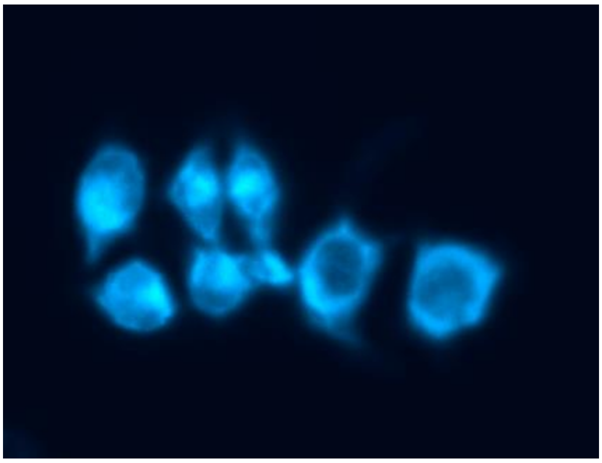

${}^{\mathrm{H/H}}\mathrm{Ir}{\bullet}\mathrm{L}^{\mathrm{2naph}}{\bullet}\mathrm{NO_3}$ 10 µM 2hr (2)

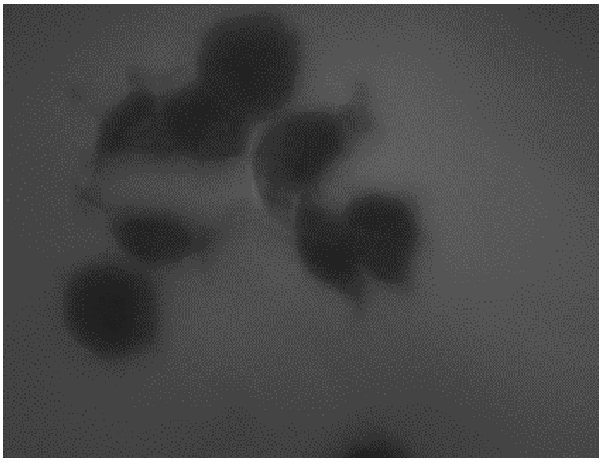

${}^{\mathrm{H/H}}\mathrm{Ir}{\bullet}\mathrm{L}^{\mathrm{2naph}}{\bullet}\mathrm{NO_3}$ brightfield (3)

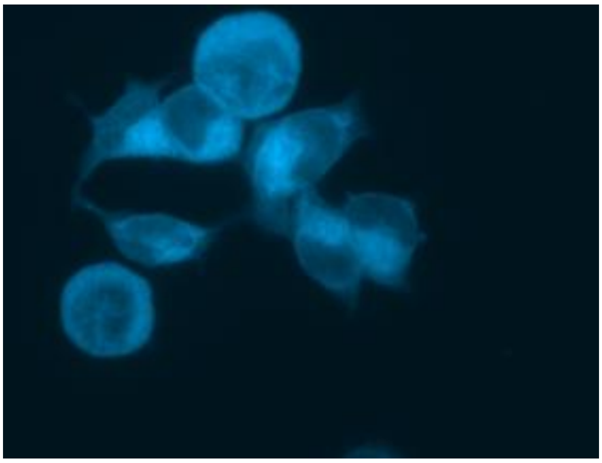

${}^{\mathrm{H/H}}\mathrm{Ir}{\bullet}\mathrm{L}^{\mathrm{2naph}}{\bullet}\mathrm{NO_3}$ 10 µM 2hr (3)

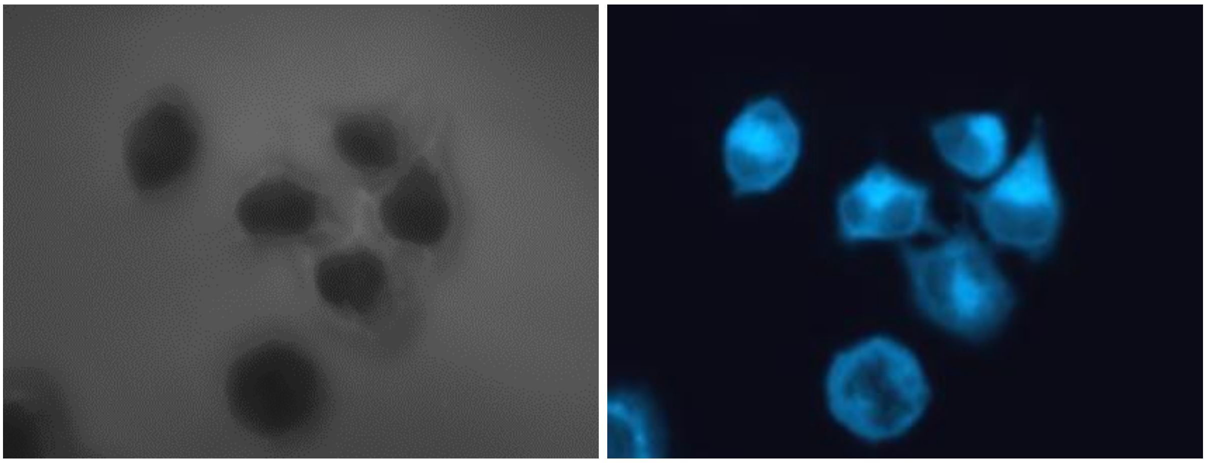

$^{H/H}$Ir•L^{2naph}•NO$_3$ brightfield (4) **$^{H/H}$Ir•L^{2naph}•NO$_3$ 10 µM 2hr (4)**

Figure 3-28 Cell imaging of EJ cells incubated with the $^{H/H}$Ir•L^{2naph}•NO$_3$10 µM (0.1% DMSO in PBS), for 2 hrs. Images recorded at 298 K, under $\lambda_{exc.}$ 358 nm, on Nikon eclipse TE200 microscope. (a) $^{H/H}$Ir•L^{2naph}•NO$_3$ brightfield image; (b) $^{H/H}$Ir•L^{2naph}•NO$_3$ emission image of the same area as in (a).

3.6.1.3 Cell imaging of EJ cells incubated with $^{F/H}$Ir•L^{Phenyl}•NO$_3$

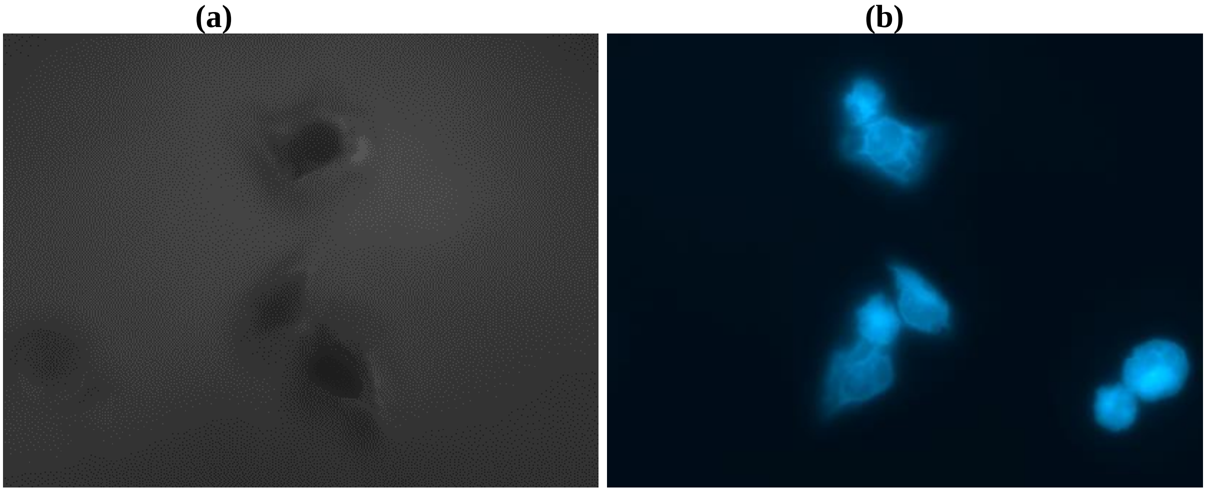

$^{F/H}$Ir•L^{Phenyl}•NO$_3$ brighfield (1) **$^{F/H}$Ir•L^{Phenyl}•NO$_3$ 10 µM 2hr (1)**

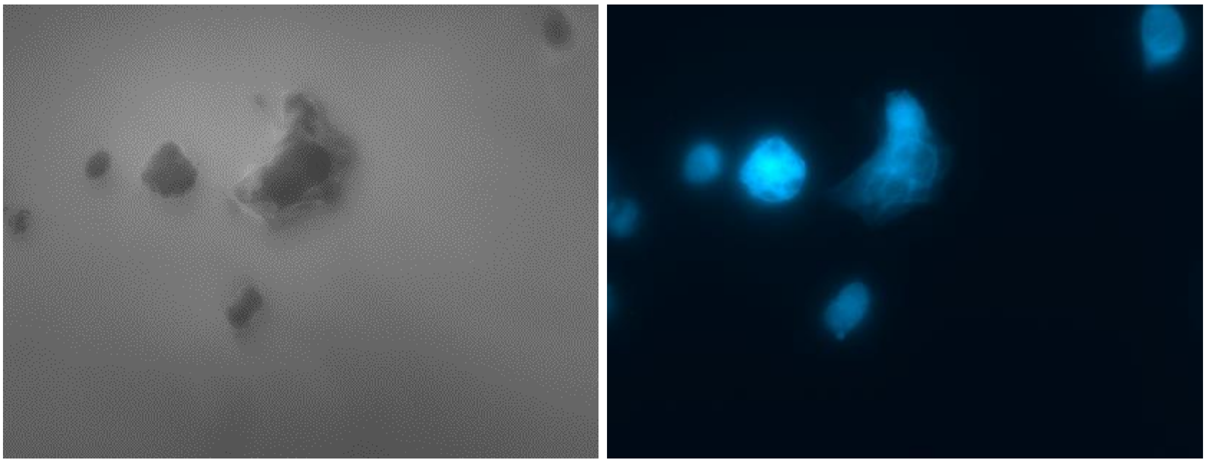

$^{F/H}$Ir•L^{Phenyl}•NO$_3$ brighfield (2) **$^{F/H}$Ir•L^{Phenyl}•NO$_3$ 10 µM 2hr (2)**

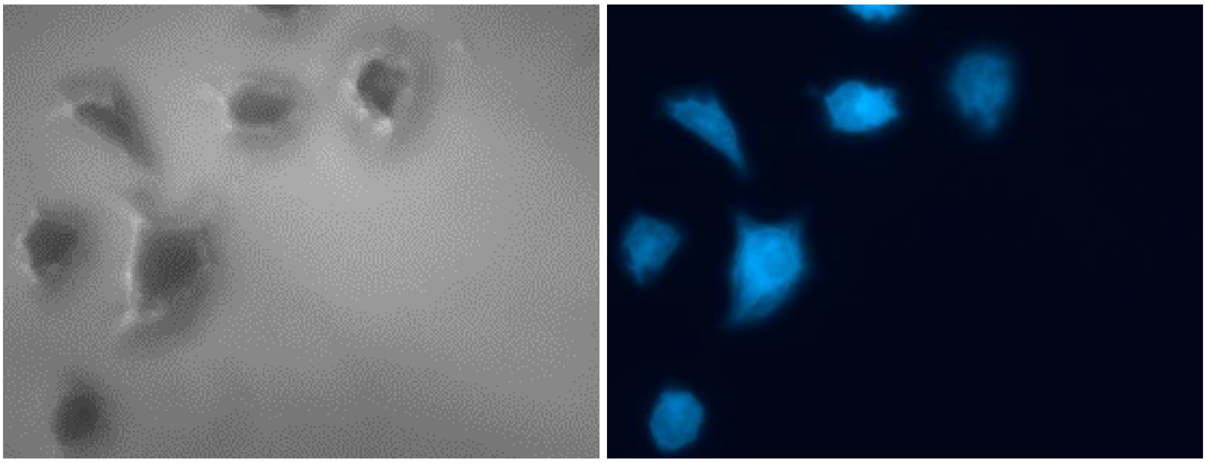

$^{F/H}$Ir•L^{Phenyl}•NO$_3$ brighfield (3) **$^{F/H}$Ir•L^{Phenyl}•NO$_3$ 10 µM 2hr (3)**

Figure 3-29 Cell imaging of EJ cells incubated with the $^{F/H}$Ir•L^{Phenyl} •NO$_3$ 10 µM (0.1% DMSO in PBS), for 2 hrs. Images recorded at 298 K, under $\lambda_{exc.}$ 358 nm, on Nikon eclipse TE200 microscope. (a) $^{F/H}$Ir•L^{Phenyl} •NO$_3$ brightfield image; (b) $^{F/H}$Ir•L^{Phenyl} •NO$_3$ emission image of the same area as in (a).

3.6.1.4 Cell imaging of EJ cells incubated with $^{F/H}$Ir•L^{2naph}•NO$_3$

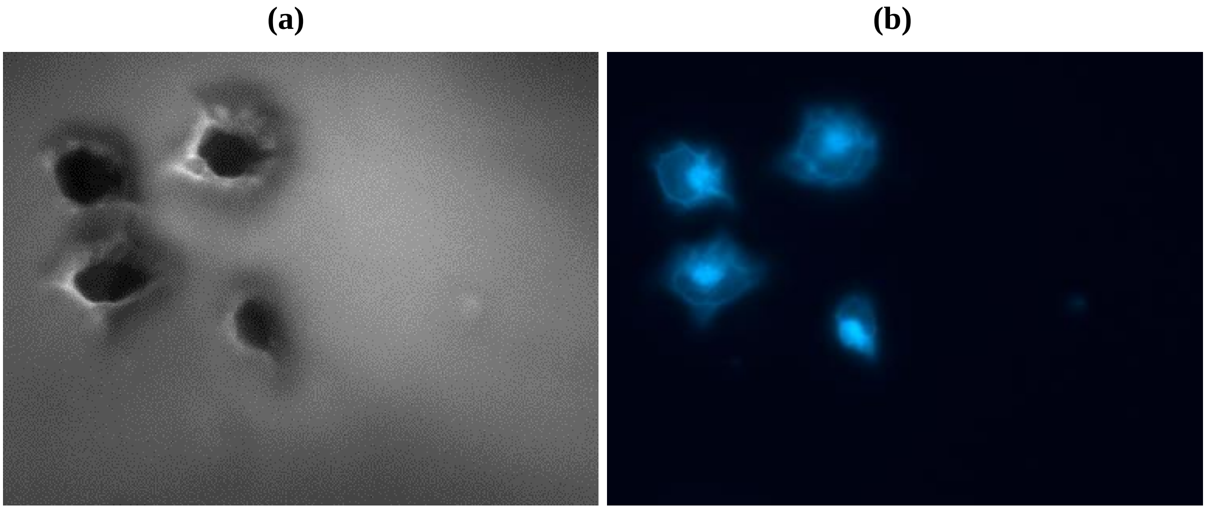

$^{F/H}$Ir•L^{2naph}•NO$_3$ brightfield (1) **$^{F/H}$Ir•L^{2naph}•NO$_3$ 10 µM 2hr (1)**

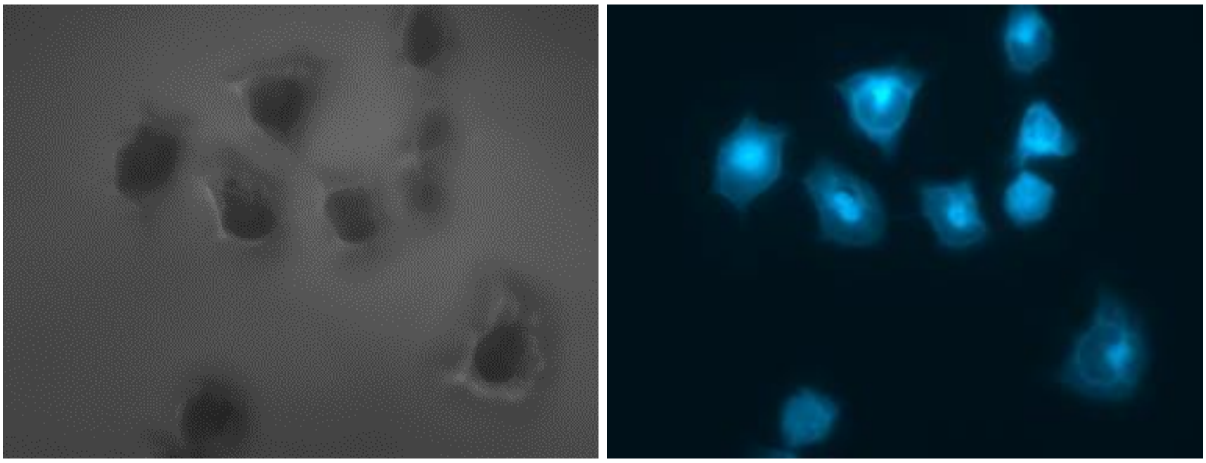

$^{F/H}$Ir•L^{2naph}•NO$_3$ brightfield (2) **$^{F/H}$Ir•L^{2naph}•NO$_3$ 10 µM 2hr (2)**

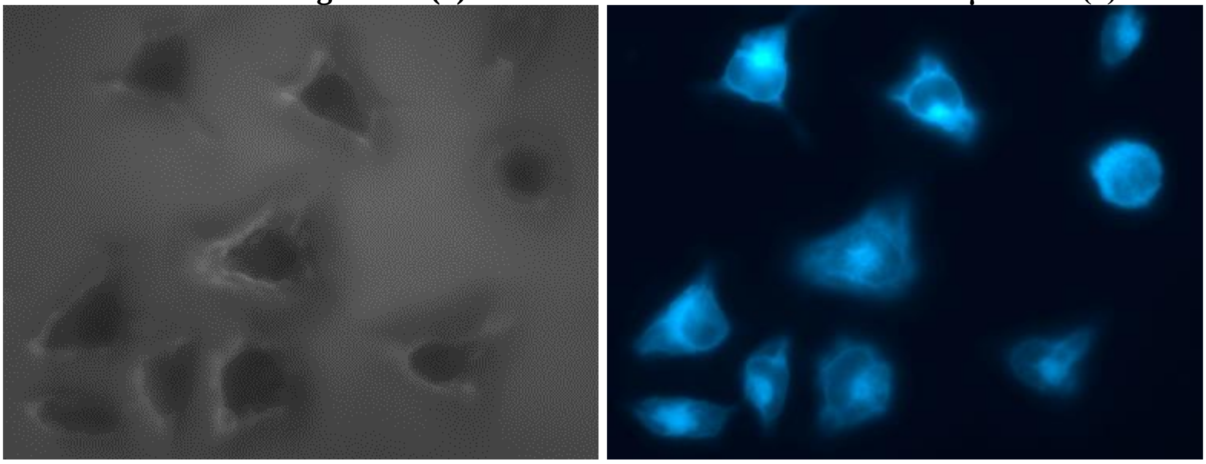

$^{F/H}$Ir•L^{2naph}•NO$_3$ brightfield (3) **$^{F/H}$Ir•L^{2naph}•NO$_3$ 10 µM 2hr (3)**

Figure 3-30 Cell imaging of EJ cells incubated with the $^{F/H}$Ir•L^{2naph} •NO$_3$10 µM (0.1% DMSO in PBS), for 2 hrs. Images recorded at 298 K, under $\lambda_{exc.}$ 358 nm, on Nikon eclipse TE200 microscope. (a) $^{F/H}$Ir•L^{2naph}•NO$_3$ brightfield image; (b) $^{F/H}$Ir•L^{2naph}•NO$_3$ emisison image of the same area as in (a).

3.6.2 Cytotoxicity of mono-Ir(III) complexes studied.

The cells incubated with $^{H/H}Ir{\bullet}L^{2naph}{\bullet}NO_3$ and $^{F/H}Ir{\bullet}L^{2naph}{\bullet}NO_3$ looked healthy under the microscope, not showing any changes in cell morphology. We therefore conclude that these compounds are not cytotoxic on the timescale of imaging (hours) and are therefore promising imaging probes for live cells.

The compounds $^{F/F}Ir{\bullet}L^{2naph}{\bullet}NO_3$ and $^{F/H}Ir{\bullet}L^{Phenyl}{\bullet}NO_3$ are considerably cytotoxic under identical conditions (10 μM, 2 hrs incubation). This was evidenced by the cells (**Figure** 3-27 and **Figure** 3-29) having changed their shape and in many cases being dead.

This observation means that under equimolar conditions the compounds $^{F/F}Ir{\bullet}L^{2naph}{\bullet}NO_3$ and $^{F\text{-}H}Ir{\bullet}L^{Phenyl}{\bullet}NO_3$ are more cytotoxic than the $^{H/H}Ir{\bullet}L^{2naph}{\bullet}NO_3$ and $^{F/H}Ir{\bullet}L^{2naph}{\bullet}NO_3$.

The cells incubated with what appears to be more toxic compounds of the series, have more of the compound accumulated in the nucleus. This may be due to cellular and nuclear membranes being compromised (become more permeable) in the process of cell death.

In the future, the dark toxicity of the compounds will be studies, in order to evaluate their potential as therapeutics.

3.7 Conclusion

Heteroleptic mononuclear Ir(III) complexes with different pypz ancillary ligands, and with substitution of F atoms on the phenyl ring of C^N cyclometalated ligands have been synthesised and fully characterized. For all these complexes, the effects of presence and absence of electron withdrawing group, di-F or mono-F or without-F, on the photophysical properties have been investigated. Most of complexes with withdrawing substituents on the C^N ligand showed slight blue shifting of luminescence, while in case $^{F/F}$Ir•L^{quinoline}•NO_3 strong blue shifting is clear compare to the other $^{F/F}$Ir complexes with different ancillary ligands. In general, all $^{F/F}$Ir complexes have high energy LC/MLCT absorption and $^{H/H}$Ir complexes absorb at lower energy while $^{F/H}$Ir complexes sometimes absorb in a region between that. Single crystals suitable for X-ray crystallography have been obtained for some of complexes described in this chapter. The main conclusion is that tunability of photophysical properties of the Ir(III) complexes could be observed because of changing the electronic structure of C^N ligand and type of substituents on the ancillary ligand, that attach to pypz via methyl group compare to $^{X/X}$Ir•pypz•NO_3.

Luminescence cell imaging study of mononuclear Ir(III) complexes as imaging agents was conducted in EJ cells. Four complexes differing in the pendant group (L$^{2\text{-}naph}$, L^{Phenyl}) have been investigated. Incubation of the live cells with 10 μm solution of the compound for 2 hr resulted in efficient uptake by the cells, with most of the compounds being localised in the cytoplasm, as is typical for Ir(III) complexes. Some uptake was noticed also in the nucleus, which is not typical for Ir(III) complexes. However, the nuclear uptake was noticed more for the complexes which were toxic to cells, and may be due to cellular/nuclear membranes being compromised due to the toxicity of the compounds in this case. $^{F/F}$Ir•L^{2naph}•NO_3 and $^{F\text{-}H}$Ir•L^{Phenyl}•NO_3 complexes were found more toxic to the cells, and therefore not good imaging agents. However, these can be investigated in the future for their potential therapeutic activity.

The other two Ir(III) complexes, $^{H/H}$Ir•L^{2naph}•NO_3 and $^{F/H}$Ir•L^{2naph}•NO_3, do not seem to be toxic to the cells under the conditions of incubation used. Therefore, they can be used as good cell imaging agents. It is also useful to note that the concentration of DMSO required for these complexes is only 0.1%, due to the compounds being more water-soluble than some of the previously studied complexes.

More specific studies, such as colocalisation studies or high-resolution microscopy, are required to understand the localisation pattern of the compounds and provide better insight about the complexes' interactions with cells.

3.8 References

1 P. Coppo, M. Duati, V. N. Kozhevnikov, J. W. Hofstraat and L. De Cola, *Angew. Chemie*, 2005, **44**, 1840–1844.

2 G. Cheng, Y. Zhang, Y. Zhao, S. Liu and Y. Ma, *Appl. Phys. Lett.*, 2006, **88**, 86–89.

3 S. Yiru, N. C. Giebink, H. Kanno, B. Ma, M. E. Thompson and S. R. Forrest, *Nature*, 2006, **440**, 908–912.

4 T. Sajoto, P. I. Djurovich, A. Tamayo, M. Yousufuddin, R. Bau, M. E. Thompson, R. J. Holmes and S. R. Forrest, *Inorg. Chem.*, 2005, **44**, 7992–8003.

5 S. Lamansky, P. Djurovich, D. Murphy, F. Abdel-Razzaq, R. Kwong, I. Tsyba, M. Bortz, B. Mui, R. Bau and M. E. Thompson, *Inorg. Chem.*, 2002, **41**, 3055–3066.

6 M. Polson, S. Fracasso, V. Bertolasi, M. Ravaglia and F. Scandola, *Inorg. Chem.*, 2004, **43**, 1950–1956.

7 I. M. Dixon, J. P. Collin, J. P. Sauvage, L. Flamigni, S. Encinas and F. Barigelletti, *Chem. Soc. Rev.*, 2000, **29**, 385–391.

8 P. J. Hay, *J. Phys. Chem. A*, 2002, **106**, 1634.

9 J. N. Demas, E. W. Harris, C. M. Flynn and D. Diemente, *J. Am Chem. Soc.*, 1975, **97**, 3838–3839.

10 A. Tsuboyama, H. Iwawaki, M. Furugori, T. Mukaide, J. Kamatani, S. Igawa, T. Moriyama, S. Miura, T. Takiguchi, S. Okada, M. Hoshino and K. Ueno, *J. Am. Chem. Soc.*, 2003, **125**, 12971–12979.

11 C. Adachi, M. A. Baldo, S. R. Forrest, S. Lamansky, M. E. Thompson and R. C. Kwong, *Appl. Phys. Lett.*, 2001, **78**, 1622–1624.

12 L. Flamigni, A. Barbieri, C. Sabatini, B. Ventura and F. Barigelletti, in *Topic in current chemistry 281, Photochemistry and Photophysics of coordination compounds: Iridium.*, 2007, pp. 143–203.

13 A. B. Tamayo, B. D. Alleyne, P. I. Djurovich, S. Lamansky, I. Tsyba, N. N. Ho, R. Bau and M. E. Thompson, *J. Am. Chem. Soc.*, 2003, **125**, 7377–7387.

14 V. V Grushin, N. Herron, D. D. Lecloux, W. J. Marshall, A. Viacheslav and Y. Wang, *Chem. Commun,* 2001, 1494–1495.

15 R. Ragni, E. a. Plummer, K. Brunner, J. W. Hofstraat, F. Babudri, G. M. Farinola, F. Naso and L. De Cola, *J. Mater. Chem.*, 2006, **16**, 1161.

16 L. L. Wu, I. W. Sun and C. H. Yang, *Organometallics*, 2007, **26**, 2017–2023.

17 S. C. Chin, M. S. Eum, S. Y. Kim, C. Kim and S. K. Kang, *Eur. J. Inorg. Chem.*, 2007, 372–375.

18 I. R. Laskar, S. F. Hsu and T. M. Chen, *Polyhedron*, 2005, **24**, 189–200.

19 K. Dedeian, J. Shi, N. Shepherd, E. Forsythe and D. C. Morton, *Inorg. Chem.*, 2005, **44**, 4445–4447.

20 M. K. Nazeeruddin, R. Humphry-Baker, D. Berner, S. Rivier, L. Zuppiroli and M. Graetzel, *J. Am. Chem. Soc.*, 2003, **125**, 8790–8797.

21 C. L. Lee, R. R. Das and J. J. Kim, *Chem. Mater.*, 2004, **16**, 4642–4646.

22 K. Dedeian, J. Shi, E. Forsythe, D. C. Morton and P. Y. Zavalij, *Inorg. Chem.*, 2007, **46**, 1603–1611.

23 M. M. Alonso, N. Busto, L. D. Aguirre, L. Berlanga, M. C. Carrión, J. V Vicente, A. M. Rodríguez, A. Carbayo, B. R. Manzano, E. Ortí, F. A. Jalón, B. García and G. Espino, *Chem. Eur. J.*, 2018, **24**, 1–19.

24 J. Torres, M. C. Carrión, J. Leal, F. A. Jalón, J. V Cuevas, A. M. Rodríguez, G. Castañeda and B. R. Manzano, *Inorg. Chem.*, 2018, **57**, 970–984.

25 E. Baranoff, B. F. E. Curchod, J. Frey, R. Scopelliti, F. Kessler, I. Tavernelli, U. Rothlisberger, M. Grätzel and M. K. Nazeeruddin, *Inorg. Chem.*, 2012, **51**, 215–224.

26 K. S. Bejoymohandas, T. M. George, S. Bhattacharya, S. Natarajan and M. L. P. Reddy, *J. Mater. Chem. C*, 2014, **2**, 515–523.

27 A. Maity, L. Q. Le, Z. Zhu, J. Bao and T. S. Teets, *Inorg. Chem.*, 2016, **55**, 2299–2308.

28 H. Cao, H. Sun, Y. Yin, X. Wen, G. Shan, Z. Su, R. Zhong, W. Xie, P. Li and D. Zhu,

J. Mater. Chem. C, 2014, **2**, 2150–2159.

29 E. Orselli, G. S. Kottas, A. E. Konradsson, P. Coppo, R. Fröhlich, L. De Cola, A. Van Dijken, M. Büchel and H. Börner, *Inorg. Chem.*, 2007, **46**, 11082–11093.

30 D. Sykes, S. C. Parker, I. V Sazanovich, A. Stephenson, J. A. Weinstein and M. D. Ward, *Inorg. Chem.*, 2013, **52**, 10500–10511.

31 C. A. Hunter and J. K. M. Sanders, *J. Am. Chem. Soc.*, 1990, **112**, 5525–2234.

32 J. A. G. Williams, A. Beeby, E. S. Davies, J. A. Weinstein and C. Wilson, *Inorg. Chem. Commun.*, 2003, **42**, 8609–8611.

33 S. J. Farley, D. L. Rochester, A. L. Thompson, J. A. K. Howard and J. A. G. Williams, *Inorg. Chem.*, 2005, **44**, 9690–9703.

34 I. Avilov, P. Minoofar, J. Cornil and L. De Cola, *J. Am. Chem. Soc.*, 2007, **129**, 8247–8258.

35 J. Li, P. I. Djurovich, B. D. Alleyne, M. Yousufuddin, N. N. Ho, J. C. Thomas, J. C. Peters, R. Bau and M. E. Thompson, *Inorg. Chem.*, 2005, **44**, 1713–1727.

36 Z. N. Zubaidi, A. J. Metherell, E. Baggaley and M. D. Ward, *Polyhedron*, 2017, **133**, 68–74.

37 E. Baggaley, J. A. Weinstein and J. A. G. Williams, *Coord. Chem. Rev.*, 2012, **256**, 1762–1785.

38 J. R. Shewring, A. J. Cankut, L. K. McKenzie, B. J. Crowston, S. W. Botchway, J. A. Weinstein, E. Edwards and M. D. Ward, *Inorg. Chem.*, 2017, **56**, 15259–15270.

CHAPTER FOUR

Use of a new Ir(III) chromophore unit as the energy-donor in d/f dyads.

4 Use of a new Ir(III) chromophore unit as the energy-donor in d/f dyads

4.1 Introduction

Many studies on cyclometalated Ir(III) complexes of 2-phenylpyridine have been performed due to their desirable optical emission properties (tunable luminescence wavelength, high quantum yield, long lifetime). In addition, they are thermally stable and kinetically inert. There is a strong influence on the energy of the emission from the position and nature of substituents on the phenyl ring of the C^N cyclometalating ligands, and also from the type of the ancillary ligand. Strongly-luminescent complexes of this type have desirable properties for use in many applications such as light-emitting diodes (LEDs),[1] LECs.[1–4] and OLEDs[5,6] which are widely used in mobile phones, watches, computers, displays and TV sets. These applications exploit useful properties of the Ir(III) complexes which include: (i) generating light efficiently with low power consumption, (ii) high performance with fast response time, (iii) low current, low maintenance and voltage operation, (iv) colour-tunability of the complexes. In addition, phosphorescent Ir(III) complexes are also of interest for bio-sensing/cell imaging if they can be made water soluble.[5,7]

Luminescent Ir(III) complexes have also been investigated as energy-donors for d-f energy transfer to give sensitised emission in Ir/Ln dyads, when Ln = Eu or Tb (with emission in the visible region) or Ln = Yb or Nd (with emission in the near-IR region). In these dyads the two metal centres are linked by two pyrazolyl-pyridine chelating units which are separated by either an aromatic or an aliphatic spacer. d-f energy transfer in these dyads is efficient because of (i) Strong absorption of light from allowed low-energy charge transfer transitions; and (ii) a long lifetime of the ^{3}MLCT excited state, which maximises the change of energy-transfer to the Ln(III) centre.[8,9] In addition, the use of pyrazolyl-pyridine chelates bound to the Ir(III) centres gives high-energy luminescence from these Ir(III) complexes. The ability of the Ir(III) unit to act as an energy-donor to the Ln(III) ion depends on the energy gap between the Ir-based triplet excited state and the emissive energy level on the lanthanide ion. For example, Ir(III) units based on the fluorinated F_2ppy ligands have high energy triplet states, giving blue emission which can sensitise emission from both Eu(III) (emissive level 17,300 cm^{-1}) and Tb(III) (emissive level 20,400 cm^{-1}) (**Figure** 4-1).[10,11]

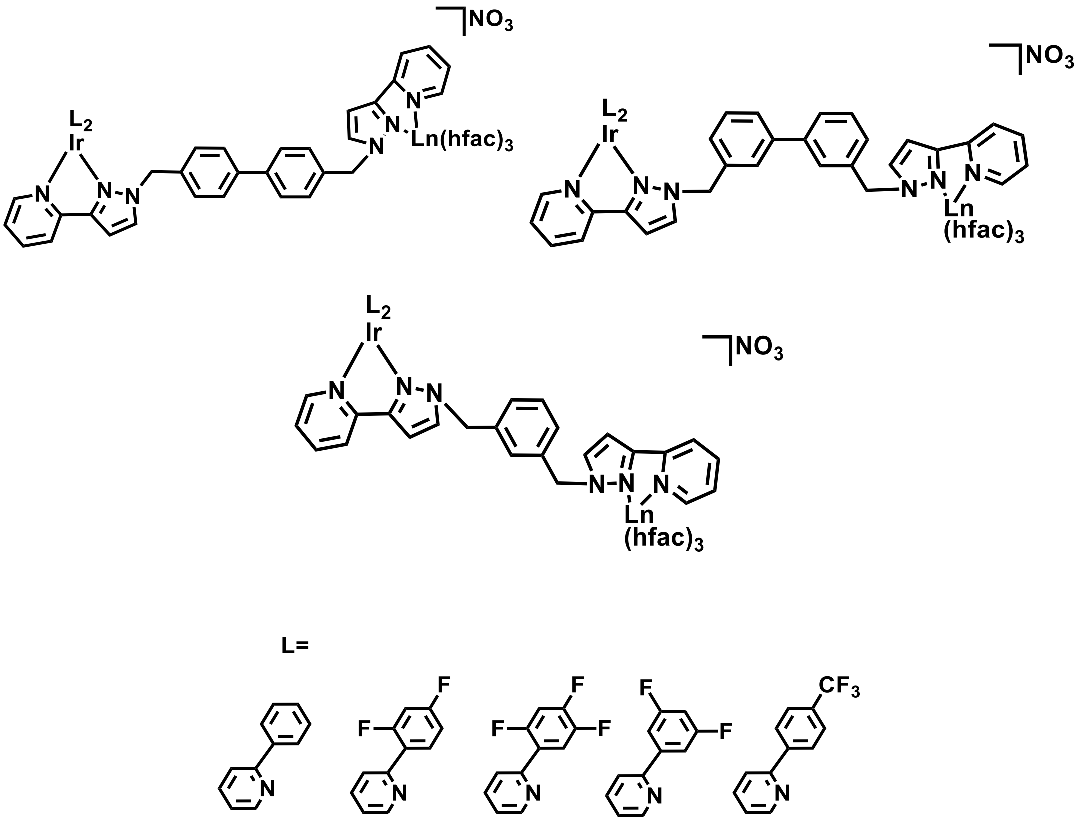

Figure 4-1 Chemical structure of Ir(L)$_2$/Ln(hfac)$_3$ dyads with different conformations and the distance spacer ligands.[11]

Thus in Ir/Tb dyads, When the Ir-based triplet excited state is high enough in energy (emitting in the blue region 450-480 nm), >80% of the Ir(III) unit emission is quenched by energy transfer to Tb(III) unit resulting in sensitisation of the characteristic $^7F_6 \rightarrow ^5D_4$ Tb-based emission at 490 nm (**Figure** 4-2).[12]

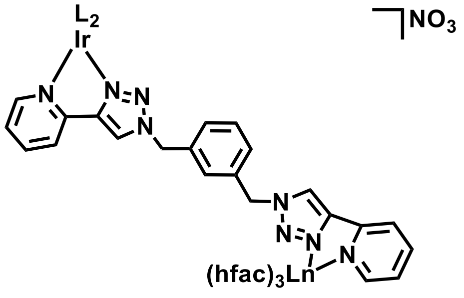

L= 2-(2,4-F$_2$-phenyl)pyridine
L= 2-(3,5-F$_2$-phenyl)pyridine

Figure 4-2 Chemical structure of Ir/Ln dyads, when Ln=Tb.[12]

The dinuclear complex [Ir(F$_2$phpy)$_2$.nap.Eu(hfac)$_3$] (**Figure** 4-3**)** behaves differently because of the presence of a photoactive naphthyl group as spacer between the Ir(III) and Eu(III) units.

Because the ^{3}nap state lies in energy between the ^{3}Ir(III) donor state and the Eu(III) excited state, the energy transfer process was facilitated in two steps, Ir→^{3}nap and ^{3}nap→Eu.[13]

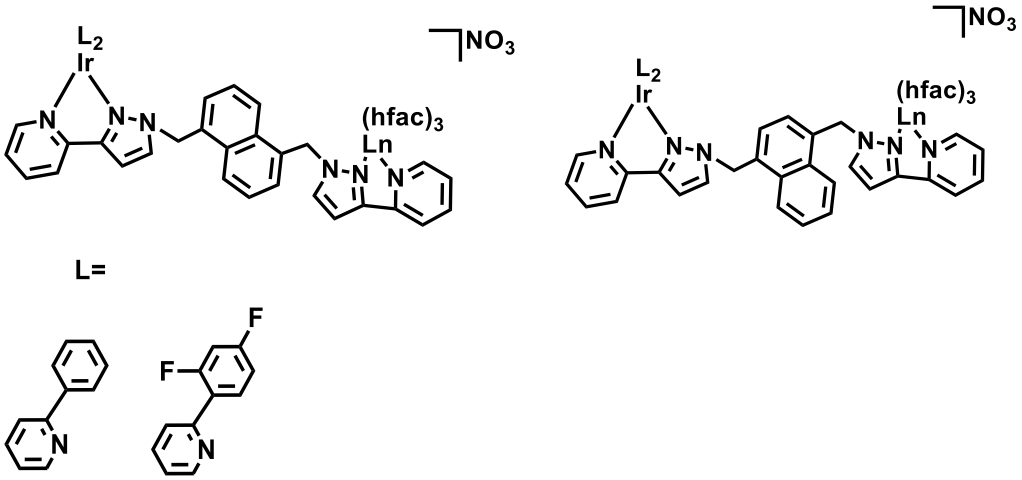

Figure 4-3 Chemical structure of Ir(L)$_2$/Ln(hfac)$_3$ dyads with naphthalene spacer ligands.[13]

Further examples of Ir(III) complexes which act as energy-donors to Eu or Tb in Ir/Ln dyads are in **Figure** 4-4, with different spacers in the bridging ligands. In all cases, partial quenching of Ir(III) emission in the presence of the lanthanide quencher, and the appearance of sensitised Ln-based emission (strong in the case of Eu and weak in case of Tb) was observed. The energy transfer process from Ir(III) to the Eu(III) or Tb(III) units occurs via PET by a combination of a initially-generated charge separated state $\{Ir^{4+}\}^{\cdot}$—$(pypz)^{\cdot-}$ and also direct PEnT by the Dexter mechanism. Also thermally-activated back energy transfer occurs from the Tb-based excited state to the Ir-based ^{3}LC/^{3}MLCT excited state followed by non-radiative decay,[10] which is why the sensitised Tb-based emission is weak.

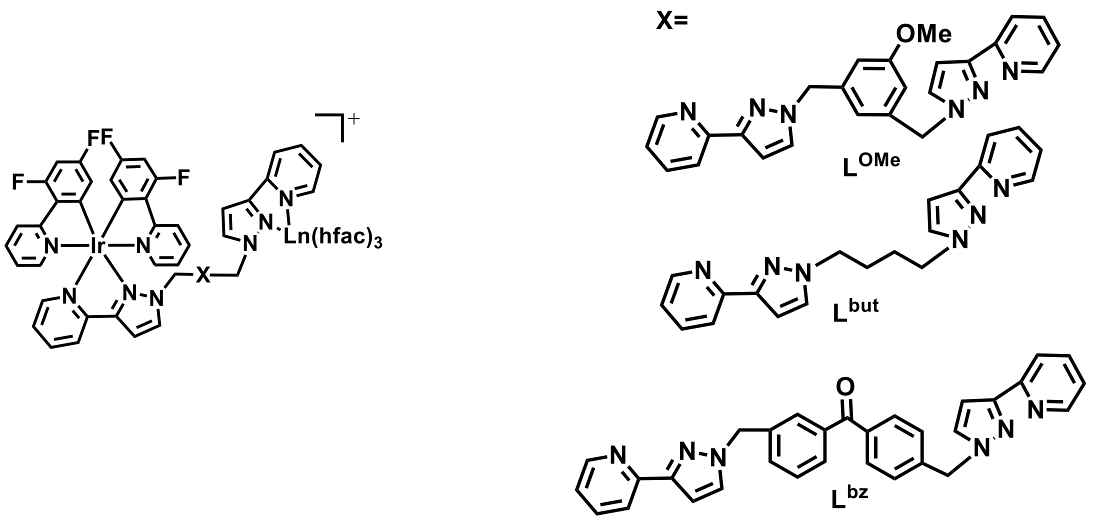

Figure 4-4 Chemical structure of Ir(F$_2$phpy)$_2$.X.Ln(hfac)$_3$ complex with different ligands, L^{OMe}, L^{but} and L^{bz}.[10]

4.2 The aims of this chapter

The aim of this work is to describe the synthesis, and characterise new Ir(III) complexes with deprotonated *N*-methyl-bipyridinium (C^N) ligands as the cyclometallating component in place of the more normal fluorinated 2-phenylpyridine units. These can be based on *N*-methylated 2,2'-, 2,3'- or 2,4'-bipyridine, acting as a cyclometallating ligand at two of the three positions around Ir(III); with a pyridyl-pyrazole based ancillary ligand at the third chelating position, as before. The photophysical properties of these new complexes will be investigated and also studied in terms of the impacts of changing the substituents of the quaternised N centre in the C^N on the emission properties. Use of these new Ir(III) units as energy-donors in Ir/Ln dyads (Ln = Eu, Tb and Gd) reveals the importance of the nature and position of the substituents in achieving luminescence sensitisation of the Ln units. In particular, we show that all three Ir(III) donor units (based on methylated 2,2'-, 2,3'- or 2,4'-bipyridine) have high-energy enough states to sensitise emission from Eu(III), but only two of them can sensitise emission from Tb(III). No luminescence sensitization was observed from Gd(III) units, used as a control, which is to be expected.

4.3 The structures of $^{N/N}$Ir•pypz•3PF$_6$ and $^{N/N}$Ir•L$^{bi\text{-}ph}$•3PF$_6$ complexes.

This chapter describe a series of new complexes $^{N/N}$Ir•Cl$_2$•PF$_{6,}$ $^{N/N}$Ir•pypz•3PF$_6$ and $^{N/N}$Ir•L$^{bi\text{-}ph}$•3PF$_6$ with different substituents positions, are given in **Figure** 4-5.

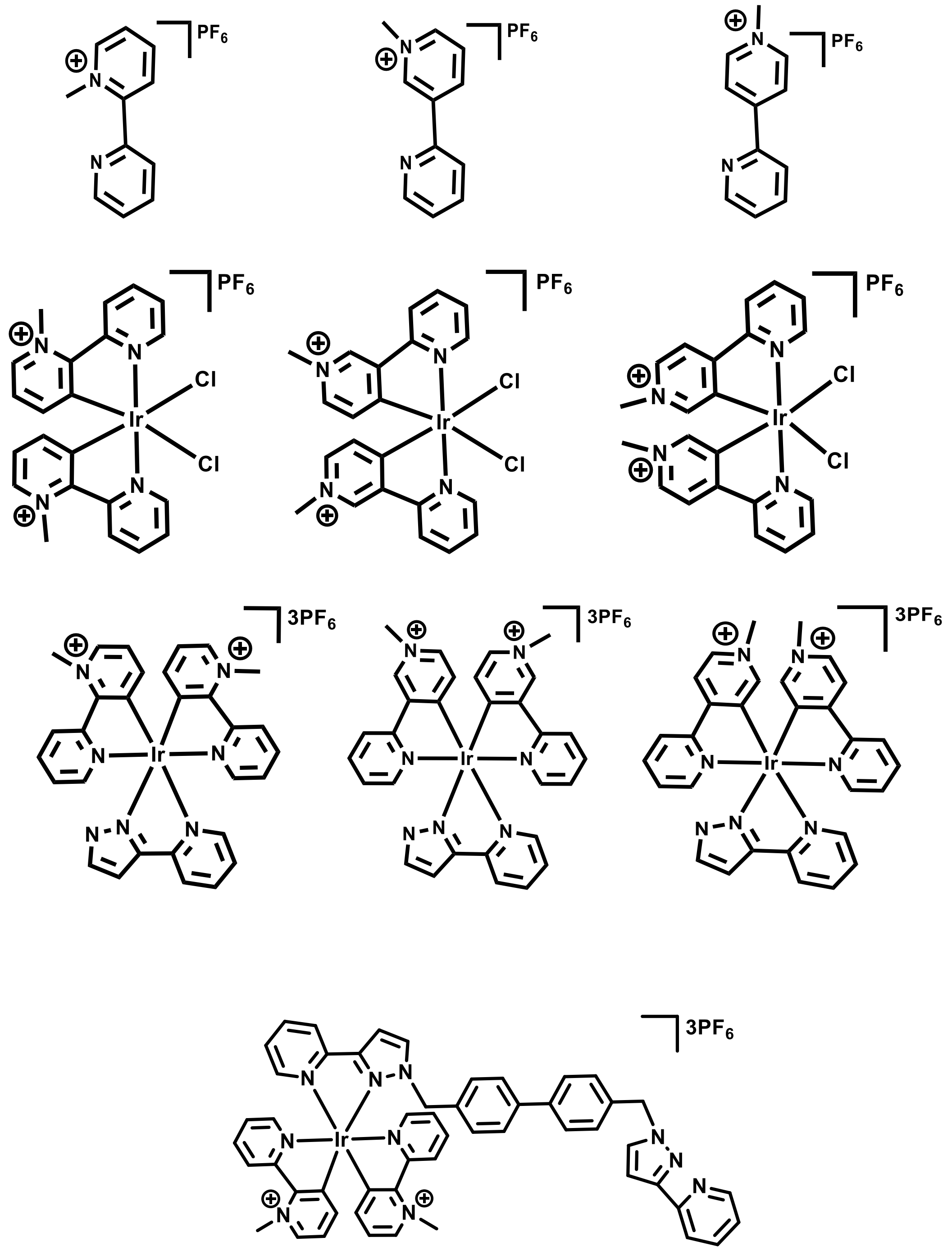

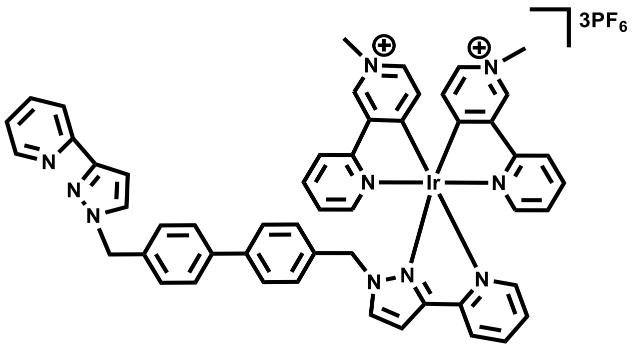

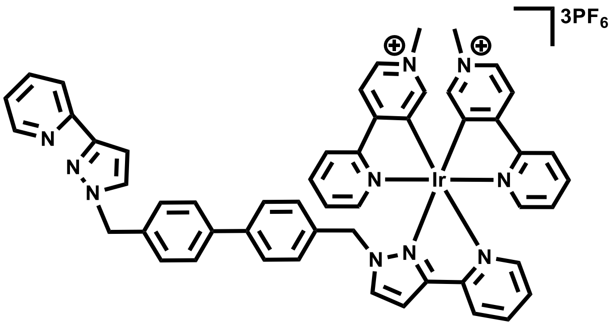

Figure 4-5 Structures of subseries of 1-methyl-pyridylpyridinum, $^{N/N}Ir{\bullet}Cl_2{\bullet}PF_6$, $^{N/N}Ir{\bullet}pypz{\bullet}3PF_6$ and $^{N/N}Ir{\bullet}L^{bi\text{-}ph}{\bullet}3PF_6$ compounds.

4.4 Synthesis and Characterisation.

4.4.1 Synthetic Studies

In this section we will describe the detailed synthesis of new Ir(III) complexes series of $^{N/N}$Ir•pypz•3PF$_6$ and $^{N/N}$Ir•L$^{bi\text{-}ph}$•3PF$_6$ with all three isomers of the cyclometallating *N*-methyl-bipyridinium ligands. Syntheses are based on a modified procedure by Coe *et.al*.[7] The starting materials $^{N/N}$Ir•Cl$_2$•PF$_6$ were received from Dr. Ben Coe and used as received to prepare the complexes $^{N/N}$Ir•pypz•3PF$_6$ and $^{N/N}$Ir•L$^{bi\text{-}ph}$•3PF$_6$. All synthetic schemes below have been drawn based on use of methylated 2,2'–bipyridine as cyclometallating ligand. The analogous 2,3- and 2,4- substituted bipyridines were also used.

4.4.1.1 Synthesis of the N-methyl-pyridylpyridinium•PF$_6$ complex.

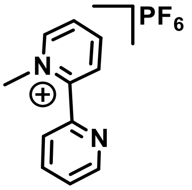

To a solution of 2,2'-bipyridine in tert-butyl methyl ether, methyl iodide was added and refluxed for 36 hr (**Figure** 4-6). An off-white precipitate was collected and washed with tert-butyl methyl ether, dried, and then dissolved in a minimum of water, and filtered to obtain a pale yellow solution. Addition of NH$_4$PF$_6$ formed a precipitate of the hexafluorophosphate salt which was filtered off and washed with cold water, then dried.

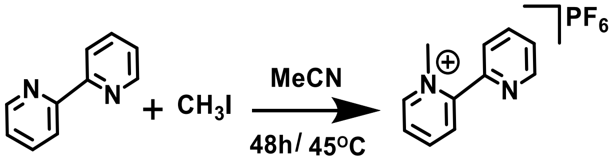

Figure 4-6 Synthesis scheme of N-methyl-pyridylpyridinium•PF$_6$.

4.4.1.2 Synthesis of the $^{22,\,23\text{ and }24}IrCl_2{\bullet}PF_6$ complex.

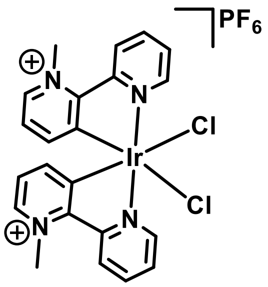

This mono-Ir(III) complex was achieved by reaction of $IrCl_3{\bullet}6H_2O$ with the aromatic *N*-methyl-bipyridinium hexafluorophosphate (1:2.5 ratio) under argon, in 2-methoxyethanol/H_2O in a ratio (22 mL / 8 mL), heated at 120 °C for 48 hr (**Figure** 4-7). The reaction was protected from light by covering the round bottom flask in foil. The reaction was cooled to room temperature, filtered and excess NH_4PF_6 was added to the filtrate to ensure that the complex cation was converted to the PF_6 salt. The solvent was evaporated and the precipitate was suspended with ice-cold water. The solid was filtered and rinsed with (4 mL) ice-cold water then washed with acetone/diethyl ether in proportion (1:3 mL) three times. This complex was characterised by mass spectroscopy which gave high resolution mass *m/z* 603.0682 for $C_{22}H_{20}Cl_2IrN_4$ molecular formula as shown in **Figure** 4-8, and ^1H NMR spectroscopy, which gave integral main peaks 20H. The characterisation data along with the crystal structure provided good evidence that the $^{N/N}IrCl_2{\bullet}PF_6$ complexes are mono-nuclear, not dimers, and these were used as starting material to synthesise $^{N/N}Ir{\bullet}pypz{\bullet}3PF_6$ and $^{N/N}Ir{\bullet}L^{bi\text{-}ph}{\bullet}3PF_6$ complexes without further purification.

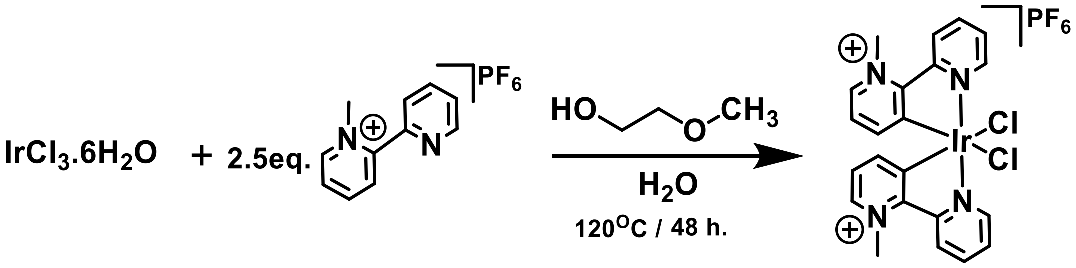

Figure 4-7 Synthesis scheme of $^{22}IrCl_2{\bullet}PF_6$ as an example for all $^{N/N}IrCl_2{\bullet}PF_6$ complexes.

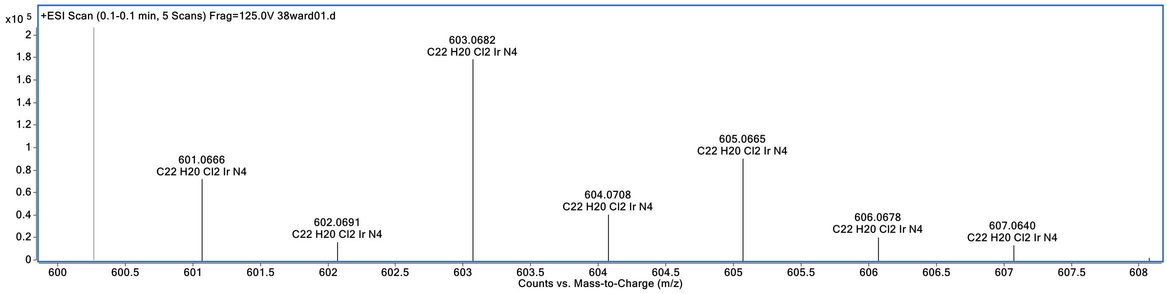

Figure 4-8 High resolution mass spectroscopy of ^{22}IrCl$_2$•PF$_6$.

4.4.1.3 Synthesis of the $^{N/N}$Ir•pypz•3PF$_6$ complex.

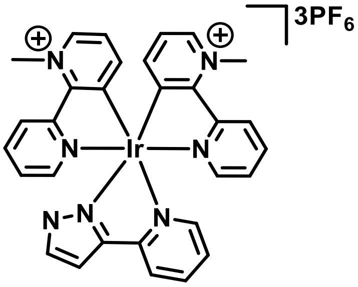

The complexes $^{22,\ 23\ \text{or}\ 24}$ Ir•pypz•3PF$_6$ were prepared by refluxing a solution of $^{2,2,\ 2,3\ \text{or}\ 2,4}$IrCl$_2$ and pypz under argon for 20 mins in H$_2$O/ 2-methoxyethanol solution, with AgPF$_6$. The Ag(I) ions react with chloride ions to form AgCl which precipitates. The overnight reaction gives crude complexes which was purified by column chromatography on silica gel eluting with DCM:MeOH (90:10), then with MeCN:aqueous KNO$_3$ (100:50), then MeCN:KNO$_3$:H$_2$O in (100:50:50) proportion and finally on Sephadex LH20 eluting with MeOH. The synthesis steps of $^{22,\ 23\ \text{and}\ 24}$Ir•pypz•3PF$_6$ are depicted in **Figure** 4-9.

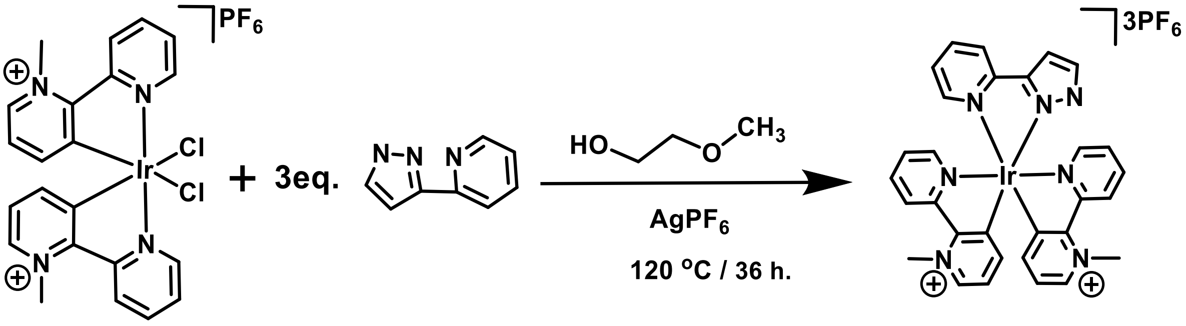

Figure 4-9 Synthesis scheme of ^{22}Ir•pypz•3PF$_6$.

4.4.1.4 Synthesis of the $^{N/N}$Ir•L$^{bi\text{-}ph}$•3PF$_6$ complexes.

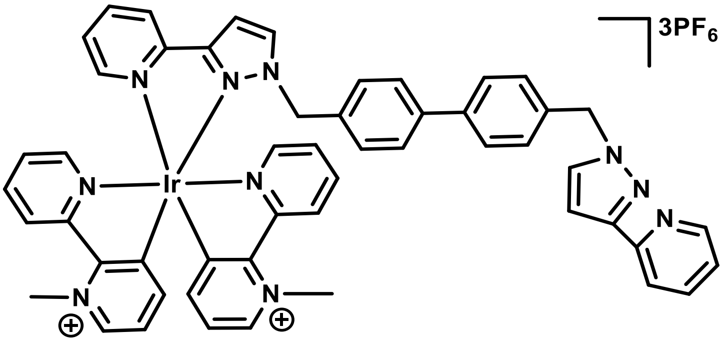

The complexes $^{22,\ 23\ \mathrm{or}\ 24}$Ir•L$^{bi\text{-}ph}$•3PF$_6$ were prepared by refluxing $^{22,\ 23\ \mathrm{or}\ 24}$Ir•Cl$_2$•PF$_6$ with 3eq. L$^{bi\text{-}ph}$ in a mixture of H_2O/2-methoxy-ethanol (1:4, v/v) as a solvent in the presence of AgPF$_6$ under argon. The reaction was heated at 120 °C for 36 hr. The crude mixture was filtered through Celite to remove AgCl and the solvent was evaporated. The precipitate was purified by column chromatography on silica gel eluting by DCM:MeOH (90:10), then MeCN:KNO$_{3(aq.)}$ (100:50), then MeCN:KNO$_{3(aq.)}$:H_2O (100:50:50) proportion, then washed by KPF$_{6(aq.)}$ to perform anion exchange, and then was finally columned on Sephadex LH20 eluting with MeOH. **Figure** 4-10 shows the synthesis of the $^{22,\ 23\ \mathrm{and}\ 24}$Ir•L$^{bi\text{-}ph}$•3PF$_6$ complexes. Also these series of complexes were characterised by using high resolution mass *m/z* 500.1639 for $C_{52}H_{44}IrN_4$•3PF$_6$ molecular formula.

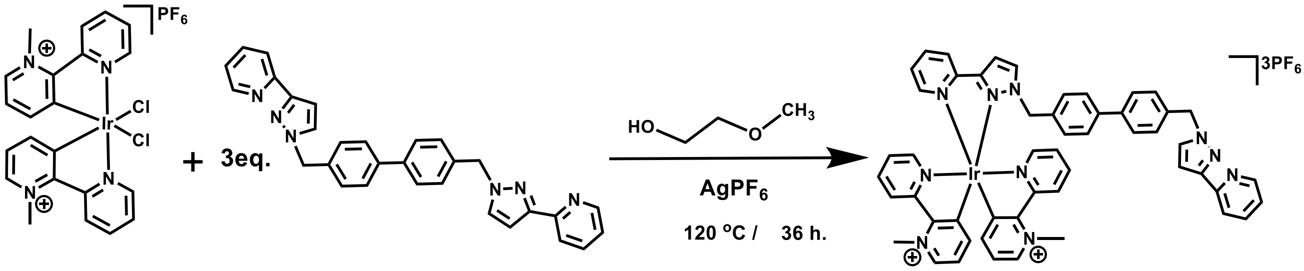

Figure 4-10 Synthesis scheme of ^{22}Ir•L$^{bi\text{-}ph}$•3PF$_6$.

4.4.2 ^{1}H NMR spectra of $^{N/N}$Ir•L$^{bi\text{-}ph}$•3PF$_6$ complexes with verify substituents.

The identity of all the complexes presented in this chapter were confirmed by ^{1}H NMR spectroscopy, by using deuterated MeCN and MeOH as solvents. The spectra of the ^{22}Ir•L$^{bi\text{-}ph}$•PF$_6$ complex, as an example, is depicted in **Figure** 4-11 and shows the correct number of ^{1}H NMR signals in the expected regions of the spectrum. Interestingly, the two methyl signals from the $^{+}$N-CH$_3$ groups are observed as a single peaks integrating to 3H each in a region between ~ $\delta_{H\,=}$ 4.1 and ~ $\delta_{H\,=}$ 4.8 ppm. In the two alkyl ethyl groups (CH$_2$), one is split into two doublet peaks, at δ_H = 5.60 with J=17.7 Hz, which belongs to one proton as inequivalent diastereotopic protons close to the chiral centre, and another doublet peak at δ_H = 4.94 with J=17.7 Hz, which belongs to equivalent proton. Another alkyl ethyl group located at δ_H =5.5 as a single peak, which is integrated to 1H.

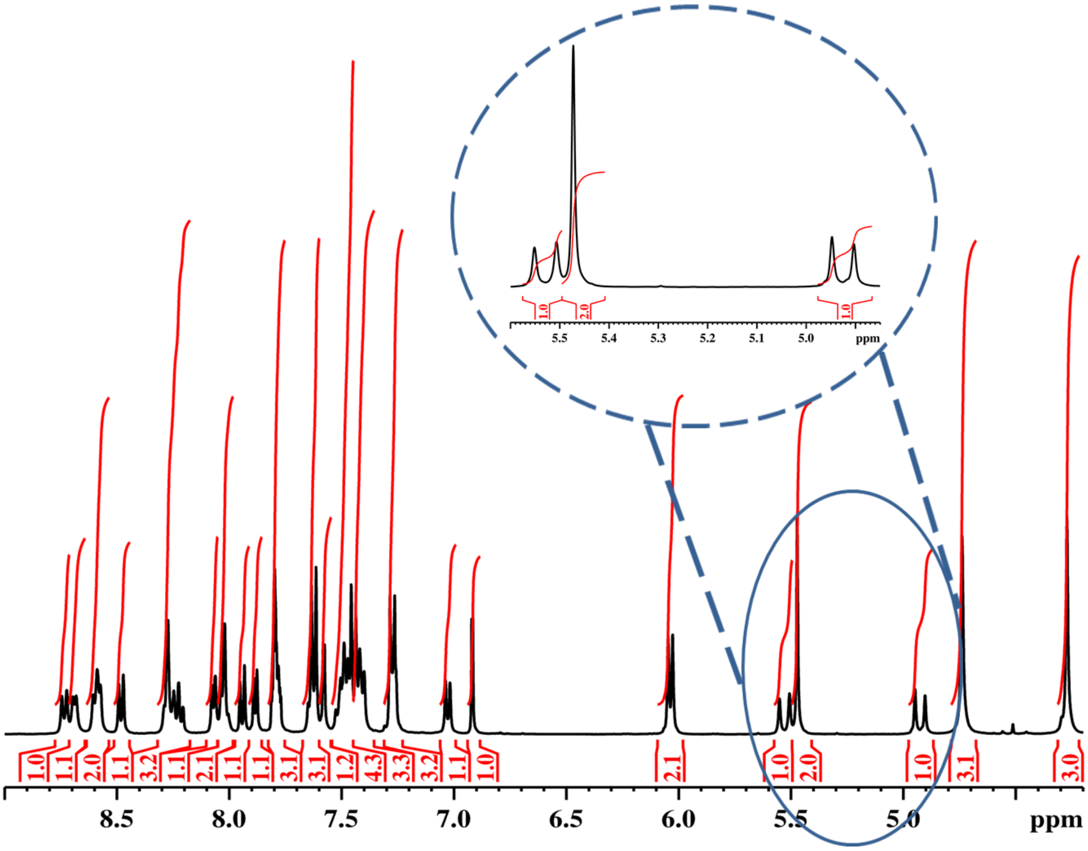

Figure 4-11 ^{1}H NMR of ^{22}Ir•L$^{bi\text{-}ph}$•PF$_6$ in CD$_3$CN.

The ^{1}H NMR spectrum of ^{23}Ir•L$^{bi\text{-}ph}$•3PF$_6$ and ^{24}Ir•L$^{bi\text{-}ph}$•3PF$_6$ complexes show the same basic pattern as the ^{22}Ir•L$^{bi\text{-}ph}$•3PF$_6$ complex. The two equivalent and inequivalent protons in methyl group which is close to and far away from the tricyclometalating-Ir unit appear in approximately the same region and have the same splitting patterns. All complexes give total signals integrating peaks to 44H. Another example of ^{1}H NMR spectrum is ^{24}Ir•L$^{bi\text{-}ph}$•3PF$_6$ (**Figure** 4-12).

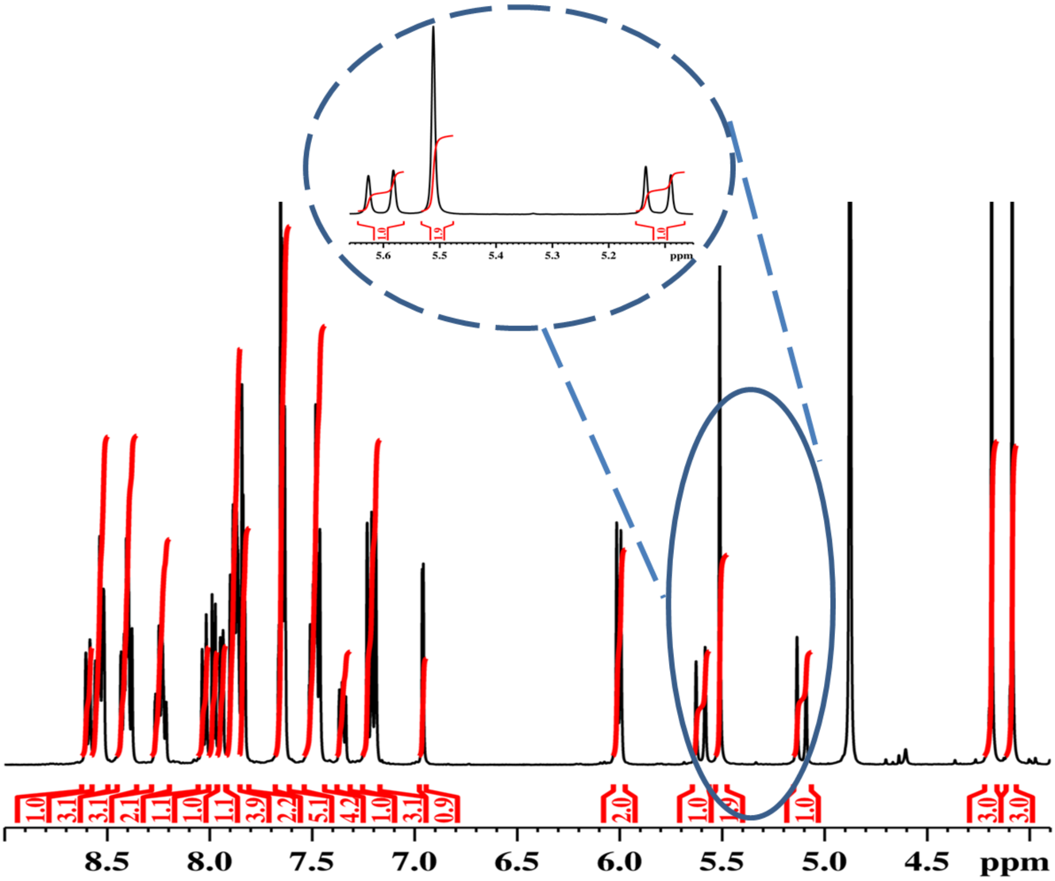

Figure 4-12 ^{1}H NMR of ^{24}Ir•L$^{bi\text{-}ph}$•3PF$_6$ in Me$_3$OD. Insert:-Expanded the doublet and singlet methyl groups.

4.4.3 X-ray crystallography.

Coe *et.al.*[7] expected the $^{N/N}IrCl_2$•PF_6 complexes to be chloride-bridged dimers of the form $[Ir_2(C^\wedge N)_4(Cl)_2][PF_6]_{4,}$[7] like other complexes in which C^N is a cyclometalating ligand derived from deprotonated 2-phenylpyridine or its derivatives. However, after growing crystals of the complex with *N*-methyl-2,2'-bipyridinium as ligand the crystal structure showed it to be a simple mononuclear complex with terminal chlorides mono-$IrCl_2$•PF_6 and not the usual chloro-bridged dimer $[Ir(C^\wedge N)_2Cl]_{2.}$[5,14,15] The structure is shown in **Figure** 4-13. For more evidence that the starting material $^{N/N}IrCl_2$•PF_6 complexes are monomers not dimers, Coe *et.al.*[7] have published the crystal structure of the additional example $^{24}IrCl_2$•PF_6.

The $^{22}IrCl_2$•PF_6 complex whose structure we report may have contained some additional chloride anions from an incomplete anion methathesis with hexafluorophosphate,[7] leading to this crystal also containing chloride as a counter-ion.

(a)

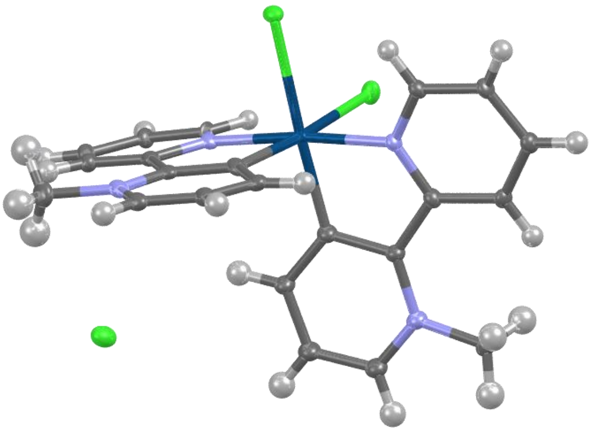

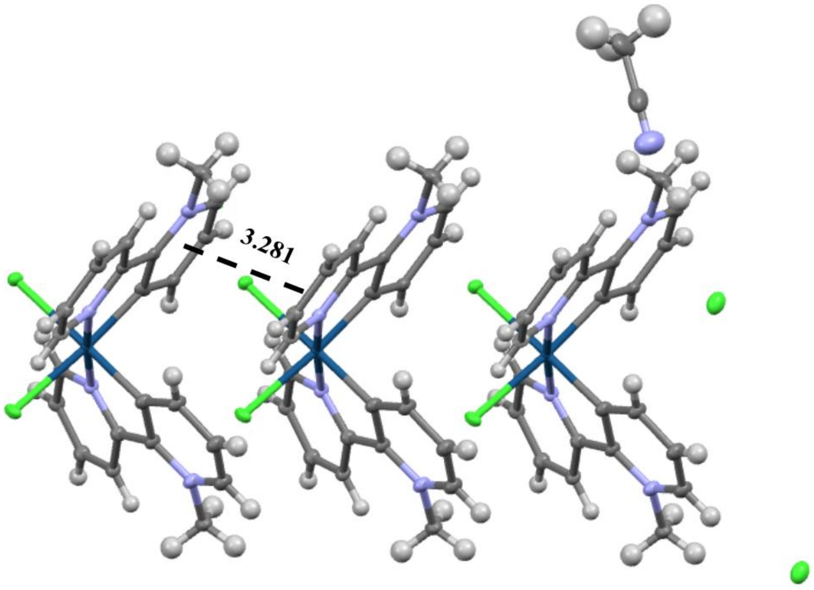

(b)

Figure 4-13 (a) X-ray crystallographic structure of $^{22}IrCl_2$•Cl(MeCN). The green balls in structure represent to Cl atoms, while the blue balls represent the N atoms. (b) The solvent MeCN clears in the thermal ellipsoids unit cell at the 50% level with π-π stacking distance 3.281 Å.

The average Ir-Cl bond distance in $^{22}IrCl_2$•Cl is slightly longer than in the previous study of $^{24}IrCl_2$•PF_6 complex as summarised in **Table 4-1** for comparison.[7]

Table 4-1 Selected distances parameters for solvate $^{22}IrCl_2$•Cl complex compared with the previously reported complex $^{24}IrCl_2$•PF_6 complex.[7]

Distances[°A]	$^{22}IrCl_2$•Cl	$^{24}IrCl_2$•PF_6
Ir-Cl $_{(1)}$	2.486 (3)	2.470 (1)
Ir-Cl $_{(2)}$	2.467 (3)	2.457 (1)
Ir-$C_{C\wedge N}$	1.988 (14)	1.998 (6)
Ir-$C_{C\wedge N}$	1.977 (14)	1.984 (6)
Ir-$N_{N\wedge N}$	2.056 (11)	2.055 (5)
Ir-$N_{N\wedge N}$	2.074 (11)	2.060 (5)

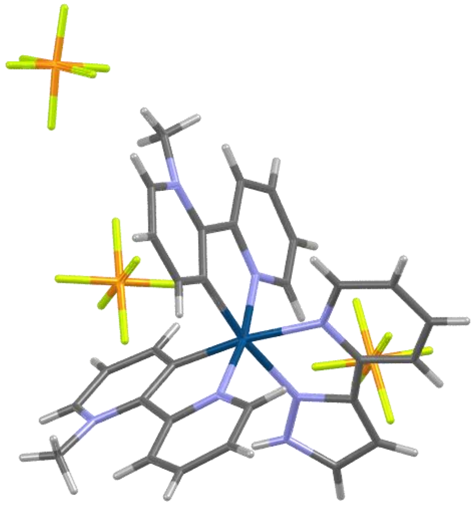

Figure 4-14 Crystal structure of ^{22}Ir•pypz•3PF$_6$ complex showing Ir(III) core (dark blue), and the purple atoms represent to N atoms with three counter anions PF$_6$.

Single crystals of the complex ^{22}Ir•pypz•3PF$_6$ (**Figure** 4-14) were grown by slow diffusion of diethyl ether into a MeCN solution of the complex in the dark. The tris-chelate complex displays an Ir(III) centre with one bidentate pypz ancillary ligand and two cyclometalating C^N ligands in a pseudooctahedral geometry and three PF$_6^-$ counter anions. Bond distances for this complex, compared to the analogue with 2,2'-bipy as co-ligand in place of pypz, are shown in **Table 4-2**.

Table 4-2 Selected distances parameters for solvate ^{22}Ir•pypz•3PF$_6$ complex compared with previous [Ir(2,2'-C^N)$_2$(bpy)]3PF$_6$ complex study.

Distances [°A]	**^{22}Ir•pypz•3PF$_6$**	**[Ir(2,2'-C^N)$_2$(bpy)]3PF$_6$**
Ir-C	1.997 (15)	2.002 (4)
Ir-C	1.988 (16)	2.003 (4)
Ir-N$_{C^N}$	2.022 (11)	2.043 (3)
Ir-N$_{C^N}$	2.041 (10)	2.044 (3)
Ir-N$_{N^N}$	2.097 (8)	2.128 (3)
Ir-N$_{N^N}$	2.122 (12)	2.133 (3)

We were unable to obtain any single crystals of any members of the series $^{22}\text{Ir}{\bullet}\text{L}^{\text{bi-ph}}{\bullet}3\text{PF}_6$, $^{23}\text{Ir}{\bullet}\text{L}^{\text{bi-ph}}{\bullet}3\text{PF}_6$ or $^{24}\text{Ir}{\bullet}\text{L}^{\text{bi-ph}}{\bullet}3\text{PF}_6$ although attempts were made using a variety of methods.

Table 4-3 Crystallographic data of $^{22}\text{IrCl}_2{\bullet}\text{PF}_6$ complex.

Complex	**$^{22}\text{IrCl}_2{\bullet}\text{Cl}$**
Formula	$C_{24}\ H_{23}\ Cl_3\ Ir\ N_5$
Molecular weight	680.02
Crystal system	Triclinic
Space group	*P-1*
a	7.0019(10) Å
b	12.446(2) Å
c	14.948(2) Å
α	105.382(5)°
β	99.618(5)°
γ	101.626(5)°
V	1196.2(3) Å^3
Z	2
T	110 (2) K
μ	5.939 mm^{-1}
Crystal size	0.210 × 0.060 ×0.060 mm^3
Final R1, wR2^{α}	0.0548, 0.1392

α The value of R1 is based on ‘observed’ data with I >2σ (I); the value of wR2 is based on all data.

4.5 Results and Discussion

For discussion of the luminescence properties of the new complexes, we divided the Ir(III) complexes studies into three groups depending on the type of the ancillary ligand that is bound to the cyclometalating Ir(III) unit. We discuss first the chloride complexes $^{N/N}IrCl_2•PF_6$ and then the complexes with the bidentate pyridyl-pyrazole ancillary ligands $^{N/N}Ir•pypz•3PF_6$ and $^{N/N}Ir•L^{bi\text{-}ph}•3PF_6$.

Part One

4.5.1 Photophysical Studies of the $^{N,N}IrCl_2•PF_6$ series.

4.5.1.1 Absorption spectra of $^{22}IrCl_2•PF_6$, $^{23}IrCl_2•PF_6$ and $^{24}IrCl_2•PF_6$.

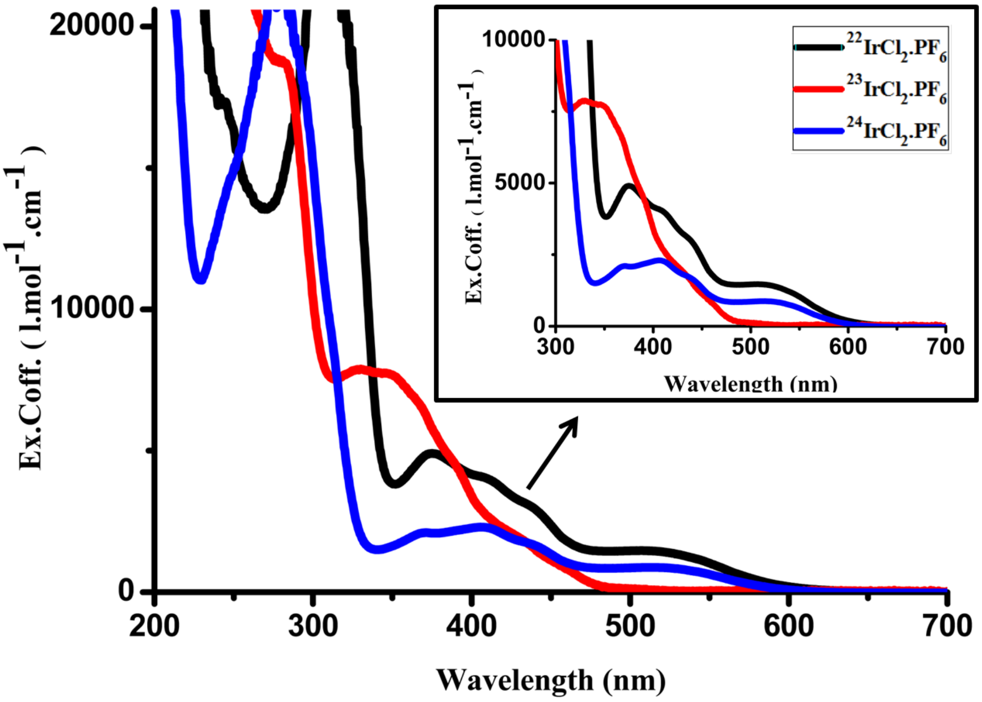

Figure 4-15 Electronic absorption spectra of $^{22}IrCl_2•PF_6$, $^{23}IrCl_2.PF_6$ and $^{24}IrCl_2•PF_6$ in MeCN at room temperature and at approximately the same concentrations. Expansion shows the range of wavelengths for each complex between 300 and 700 nm.

Interestingly, **Figure** 4-15 shows that the main features of the absorption spectra of $^{22}IrCl_2•PF_6$ and $^{24}IrCl_2•PF_6$ complex are at lower energy than for $^{23}IrCl_2•PF_6$. It is clear that substitution position does affect the shape and position of the peaks, as was shown originally by Coe who first prepared complexes based on these starting materials.[7] The intense peaks at < 400 nm could be attributed to the spin allowed LC electronic transition, while at > 400 nm the less intense peaks are assigned to mixture of LC/CT electronic transitions (**Table 4-4**).[16] summarises the extinction coefficients for all three $^{N/N}$IrCl$_2$•PF$_6$ complexes.

Table 4-4 Wavelengths and extinction coefficients data for ^{N,N}IrCl$_2$•PF$_6$ complexes series.

$^{N/N}$IrCl$_2$•PF$_6$ complexes	λ (nm) / ε (L.mol^{-1}.cm^{-1})
^{22}IrCl$_2$•PF$_6$	520 (1400), 440 (2900), 411 (4000), 374 (4900), 311 (24100)
^{23}IrCl$_2$•PF$_6$	340 (7700), 436 (1700), 390 (4470), 283 (4500), 283 (18600), 260 (21000), 233 (34300)
^{24}IrCl$_2$•PF$_6$	520 (870), 440 (1700), 405 (2300), 370 (2100), 278 (22500)

4.5.1.2 Luminescence of the ^{N,N}IrCl$_2$•PF$_6$ series.

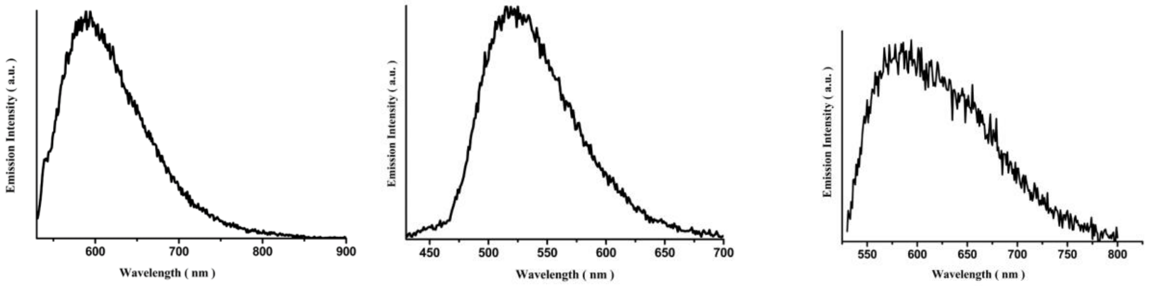

Emission spectrum of ^{22}IrCl$_2$•PF$_6$ **Emission spectrum of ^{23}IrCl$_2$•PF$_6$** **Emission spectrum of ^{24}IrCl$_2$·PF$_6$**

Figure 4-16 Emission spectra of ^{22}IrCl$_2$•PF$_6$, ^{23}IrCl$_2$•PF$_6$ and ^{24}IrCl$_2$•PF$_6$ in MeCN at room temperature.

The luminescence spectra were measured in MeCN and are shown in **Figure** 4-16, while other photophysical details are summarized **Table 4-5**. Unstructured emission spectra of ^{22}IrCl$_2$•PF$_6$, ^{23}IrCl$_2$•PF$_6$ and ^{24}IrCl$_2$•PF$_6$ complexes were observed. The ^{23}IrCl$_2$•PF$_6$ complex emission is clearly blue-shifted compared to the emission from ^{22}IrCl$_2$•PF$_6$ and ^{24}IrCl$_2$•PF$_6$, consistent with what was seen in the UV/Vis spectra. The quantum yields of these complexes were measured in MeCN as solvent and using PtLCl complex, when L=1,3-di(2-pyridyl)benzene, as reference and in calculation data of quantum yield using **eq.2-1**. The quantum yield data shows that ^{23}IrCl$_2$•PF$_6$ luminescence is much weaker than luminescence from the ^{22}IrCl$_2$•PF$_6$ and ^{24}IrCl$_2$•PF$_6$ complexes. The luminescence lifetimes in both aerated and degassed MeCN solutions were also recorded for all complexes. For ^{23}IrCl$_2$•PF$_6$ the luminescence was fitted to two lifetimes to get a better χ^2 value, while the other complexes were fitted to one lifetime. $^{23}IrCl_2•PF_6$ complex shows shorter-lived luminescence than $^{22}IrCl_2•PF_6$ and $^{24}IrCl_2•PF_6$, in keeping with the lower intensity of luminescence. The luminescence lifetime in degassed solution for all complexes is longer than the lifetime measured in air due to removal of quenching by collision with O_2, which is excluded upon dealing with the radiationless (deactivation) pathways of the triplet emissive state. Also, at 77K case all complexes have shifted to the blue region.

Table 4-5 Photophysical subseries data of $^{N,N}IrCl_2•PF_6$ complexes in MeCN solvents.

In MeCN					
$^{N/N}IrCl_2.PF_6$ complexes	$\lambda_{Excitation}$ / nm	λ_{max} / nm in air	ϕ	τ (ns) in air	τ (ns) in degasses
$^{22}IrCl_{2.}PF_6$	520	590	0.062	τ_1= 380, χ^2= 1	τ_1 = 712, χ^2= 1.1
$^{23}IrCl_{2.}PF_6$	360	520	0.004	τ_1= 137, τ_2=37, χ2= 1.1	τ_1 = 307, τ_2 = 55, χ^2= 1.4
$^{24}IrCl_{2.}PF_6$	520	590	0.021	τ_1= 469, χ^2= 0.99	τ_1 = 624, τ_2 = 200, χ^2= 0.92

Part Two

4.5.2 Photophysical Studies of ^{N,N}Ir•pypz•3PF$_6$ series.

4.5.2.1 Electronic absorption spectroscopy subseries of ^{22}Ir•pypz•3PF$_6$, ^{23}Ir•pypz•3PF$_6$ and ^{24}Ir•pypz•3PF$_6$

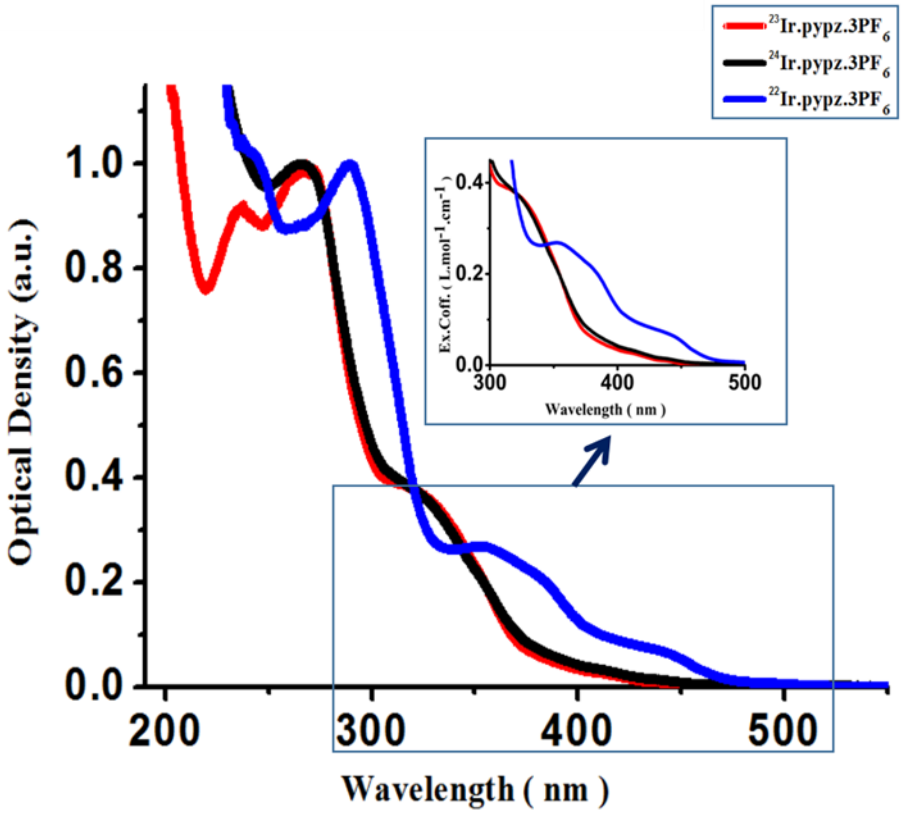

Figure 4-17 Normalised electronic absorption spectra of ^{22}Ir•pypz•3PF$_6$, ^{23}Ir•pypz•3PF$_6$ and ^{24}Ir•pypz•3PF$_6$ in MeCN at 298 K. Insets: Expansion shows the low field energy region which is the excitation wavelength interesting area for each complex.

The electronic abosrbtion spectra for all $^{N/N}$Ir•pypz•3PF$_6$ complexes were measured in MeCN solution at 298 K (**Figure 4-17**): spectroscopic information is summarised in **Table 4-6**. All $^{N/N}$Ir•pypz•3PF$_6$ complexes display high energy absorptions in high energy field < 300 nm, which are attributed to $^1\pi$-π^* and ^{1}MLCT electronic transitions of both C^N and N^N ligands.[7] Interestingly, all $^{N/N}$Ir•pypz•3PF$_6$ complexes display a broad peak in visible region between 350 – 500 nm which is assigned to the ^{3}MLCT absorption of the complexes, arising from high spin orbit coupling $\xi = 4430$ cm $^{-1}$.[16]

Table 4-6 Summary of UV/Vis spectroscopic data for the ^{N,N}Ir•pypz•3PF$_6$ complexes series.

$^{N/N}$Ir•pypz•3PF$_6$ complexes	λ (nm) / ε (L.mol^{-1}.cm^{-1})
^{22}Ir•pypz•3PF$_6$	245(44400), 287(3200), 360 (1900), 440 (530)
^{23}Ir•pypz•3PF$_6$	235 (3400), 265 (3800), 315 (3500), 440 (300)
^{24}Ir•pypz•3PF$_6$	320 (3750), 438 (380)

4.5.2.2 Photoluminescence study of ^{N,N}Ir•pypz•3PF$_6$ complexes.

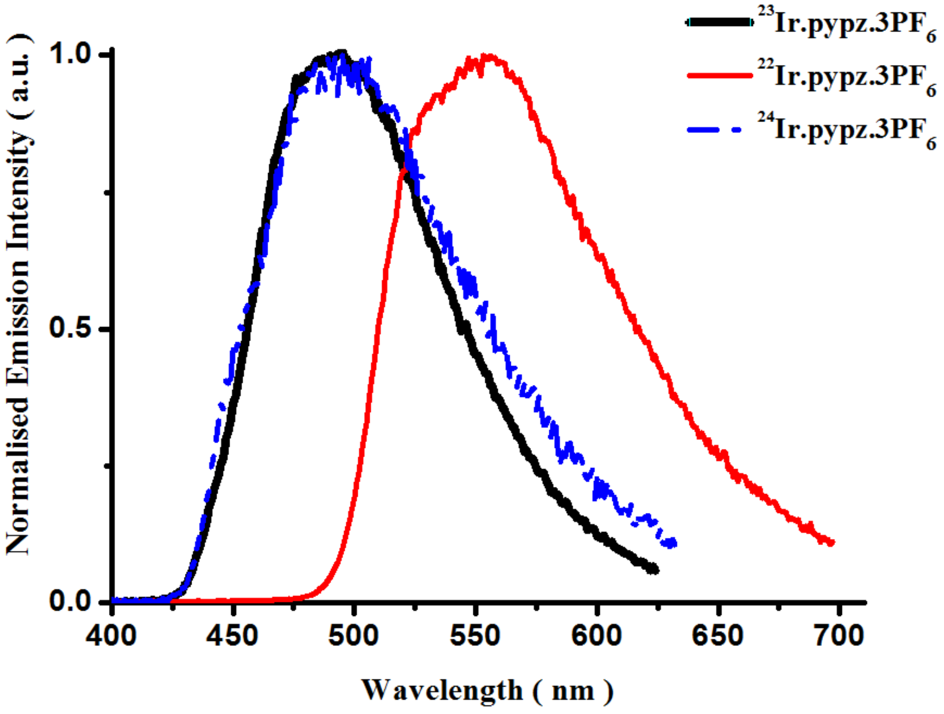

Figure 4-18 Normalised luminescence spectra of $^{N/N}$Ir•pypz•3PF$_6$ in MeCN at 298 K.

The emission spectra and emission lifetimes for the $^{N/N}$Ir•pypz•3PF$_6$ complexes were measured in aerated and degassed MeCN solutions at 298 K and at 77K, and are summarised in **Table 4-7**. The excitation wavelength for each $^{N/N}$Ir•pypz•3PF$_6$ complex was chosen to be in the low energy ^{3}MLCT absorption region. The complexes ^{22}Ir•pypz•3PF$_6$ and ^{23}Ir•pypz•3PF$_6$ display broad luminescence with a maximum at 490 – 495 nm the broad, featureless profiles indicate emission from the ^{3}MLCT state (**Figure** 4-18).[17, 18] In contrast, the emission of ^{22}Ir•pypz•3PF$_6$ is red-shifted with a maximum at 553 nm. Compared to the analogous complexes with 2,2'-bipy as the co-ligand instead of pypz, the spectra are generally similar (with differences arising because pyrazole is a less pi-acceptor than bipy). However, one important difference is that in our pypz complexes there are two 'high-energy' emission spectra, from the ^{23}Ir and ^{24}Ir complexes, with the ^{22}Ir complex showing substantially lower-energy emission. With bipy in place of pypz,[17] there is one high-energy luminescence (from the ^{23}Ir•L^{bipy} complex) and two that are at substantially lower energy (^{22}Ir•L^{bipy} and ^{24}Ir•L^{bipy}). This the pattern of higher-energy or lower-energy emission is not just from which isomer of the *N*-methyl-bipyridinium ligand is used but also depends on the co-ligand (bipy *vs.* pypz).

The emission spectra at 77K for ^{23}Ir•pypz•3PF$_6$ and ^{24}Ir•pypz•3PF$_6$ showed blue-shifts of the emission maximum due to the usual rigidochromism, which supports nature of the emission from a ^{3}MLCT excited state.[17] However, luminescence from ^{22}Ir•pypz•3PF$_6$ complex at 77K was very weak.

In air at 298 K, the luminescence lifetime of ^{22}Ir•pypz•3PF$_6$ is surprisingly long (1100 ns). ^{23}Ir•pypz•3PF$_6$ and ^{24}Ir•pypz•3PF$_6$ displayed much shorter emission lifetimes, which could be fitted to two exponential decay. For ^{23}Ir•pypz•3PF$_6$ the lifetime components are 83 ns (82%) and 260 ns (17%), whereas for ^{24}Ir•pypz•3PF$_6$ the lifetime components are 83 ns (84%) and ^{24}Ir•pypz•3PF$_6$ = 303 ns (15%). In degassed solutions at 298 K, the emission lifetimes for all $^{N/N}$Ir•pypz•3PF$_6$ complexes substantially increased, up to 2000 ns for ^{22}Ir•pypz•3PF$_6$ and ^{22}Ir•pypz•3PF$_6$.[19] Data are collected in **Table 4-7**.

Table 4-7 The photophysical properties of $^{N/N}$Ir•pypz•3PF$_6$, the χ^2 value of fitting lifetime for all complexes in air, at 77K and in degasses between 1.01 and 1.08.

$^{N/N}$Ir•pypz•3PF$_6$ complexes	**$\lambda_{.Excitation}$ (nm)**	**$\lambda_{max.}$(nm)**	**τ (ns) <± 50**	**ϕ_{yield}**	**Energy excited state (cm^{-1})**
^{22}Ir•pypz•3PF$_6$	440	**RT** 553 **77 K** -	**RT (in air)** τ_1=1100 **degassed** τ_1= 2000 (91%), τ_2=74 (6%), τ_3 = 10 (3%). **77 K** τ_1= 1560 (67%), τ_2=175 (33%)	0.16	16.806
^{23}Ir•pypz•3PF$_6$	315	**RT** 490 **77 K** 480	**RT (in air)** τ_1=83 (82%), τ_2=264 (18%) **degassed** τ_1= 2000 ± 20 (97%).* **77 K** τ_1= 250 (95%),* τ_2= <5ns.	0.27	20.833
^{24}Ir•pypz•3PF$_6$	320	**RT** 495 **77 K** 480	**RT (in air)** τ_1=83 (84%), τ_2=303 (16%). **Degassed** τ_1=217(83%), τ_2=659(16%). **77 K** τ_1=234 (97%), τ_2=6 (3%).	0.6	20.833

- a small contribution from the short-lived component is due to scattering of the excitation wavelength,
*** Minor component.**

Part Three

4.5.3 Series of ^{N,N}Ir•L$^{bi\text{-}ph}$•3PF$_6$ complexes

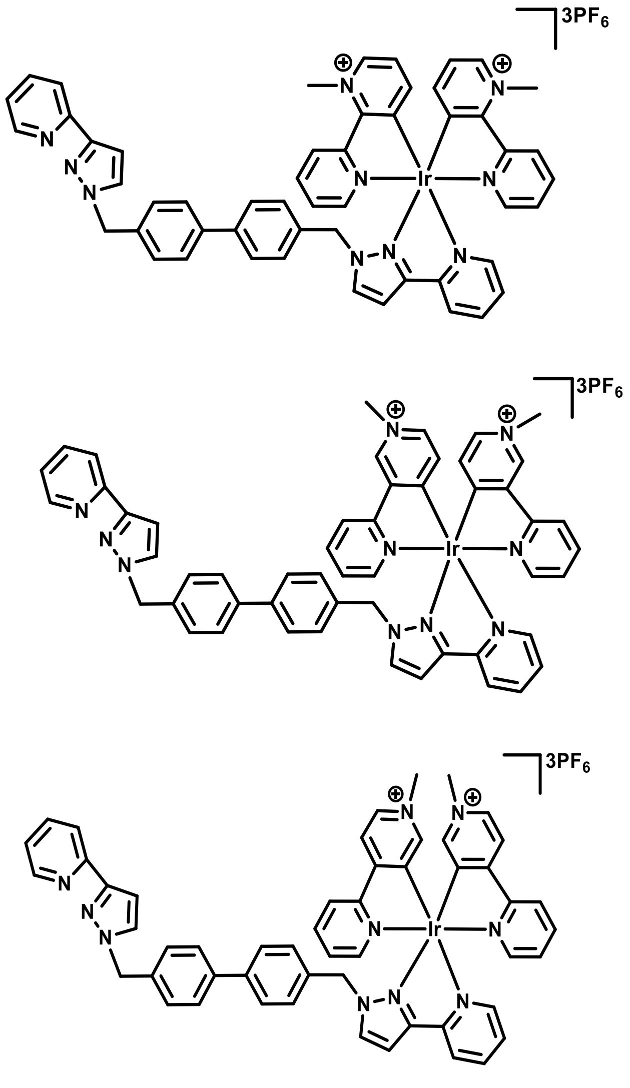

Figure 4-19 Chemical structures of complexes ^{22}Ir•L$^{bi\text{-}ph}$•3PF$_6$ (top), ^{23}Ir•L$^{bi\text{-}ph}$•3PF$_6$ (middle) and ^{24}Ir•L$^{bi\text{-}ph}$•3PF$_6$ (bottom).

This part of the work aims to prepare d/f dyads, based on the new Ir(III) chromophores with *N*-methyl-bipyridinium cyclometallating ligands (**Figure** 4-19), to study the d-f energy transfer and how it varies based on the nature and position of the substitution pattern on the cyclometalating C^N ligands. To do this, we use the bridging ligand L$^{bi\text{-}ph}$, such that the Ir(III) complexes have a vacant coordination site to which can be attached Eu(hfac)$_3$, Tb(hfac)$_3$ or Gd(hfac)$_3$ units.

4.5.3.1 UV-Vis spectroscopy of the ^{N,N}Ir•L$^{bi\text{-}ph}$•3PF$_6$ complexes.

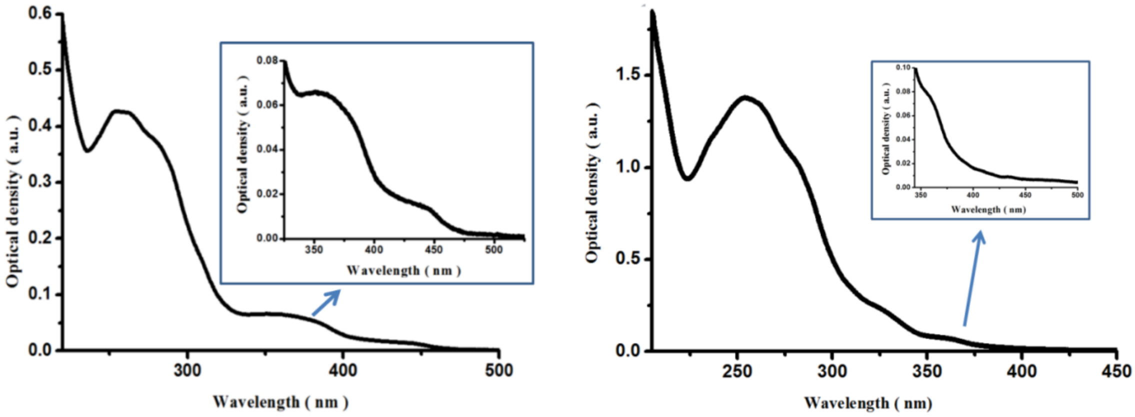

UV/Vis spectrum of ^{22}Ir•L$^{bi\text{-}ph}$•3PF$_6$

UV/Vis spectrum of ^{23}Ir•L$^{bi\text{-}ph}$•3PF$_6$

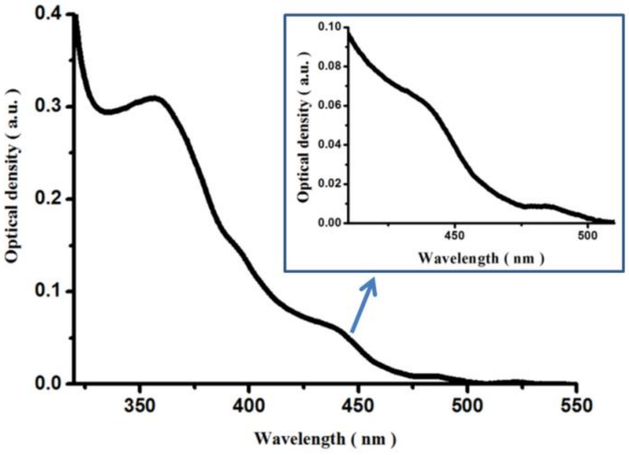

UV/Vis spectrum of ^{24}Ir•L$^{bi\text{-}ph}$•3PF$_6$

Figure 4-20 (1) Top: Absorption spectra of ^{22}Ir•L$^{bi\text{-}ph}$•3PF$_6$, ^{23}Ir•L$^{bi\text{-}ph}$•3PF$_6$ and ^{24}Ir•L$^{bi\text{-}ph}$•3PF$_6$ measured in MeCN at 298 K.

The UV/Vis absorption spectra of all three ^{N,N}Ir•L$^{bi\text{-}ph}$•3PF$_6$ complexes series were measured in MeCN at room temperature. The spectra are shown in **Figure** 4-20 and summarised in **Table 4-8**. They show the usual combination of high-energy ligand-centred transitions and lower-energy transitions in the 400 – 500 nm region. The spectra of the complexes ^{22}Ir•L$^{bi\text{-}ph}$•3PF$_6$, ^{24}Ir•L$^{bi\text{-}ph}$•3PF$_6$ have absorption bands, that are assigned to $^1\pi$-π* and ^{1}MLCT electronic transitions of both C^N and N^N ligands.

Overall, some variations were detected for the electronic absorption of ^{22}Ir•L$^{bi\text{-}ph}$•3PF$_6$, ^{23}Ir•L$^{bi\text{-}ph}$•3PF$_6$ and ^{24}Ir•L$^{bi\text{-}ph}$•3PF$_6$ complexes, in terms of intensities and transition energies, due to different $^+$N-CH$_3$ substitution position in the C^N phenyl ring. All data obtained will be contrasted later with the previously-reported $^{F/F}$Ir•L$^{bi\text{-}ph}$•3PF$_6$ complex which has the same ancillary ligand L$^{bi\text{-}ph}$ but a more convention fluorinated phenyl-pyridine cyclometallating ligand.[12]

Table 4-8 UV/Vis. information of ^{22}Ir•L$^{bi\text{-}ph}$•3PF$_6$, ^{23}Ir•L$^{bi\text{-}ph}$•3PF$_6$ and ^{24}Ir•L$^{bi\text{-}ph}$•3PF$_6$ complexes in MeCN at 298 K.

$^{N/N}$Ir•L$^{bi\text{-}ph}$•3PF$_6$ complexes	**λ (nm) / ε (L.mol^{-1}.cm^{-1})**
^{22}Ir•L$^{bi\text{-}ph}$•3PF$_6$	252 (2481), 283 (2244), 360 (430), 445 (120), 493 (20)
^{23}Ir•L$^{bi\text{-}ph}$•3PF$_6$	255 (3500), 325 (4000), 360 (1240)
^{24}Ir•L$^{bi\text{-}ph}$•3PF$_6$	355 (3300), 397 (2600), 435 (1200), 485 (360)

4.5.3.2 Luminescence of tricationic ^{N,N}Ir•L$^{bi\text{-}ph}$•3PF$_6$ complexes

All mononuclear $^{N/N}$Ir•L$^{bi\text{-}ph}$•3PF$_6$ complexes in this chapter have been investigated to see if their luminescent excited states are energetic enough to sensitise the luminescence from Eu(III) and, if possible, Tb(III) emissive excited states at room temperature. The $^{N/N}$Ir•L$^{bi\text{-}ph}$•3PF$_6$ complexes have been prepared as described above with different substitution patterns of the quaternised N atom in the *N*-methyl-bipyridinium ligands, to probe the effect of this substitution pattern on the energy-transfer capabilities of the Ir units. The addition of electron-withdrawing substituents (typically F atoms or CF$_3$ groups) at different positions on the cyclometallating phenylpyridine ligands in their Ir(III) complexes chromophore complex is commonly utilised to alter the triplet energy of the excited state by changing the ligand-centred orbital energies.[6] Therefore, the variation of electron-withdrawing substituents on the cyclometallating ligands allows d-f energy transfer to be controlled.

4.5.3.2.1 Emission spectroscopy study of $^{N/N}$Ir•L$^{bi\text{-}ph}$•3PF$_6$

The luminescence spectrum and lifetimes of $^{N/N}$Ir•L$^{bi\text{-}ph}$•3PF$_6$ complexes were recorded in oxygenated and deoxygenated MeCN at room temperature and also at 77K in a EtOH-MeOH glass. The spectra are depicted in **Figure** 4-21 below, with all photophysical properties summarized in **Table** 4-9.

The excitation wavelengths for each complex were in the low-energy ^{3}MLCT region. The emission spectra, both at room temperature and 77K, show a significant fine structuring characteristic of a vibronic progression which is typical of emission from a ^{3}LC excited state (while with the broad, featureless bands observed earlier are more indicative of MLCT-based excited states),[6,20,21] The highest-energy luminescence features of ^{22}Ir•L$^{bi\text{-}ph}$•3PF$_6$, ^{23}Ir•L$^{bi\text{-}ph}$•3PF$_6$ and ^{24}Ir•L$^{bi\text{-}ph}$•3PF$_6$ occur at 524, 440 and 512 nm, respectively, with ^{23}Ir•L$^{bi\text{-}ph}$•3PF$_6$ clearly having a much higher-energy excited state than the other two isomers. From the emission spectra at 77K could be investigated the triplet excited state energy of each complex: the highest-energy emission features in the 77K emission spectrum which give the 0-0 energy of the ^{3}MLCT emissive states are 19,531, 22,727 and 19,493 cm^{-1} for ^{22}Ir•L$^{bi\text{-}ph}$•3PF$_6$, ^{23}Ir•L$^{bi\text{-}ph}$•3PF$_6$ and ^{24}Ir•L$^{bi\text{-}ph}$•3PF$_6$ respectively. For comparison the previously-published analogue $^{F/F}$Ir•L$^{bi\text{-}ph}$•PF$_6$ (based on a fluorinated phenylpyridine ligand) has an excited-state energy of 21,978 cm^{-1}.[12]

In air-equilibrated MeCN at room temperature, the luminescence lifetimes for ^{22}Ir•L$^{bi\text{-}ph}$•3PF$_6$ and ^{24}Ir•L$^{bi\text{-}ph}$•3PF$_6$ are quite long at 1700 ns and 1620 ns respectively, which have good fit of the luminescence decay data to a single exponential component in each case. While the more intense luminescence from ^{23}Ir•L$^{\text{bi-ph}}$•3PF$_6$ displays a similar lifetime of 1500 ns under these conditions (**Table** 4-9**)**. Degassing the solutions increase the lifetimes further, with all being in the region of 2 µs as list in **Table** 4-9**.**

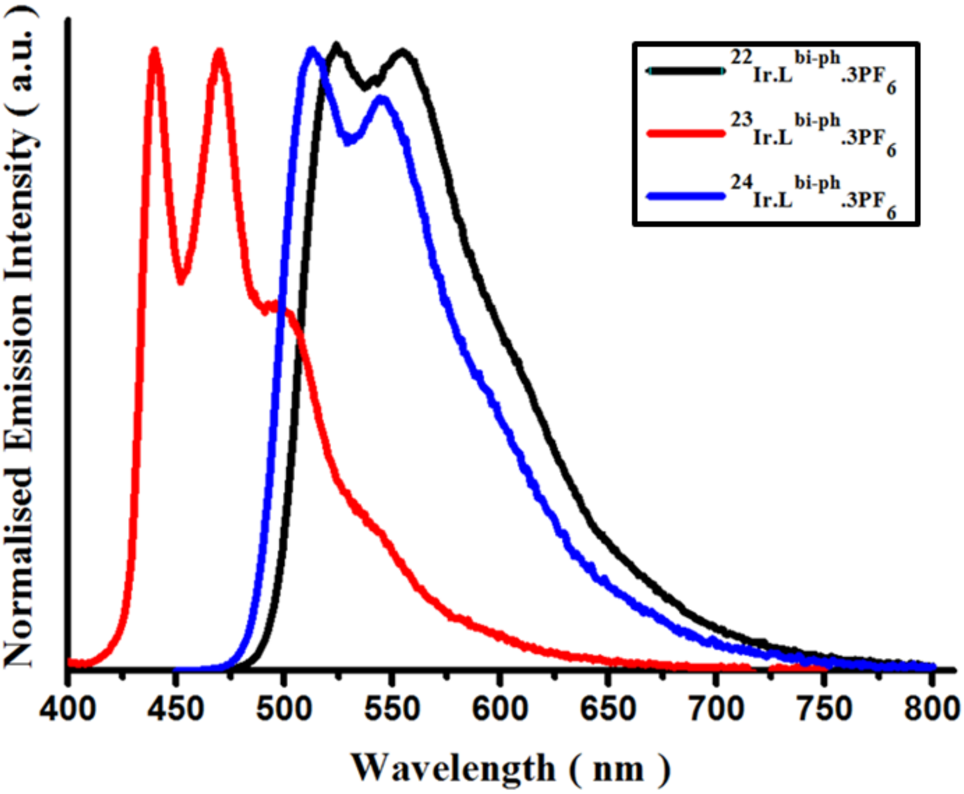

Figure 4-21 Overlapping, normalised emission spectra of ^{22}Ir•L$^{\text{bi-ph}}$•3PF$_6$ with λ_{exc} at 360 nm, ^{23}Ir•L$^{\text{bi-ph}}$•3PF$_6$ with $\lambda_{\text{exc.}}$ at 360nm and ^{24}Ir•L$^{\text{bi-ph}}$•3PF$_6$ with $\lambda_{\text{exc.}}$ at 435nm. All emissions measured at 298 K in MeCN.

Table 4-9 Summary of photophysical properties of $^{N/N}$Ir•L$^{bi\text{-}ph}$•3PF$_6$ complexes in MeCN solvent at 298 K. Quantum yield calculated relative to Pt(N^C^N)Cl complex.[22]

$^{N/N}$Ir•L$^{bi\text{-}ph}$•3PF$_6$ complexes	**$\lambda_{Ex.}$ (nm)**	**$\lambda_{max.}$(nm)**	**τ (ns) <± 50**	**ϕ**	**Energy excited state (cm^{-1})**
^{22}Ir•L$^{bi\text{-}ph}$•3PF$_6$	360	**RT** 524 **77 K** 519	**RT (in air)** τ_1=1700 **degassed** τ_1=2225 **77 K** τ_1=2520 (83%), τ_2=6 (17%)	0.01	19.531
^{23}Ir•L$^{bi\text{-}ph}$•3PF$_6$	360	**RT** 440 **77 K** 440	**RT (in air)** τ_1=1500 **degassed** τ_1=2910 **77 K** τ_1=1587 (97%), τ_2=150 (<3%)	0.054	22.727
^{24}Ir•L$^{bi\text{-}ph}$•3PF$_6$	435	**RT** 512 **77 K** 513	**RT (in air)** τ_1=1620 **degassed** τ_1=2000 **77 K** τ_1=2000	0.07	19.493

To conclude, incorporation of $^{+}$N-CH$_3$ electron-withdrawing substituents into a cyclometallating N/C ligand gives a high-energy excited state, comparable in some cases to that given by fluorinated phenylpyridine ligands. The excited state energies and long emission lifetimes of these Ir(III) complexes suggest that they might be able to sensitise luminescence from Eu(III) and Tb(III) in d/f dyads. The difference in the structure emission of $^{N/N}$Ir•L$^{bi\text{-}ph}$•3PF$_6$ could be related to the combination between ^{3}LC with possible some of ^{3}MLCT character, while in structureless emission of $^{N/N}$Ir•pypz•3PF$_6$ related to ^{3}MLCT character.

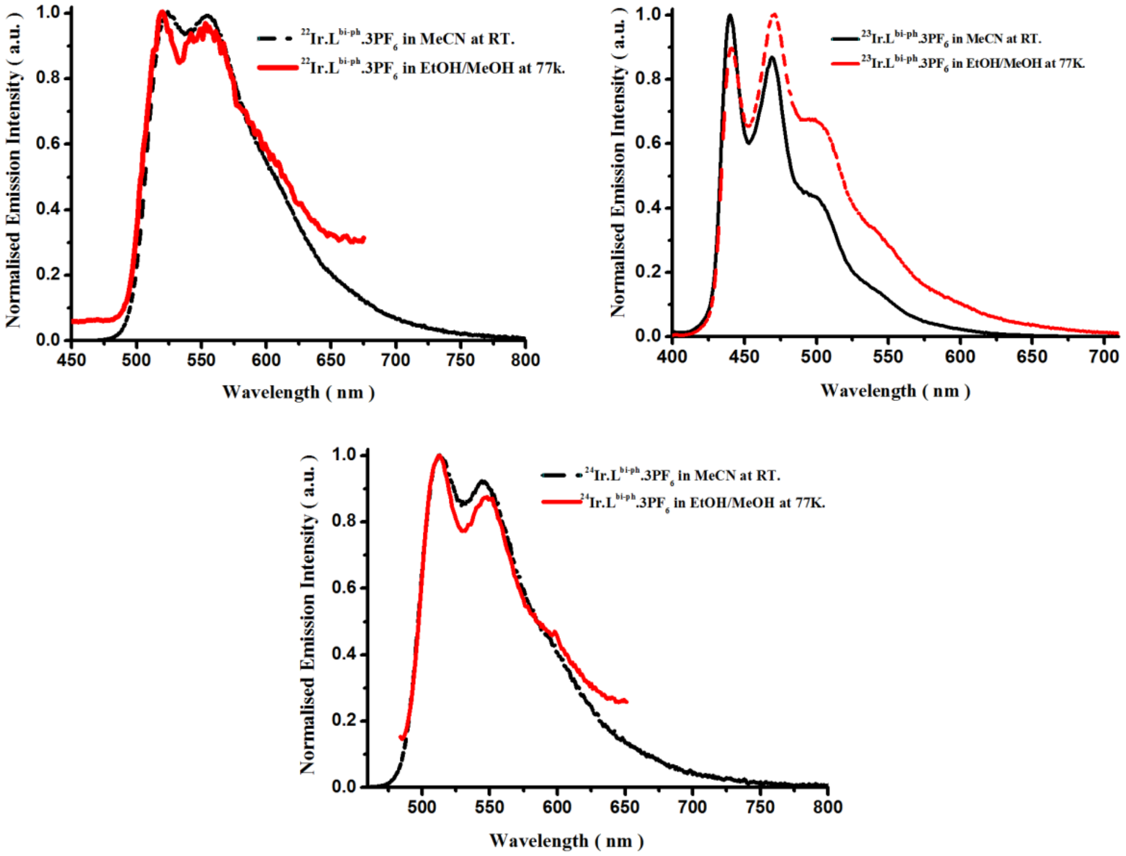

Figure 4-22 Normalised at 298 K and 77K emission spectra of ^{22}Ir•L$^{bi\text{-}ph}$•3PF$_6$, ^{23}Ir•L$^{bi\text{-}ph}$•3PF$_6$ and ^{24}Ir•L$^{bi\text{-}ph}$•3PF$_6$ complexes.

In the frozen glassy solvent EtOH/MeOH (4:1), there is almost no change in the emission spectra compared to fluid solution (in MeCN). This lack of rigidichromism implies an excited state with no charge-transfer character, *i.e.* a ^{3}LC excited state (the fine structure of the emission is also consistent with this). This is shown in **Figure** 4-22 which spectra at room temperature and at 77K are superimposed.

4.6 Titration of $^{N/N}$Ir•L$^{bi\text{-}ph}$•3PF$_6$ with Ln(hfac)$_3$•2H$_2$O and the photopysical properties of the Ir/Ln dyads.

As noted above the photophysical properties of the three complexes $^{N/N}$Ir•L$^{bi\text{-}ph}$•3PF$_6$ differ from one another because of the different pattern of substitution of the *N*-methyl-pyridinium withdrawing group on the cyclometallating ligands. Titration of $^{N/N}$Ir•L$^{bi\text{-}ph}$•3PF$_6$ complexes with Ln(hfac)$_3$•2H$_2$O, when Ln = Eu, Tb and Gd, wil allow formation of Ir•Ln dyads by coordination of the Ln(hfac)$_3$ unit to the vacant pypz site (**Figure** 4-23), so allows us to investigate how the substitution pattern affects Ir-Ln energy-transfer.[23,24] The emissive levels of these Ln(III) ions lie at ≈ 17300 cm^{-1} for Eu(III), at ≈ 20400 cm^{-1} for Tb(III) and at > 30000 cm^{-1} for Gd(III),[12] which therefore acts as a non-emissive control.[13]

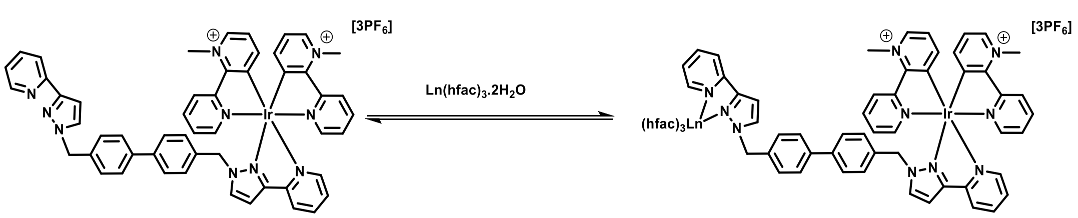

Figure 4-23 Titration of ^{22}Ir•L$^{bi\text{-}ph}$•3PF$_6$ with Ln(hfac)$_3$•2H$_2$O (Ln = Eu, Tb, Gd) in MeCN at 298 K. Also ^{23}Ir•L$^{bi\text{-}ph}$•3PF$_6$ and ^{24}Ir•L$^{bi\text{-}ph}$•3PF$_6$ complexes follow the same reaction when titrated with Ln(hfac)$_3$•2H$_2$O.[10]

4.6.1 Titration of $^{N/N}$Ir•L$^{bi\text{-}ph}$•3PF$_6$ with Eu(hfac)$_3$•2H$_2$O

Portions of stock solution (~ 10^{-4}-10^{-3} M) of Eu(hfac)$_3$•2H$_2$O salt was titrated with (~ 10^{-5}-10^{-4} M) $^{N/N}$Ir•L$^{bi\text{-}ph}$•3PF$_6$ in MeCN at room temperature. An Eu(hfac)$_3$ unit ends up being bound to the pypz binding site to generate an Ir•Eu dyad. The excitation wavelengths used for each Ir•Eu complex are summarised on **Table 4-10** and involve excitation into the Ir-based absorption manifold. This means that absorption at the excitation wavelength is solely into the Ir(III) chromophore and remains constant during the titration, such that changes in luminescence intensity indicate real changes in emission quantum yield. This also means that any emission observed from Eu(hfac)$_3$ can only arise as a result of Ir(III)→Eu(III) energy transfer because free Eu(hfac)$_3$•2H$_2$O in the equilibrium (**Figure** 4-24) does not absorb any excitation light.

As the Eu(hfac)$_3$ unit coordinates to give the Ir•Eu dyads, in all three cases we see progressive quenching of the Ir(III) emission accompanied by growing in Eu(III) emission, which confirms the occurrence of Ir-Eu energy-transfer. We assume that this is principally the Dexter mechanism which requiers donor - acceptor orbitals overlap, because of connection Ir(III) and Eu(III) units via a biphenyl conjucated bridging ligand which facilitates the electronic coupling process through the orbitals of the bridging linker ligand,[11,12] as observed previously by Ward's group.[10]

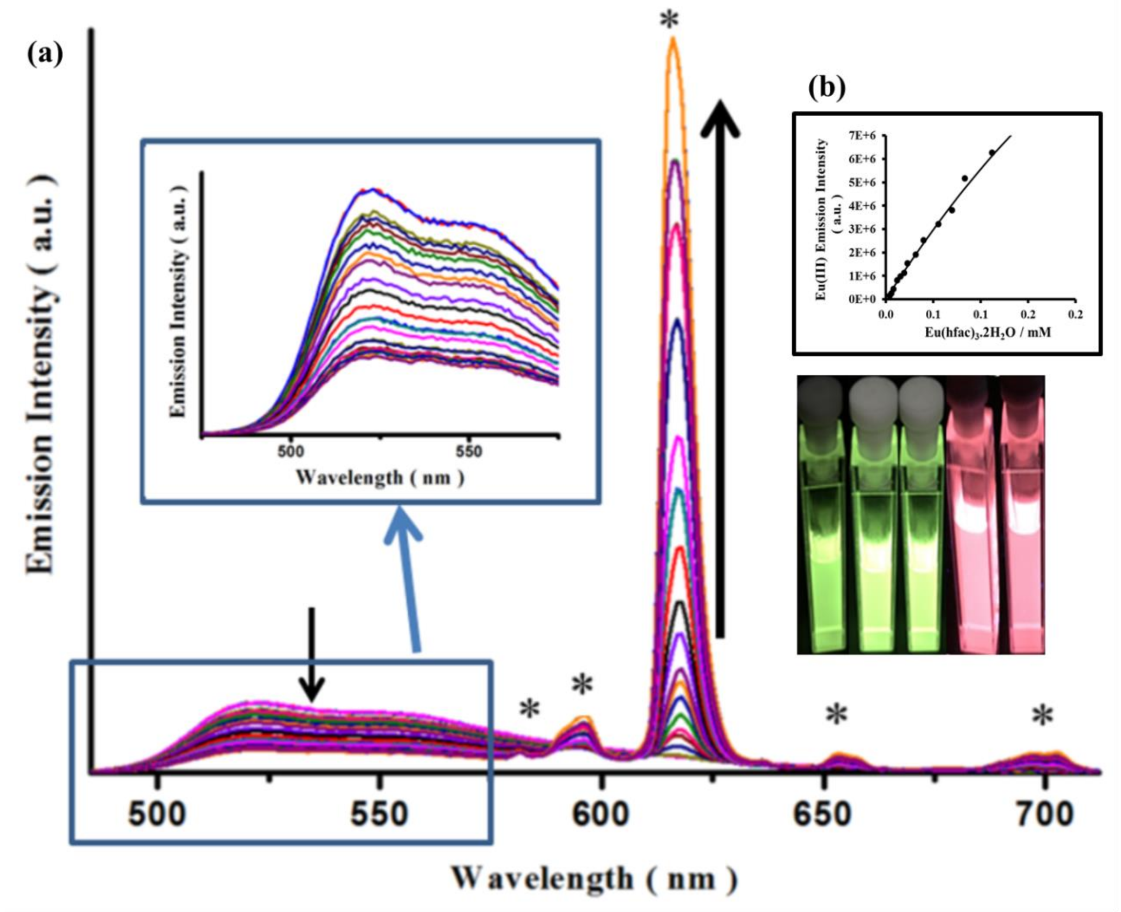

Figure 4-24 (a) Luminescence titration of ^{22}Ir•L^{bi-ph}•3PF$_6$ with Eu(hfac)$_3$•2H$_2$O in MeCN, at 298 K and excitation at 360 nm, showing steady quenching of Ir-based emission and appearance of sensitised Eu-based emission the dyad ^{22}Ir•L^{bi-ph}•Eu forms. Inset the Ir-based quenching in region 460 – 585 nm and the colour changing from green, which represents Ir(III)-based emission under a hand UV- lamp, to red which represents Eu(III)-based emission. (b) Fitting of a 1:1 binding isothermal for the binding of ^{22}Ir•L^{bi-ph}•3PF$_6$ with Eu(hfac)$_3$ in MeCN, K$_a$= 1×10^4 M^{-1}.

As the ^{22}Ir•L^{bi-ph}•Eu complex is formed due to the titration, the Ir(III)-based emission between 460 and 585 nm is gradually quenched, and this decrease was accompanied by increasing Eu(III) emission in the 585-725 nm region attributed to the transitions $^5D_0 \rightarrow {}^7F_n$. Quenching of Ir(III)-based emission was completed after addition of *ca.* 9 equiv. of [Eu(hfac)$_3$(H$_2$O)$_2$], and resulted in a 65% loss of intensity because of Ir-Eu energy transfer providing an additional deactivation pathway.

During the titration, the Ir-based emission lifetime was recorded (using a band pass filter in the range 525-575 nm to prevent interference from Eu(III) emission). The decay profile was best fitted to two exponential components $\tau \approx$1100 ns (97%) and 580 ns (3%), possibly indicating that there are two different conformers of ^{22}Ir•L$^{bi\text{-}ph}$•Eu complex with two energy transfer rate constant 3.3×10^5 s^{-1} and 4.6×10^5 s^{-1}. The energy transfer was calculated based on the **eq. (4-1).**[10]

$$\mathbf{k_{EnT} = 1/\tau_q - 1/\tau_{uq}} \qquad \textbf{eq. (4-1)}$$

K_{EnT} : Rate constant energy transfer.
τ_q : Quenched Ir-based lifetime of Ir(III)/Eu(III) dyad.
τ_{uq} : Unquenched Ir-based lifetime of Ir(III)/Gd(III) dyad.

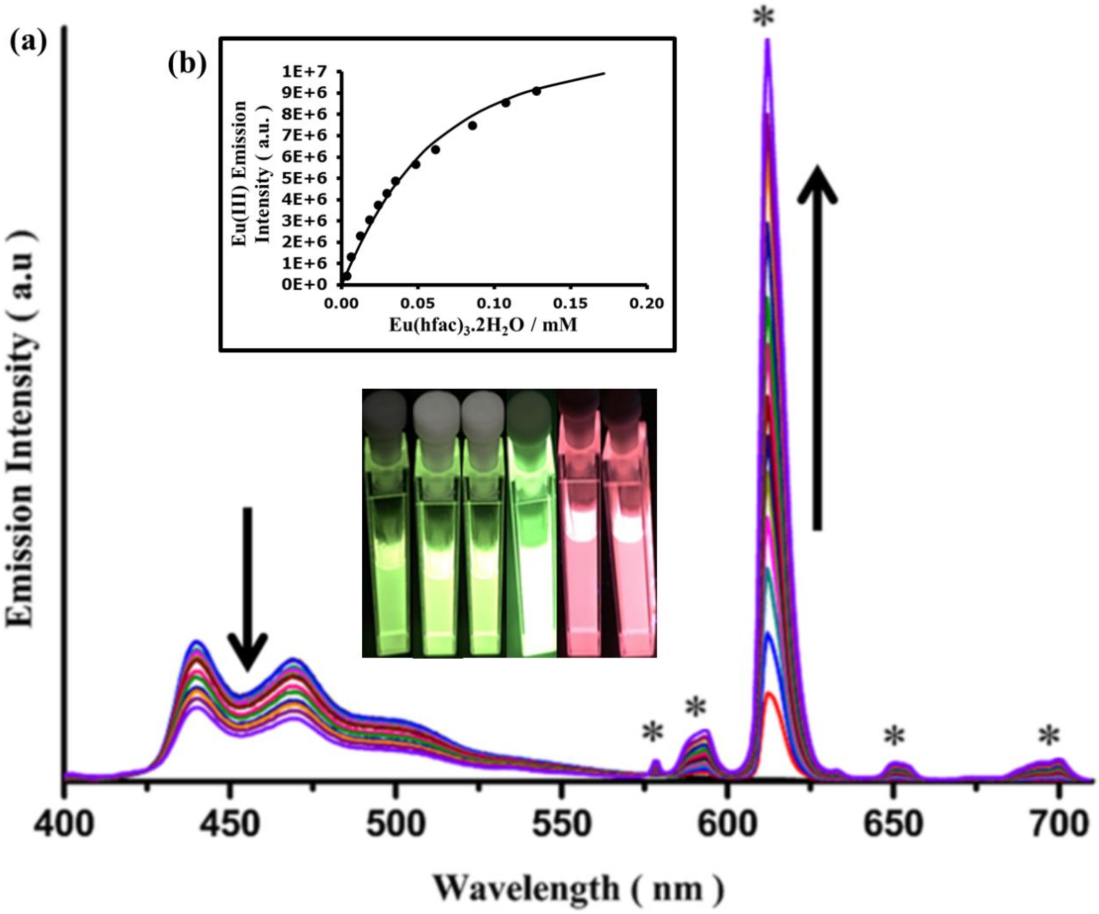

Figure 4-25 (a) Results of luminescence titration of ^{23}Ir•L^{bi-ph}•3PF$_6$ with Eu(hfac)$_3$•2H$_2$O in MeCN, at 298 K using excitation at 360 nm, showing steady Ir-based quencging and appearance of sensitised Eu-based emission as the ^{23}Ir•L^{bi-ph}•Eu dyad is formed (b) Fitting binding isothermal curve in a ratio 1:1 for ^{23}Ir•L^{bi-ph}•3PF$_6$ with Eu(hfac)$_3$•2H$_2$O with K$_a$ = 3.1×10^4 M^{-1}.

Titration of ^{23}Ir•L$^{\text{bi-ph}}$•3PF$_6$ (3.9×10^{-5}M) with Eu(hfac)$_3$(H$_2$O)$_2$ (6.2×10^{-4}M) was performed in exactly the same way in MeCN solution. The same result was observed with steady quenching of Ir-based emission intensity in the 425 – 550 nm region, and steady increase in the Eu(III)-based emission intensity in the 575-725 nm region (**Figure** 4-25). No further significant changes were observed after addition 6 equiv. of Eu(hfac)$_3$(H$_2$O)$_2$. At the end of titration the perecentage of the Ir(III) based emission was reduced approximately 60% due to Ir→Eu energy transfer in the dyads.

Time-resolved measurements of the Ir-based emission were again performed in the region 475 – 525 nm using a bandpass filter. The decay profile fitted to a single exponential lifetime with τ_1 = 1370 ns (a short-lived ocmponent of <2% of total emission was ignored as likely due to light scattering). On this basis, the Ir-Eu energy transfer rate was calculated as $K = 1.8\times10^5$ s^{-1} in these dyads.

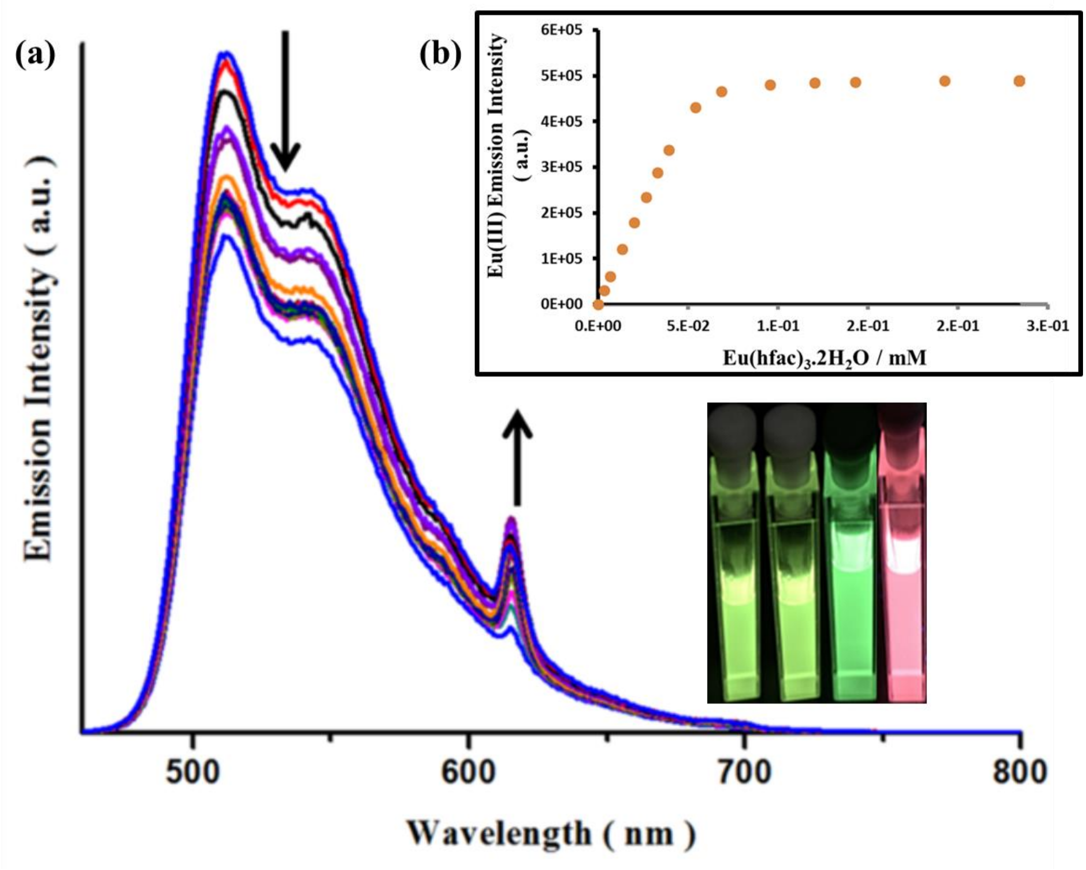

Figure 4-26 (a) Results of luminescence titration of ^{24}Ir•L$^{\text{bi-ph}}$•3PF$_6$ with Eu(hfac)$_3$•2H$_2$O in MeCN, at 298 K and excitation at 435 nm, showing partial quenching of the Ir-based emission and very slight sensitised Eu-based emission at 615 nm as the ^{24}Ir•L$^{\text{bi-ph}}$•Eu dyad forms.

The ^{24}Ir•L^{bi-ph}•Eu dyad was formed by titration of Eu(hfac)$_3$(H$_2$O)$_2$ (7.0×10^{-4}M) into a solution of ^{24}Ir•L^{bi-ph}•3PF$_6$ (5.4×10^{-5}M) complex in MeCN (**Figure** 4-26**)**. Again quenching Ir(III)-based emission between 480 and 590 nm was monitored. Interestingly, the efficiency of sensitisation of Eu(III) is clearly very weak compared what was observed with ^{22}Ir•L^{bi-ph}•3PF$_6$ and ^{23}Ir•L^{bi-ph}•3PF$_6$ which showed much stronger Eu-based sensitised emission. The Ir(III) emission intensity was reduced by only 20% after addition of 5 equivalents of Eu(hfac)$_3$(H$_2$O)$_2$. Changes in the Ir-based lifetime before and after addition of the Eu(III) unit were too small to reliably calculate an energy transfer rate constant. However, there is a clear evidence of some Ir-Eu energy-transfer from the appearance of Eu(III) sensitised emission.

We can explain the differences between the energy-transfer efficiencies by considering the energy of the Ir-based excited state in each case. The complex ^{23}Ir•L^{bi-ph}•3PF$_6$ has the highest ^{3}Ir state energy *ca.* 22727 cm^{-1}, which easily sensitised Eu(III)-based emission (excited-state energy level at ca. 17500 cm^{-1}. A ^{22}Ir•L^{bi-ph}•3PF$_6$ also acts as a good sensitizer to Eu(III) emission, with the ^{3}Ir excited state energy of *ca.* 19531 cm^{-1}. Although ^{22}Ir•L^{bi-ph}•3PF$_6$ and ^{24}Ir•L^{bi-ph}•3PF$_6$ complexes have basically the same excited state energy *ca.* 19500 cm^{-1} with identical spacer but unexpected behaver sensitisation of Eu(III) emission was observed. The titration spectra show that ^{22}Ir•L^{bi-ph}•3PF$_6$ complex is a good energy donor to Eu(III) unit while ^{24}Ir•L^{bi-ph}•3PF$_6$ complex is clearly the poorest energy-donor to Eu(III). Data are summarised in **Table 4-11**.

Table 4-10. Summary of the photophysical properties of all $^{N/N}$Ir•L^{biph}•3PF$_6$ titrations with Eu(hfac)$_3$•2H$_2$O.

$^{N/N}$Ir•L^{biph}•Eu(hfac)$_3$ •3PF$_6$ complexes	λ.Exc. (nm)	eq. end of titration	[Eu] M in solution / τ (ns) < ± 50	Binding constant (M^{-1})	Energy transfer rate constant, K$_{En.T}$, (s^{-1})
^{22}Ir•L^{biph}•Eu(hfac)$_3$	360	9	0 / 1700 (start of titration) 1.1×10^{-3} / τ$_1$=1100 (97%), τ$_2$=580 (3%) (end of titration)	1×10^4	3.3×10^5 / 4.6×10^5
^{23}Ir•L^{biph}•Eu(hfac)$_3$	360	6	0 / 1370 (start of titration) 1.7×10^{-4} / 849 (end of titration)	3×10^4	1.8×10^5
^{24}Ir•L^{biph}•Eu(hfac)$_3$	435	5	0 / 1600 (start of titration) 2.7 × 10^{-4} / (1600 - 1800) (end of titration) almost no change in lifetime.	Weak data to measure correct binding constant.	*

*The changes in lifetime were too small to reliably calculate K$_{En.T}$.

4.6.2 Titration $^{N/N}$Ir•L$^{bi\text{-}ph}$•3PF$_6$ with Tb(hfac)$_3$•2H$_2$O.

Having seen Ir-Eu energy-transfer to some extent in all three complexes, we were also interested to examine whether Ir-Tb energy-transfer could occur, given the higher-energy of the Tb(III) emissive excited state. The results from titration of $^{N/N}$Ir•L$^{bi\text{-}ph}$•3PF$_6$ with Tb(hfac)$_3$•2H$_2$O showed a weak sensitisation Tb(III) luminescence from ^{23}Ir•L$^{bi\text{-}ph}$•3PF$_6$ complex, whereas with ^{22}Ir•L$^{bi\text{-}ph}$•3PF$_6$ and ^{24}Ir•L$^{bi\text{-}ph}$•3PF$_6$, which have lower-energy excited states, no sensitisation was observed. The results are further supported by time-resolved measurements.

The same procedure was used as with the Ir/Eu dyads. To a solution of $^{N/N}$Ir•L$^{bi\text{-}ph}$•3PF$_6$ complexes was added small portions of Tb(hfac)$_3$•2H$_2$O to form the Ir/Tb dyad: the concentrations that used and further photophyscial information are summarised in **Table** 4-11.

4.6.3 Titration of ^{22}Ir•L^{bi-ph}•3PF$_6$, ^{23}Ir•L^{bi-ph}•3PF$_6$ and ^{24}Ir•L^{bi-ph}•3PF$_6$ with Tb(hfac)$_3$•2H$_2$O.

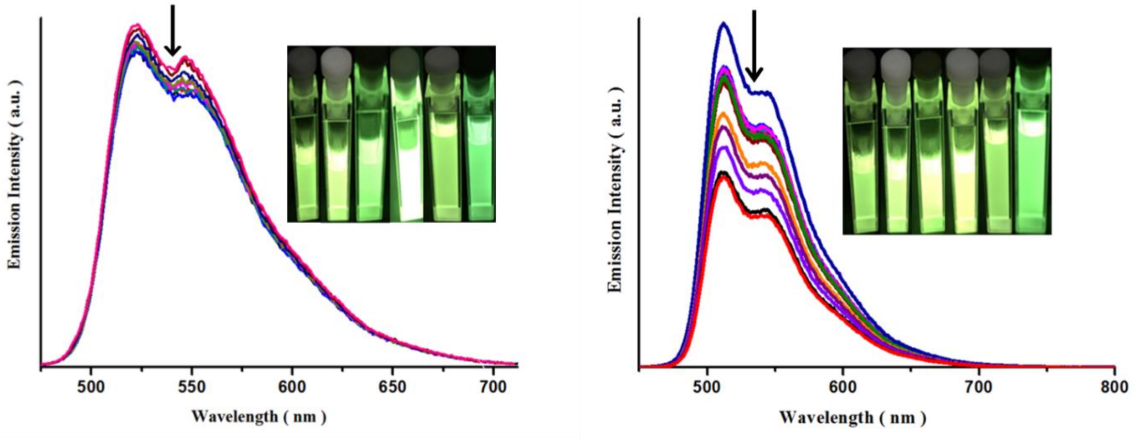

^{22}Ir•L^{bi-ph}•Tb **^{24}Ir•L^{bi-ph}•Tb**

Figure 4-27 Results of luminescence titrations of ^{22}Ir•L^{bi-ph}•3PF$_6$ and ^{24}Ir•L^{bi-ph}•3PF$_6$ with Tb(hfac)$_3$•2H$_2$O in MeCN, at 298 K using excitation at 360 nm and 435nm, respectively, showing no sensitisation of Tb-based emission in the Ir/Tb dyads.

As illustrated in **Figure** 4-27, with ^{22}Ir•L^{bi-ph}•3PF$_6$ and ^{24}Ir•L^{bi-ph}•3PF$_6$ there is some quenching of Ir-based emission (by approximately 20% and 40 % respectively) when the Ir/Tb dyads form, but there is no sensitisation of the Tb(III) emission with no evidence for the characteristic sharp Tb-based emission lines appearing. This indicates that the energy gap between the ^{3}Ir energy state for ^{22}Ir•L^{bi-ph}•3PF$_6$ and ^{24}Ir•L^{bi-ph}•3PF$_6$ and the emissive level of Tb(III) is too small for energy-transfer to occur. Energy transfer at room temperature requires a donor/acceptor gradient of about ~1700 cm^{-1} to achieve the energy transfer process successfully.[12] The ^{3}Ir energy excited state at 19531, 19493 cm^{-1} for ^{22}Ir•L^{bi-ph}•3PF$_6$ and ^{24}Ir•L^{bi-ph}•3PF$_6$ complexes, respectively, means that these excited states lie about 900 cm^{-1}, respectively, below the Tb(III) emissive excited state which is not enough to sensitise Tb(III) luminescence and prevent back energy transfer. However, some quenching of the ^{3}Ir energy state emission was observed could be attributed to some PET process because the pypz unit coordinated to a Ln(III) ion is a good electron-acceptor.[10]

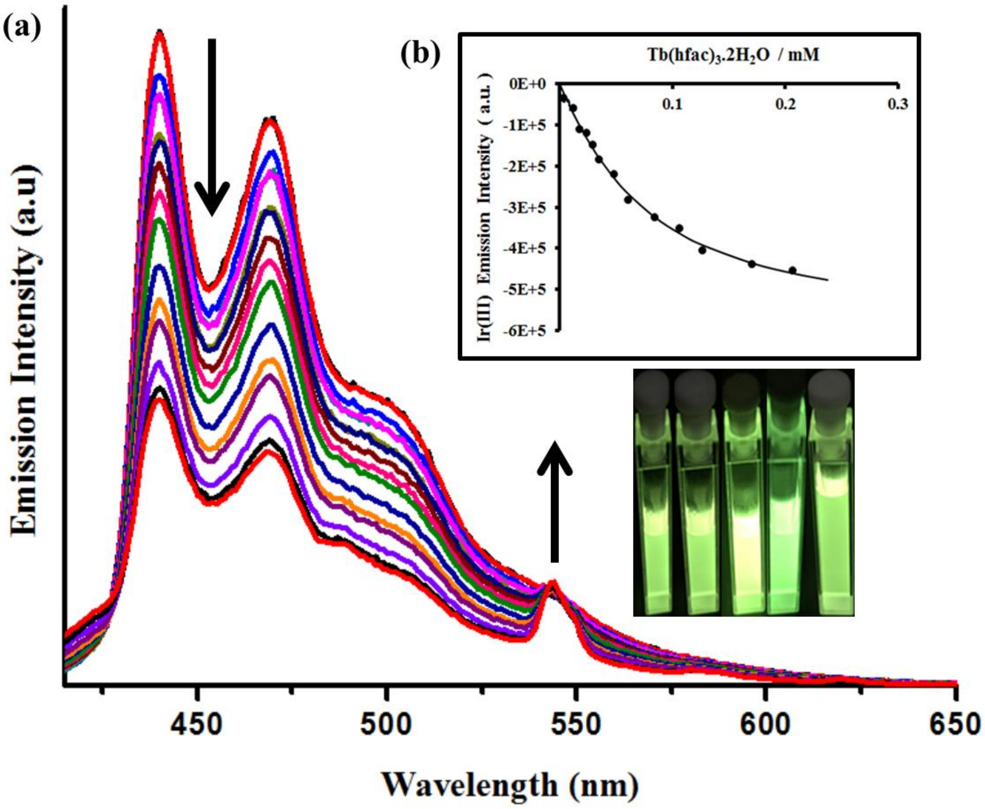

Figure 4-28 Results of luminescence titration of ^{23}Ir•L$^{bi\text{-}ph}$•3PF$_6$ with Tb(hfac)$_3$•2H$_2$O in MeCN, at 298 K and with excitation at 360 nm, showing weak sensitisation of Tb-based emission and quenching of Ir-based emission, as the ^{23}Ir•L$^{bi\text{-}ph}$•Tb dyad is formed.

With the complex ^{23}Ir•L$^{bi\text{-}ph}$•3PF$_6$ (**Figure** 4-28), however, we see some sensitisation of the Tb(III) emission with a weak signal apparent at 545 nm, which is the main Tb-based ^{5}D$_4$ – ^{7}F$_5$ transition, supermiposed on the tail end of the residual Ir-based emission. The titration process was completed after addition of ~ 6 equiv. of Tb(hfac)$_3$•2H$_2$O with no further luminescence changes occurring. Because of the higher energy excited state of ^{23}Ir•L$^{bi\text{-}ph}$•3PF$_6$ complex which now lies well above the ^{5}D$_4$ emissive state, there is weak sensitisation of the Tb(III) luminescence. The degree of quenching ^{3}Ir excited state emission in ^{23}Ir•L$^{bi\text{-}ph}$•Tb(hfac)$_3$ is greater than ^{22}Ir•L$^{bi\text{-}ph}$•Tb(hfac)$_3$ and ^{24}Ir•L$^{bi\text{-}ph}$•Tb(hfac)$_3$ dyads in agreement with the presence of the additional Ir-Tb energy-transfer pathway. Time-resolved measurements was recorded during the titration by using the 475 - 525 nm bandpass filter. The resulting dominant lifetime component of 635 ns indicates an Ir-Tb energy transfer rate constant of 7.5×10^5 s^{-1}. The triplet excited state energy of the ^{23}Ir•L$^{bi\text{-}ph}$•3PF$_6$ unit *ca.* 22700 cm^{-1} is just high enough to achieve partial Ir-Tb energy-transfer at room temperature, probably (as we have oberved before) by the Dexter mechanism.

Table 4-11 A result summary of the photophysical properties of all $^{N/N}$Ir•L$^{bi\text{-}ph}$•3PF$_6$ titrations with Tb(hfac)$_3$•2H$_2$O.

$^{N/N}$Ir•L$^{bi\text{-}ph}$•Tb(hfac)$_3$ complexes	**λ. Excitation (nm)**	**eq. end of titration**	**[Eu] M in solution / τ (ns) < ± 50**	**Energy transfer rate constant, K$_{En.T}$, (s^{-1})**
^{22}Ir•L$^{bi\text{-}ph}$•Tb(hfac)$_3$	360	-	*	No E.T
^{23}Ir•L$^{bi\text{-}ph}$•Tb(hfac)$_3$	360	~ 6	0 / 1370 **(start of titration)** 2.4×10^{-4} / τ_1=635 (98%), τ_2= 3.5 (2%) **(end of titration)**	5.8×10^5
^{24}Ir•L$^{bi\text{-}ph}$•Tb(hfac)$_3$	435	-	*	No E.T

*Almost no change in lifetime during the titration process.

4.6.4 Control experiments: titrations of $^{N/N}$Ir•L^{bi-ph}•3PF$_6$ with Gd(hfac)$_3$•2H$_2$O

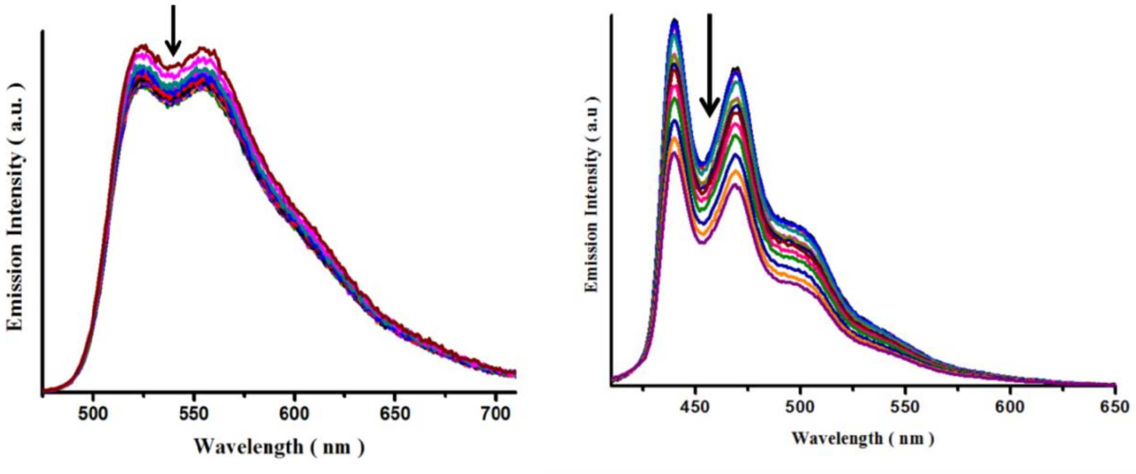

^{22}Ir•L^{bi-ph}•Gd **^{23}Ir•L^{bi-ph}•Gd**

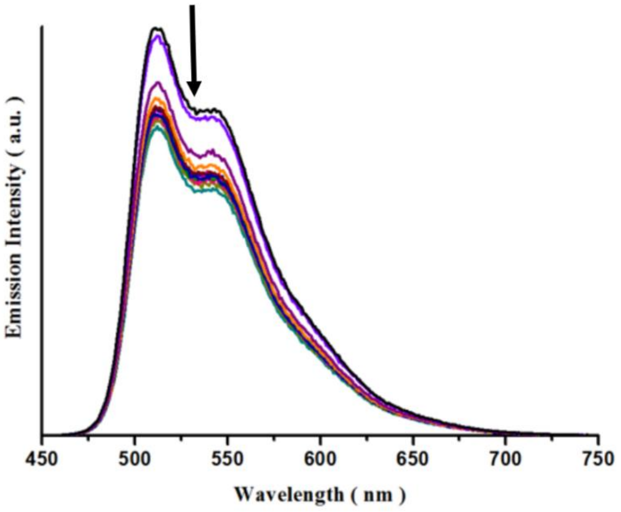

^{24}Ir•L^{bi-ph}•Gd

Figure 4-29 Results of luminescence titrations of ^{22}Ir•L^{bi-ph}•3PF$_6$, ^{23}Ir•L^{bi-ph}•3PF$_6$ and ^{24}Ir•$^{Lbi-ph}$•3PF$_6$ with Gd(hfac)$_3$•2H$_2$O in MeCN, at 298 K using excitation at 360 nm, 435 nm and 360 nm respectively, showing no sensitisation of Gd-based emission.

We performed identical titrations with Gd(hfac)$_3$•2H$_2$O to make the dyads $^{N/N}$Ir•L^{bi-ph}•Gd as control experiments: in these cases the high energy of the lowest excited state of Gd(III) cannot act as an energy-acceptor so we can see the effects of coordinating a Ln(III) ion to the pypz site without any energy-transfer occurring. **Figure** 4-29 shows the series of emission spectra of $^{N/N}$Ir•L^{bi-ph}•PF$_6$ complexes recorded during these titrations to make the Ir/Gd dyads. No energy-transfer to Gd(III) is possible, but we still see some quenching of the Ir-based emission in each case arising from some photoinduced electron-transfer from the ^{3}Ir excited state. Ward *et.al.*[25] explained the reason for this phenomenon which is that, when Gd(III) ion is bound to the vacant pypz site, that aromatic ligand becomes a good electron acceptor leading to some quenching of Ir-based emission. However the additional quenching arising from energy-transfer to a luminescent lanthanide ion is completely absent. Furthermore, the Ir-based emission lifetime recorded was a single exponential decay in each case and showed very little change compared to the starting Ir-based emission.

4.7 Conclusion

In this chapter, a new series of Ir(III) complexes is reported based on different isomers of *N*-methyl-bipyridinium C,N-donor cyclometallating ligands. The $^{N/N}IrCl_2•PF_6$, $^{N/N}Ir•pypz•3PF_6$ and $^{N/N}Ir•L^{bi-ph}•3PF_6$ complexes were clearly characterised and confirmed by electrospray mass spectroscopy and ^{1}H NMR spectroscopy.[16] Unexpectedly, the X-ray crystallography of the starting material $^{N/N}IrCl_2•PF_6$ showed that is monomeric and not the usual chloride-bridged dimer.

These Ir complexes show strong luminescence similar to what is more commonly found in complexes with fluorinated phenyl-pyridine cyclometallating ligands, indicating that the electronic effects of electron-withdrawing F substituents, and pyridnium groups, are broadly comparable.

In addition, titration of the series $^{N/N}Ir•L^{bi-ph}•3PF_6$ with Eu(III), Tb(III) and Gd(III) were performed to prepare the related Ir/Ln dyads, and investigate d→f energy transfers in a series of Ir(III)/Ln(III) dyads. The varying position substitution of the $^+N-CH_3$ group (on the cyclometalating ligands) significantly affect the energy of the lowest-energy absorptions and the luminescence, with *N*-methyl-2,3'-bipyridinium as the cyclometallating ligand giving a higher-energy excited state at the Ir(III) centre than the 2,2'- or 2,4'-isomers. The optical properties showed a red-shifted emission in both ortho- and para-$^+N-CH_3$ substituted cyclmetalating C atom. However, when the subtitution is located on *meta* to the C atom blue-shifted emission was observed.

The different excited state energies of the isomeric complexes $^{N/N}Ir•L^{bi-ph}•3PF_6$ results in different abilities to transfer energy to the emissive excited states of Eu(III) and Tb(III). Whereas all three can sensitise Eu(III)-based emission, only $^{23}Ir•L^{bi-ph}•3PF_6$ has an excited state high enough in energy to perform Ir-Tb energy transfer and generate (weak) sensitised Tb(III) emission. This is an important step to understanding the factors affecting energy transfer in Ir(III)/Ln(III) dyads.

In particular **Figure** 4-30 shows energy excited states levels of $^{23}Ir•L^{bi-ph}•3PF_6$ as energy donor, which is capable of sensitising Tb(III) luminescence. A $^{23}Ir•L^{bi-ph}•3PF_6$ has an acceptable gradient to transfer energy to Tb(III) unit.

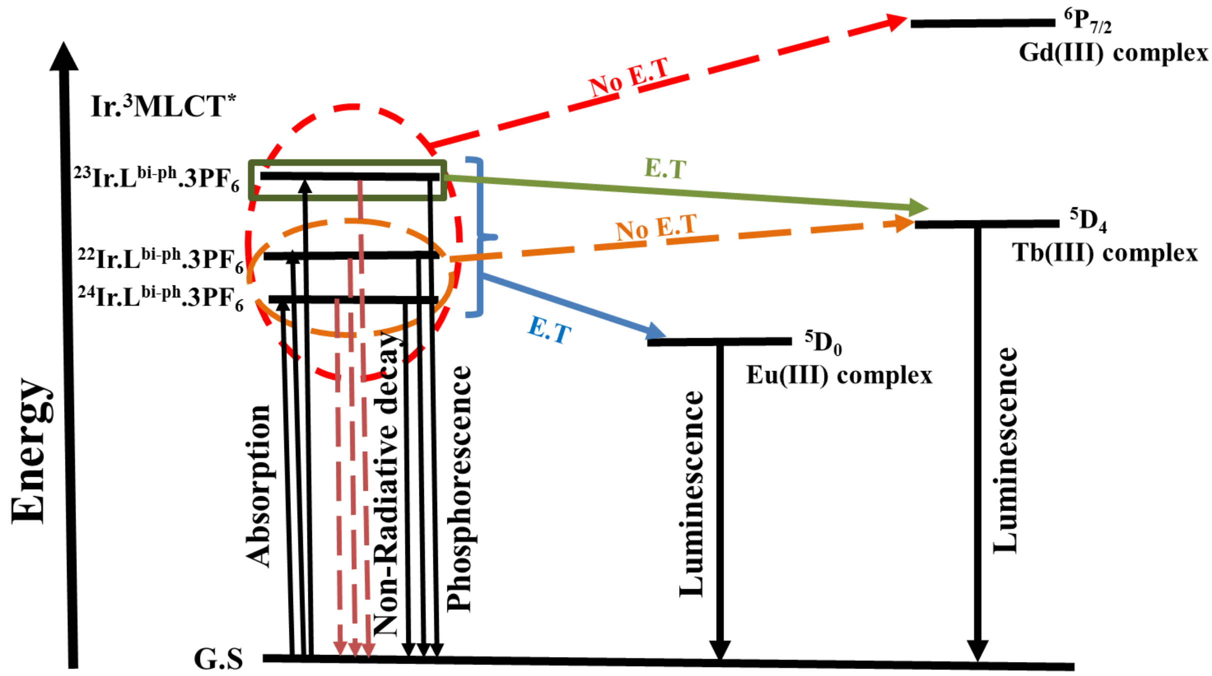

Figure 4-30 Energy level diagram of Ir/Ln dyads based on the $^{N/N}$Ir•L$^{bi\text{-}ph}$•3PF$_6$ energy donor unit connected to {Ln(hfac)$_3$} units (Ln = Eu, Tb, Gd).

4.8 References

1 Z. Yu, L. Li, H. Gao and Q. Pei, *Sci. China Chem.*, 2013, **56**, 1075–1086.

2 R. D. Costa, E. Ortí, H. J. Bolink, F. Monti, G. Accorsi and N. Armaroli, *Angew. Chemie - Int. Ed.*, 2012, **51**, 8178–8211.

3 S. B. Meier, D. Tordera, A. Pertegás, C. Roldán-Carmona, E. Ortí and H. J. Bolink, *Mater. Today*, 2014, **17**, 217–223.

4 S. Bayatpour, D. Isik and C. Santato, *J. Electron. Mater.*, 2018, **47**, 402–408.

5 K. Hasan, A. K. Bansal, I. D. W. Samuel, C. Roldán-carmona, H. J. Bolink and E. Zysman-Colman, *Sci. Rep.*, 2015, **5**, 1–16.

6 M. Kim and M. H. Lee, *J. Organomet. Chem.*, 2018, **870**, 1–7.

7 B. J. Coe, B, M. Helliwell, S. Sánchez, M. K. Peers and N. S. Scrutton, *Dalton Trans.*, 2015, **44**, 15420–15423.

8 M. D. Ward, *Coord. Chem. Rev.*, 2007, **251**, 1663–1677.

9 X. L. Li, K. J. Zhang, J. J. Li, X. X. Cheng and Z. N. Chen, *Eur. J. Inorg. Chem.*, 2010, **0**, 3449–3457.

10 D. Sykes, A. J. Cankut, N. M. Ali, A. Stephenson, S. J. P. Spall, S. C. Parker, J. A. Weinstein and M. D. Ward, *Dalton Trans.*, 2014, **43**, 6414–6428.

11 D. Sykes, I. S. Tidmarsh, A. Barbieri, I. V. Sazanovich, J. A. Weinstein and M. D. Ward, *Inorg. Chem.*, 2011, **50**, 11323–11339.

12 D. Sykes and M. D. Ward, *Chem. Commun.*, 2011, **47**, 2279–2281.

13 D. Sykes, S. C. Parker, I. V Sazanovich, A. Stephenson, J. A. Weinstein and M. D. Ward, *Inorg. Chem.*, 2013, **52**, 10500–10511.

14 K. A. McGee and K. R. Mann, *Inorg. Chem.*, 2007, **46**, 7800–7809.

15 M. Y. Wong, G. Xie, C. Tourbillon, M. Sandroni, D. B. Cordes, A. M. Z. Slawin, I. D. W. Samuel and E. Zysman-Colman, *Dalton Trans.*, 2015, **44**, 8419–8432.

16 L. Flamigni, A. Barbieri, C. Sabatini, B. Ventura and F. Barigelletti, in *Topic in current chemistry 281, Photochemistry and Photophysics of coordination compounds:*

Iridium, Springer, Verlag Berlin Heidelberg, 2007, pp. 143–203.

17 A. Tsuboyama, H. Iwawaki, M. Furugori, T. Mukaide, J. Kamatani, S. Igawa, T. Moriyama, S. Miura, T. Takiguchi, S. Okada, M. Hoshino and K. Ueno, *J. Am. Chem. Soc.*, 2003, **125**, 12971–12979.

18 S. Lamansky, P. Djurovich, D. Murphy, F. Abdel-Razzaq, H. E. Lee, C. Adachi, P. E. Burrows, S. R. Forrest and M. E. Thompson, *J. Am. Chem. Soc.*, 2001, **123**, 4304–4312.

19 L. R. Joseph, *Principles of Fluorescence Spectroscopy*, Springer Science+Business Media, LLC, USA, University of Maryland School of Medicine, Baitimore, Maryland, USA, Third., 2010.

20 S. C. Vincenzo Balzani, *Photochemistry and Photophysics of Coordination Compounds II*, Lucia Flamigni, Andrea Barbieri, Cristiana Sabatini, Barbara Ventura, Francesco Barigelletti, Verlag Berlin Heidelberg, springer., 2007, vol. 281.

21 T. Sajoto, P. I. Djurovich, A. B. Tamayo, J. Oxgaard, W. A. Goddard and M. E. Thompson, *J. Am. Chem. Soc.*, 2009, **131**, 9813–9822.

22 J. A. G. Williams, A. Beeby, E. . S. Davies, J. A. Weinstein and C. Wilson, *Inorg. Chem. Commun.*, 2003, **42**, 8609–8611.

23 N. M. Shavaleev, L. P. Moorcraft, S. J. A. Pope, Z. R. Bell, S. Faulkner and M. D. Ward, *Chem. Eur. J.*, 2003, **9**, 5283–5291.

24 N. M. Shavaleev, G. Accorsi, D. Virgili, Z. R. Bell, T. Lazarides, G. Calogero, N. Armaroli and M. D. Ward, *Inorg. Chem.*, 2005, **44**, 61–72.

25 T. Lazarides, M. A. H. Alamiry, H. Adams, S. J. A. Pope, S. Faulkner, J. A. Weinstein and M. D. Ward, *Dalton Trans.*, 2007, 1484–1491.

CHAPTER FIVE

New ligand spacer, Ir•L^{naph}•NO_3 and Ir(III)/Re(I): Structural, Photophysical and Energy Transfer Process Study.

5 New ligand spacer, Ir•L^{naph} and Ir(III)/Re(I): Structural, Photophysical and Energy Transfer Process Study.

In the **introduction chapter 1** and in the other chapters, the photophysical properties and studies of mononuclear Ir(III) complexes have been explained briefly. In this chapter we will introduce Re(I) complexes of the type $Re(CO)_3(N\text{-}N)X$. This introduction covers briefly the following: the luminescence of Re(I) complexes with CO as a co-ligand, including recent work from Ward's and other research groups.

5.1 Introduction to Chemistry of Rhenium Metal.

5.1.1 Metal Carbonyl complexes

Transition metal-carbonyl complexes have been studied widely. A characteristic of many electron-rich transition metal ions is the ability to form complexes with CO due to the synergistic nature of the bonding.[1] This bonding can be described as the following; donation of a lone pair of electrons on the carbon atom (HOMO of CO) to a vacant transition metal σ-orbital (LUMO), accompanied by back-transfer of electron density from a d_π-orbital (HOMO) to an empty π^*-orbital of the CO (LUMO of CO) which removes the added electron density from the metal centres. This combination of σ-donation and π back-donation is illustrated in **Figure** 5-1.[1]

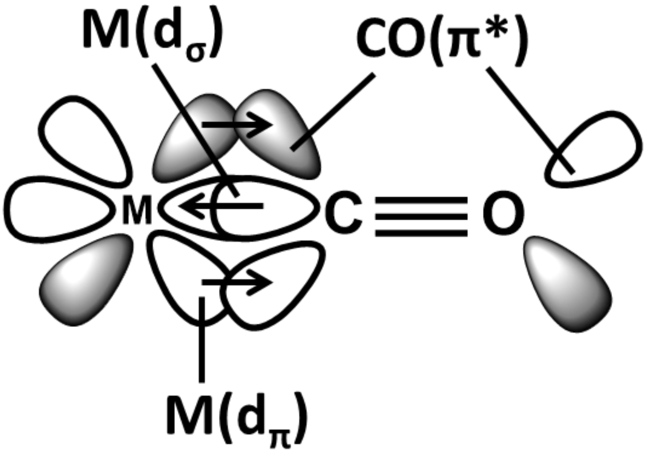

Figure 5-1 The contributions to metal/carbonyl bonding.[1]

5.1.2 Luminescence of Rhenium-carbonyl Complexes

Re(I) d^6 low-spin complexes of the type [Re(diimine)$(CO)_3$Cl] display similar photophysical properties to complexes such as $[Ru(bipy)_3]^{2+}$. Their lowest excited state is often of MLCT Re(I)→(diimine) nature. The emissive state is often a^{3}MLCT that shows luminescence at around 600 nm. As with other d^6 complexes, the photophysical properties are easily tunable by varying the ligand or adding ligand substituents.[2] Consequently, polypyridyl Re(I) tricarbonyl complexes have been used in different applications such as luminescent sensors,[3] photocleavage of DNA,[4] and as probes for polymerisation.[5]

The luminescence properties of these Re(I) (polypyridine) complexes can be exploited because of the following properties:

(a) Using various different diimine ligands can change the MLCT emission energy;

(b) Long lifetimes of emission can offer higher sensitivity to various quenchers (oxygen, small ions, and others) and applications in time-resolved detection techniques;

(c) The effect of self-quenching, which is commonly observed in biomolecules with fluorescent organic dyes, is minimised by the large Stokes shift.

Other excited state properties include the ability to perform photoinduced electron transfer and/or photoinduced energy transfer to other species.

5.2 Previous work.

The luminescence behaviour of complexes of the type [Re$(CO)_3$(diimine)Cl] was reported first by Wrighton *et.al.*[6] who demonstrated long-lived phosphorescence associated with the rich ^{3}MLCT excited state properties. Intense (CO) stretches allow the complexes to be probed by time-resolved infrared spectroscopy to follow excited state dynamic behaviour, as the CO stretches are sensitive to changes in the local electron density distribution.[6, 7]

Williams *et.al.*[8] prepared a series of hydrophilic and lipophilic *fac*-[Re(bisim)L$(CO)_3$]$^+$ complexes, where bisim represents a bisimine ligand (*e.g.* bipyridine or phenanthroline) and L is a pyridine ligand: lipophilicity cause their membrane permeability, making them suitable for cell imaging.

The Ward group[9] has studied the properties of Re(I)/Ru(II) dyads, in particular photoinduced energy-transfer between the two components, using both luminescence and time–resolved IR (TRIR) methods. The Re(I)→Ru(II) energy-transfer originating from the Re-based ^{3}MLCT excited state was demonstrated by quenching of the Re(I)-based emission and sensitisation of the Ru(II)-based emission (**Figure** 5-2).

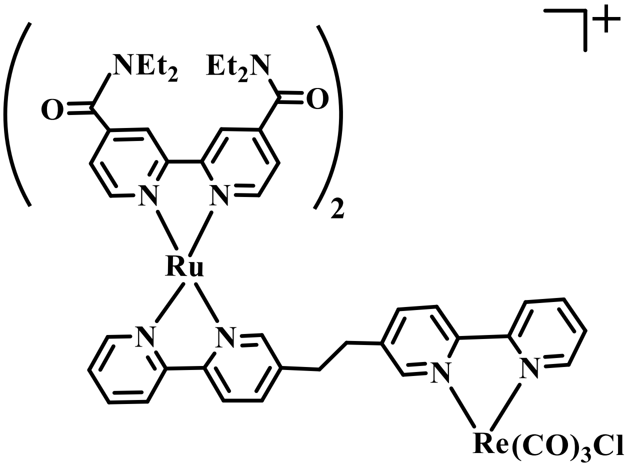

Figure 5-2 Chemical structure of Re-L-Ru complex.[9]

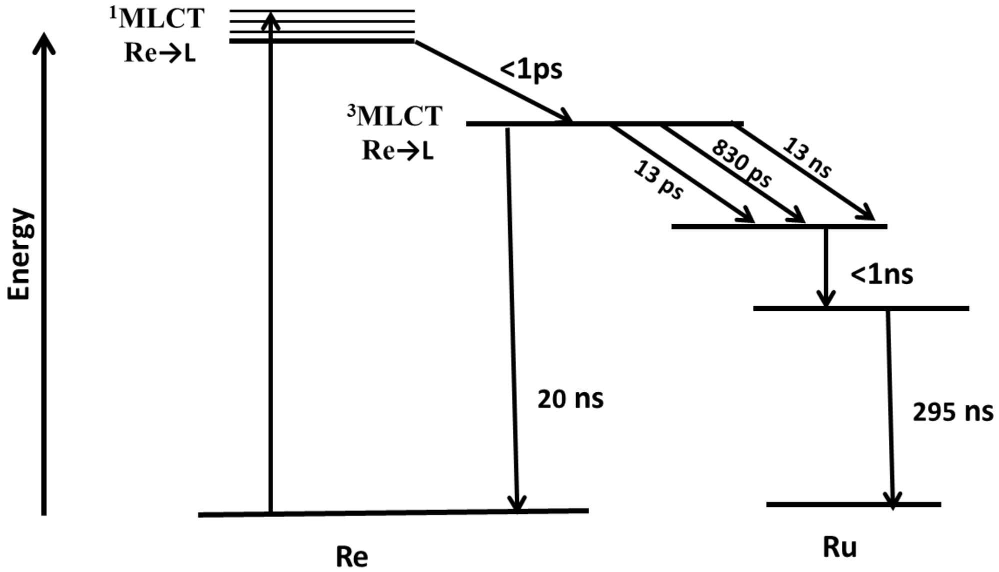

Figure 5-3 Energy transfer rates of Re→L to Ru→L.[9]

The presence of the (CO) groups attached directly to the Re(I) unit at one terminus, and the bipyridyl ligands coordinated to the Ru(II) terminus, allows the excited-state dynamics to be studied in detail by TRIR spectroscopy.

5.3 Aims of the work

In this chapter. we report the synthesis, crystal structures and photophysical properties of a novel homonuclear Ir(III) complex and heterodinuclear (Ir/Re and Ir/Ir) complexes based on a new bis(pyrazolyl-pyridine) ligand L^{naph}. The study of inter-component energy transfer either between the same metals or different metals have been of extensive interest. The mononuclear Ir(III) complex of L^{naph} has been used to investigate the sensitisation of Eu(III) and Tb(III) luminescence emission through energy transfer from the Ir(III) centre.

5.4 Results and discussions

Figure 5-4 shows the chemical structures of the new ligand L^{naph} and its complexes.

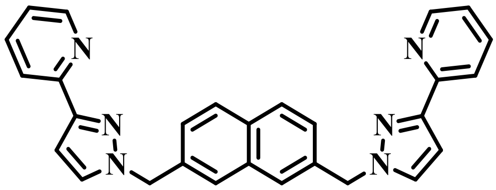

L^{naph}

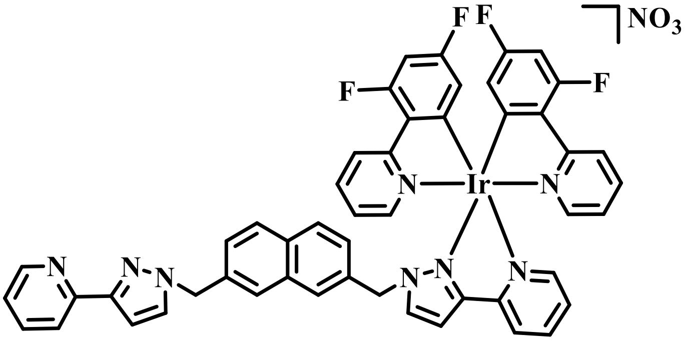

Ir•L^{naph}•NO$_3$

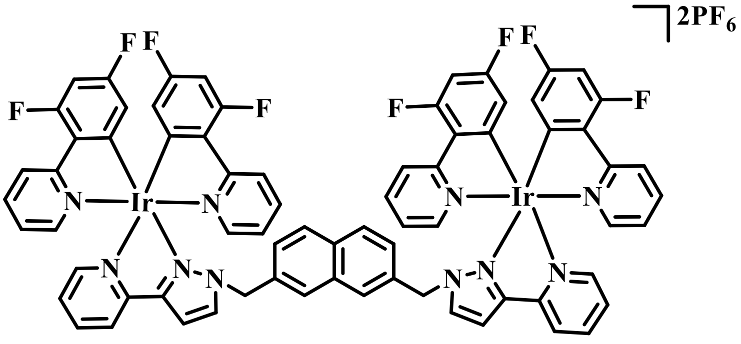

[Ir•L^{naph}•Ir]2PF$_6$

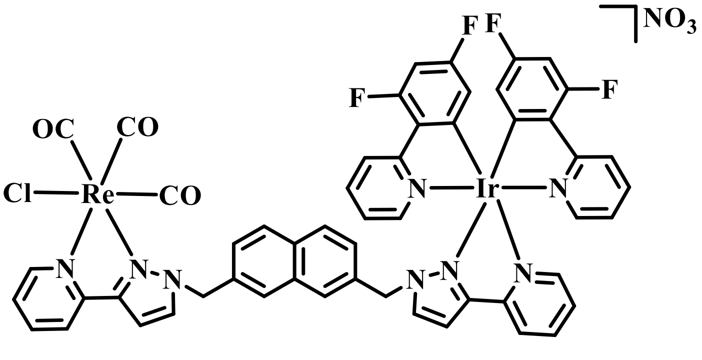

Ir•L^{naph}•Re•NO$_3$

Figure 5-4 Chemical structures of the ligand L^{naph} and its complexes discussed in this Chapter.

5.4.1 Synthesis and design of L^{naph}.

L^{naph} can be described as having an aromatic naphthalene spacer with two attached chelating bidentate pyrazolyl-pyridine groups attached at the 2,7 positions via flexible methylene units, (**Figure** 5-4**)**. The chelating bidentate groups can be used to coordinate to the cyclometalated {Ir(F_2ppy)$_2$} unit from one side and to another metal complexes unit such as {Ir(F_2ppy)$_2$}, Re(CO)$_3$Cl or Ln(hfac)$_3$ on the other side. L^{naph} was synthesised by reaction of 2,7-bis(bromomethyl)naphthalene with pypz under basic conditions, and purified by silica gel chromatography. L^{naph} was characterised by using electrospray mass spectrometry, ^{1}H NMR spectroscopy, elemental analysis and X-ray crystallography.

5.4.2 Synthesis of mononuclear Ir•L^{naph}•NO_3 complex and dinuclear Ir•L^{naph}•Ir•NO_3 complexes.

Mononuclear Ir•L^{naph}•NO_3 and dinuclear Ir•L^{naph}•Ir•NO_3 complexes (**Figure** 5-4) have been prepared by refluxing L^{naph} with the chloride-bridged dimer [(C^N)$_2$Ir(μ-Cl)$_2$Ir(C^N)$_2$] in DCM/MeOH which provided a mixture of mononuclear Ir•L^{naph}•NO_3 and dinuclear [Ir•L^{naph}•Ir]2NO_3. The percentage of the mononuclear or dinuclear complexes depends on the L^{naph} :Ir-dimer ratio. A lower L^{naph} proportion compared to Ir(III) starting material gives more chance to form the dinuclear [Ir•L^{naph}•Ir]2NO_3 complex. The two complexes were separated and purified by silica gel chromatography eluting with MeCN/$KNO_{3(aq.)}$/H_2O. Then for [Ir•L^{naph}•Ir]2NO_3 complex solvents were evaporated and anion convert to PF_6 through metathesis with $KPF_{6(aq.)}$. Complex was collected as $^{F/F}$Ir•L^{naph}•Ir•2PF_6 as a yellow solid. The complexes were identified by using electrospray mass spectrometry, ^{1}H NMR spectroscopy, elemental analysis and X-ray crystallography.

Interestingly, ^{1}H NMR spectrum of [Ir•L^{naph}•Ir]2PF_6 was particularly complex due to a mixture of two diastereiosomers that associated with the chirality of the two Ir centres. This means that a given proton environment can be split into two similar but overlapping components, whereas the total number of proton signals is correct taking this into account (**Figure** 5-5).[10]

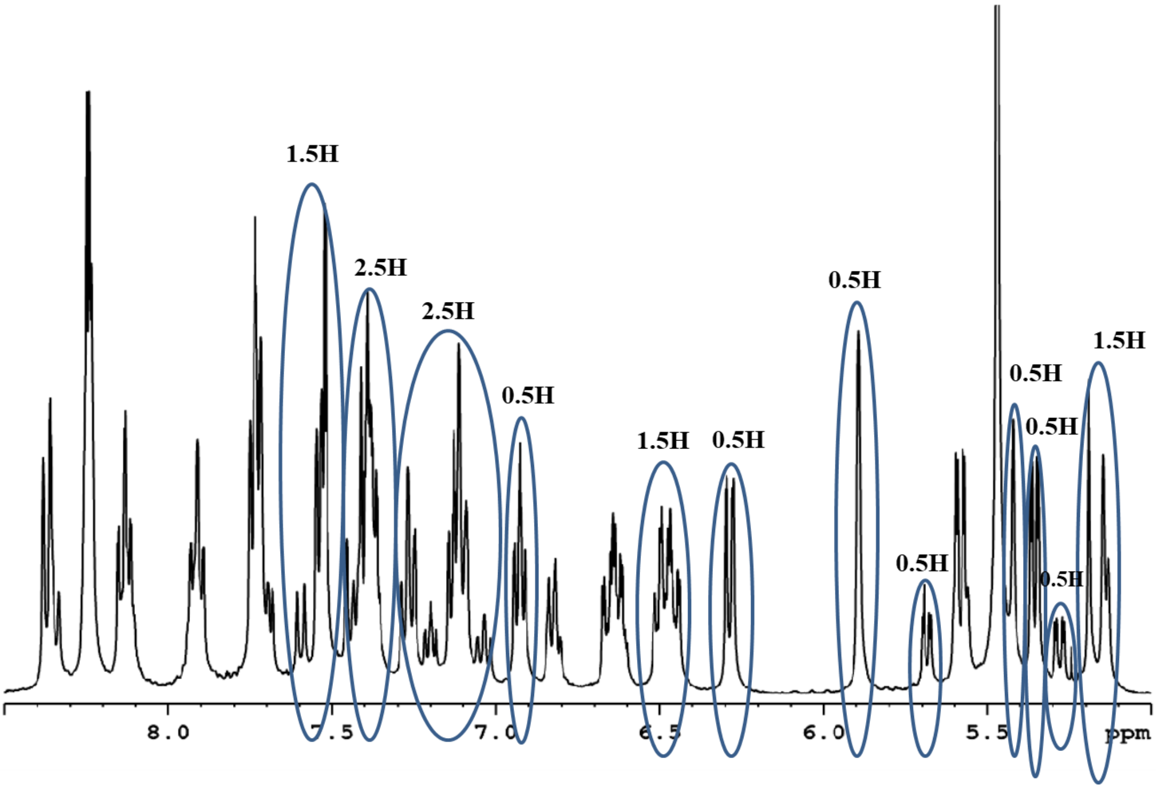

Figure 5-5 ^{1}H NMR of [Ir•L^{naph}•Ir]2PF_6 complex in CD_3CN solvent at room temperature.

5.4.3 Synthesis and design of dinuclear Ir•L^{naph}•Re•NO_3 complexes.

The dinuclear complex Ir•L^{naph}•Re•NO_3 complex (**Figure** 5-4) was prepared by refluxing Ir-L^{naph} with $Re(CO)_5Cl$ complex in a 1:1 ratio in MeCN solvent. In this complex a $\{Re(CO)_3Cl\}$ unit is bound directly to the vacant chelating pypz unit of the bridging ligand. The complex Ir•L^{naph}•Re•NO_3 complex was identified by electrospray mass spectrometry, X-ray crystallography and an infrared spectrum (IR) which showed a strong ν_{CO} signal with unresolved shoulders at 1877 cm^{-1}. In the ^{1}H NMR spectrum, signals with relative intensity of 0.5H was observed. This is because the two chiral centres generate a 1:1 mixture of diastereoisomers, as with the [Ir•L^{naph}•Ir]•2PF_6 complex, which splits some of the signals (**Figure** 5-6). That means the signal from one isomer can be separately resolved and easily separated from the equivalent signal in the distereoisomer.[10]

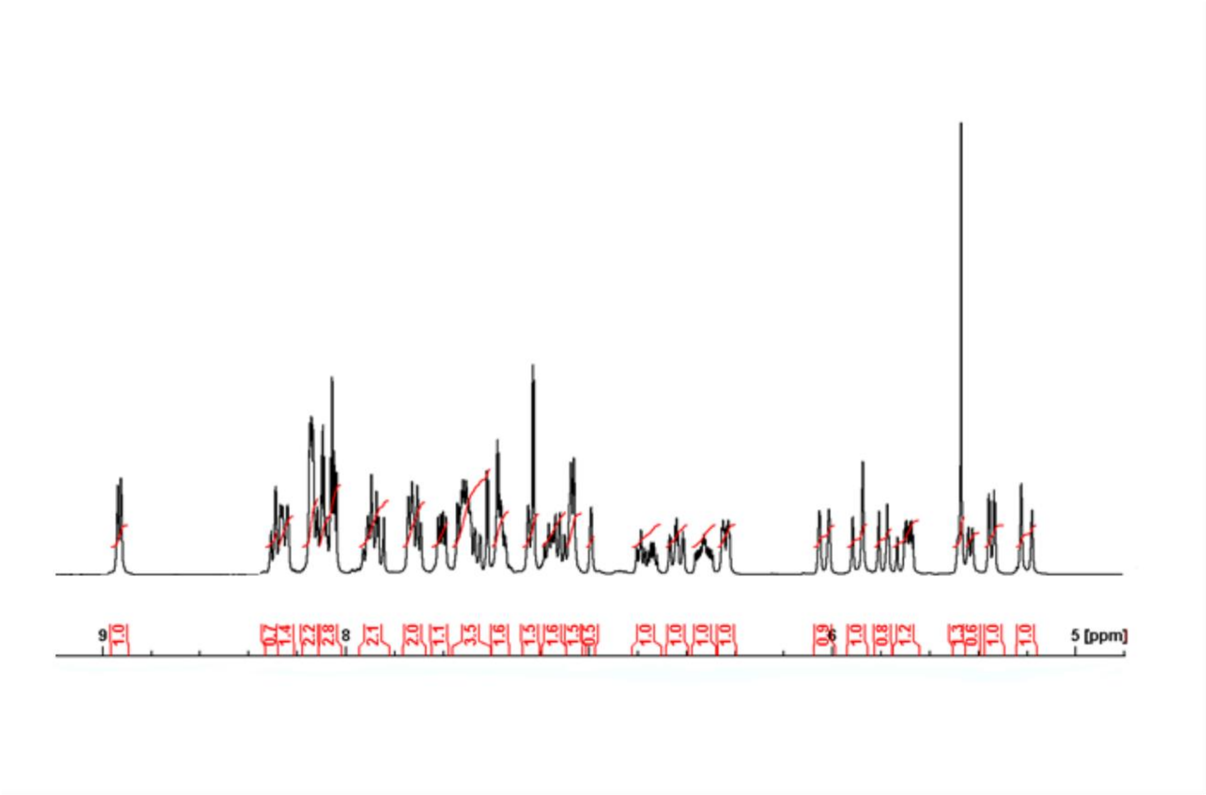

Figure 5-6 ^{1}H NMR of Ir•L^{naph}•Re•NO$_3$ complex in CD$_3$CN solvent at room temperature.

5.5 X-ray Crystallography.

5.5.1 L^{naph}

A single crystal of L^{naph} was obtained by recrystallisation from chloroform. Crystals of mononuclear Ir•L^{naph}•NO$_3$ and dinuclear Ir•L^{naph}•KNO$_3$, [Ir•L^{naph}•Ir]•2PF$_6$ and Ir•L^{naph}•Re•NO$_3$ were obtained through diffusion of ether into MeCN solutions of the complexes.[10]

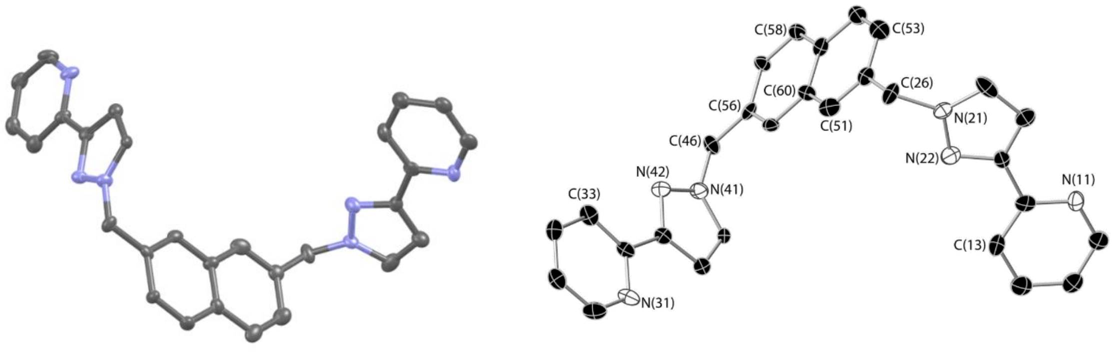

Figure 5-7 X-ray structure of L^{naph}. Thermal ellipsoids shown at 50% probability.[10]

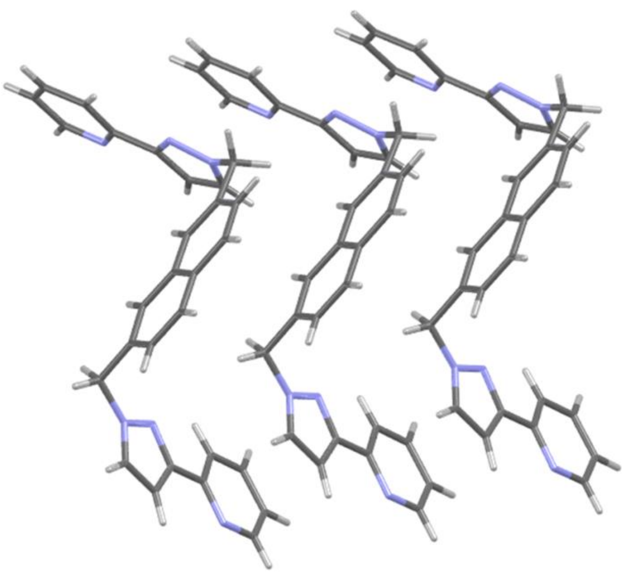

Figure 5-8 *π-π* stacking between molecules of L^{naph}.[10]

The crystal structure of L^{naph} (**Figure** 5-7) shows that the two pypz units are arranged in a transoid manner around the central naphthyl spacer. The mean plane of the naphthyl unit is substantially twisted away from the mean planes of the pypz groups, with the torsion angles N(21)-C(26) and N(41)-C(46) being 71.5º and 85.3º respectively. The *π-π* stacking was observed between adjacent molecules with a distance between planes equal 3.778 Å, angle 1.013 Å and shift 1.272 Å (**Figure** 5-8). All crystallographic data is summarised in **Table 5-1**.[10]

5.5.2 Ir•L^{naph}•KNO_3 and Ir•L^{naph}•NO_3

When purifying the Ir•L^{naph}•NO_3 complex by using a mixture of MeCM/$KNO_{3(aq.)}$/H_2O on silica gel, a few crystals of Ir•L^{naph}•KNO_3 were unexpectedly obtained although excess of KNO_3 was removed during the final workup. The Ir•L^{naph}•KNO_3 complex was obtained due to a $\{K(NO_3)_3(H_2O)\}^{2-}$ unit being coordinated to the second pypz site provided by the Ir•L^{naph} cation (**Figure** 5-9).

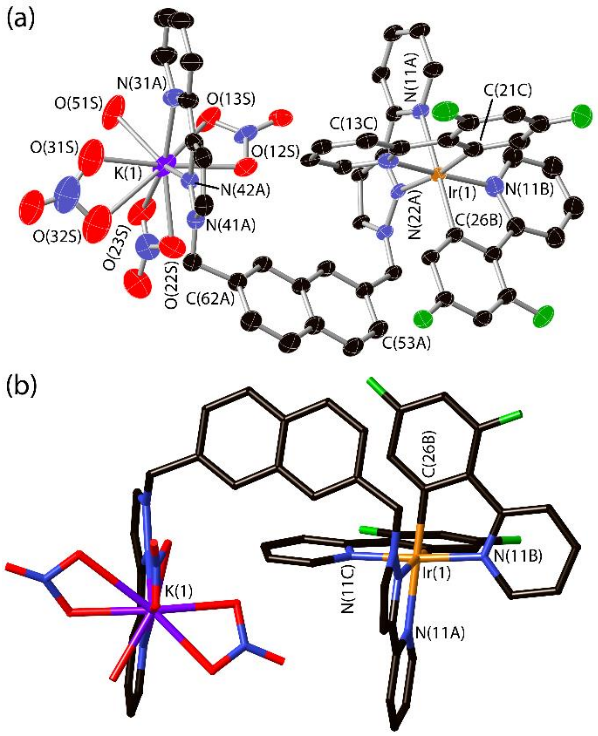

Figure 5-9 X-ray structure of Ir•L^{naph}•KNO$_3$ (a) Thermal ellipsoids shown at 30% probability. (b) a view emphasising the confirmation of the bridging spacer naphthalene unit being perpendicular to the two pypz chelating groups.

The crystal structure of Ir•L^{naph}•KNO$_3$ complex can be described as follows: the K$^+$ ion is coordinated by three- bidentate NO$_3$ ligands, one-chelating pypz ligand and one H$_2$O ligand giving K$^+$ ion coordination of nine. The K-O and K-N bonds have distances in the 2.5 and 2.4 Å region, respectively. One of the nitrates N(31S) is bound asymmetrically however with the K(1)-O(32S) distance being considerably longer than average, at 2.82Å. The water ligand and one of the nitrate ligands show twofold disorder, in addition a substantial part of the entire Ir(III) complex is disordered over two positions, but only the major component is shown in **Figure** 5-9. The charge on the entire complex based on the components that can be identified is -1, therefore, a cation in the structure would be expected to be observed but it could not be modelled. Probably, the positive charge needed is something small like H$_3$O$^+$ (protonated water) which is disordered and has been removed from the refinement of the structure through SQUEEZE command in PLATON. But there must be a positive ion somewhere even if we cannot locate it explicitly.[10]

Table 5-1 Summary of coordination-sphere bond distances around the metal complex centers in the crystal Ir•L^{naph}•KNO_3 structure.

Ir(1)-N(11B) [a]	2.011(8)	Ir(2)-N(11Z) [b]	1.97(2)
Ir(1)-C(26C)	2.015(8)	Ir(2)-N(11X)	2.005(18)
Ir(1)-C(26B)	2.033(9)	Ir(2)-C(26Z)	2.03(3)
Ir(1)-N(11C)	2.045(7)	Ir(2)-C(26X)	2.07(2)
Ir(1)-N(22A)	2.083(9)	Ir(2)-N(11Y)	2.115(16)
Ir(1)-N(11A)	2.157(6)	Ir(2)-N(22Y)	2.24(2)
K(1)-O(51S)	2.37(2)	K(1)-N(31A)	2.491(7)
K(1)-O(31S)	2.405(15)	K(1)-N(42A)	2.575(5)
K(1)-O(13S)	2.464(9)	K(1)-O(42S)	2.74(4)
K(1)-O(23S)	2.470(11)	K(1)-N(41S)	2.76(4)
K(1)-O(12S)	2.472(9)	K(1)-O(32S)	2.817(19)
K(1)-O(22S)	2.483(11)		

[a] Major disorder component associated with Ir(1).

[b] Minor disorder component associated with Ir(2).

5.5.3 Ir•L^{naph}•NO_3

Figure 5-10 shows the main features of the Ir•L^{naph}•NO_3 complex crystal structure, i.e. an Ir(III) unit with 6-coordinate geometry from 2-cyclometalating phenylpyridine and one bidentate pyrazolyl-pyridine chelate ligands.[11–13] The plane of the naphthyl group is twisted with respect to the pendant pyrazolyl-pyridine plane. A π-stacking interaction was observed between the naphthalene plane and one of the F_2ppy ligands, containing N(11C) and C(26C), which lies in the range 3.2-3.4 Å from the mean plane of the naphthyl group.[13] Furthermore, a CH····π interaction is observed between H(14C) of F_2ppy ligand and [N(41A)-C(45A)] pyrazolyl ring of the pendant pyrazolyl-pyridine ring, as clarified in the **Figure** 5-10**.**[10]

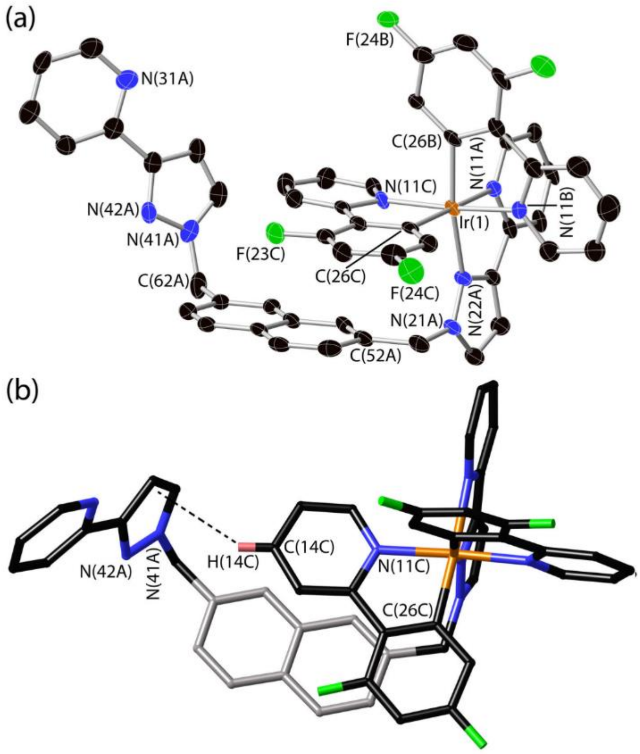

Figure 5-10 X-ray structure of Ir•L^{naph}•NO_3 (a) Thermal ellipsoids shown at 40% probability. (b) a view emphasising the aromatic stacking between the coordinated F_2ppy ligands and naphthyl aromatic rings. Also, H-bonding between CH···π interaction of pypz ring.

Table 5-2 Summary of coordination-sphere bond distances around the metal complex centers in the crystal Ir•L^{naph}•NO_3 structure.

Ir(1)-C(26B)	2.013(8)	Ir(1)-N(11C)	2.047(7)
Ir(1)-C(26C)	2.035(8)	Ir(1)-N(22A)	2.142(7)
Ir(1)-N(11B)	2.044(7)	Ir(1)-N(11A)	2.165(7)

5.5.4 [Ir•L^{naph}•Ir]•2PF_6 complex.

The structure of dinuclear [Ir•L^{naph}•Ir]2PF_6 obtained from crystallographic data is shown in **Figure** 5-11. The coordination geometry is octahedral around each Ir(III) unit. It is clear that the naphthyl unit is lying sandwiched between two bidentate pypz units, one of which is coordinated to Ir(1) while the another is coordinated to Ir(2), thus, three components form a π-stacked array with a distance of *ca.* 3.4 Å between components. The [Ir•L^{naph}•Ir]2PF_6 complex occurs in the crystal structure as the racemic form (ΔΔ/ΔΔ) form.[10] However, the ^{1}H NMR spectrum showed that both diastereoisomers were present in the sample (both *meso* and *racemic*), so only the *racemic* form has crystallised.

Table 5-3 Summary of coordination-sphere bond distances around the metal complex centers in the crystal [Ir•L^{naph}•Ir]2PF_6 structure.

Ir(1)-C(26B)	1.994(5)	Ir(2)-C(26D)	2.001(5)
Ir(1)-C(26C)	2.021(5)	Ir(2)-C(26E)	2.020(5)
Ir(1)-N(11B)	2.044(4)	Ir(2)-N(11D)	2.043(4)
Ir(1)-N(11C)	2.045(4)	Ir(2)-N(11E)	2.045(4)
Ir(1)-N(42A)	2.145(4)	Ir(2)-N(22A)	2.154(5)
Ir(1)-N(31A)	2.164(4)	Ir(2)-N(11A)	2.159(4)

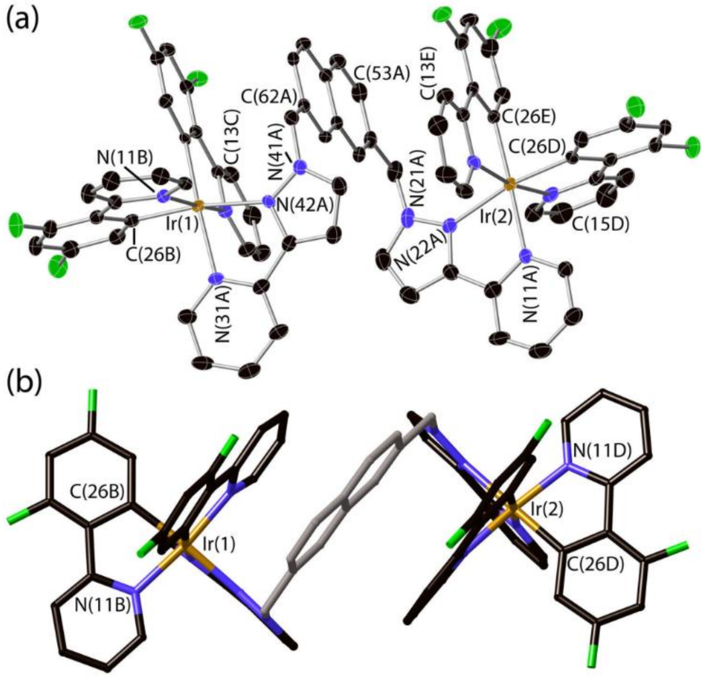

Figure 5-11 X-ray crystal structure of [Ir•L^{naph}•Ir]2PF_6 complex with 6MeCN from crystallographic data. (a) Thermal ellipsoids shown at 40% probability. (b) a view emphasising a three- component π-stacked array in helical conformation of the naphthyl unit sandwiched between two F_2ppy ligands.

5.5.5 Ir•L^{naph}•Re•NO_3 Complex.

Figure 5-12 shows that the main features are observed in the structure of this dinuclear Ir/Re crystal structure is π-stacking with a separation of 3.4-3.5 Å between the naphthyl bridge ligand and one pyridine N(11C)-C(16C) of a F_2ppy ligand coordinated to the Ir(III) unit. The central naphthyl unit lies approximately perpendicular to the two pypz groups. The distance between two centre metals Ir(III) and Re(I) is 8.10 Å. There is twofold disorder between the Cl and CO [C(31D)/O(32D)] around the Re(I) metal (only the major component is shown in the **Figure** 5-12). H-bonding between a lattice water molecule and the chloride ligand (Cl•••O distance) 3.21 Å is apparent.[10]

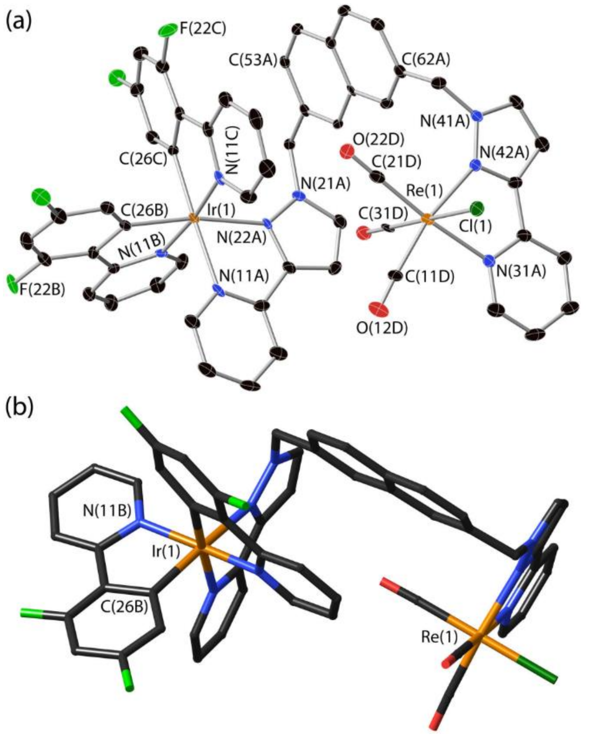

Figure 5-12 X-ray structure of [Ir•L^{naph}•Re]NO_3 complex with MeCN and 0.64 H_2O from crystallographic data. (a) Thermal ellipsoids shown at 40% probability. (b) A view emphasising the conformation of the naphthyl unit being a perpendicular to two pypz chelating ligands.

Crystallographic data for Ir•L^{naph}•KNO_3 complex is summarised in **Table 5-4**, while all crystallographic data for L^{naph}, Ir•L^{naph}•NO_3, dinuclear [Ir•L^{naph}•Ir]2PF_6 and Ir•L^{naph}•Re•NO_3 are summarised in **chapter 7**.

Table 5-4 Crystal parameters, data collection and refinement details for the Ir•L^{naph}•KNO_3 structures.

Compound	**$H[Ir(F_2ppy)_2(L^{naph})K(NO_3)_3(H_2O)]$**
Formula	$C_{50}H_{34}F_4IrKN_{11}O_{10}$
Molecular weight	1256.18
T	1100(2)
Crystal system	Monoclinic
Space group	*I*2/a
a	17.5169(7) Å
b	16.6681(7) Å
c	40.477(2) Å
α	90 deg
β	99.688(4) deg
ϒ	90 deg
V	11649.7(9)
Z	8
ρ	1.432
Crystal size	0.26 x 0.24 x 0.16
μ	2.437
Data, restraints, parameters	10343 / 1876 / 909
Final *R*1, *wR*2[a]	0.082, 0.215

5.6 UV-Vis absorption spectra

Absorption spectra and extinction coefficients for all complexes in this chapter were measured in MeCN solvent at 298 K; the data are summarised in **Table 5-5**.

Table 5-5 Luminescence data for Ir•L^{naph}•NO_3, [Ir•L^{naph}•Ir]2PF_6 and Ir•L^{naph}•Re•NO_3 complexes series at 298 K in MeCN solvent.

Complex	**UV/Vis** [λ_{max} / nm (10^{-3} ε / M^{-1} cm^{-1})]	**Excitation** λ (nm)	**Emission** (λ_{max} / nm)	ϕ_{lum}	**Emission** τ / ns
Ir•L^{naph}•NO_3	226 (88), 246 (64), 279 (43), 315 (15), 360 (5.5)	360	455, 485	0.004	36, 365
[Ir•L^{naph}•Ir]2PF_6	228 (136), 244 (123), 290 (67), 360 (13)	360	455, 485	0.009	37, 224, 767
Ir•L^{naph}•Re	227 (103), 254 (62), 281 (46), 298 (36), 360 (7.8), 418 (0.5)	380	455, 485, 520	0.005	52, 330

5.6.1 Ir•L^{naph}•NO_3 and [Ir•L^{naph}•Ir]2PF_6.

As shown in **Figure** 5-13, an absorption feature (poorly-defined shoulder) at 360 nm is observed that can be assigned to a mixed LC/MLCT electronic transition.[11, 14, 15] The intensity of this transition for dinuclear [Ir•L^{naph}•Ir]2PF_6 is approximately double compare to mononuclear Ir•L^{naph}•NO_3 complex[10] which helps to confirm the assignment. Higher-energy absorptions in the UV region are ligand-centred π-π* transitions.

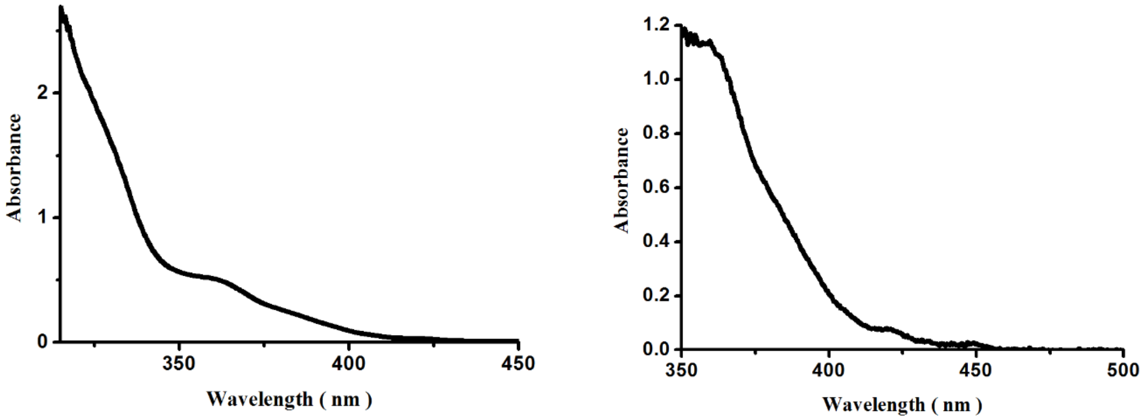

(a) **(b)**

Figure 5-13 UV-Vis absorption spectra for (a) Ir•L^{naph}•NO$_3$ and (b) [Ir•L^{naph}•Ir]2PF$_6$ in MeCN at 298 K.

5.6.2 Ir•L^{naph}•Re•NO$_3$

In this complex, a weak shoulder peak at 420 nm was observed which was not present for the Ir•L^{naph}•NO$_3$ complex: this is the ^{1}MLCT electronic transition associated with Re(I)/diimine unit (**Figure** 5-14).[10, 16]

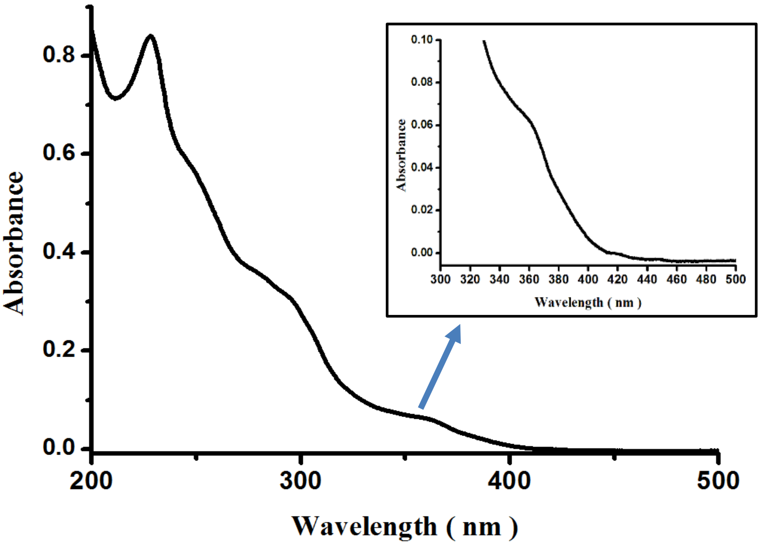

Figure 5-14 UV-Vis absorption spectra for Ir•L^{naph}•Re•NO$_3$ in MeCN at 298 K.

5.7 Photophysical Studies of Ir•L^{naph}•NO$_3$, [Ir•L^{naph}•Ir]$_2$PF$_6$ and Ir•L^{naph}•Re•NO$_3$ series.

5.7.1 Ir•L^{naph}•NO$_3$ and [Ir•L^{naph}•Ir]2PF$_2$

These complexes showed weak and structured luminescence emission in the blue region that is assigned predominantly to ^{3}LC excited state, with emission arising from the [Ir(F$_2$ppy)$_2$(pypz)]$^+$ units (**Figure** 5-15**)**.[12, 17–19] The weakness of the emissions, with the Φ value < 1% in MeCN at 298 K (**Table 5-5**).[18] is attributed to the partial quenching of the Ir(III) unit excited state by energy-transfer to the ^{3}naph excited state of the bridging ligand which lies *ca.* 800 cm^{-1} below the Ir(III)-based excited state.[13] The good evidence for the ease of this comes from the crystal structure which shows close association of the Ir(III) complex core with the naphthyl group through aromatic stacking.[10]

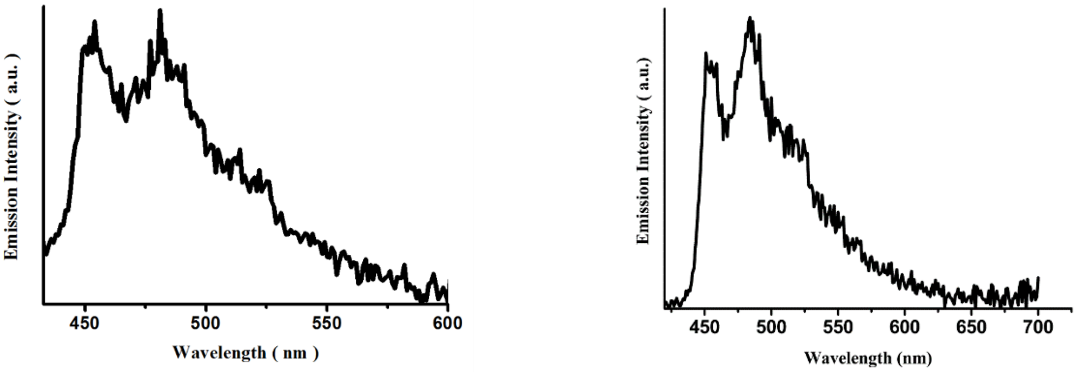

(a) **(b)**

Figure 5-15 Luminescence spectrum of (a) Ir•L^{naph}•NO$_3$ and (b) [Ir•L^{naph}•Ir]2PF$_6$ complexes in MeCN, λexc=360 nm, at 298K.

The lifetime decay of Ir•L^{naph}•NO$_3$ required two exponential emission components to get a good fit with a satisfactory χ^2 value, implying that Ir•L^{naph}•NO$_3$ exists as a mixture of conformers in solution with two rates of internal Ir-naph energy-transfer. The major lifetime component is 365 ns while the minor component is 36 ns.[10] The conformational flexibility probably arises from the methylene groups in the L^{naph} ligand which allow the groups pendant from the metal centre to adopt a range of conformations. The naphthyl group is free to move away from the position observed in the crystal structure where it lies stacked with the F$_2$ppy ligand attached directly to the Ir core.[10, 20]

The time-resolved luminescence measurements on [Ir•L^{naph}•Ir]2PF$_6$ are different, requiring three exponential decay components to get a satisfactory fit to the observed data. The two major components are 767 and 224 ns while the minor component is 37 ns. The presence of several decay components may again be attributed to range of confirmations in the solution arising from the ligand flexibility.[10]

5.7.2 Ir•L^{naph}•Re•NO$_3$

The luminescence of the Ir•L^{naph}•Re•NO$_3$ complex (**Figure** 5-16) shows more complex behaviour. There are two structured peaks in the range 450 - 500 nm which associated with the Ir unit emission. In addition, a broad emission in the low-energy region at 525 nm is assigned to emission from the ^{3}MLCT excited state of the Re(I) core. The ^{3}naph group lies above the ^{3}MLCT energy of the Re(I) unit excited state and so, when it is populated by energy-transfer from the Ir-based excited state, can pass on the energy to the Re(I) centre leading to the characteristic emission.[10]

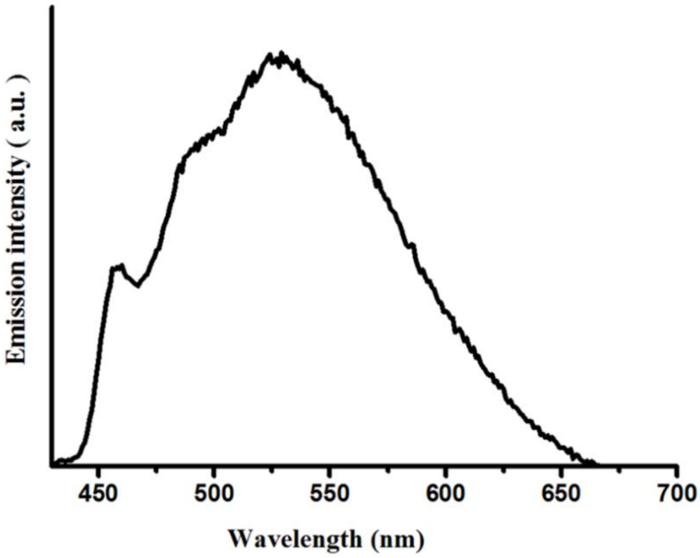

Figure 5-16 Luminescence spectrum of Ir•L^{27naph}•Re•NO$_3$ complex in MeCN, λexc = 360 nm, at 298K.

The luminescence decay of this complex can be fitted to two exponential emission components with lifetimes of *ca*. 50 ns (the minor component) and *ca.* 400 ns (the major component). Interestingly, there is no detectable grow-in for the sensitised Re(I) luminescence emission which means that the energy transfers processes (firstly from the Ir(III) excited state to ^{3}naph state, and secondly from the ^{3}naph state to the Re(I) state) are fast compared to the lifetime resolution of the instrument, *ca.* 1 ns.[10]

5.8 Titration with $Ln(hfac)_3$•$2H_2O$

The mononuclear Ir(III) complex Ir•L^{naph}•NO_3 was dissolved in 50 ml MeCN, and titrated by addition of portions of $Ln(hfac)_3$•$2H_2O$ at 298 K. Titration with $Gd(hfac)_3$•$2H_2O$ was used as a control experiment because excited state of Gd(III) is higher in energy than the excited state of mono-Ir-complex as described briefly before, so cannot act as an energy-transfer acceptor.

5.8.1 Titration Ir•L^{naph}•NO_3 with $Eu(hfac)_3$•$2H_2O$.

The complex Ir•L^{naph}•NO_3 was titrated with $Eu(hfac)_3$•$2H_2O$ salt to make an Ir•Eu dyad. This titration results in quenching of the (already very weak) emission of the Ir-based excited state by an additional energy-transfer pathway to the Eu(III) centre, and an increase in Eu-based emission as the {$Eu(hfac)_3$} unit coordinates to form the dyad, as shown in **Figure** 5-17. The excitation wavelength was 360 nm assigned to the Ir-based absorption band. Thus, upon addition of 20µl (0.3 eq.) of $Eu(hfac)_3$•$2H_2O$ solution the sensitised Eu(III)-based emission peaks were observed clearly at the following λ_{max}= 515 nm, 540 nm, 550 nm, 580 nm which are attributed to the Eu(III) transitions ($^5D_0 \rightarrow {}^7F_0$), ($^5D_0 \rightarrow {}^7F_2$), ($^5D_0 \rightarrow {}^7F_3$), ($^5D_0 \rightarrow {}^7F_4$) respectively. The quenching of mono-Ir(III) complex absorption intensity and growing in the absorption intensity of Eu(III) complex, and in particular the fact that excitation of the Ir unit resulted in Eu-based emission appearing was used as an indicator that the energy transfer successfully occurred from Ir(III)→Eu(III). The quenching of Ir(III)-based emission was completed after (420µl) (≈4 eq.) of Eu(III) complex was added. At this point the luminescence color was approximately white (**Figure** 5-17) under long –wavelength UV-light excitation, as a result from a balance of blue/red emission components.

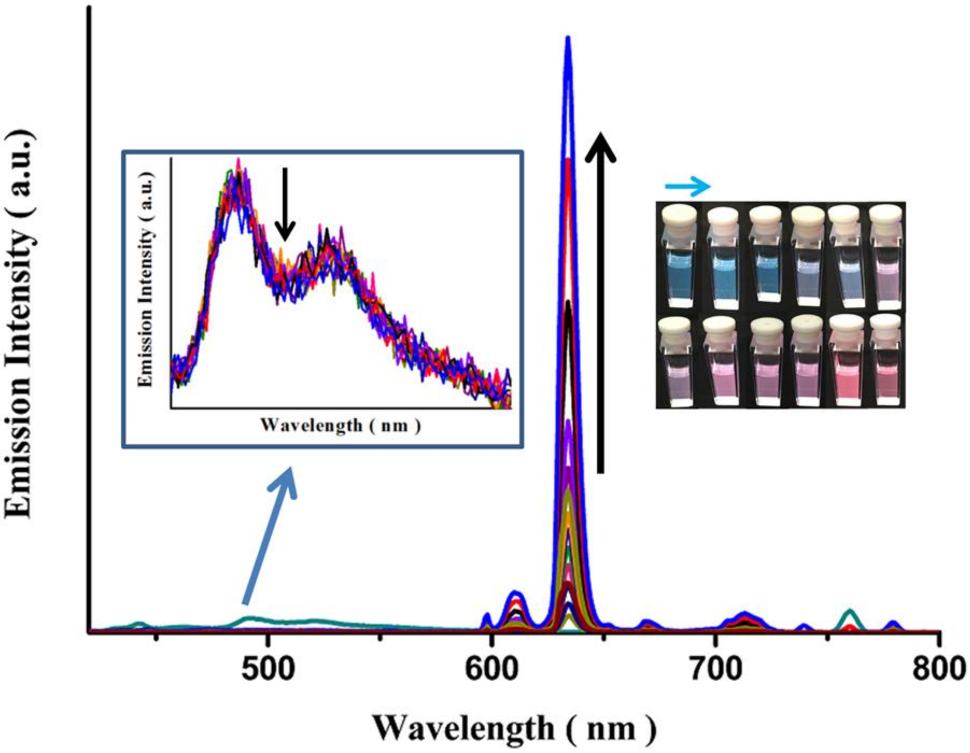

Figure 5-17 Quenching in the Ir(III) unit emission with energy transfer upon addition Eu(hfac)$_3$(H$_2$O)$_2$ to Ir•L^{naph}•NO$_3$ in MeCN at 298 K. $\lambda_{exc.}$=360 nm.

5.8.2 Titration of Ir•L^{naph}•NO$_3$ with Tb(hfac)$_3$•2H$_2$O

Ir•L^{naph}•NO$_3$ was also titrated with Tb(hfac)$_3$•2H$_2$O salt to make an **Ir•Tb** dyad in which an energy transfer process from Ir(III) complex to the Tb(III) centre was apparent, as shown in **Figure** 5-18**.** The excitation wavelength was again 360 nm into the Ir(III)-based absorption band. After addition Tb(hfac)$_3$•2H$_2$O solution to form the **Ir•Tb** dyad, an increase in a Tb(III)-based emission peak was observed at 550 nm which was attributed to the Tb(III) transitions (^{5}D$_4$→^{7}F$_5$). As the proprtion of the **Ir•Tb** grew during the titration, the emission intensity of the Ir(III) unit steadily decreased and the intensity emission of Tb(III) complex was increased until addition of *ca.* 5 eqiv. of Tb(hfac)$_3$•2H$_2$O.

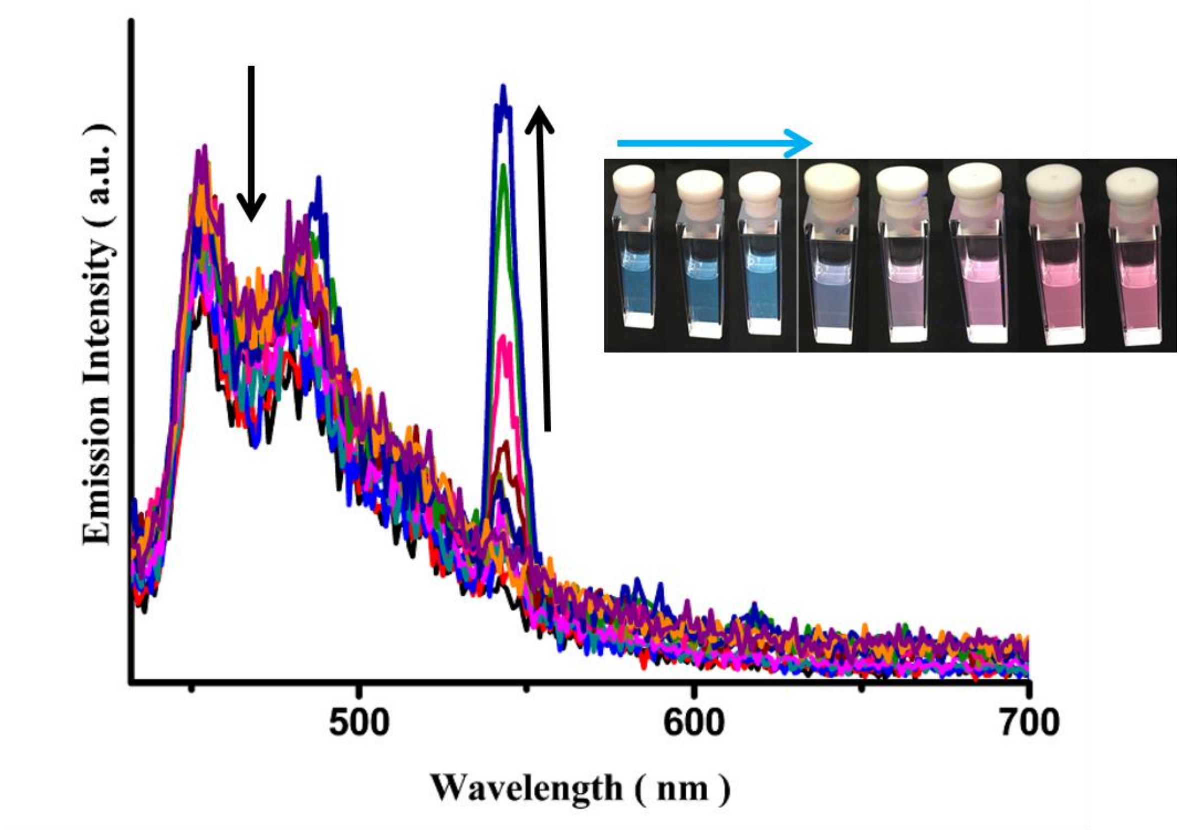

Figure 5-18 Quenching in the Ir(III) unit emission with weak energy transfer on addition $Tb(hfac)_3(H_2O)_2$ to Ir•L^{naph}•NO_3 in MeCN at 298 K. λ exc.=360 nm.

5.8.3 Titration Ir•L^{naph}•NO_3 with $Gd(hfac)_3$•$2H_2O$

Figure 5-19 shows the results of a control experiment – emission spectra recorded during titration of Ir•L^{naph}•NO_3 with $Gd(hfac)_3$•$2H_2O$. The titration showed very little change in the Ir-based emission as the **Ir•Gd** dyad formed, as would be expected in the absence of any energy-transfer to Gd(III). Furthermore, the Ir-based emission lifetime remained constant during the titration, and obeys a single exponential decay, with a 260±25 ns lifetime.

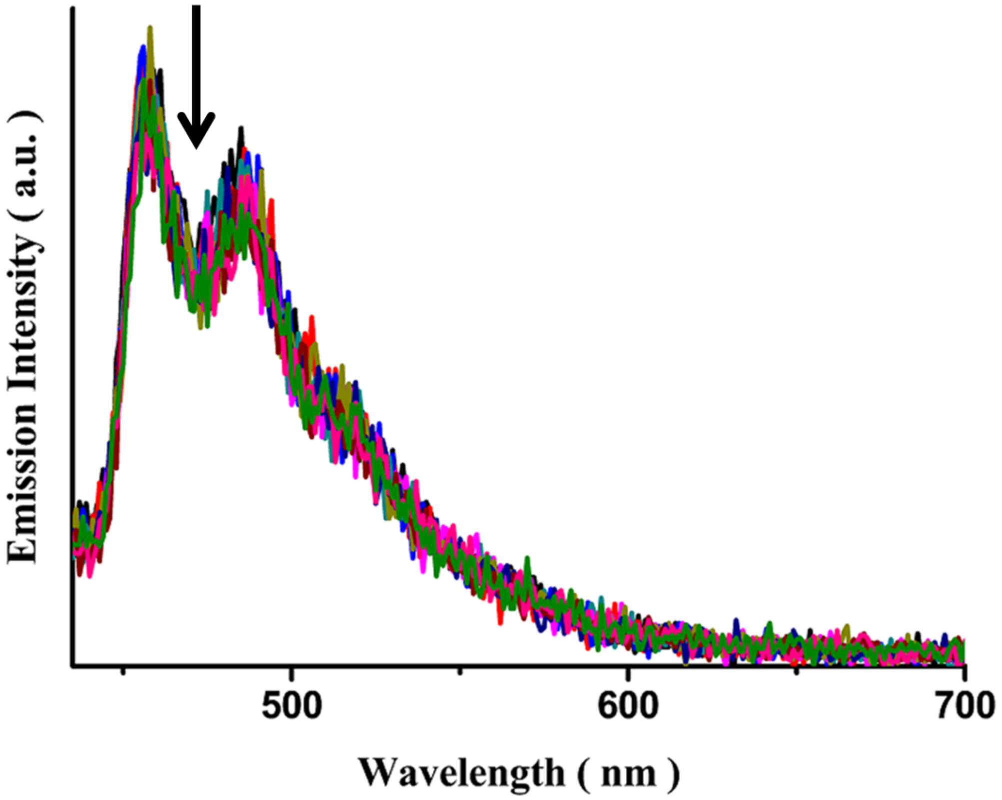

Figure 5-19 The Ir(III) unit emission with no energy transfer on addition Gd(hfac)$_3$(H$_2$O)$_2$ to Ir•L^{naph}•NO$_3$ in MeCN at 298 K. λ exc.=360 nm.

5.9 Conclusion

The new ligand L^{naph} was synthesised and characterised. The following Ir(III) complexes of this ligand were synthesised and characterised: mononuclear Ir•L^{naph}•NO$_3$ and two dinuclear [Ir•L^{naph}•Ir]2PF$_6$ and Ir•L^{naph}•Re•NO$_3$ complexes. For all complexes the photophysical properties were investigated. The results suggested the participation of the naphthyl spacer (triplet state) as an intermediate lying below the Ir-based emissive state but higher than the excted state of the acceptor, Re-unit. Consequently in the dinuclear complex Ir•L^{naph}•Re•NO$_3$, the ^{3}naph state of L^{naph} acts as a “Stepping stone” between the two metal-centred excited state energy levels which makes photoinduced energy transfer process fast (<1 ns) (**Figure** 5-20).[10] Energy transfer was observed in Ir/Eu and Ir/Tb dyads, with excitation into te Ir-based absorption band resulting in sensitised Eu-based or Tb-based emission.[13]

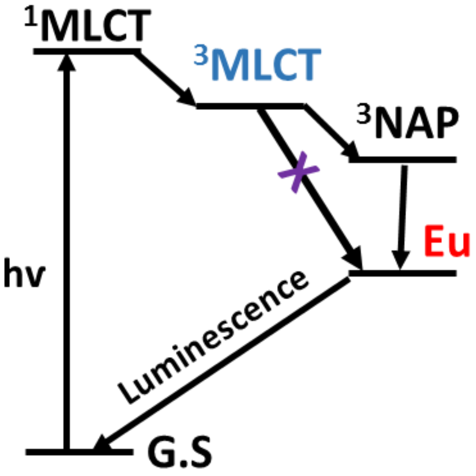

Figure 5-20 Outline photophysical scheme summarizing the energy-transfer pathways from ^{3}Ir unit to the Eu unit centre.

5.10 References

1 A. Banu, PhD thesis, Cardiff University, 2009.

2 I. E. Pomestchenko, D. E. Polyansky and F. N. Castellano, *Inorg. Chem.*, 2005, **44**, 3412–3421.

3 L. Sacksteder, M. Lee, J. N. Demas and B. A. DeGraff, *J. Am Chem. Soc.*, 1993, **115**, 8230–8238.

4 V. W. Yam, K. K. Lo, K. Cheung and R. Y. Kong, *J. Chem. Soc. Dalton Trans.*, 1997, **14**, 2067–2072.

5 T. G. Kotch, A. J. Lees, S. J. Fuerniss, K. I. Papathomas and R. W. Snyder, *Inorg. Chem.*, 1993, **32**, 2570–2575.

6 G. L. Geoffroy and M. S. Wrighton, *Organometallic Photochemistry*, Academic Press, New York, 1979.

7 C. Ko, L. T. Lo, C. Ng and S. Yiu, *Chem. Eur. J.*, 2010, **16**, 13773–13782.

8 A. J. Amoroso, M. P. Coogan, J. E. Dunne, V. Ferna, J. B. Hess, A. J. Hayes, D. Lloyd, C. Millet, S. J. A. Pope and C. Williams, *Chem. Commun.*, 2007, 3066–3068.

9 T. L. Easun, W. Z. Alsindi, M. Towrie, K. L. Ronayne, X. Sun, M. D. Ward, M. W. George, *Inorg. Chem.*, 2008, **47**, 5071–5078.

10 Z. N. Zubaidi, A. J. Metherell, E. Baggaley and M. D. Ward, *Polyhedron*, 2017, **133**, 68–74.

11 E. Orselli, G. S. Kottas, A. E. Konradsson, P. Coppo, R. Fro, L. De Cola, A. Van Dijken, M. Bu, H. Bo, P. Institut, N. Centech, W. Centre and B. U. V, *Inorg. Chem.*, 2007, **46**, 1441–1448.

12 T. Sajoto, P. I. Djurovich, A. B. Tamayo, J. Oxgaard, W. A. Goddard and M. E. Thompson, *J. Am. Chem. Soc.*, 2009, **131**, 9813–9822.

13 D. Sykes, S. C. Parker, I. V Sazanovich, A. Stephenson, J. A. Weinstein and M. D. Ward, *Inorg. Chem.*, 2013, **52**, 10500–10511.

14 L. Flamigni, A. Barbieri, C. Sabatini, B. Ventura and F. Barigelletti, in *Topic in*

current chemistry 281, Photochemistry and Photophysics of coordination compounds: Iridium, Springer, Verlag Berlin Heidelberg, 2007, pp. 143–203.

15 M. Mydlak, C. Bizzarri, D. Hartmann, W. Sarfert, G. Schmid and L. De Cola, *Adv. Funct. Mater.*, 2010, **20**, 1812–1820.

16 D. J. Stufkens, *Comments Inorg. Chem.*, 1992, **13**, 359–385.

17 D. Sykes, I. S. Tidmarsh, A. Barbieri, I. V. S, J. A. Weinstein and M. D. Ward, *Inorg. Chem.*, 2011, **50**, 11323–11339.

18 D. Sykes, A. J. Cankut, N. M. Ali, A. Stephenson, S. J. P. Spall, S. C. Parker, J. A. Weinstein and M. D. Ward, *Dalton. Trans.*, 2014, **43**, 6414–6428.

19 L. He, L. Duan, J. Qiao, R. Wang, P. Wei, L. Wang and Y. Qiu, *Adv. Funct. Mater.*, 2008, **18**, 2123–2131.

20 S. J. A. Pope, C. R. Rice, M. D. Ward, A. F. Morales, G. Accorsi, N. Armaroli and F. Barigelletti, *J. Chem. Soc. Dalton Trans.*, 2001, 2228–2231.

CHAPTER SIX

Ir(III)/Eu(III) dyad probes for anions.

6 Ir(III)/Eu(III) dyad probes for anions

This study will discuss our approach to anion (dihydrogen phosphate, acetate, benzoate and hydrogen sulfate) recognition utilising an Ir(III)/Eu(III) dyad as a luminescent probe. The anions binding to the Eu(III) unit was investigated *via* monitoring the relative emission intensity change between the two components. This results in a ratiometric sensor in which the proportions of the two different emission components change in the presence of the analyte ions.

6.1 Introduction.

The content of this chapter gives an introduction into the design of luminescent dyads containing Ir(III) and Eu(III) units, that undergo PEnT from the Ir to the Eu units, and which can be used to probe various anions in solutions.

This first part briefly describes general principles of such design, focusing on the indirect sensitisation of Eu(III) unit. The second part is devoted to the study of luminescence quenching by anions. A titration method was used to measure the concentrations of anions in MeCN solution by monitoring changes in the intensity of Eu(III) emission. Luminescent quenching results are discussed in terms of binding of the Eu(hfac)$_3$ unit with anions which releases it from the pypz binding site.

6.2 Lanthanide luminescent probes.

In spite of vast amount of data that has been already published on the sensitisation of Ln(III) ions, it is still an attractive area of research because of desirable photophysical properties of Ln(III) ions such as sharp emission bands, large Stokes shifts and long lifetimes. These properties allow the use of Ln(III) ions as luminescent probes in various applications such as labels of antigens in fluorescence based bioassays, on the study of the effects of thermal and chemical treatment on catalysts, and analysis of inorganic anions and cations.[1] Of the lanthanide ions, Eu(III) is typically used as a luminescent probe because it has emission in visible region. As mentioned above, Eu(III) has sharp (narrow) absorption and emission bands due to f-f transitions. This is due to 4f orbitals being shielded from their coordination environment by the occupied $5s^2$ and $5p^6$ orbitals. The sharp bands allow for favourable signal/noise ratio which can provide high detection sensitivity of luminescent probes for anions.[2–5] The choice of Eu(III) is also due to the relatively low excited-state energy (compared to Tb(III) required to sensitise its emissive excited states.[4] Another advantage is that, in general, the lifetimes of the Ln(III) excited states are long, due to Laporte forbidden f-f transitions. Long lifetimes are very useful for sensing purposes, however, the fact that f-f transitions are forbidden also means that direct excitation of Ln(III) ions is very inefficient (molar absorptivity Ɛ less than 1 M^{-1} cm^{-1}).[2] To overcome this problem, one can use an indirect sensitisation by a strongly light-absorbing antenna,[6] (as will be explained briefly in the next section). Typically, antennae are organic molecules which absorb strongly in UV region, due to an allowed π-π* transition. Transition metal complexes, in contrast to most organic molecules, absorb efficiently in the visible region, and can also be used as antennae for sensitised Ln(III)-based emission from lower-energy excited states as well.

There are many studies that report the use of lanthanide ion complexes with functional organic ligands in anion-probing process. For example, Bulter[7] has designed the cyclen-derived complexes (**Figure** 6-1)Figure 6-1. Luminescent Eu.L1and Eu.L2 complexes as anion sensors.[7] in two of the derivatives, two pendant quinoline and two acetate arms are used as anion receptors. The presence of the sensing arm leads to an increase of the coordination number (CN) of Eu(III) ion It is worth noting that the luminescence intensity of Eu(III) is increased (as monitored in the 596 nm emission band) upon addition of the F^- anion with no change in the emission band at 601nm (**Figure** 6-2). The feature responsible for this is likely to be a hydrogen bonding interactions from the nearby quinoline, as C-H…F.[7]

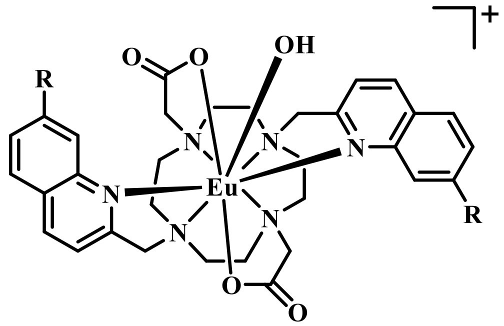

$[Eu.L^1]^+$ (R = NHCOMe)
$[Eu.L^2]^+$ (R = H)

Figure 6-1. Luminescent Eu.$L^1$and Eu.L^2 complexes as anion sensors.[7]

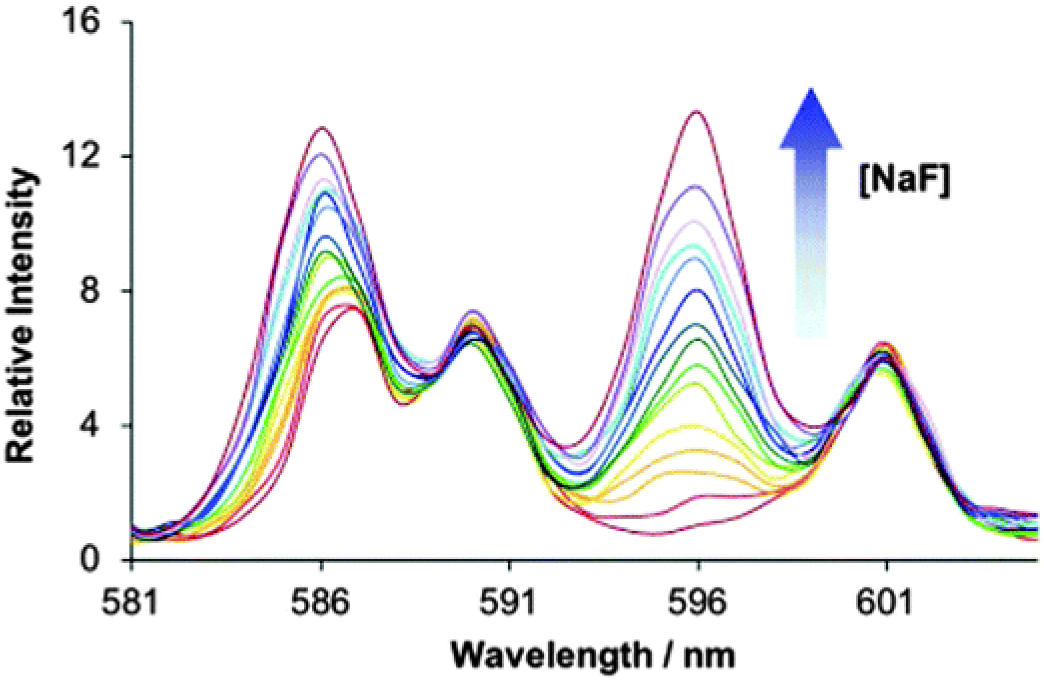

Figure 6-2. Gradual changes in the Eu(III) emission spectra upon addition F^- anion at room temperature. λ_{ex} 332 nm. Figure was reused from reference (5) with permission from the Royal Society of Chemistry.

Another approach is to utilize dinuclear Ln(III) complexes with an organic linker between the metals as sensors for biological anions. For example, Caffrey and Gunnlaugsson[8] tested a dinuclear Tb(III) complex, which coordinated to two DO_3A units and were connected through a dipicolylamide linker spacer (**Figure** 6-3), as luminescent probes for anions $H_2PO_4^-$, $H_2P_2O_7^{2-}$, NO_3^-, AcO^- and Cl^- in MeOH. Upon addition of $H_2PO_4^-$ anion, a sharp Tb(III) emission band was quenched, due to binding of the $H_2PO_4^-$ anion to the Tb(III) unit with two binding equilibria $\log K_{1:1}$ 6.6 and $\log K_{1:2}$ 7.2. Strong quenching of the emission from the same complex by pyrophosphate anion $H_2P_2O_7^{2-}$ occurred via multiple steps and could not be reliably fitted with one or two equilibria constants. NO_3^- anions caused dynamic quenching with a Stern-Volmer constant $\log K_{1:1} = 4.70 \pm 0.01$, whilst only weak binding was reported with AcO^- and Cl^- anions.[8]

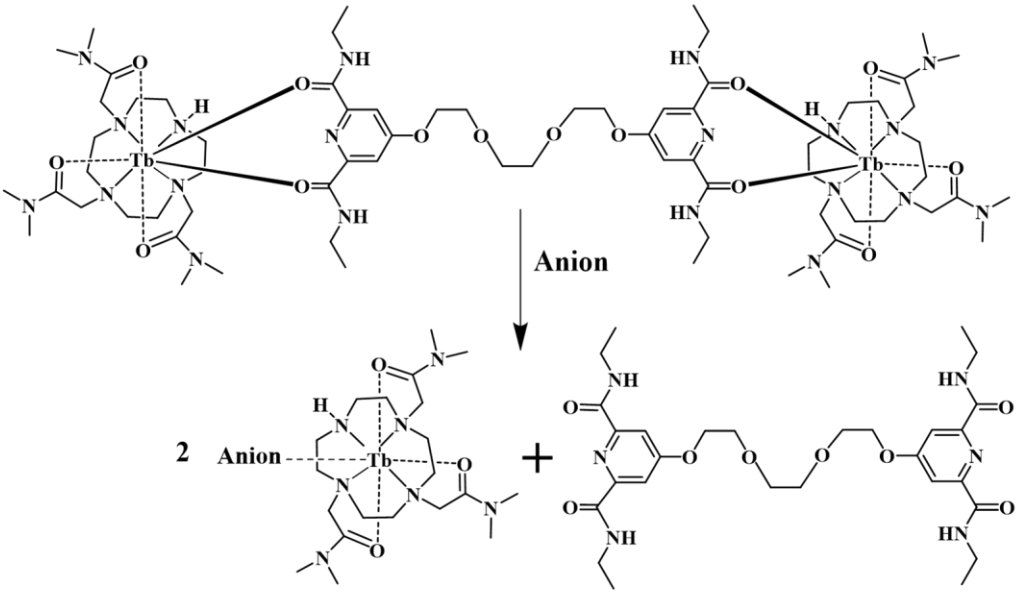

Figure 6-3. Switch (on/off) emission of di-Tb complex upon binding with anions and release of the linker spacer.[8]

Another study has used a luminescent Eu(III) complex as a probe for adenosine-5-triphosphate (ATP) which is selective for ATP over adenosine monophosphate (AMP) and adenosine diphosphate (ADP). Liu and coworkers[9] reported a Eu(III) complex derivative of cyclen (1,4,7,10- tetra-azocyclo dodecane) (**Figure** 6-4) as a luminescent probe for ATP. The Eu(III) unit is coordinated with three acetamide arms pendant from the cyclen backbond that stabilize the Eu(III) unit kinetically and thermodynamically. A fourth pendant arm is conjugated to a terpyridine substituent. The ATP anion was bound to this through two sites: the phosphate unit binds to the unsaturated Eu(III) unit, when its CN was 7, and to the terpyridine arm, *via* π-π stacking interactions. The luminescence titration shows that the emission of the Eu(III) unit was first increased upon addition of the ATP anion, and then quenched gradually with excess addition of the anion. It is suggested that anion binding between Eu(III) complex and ATP anion occurred in a 2:1 sandwich complex, where a phosphate group has coordinated to the Eu(III) metal center, and where energy transfer mechanism from the terpyridine unit as antenna to Eu(III) unit.[9]

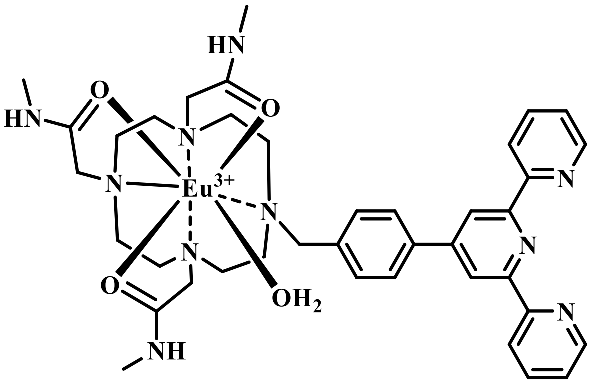

Figure 6-4. Structure of the Eu(III) probe.[9]

6.3 Luminescent d-metal complexes as anion probes.

Much exciting work in the area of anion binding using transition metal complexes has developed in the last five years. Herein, some of the luminescent complexes as probes for anions in biological applications will be discussed.

Hu *et.al.*[10] have designed a new Ir(III) complex with two ethyl naphthalene groups as a chiral barrier site, two urea groups as anion binding sites, and Ir(III) unit as a "phosphor" site (**Figure** 6-5). An Ir(III) complex was used as phosphorescence sensor for chiral anions t-Boc-amino acid like phenylglycine, phenylalanine, valine and threonine in MeCN. The urea group act as a cavity for anions due to two acidic N-H hydrogen atoms. Anions could be binding with the urea site through hydrogen bonding and electrostatic interactions. Ir(III) complex was excited at 360 nm and a Stokes-shifted emission was observed in the blue region at 560 nm upon binding with the anion. Anion was binding with Ir(III) complex in a 1:1 stoichiometry. This Ir(III) complex can thus be considered as enantioselective for small and bulky chiral guests due to the high ratio of K_D/K_L determined in these experiments.[10]

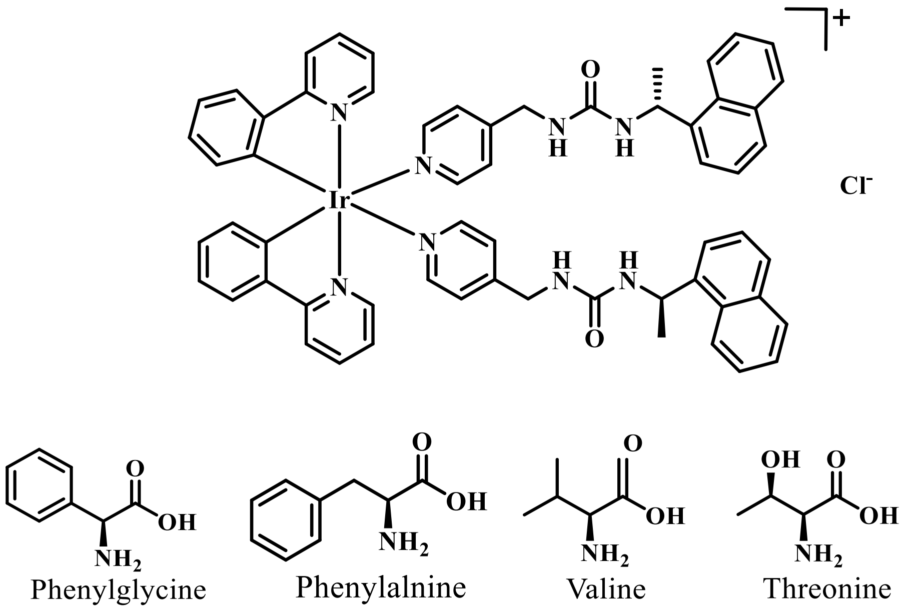

Figure 6-5. Iridium(III) complex structure and a series of amino acids tested in above work.[10]

Similarly, the coordination of the urea functionality into Ru(II)-polypyridyl complex assists the coordination sphere to be effective as a fluorescence probe for anions in the long wavelength region. Kitchen and co-workers[11] reported a new [Ru(bpy)$_3$]-based complex with urea functionality. The switch on/off principle was used to distinguish between phosphate [$H_2PO_4^-$] and pyrophosphate [$HP_2O_7^{3-}$]: emission intensity at 625 nm (450 nm excitation) was increased upon addition of [$H_2PO_4^-$] but quenched upon addition [$HP_2O_7^{3-}$]. ^{1}H NMR titration results confirmed hydrogen bonding of the phosphate substrates with the urea receptor moiety. Both anions were binding in a 1:1 ratio due to fitting non-linear Stern-Volmer plot to both cases. The interaction of the complex **Ru.NO$_2$** (**Figure** 6-6) with AcO$^-$ was investigated and showed that 1 equivalent of AcO$^-$ binds to the pendant urea moiety, whereas the second equivalent binds with metal ion centre via electrostatic interaction. Interestingly, there are no luminescence no changes seen in the presence of F$^-$.[11]

Elmes *et.al.*[12] demonstrated another Ru(II) polypyridyl complex system, **Ru.Nap.NH$_2$** (**Figure** 6-6) for anion sensing in MeCN. This complex has shown contrasting behaviour to that of **Ru.NO$_2$**, **Figure** 6-6. **Ru.Nap.NH$_2$** complex showed >90% luminescence quenching emission with F$^-$, while the other anions like Cl$^-$, AcO$^-$ and $H_2PO_4^-$ also give quenching but to a smaller degree due to competition between hydrogen bonding and deprotonation at 4-amino unit of the naphthalimide fluorophore.[12]

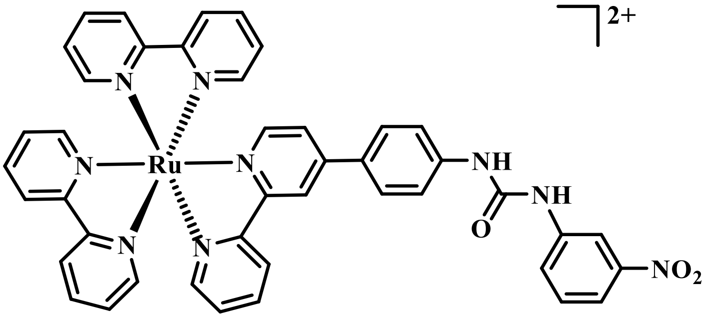

Ru.NO2

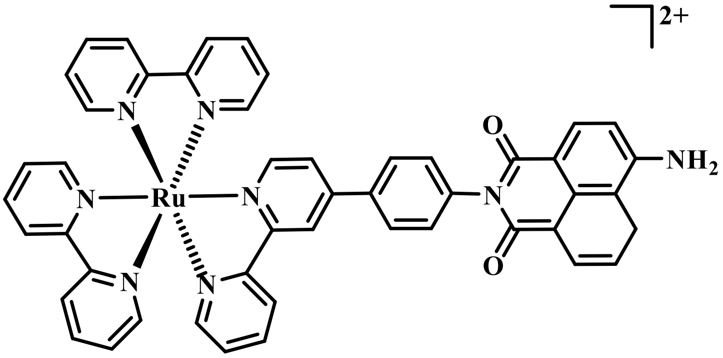

Ru.Nap.NH2

Figure 6-6. Structures of the anion-sensing complexes Ru.NO2 and Ru.Nap.NH2.[12]

More examples of metal complexes that can be used as luminescence sensors for anions due to utilising various ligands can be given. Li *et.al.*[13] has selected two different ligands and coordinated them with different metals (Re, Pt, Rh) to prepare probe systems (**Figure** 6-7**)**. All these complexes were demonstrated to be highly efficient probes for anions. L1 has an NH group while L2 has methyl substituents on the N atoms. Upon addition of F^- anion to complexes, the luminescence emission from **Re.1** were increased due to deprotonation of the NH group in the imidazole ring. However, this deprotonation cannot happen in **Re.2** which does not show this effect.[13]

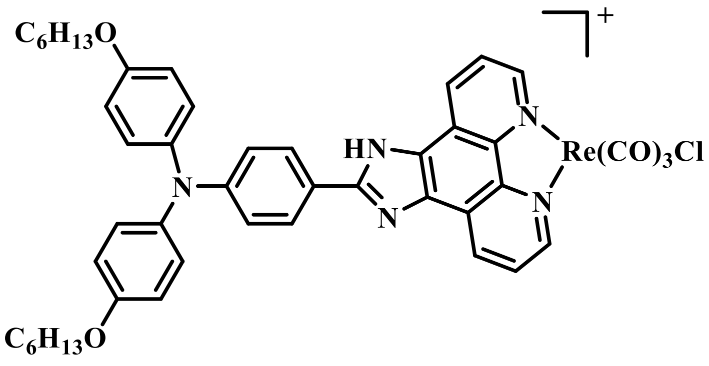

Re.1

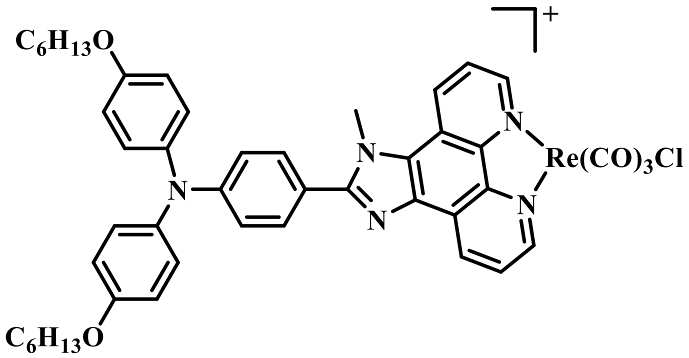

Re.2

Figure 6-7. Structures of Re.1 and Re.2 complexes.[13]

Luminescence quenching by Cl$^-$ ion of the emission of the Pt(II) complex [Pt(NCN)(S)]TfO , (NCN = 1,3-bis(2-*N*-phenylbenzimidazolyl)benzene, S = solvent and TfO$^-$ = triflate anion), was examined in aqueous solution. Dorazco-Gonzalez[14] reported Pt(II)-based (**Figure** 6-8) probes for Cl$^-$ in DMF and MeCN solution. Excitation of this Pt(II) complex at 360 nm showed emission peaks at 500 nm and 537 nm, which were quenched upon addition Cl$^-$ anion with low binding constant log$K_{1:1}$=2-3.[14]

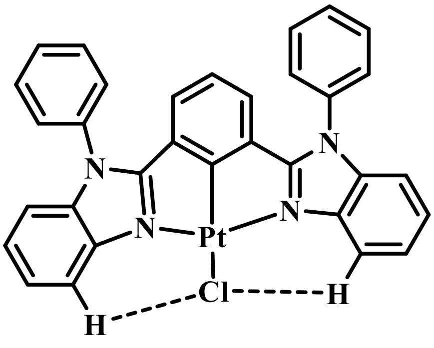

Figure 6-8. Structure of Pt(II) complex.[14]

6.4 Luminescence quenching and Stern-Volmer equation.

Luminescence quenching can result from a variety of processes that decrease the luminescence of a substance due to the interaction of the luminophore with another molecule.[15] Luminescence quenching can occur due to many processes, such as energy transfer, collisional quenching, static (complex formation in the ground state) quenching and electron transfer reactions from the excited state.

6.4.1 Static and Dynamic quenching.

There are two types of emission quenching: static and dynamic quenching. The two scenarios require collision between the luminophore and quencher. In dynamic quenching, the molecule of the luminophore in its excited state collides with the quencher, and returns from the excited state to the ground state with no emission of a photon. In static quenching, a complex is formed between the ground state of the luminophore, and the quencher. This chapter will concern with types of quenching, whether quenching depends on formation of ground state complexes (static quenching) or diffusion collisions (dynamic quenching) or a mixture of both of them.

In order to better understand the quenching of Eu(III) luminescence, dynamic or static quenching will be assessed utilising a Stern-Volmer plot. This is a plot of the ratio of emission intensities (I_0/I) on the y-axis, as a function of the quencher's concentration on the x-axis. If the plot is linear, the slope represents the Stern-Volmer constant (in the static quenching), or a product of quenching rate constant and emission lifetime (τ_0) in the absence of the quencher (dynamic quenching). A Stern-Volmer equation in two models of luminescence quenching, dynamic and static quenching, are: -

$I_0/I = 1 + k_q\tau_0[Q]$ ………………….(eq.1) Dynamic quenching process.

$I_0/I = 1 + K_{SV}[Q]$ ………………….. (eq.2) Static quenching process.

I_0 = the luminescence intensity without quencher.

I = the luminescence intensity with quencher.

k_q = bimolecular quenching rate constant, $M^{-1}\ s^{-1}$.

τ_0 = lifetime of the excited state of the complex in the absence of the quencher.

[Q] = molar concentration of the quencher.

K_{SV} = Stern – Volmer quenching constant, M^{-1}.

The most common quenching form is collisional quenching. This type of quenching is caused from collisions between quencher and luminophore during the lifetime of the excited state, which creates another deactivation pathway in competition with the luminescence emission. The efficiency of the quenching process depends on the rate of diffusion of the quencher in solution and the rate of collision with the luminophore in its excited state. Increase in the quencher's concentration affects emission intensity and lifetime of the excited state of the luminophore. One of the best-known substances that act as a collisional quencher is molecular oxygen; other typical quenchers are molecules with heavy atoms. Transition metal complexes emit (in almost all cases) from a triplet excited state, which is long lived, and thus there is ample time for quenching with dioxygen, which has a triplet ground state. The type of quenching depends upon the type of luminophore and quencher, and could be either EnT or PET.mechanism, or in some cases, a combination of the two (these mechanisms were briefly explained in the **Chapter 1**.

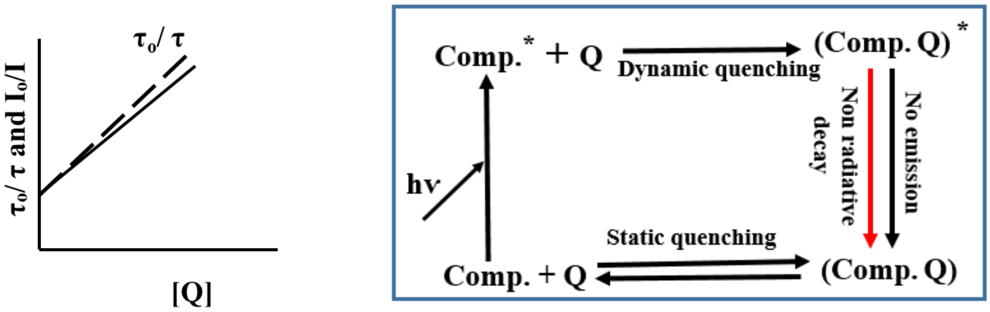

Figure 6-9. Dynamic quenching plot.

6.4.1.1 Static quenching.

Static quenching can be defined as the interaction between quencher and luminophore in the ground state. In this case, only the emission intensity is reduced on increasing of the concentration of the quencher due to increased luminophore-quencher associations, while there is no change in the emission lifetime. This definitive feature allows to distinguish between dynamic and static quenching. In such a case, luminescence quenching is a function of quencher concentration, Stern-Volmer eq. (2) describes the static quenching through complex formation. The slope can be defined as the association constant between quencher and luminophore. From knowing the slope and emission lifetime without the quencher, one can easily calculate the quenching rate constant.

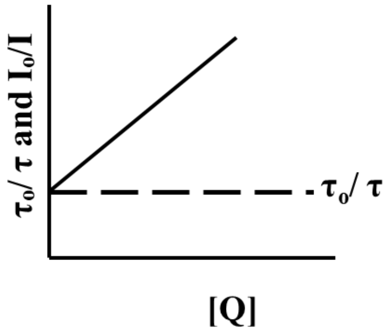

Figure 6-10. Static quenching Stern-Volmer plot.

6.4.1.2 Mixture of static and dynamic quenching.

In many cases, a quencher can be quenching the luminophore emission by both static and by dynamic routes at the same time. The resulting Stern-Volmer plot shows upward curvature and the following relation holds: -

$I_0/I= (1+K_q\tau_0[Q])\ (1+K_D[Q])$ ………..(eq. 3) Dynamic and static quenching.

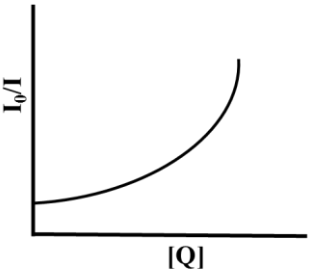

Figure 6-11. Upward curvature plot of combined between two processes complex formation (static quenching) and collision (dynamic quenching).

6.5 Basic design principles for luminescent probes: an Ir(III)/Eu(III) dyad.

The use of chelating antennae groups coordinated to lanthanide ions is a suitable way to sensitize Ln(III) and achieve energy transfer because of the greater molar absorption coefficient of the antenna, and higher association constant and kinetic inertness due to chelate effect. A chelating ligand as an antenna design also protects the Ln centre from water molecule coordination, thus preventing luminescence quenching of the Ln(III) centre by water molecules via energy transfer to the O-H vibration.[16–18]

The bis-bidentate bridging ligand ($L^{bi\text{-}ph}$) (crystal structure shown in **Figure** 6-12)**,** contains biphenyl linker spacer connected in both ends with chelating pypz unit so that it can form dinuclear complexes. One bidentate pypz chelating unit coordinates to a Ir(III)/bis(phenylpyridine) unit to give a strongly luminescent metal centre (**Figure** 6-13).[19] On the other hand, second chelating pypz ligand site can coordinate with a Ln(III) unit to give an Ir/Ln dyad **Figure** 6-14. Interestingly, as shown in **Figure** 6-12, the pypz rings are not arranged in the usual transoid manner when they are un-coordinated, but they form a 5-membered chelate ring with the chloroform protons because of H-bonding.

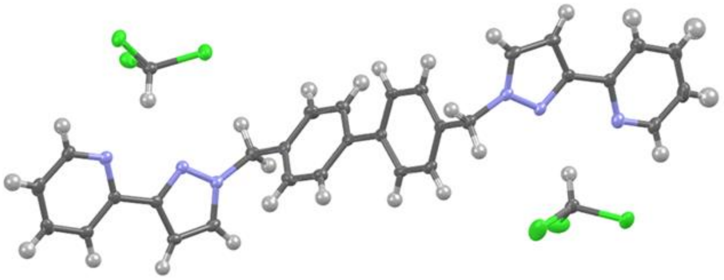

Figure 6-12. Crystal structure of $L^{bi\text{-}ph}$ created by slow evaporation of $CHCl_3$ solution in the NMR tube. Thermal ellipsoids shown at 50% probability.

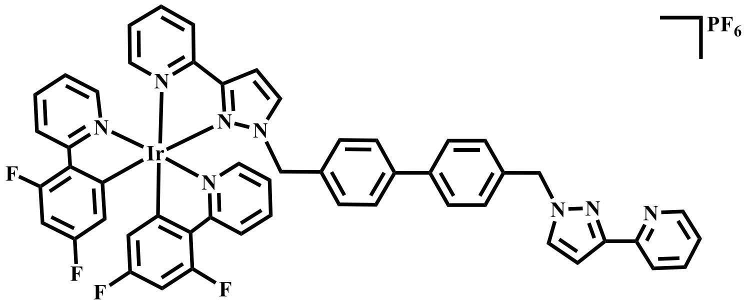

Figure 6-13. Structure of the Ir(III) antenna chromophore.

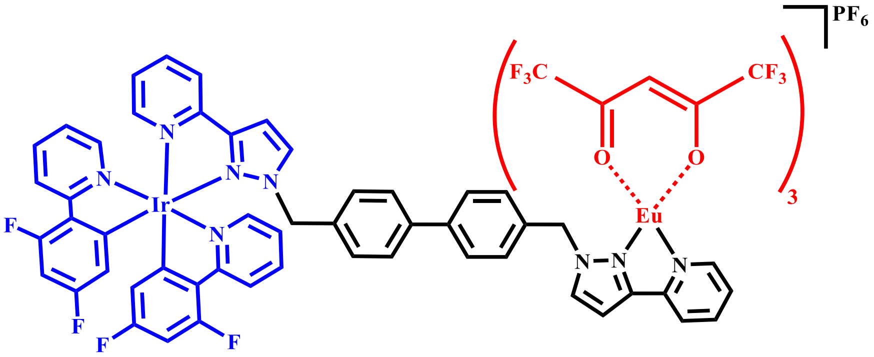

Figure 6-14. Structure of Ir(III)/ Eu(III) dyad in $^{F/F}$Ir•L$^{bi\text{-}ph}$•Ln when Ln=Eu (III).

The other characteristics of our design are high spin orbit coupling of Ir(III) (ε_{Ir} = 4430 cm^{-1}), the long lifetime and high energy of the Ir(III)-based excited state (mixed ^{3}MLCT and ^{3}LC character), thermal stability and kinetic inertness.[19] The successful energy transfer process from the Ir(III) unit to the Eu(III) unit requires the antenna group ($^{F/F}$Ir•L$^{bi\text{-}ph}$) to have an excited state energy higher than the emissive ^{5}D state of the Eu(III) ion to prevent reverse thermal repopulation of the $^{F/F}$Ir•L$^{bi\text{-}ph}$•PF$_6$ triplet state, as will be explained.[20–22] In addition, the length of the linker between Ir(III) unit and Eu(III) unit affects energy transfer according to either the Dexter or Förster mechanisms (the mechanisms explained briefly in **Chapter 1**).

On initial excitation of the Ir(III) unit, it is excited from the ground state to the singlet excited state. Secondly, an ISC process, converts the singlet excited state to the triplet excited state which is long-lived and normally phosphorescent. Formation of the Ir(III)-based triplet state is followed by energy transfer from the d-metal center to the f-f excited state of the lanthanide ion. Finally, the f-f excited state of the Ln(III) deactivates to the ground state, emitting its characteristic luminescence, as shown in **Figure** 6-15.[2] From the photophysical properties of $^{F/F}$Ir•L$^{bi\text{-}ph}$•PF$_6$ complex, it can be considered a good chromophore to sensitise Eu(III) unit with the wavelength of light which is suitable for many biological studies.

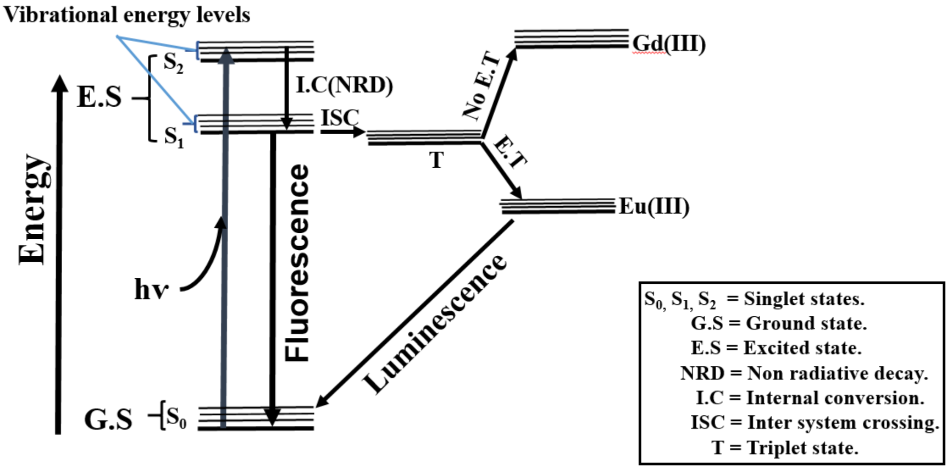

Figure 6-15 Shows photochemical process of sensitising Eu(III) luminescence emission. Absorption spectrum of the $^{F/F}$Ir•L$^{bi\text{-}ph}$•PF$_6$.

The absorption spectrum of mononuclear $^{F/F}$Ir•L$^{bi\text{-}ph}$•PF$_6$ is shown in **Figure** 6-16 in MeCN at 298K. The $^{F/F}$Ir•L$^{bi\text{-}ph}$•PF$_6$ complex exhibit bands in the UV and in the Visible region. The broad band between 300 and 350 nm can be related to the spin allowed singlet ^{1}(π-π*) transition, which is localised on the cyclometallating (C^N) phenylpyridine ligands, and (N^N) bipyridine (bpy) ancillary ligand. In the visible region between 350 – 400 nm, a weaker band can be assigned to the mixture of singlet and triplet MLCT and (π-π) transitions. A mixture of ^{1}MLCT/^{3}LC can form the lowest energy absorption band,[23] while a weak band past 400 nm represents a spin-forbidden charge-transfer transition.[20] The absorption spectrum of $^{F/F}$Ir•L$^{bi\text{-}ph}$•PF$_6$ is similar to that of the other Ir(III)-phenylpyridine type complexes.[24]

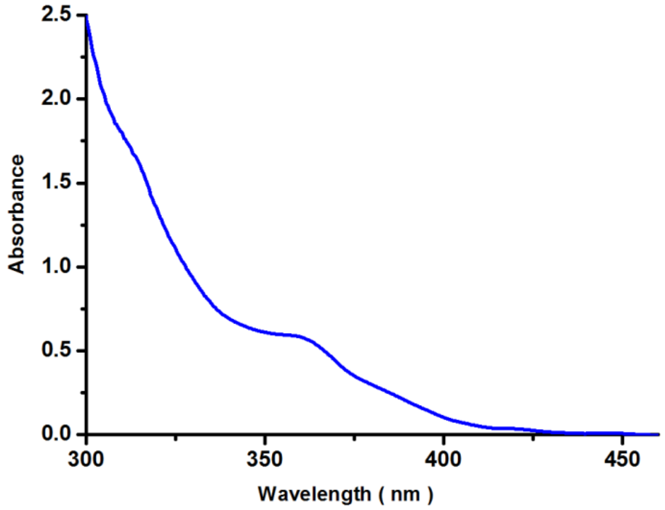

Figure 6-16. UV-Vis absorption spectra for $^{F/F}$Ir•L$^{bi\text{-}ph}$•PF$_6$ in MeCN at 298 K.

6.6 Emission properties of the $^{F/F}$Ir•L$^{bi\text{-}ph}$•PF$_6$.

Luminescence of $^{F/F}$Ir•L$^{bi\text{-}ph}$•PF$_6$ was measured in MeCN solution at room temperature when excited at 360 nm. The complex emission (**Figure** 6-17) is vibronically structured, with two lower-energy features at around 480 and 515 nm. The luminescence arises principally from an ^{3}LC state probably with an admixture of ^{3}MLCT state character.

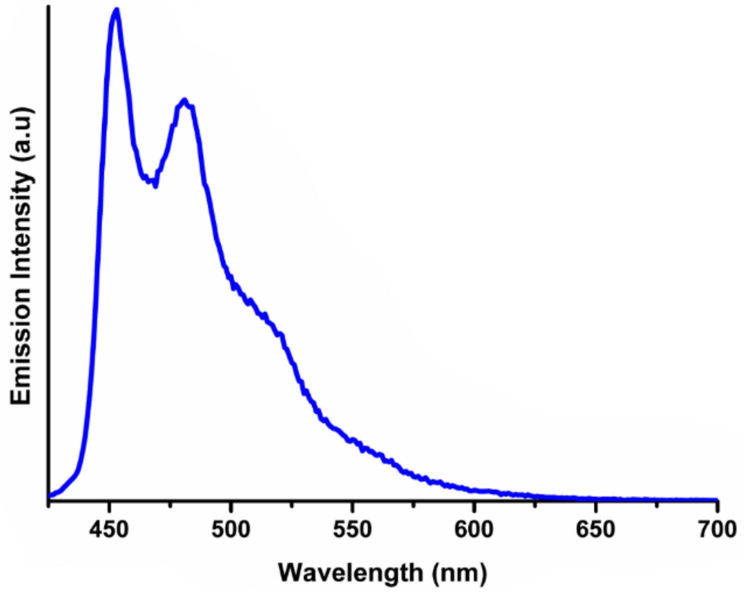

Figure 6-17. Luminescence spectrum of $^{F/F}$Ir•L$^{bi\text{-}ph}$•PF$_6$ complex in MeCN, $\lambda_{exc.}$=360 nm at 293K.

6.7 Absorption spectrum for $^{F/F}$Ir•L$^{bi\text{-}ph}$•PF$_6$ in the course of titration with Eu(hfac)$_3$•2H$_2$O and Gd(hfac)$_3$•2H$_2$O.

The UV-Vis absorption measurements were recorded during titration of $^{F/F}$Ir•L$^{bi\text{-}ph}$•PF$_6$ with Eu(hfac)$_3$•2H$_2$O and Gd(hfac)$_3$•2H$_2$O in MeCN at 298K. The absorption spectra are shown in **Figure** 6-18 and **Figure** 6-19, respectively. The shape of the absorption spectrum for both absorption titrations with Ln (Eu and Gd) does not change at the wavelength 360 nm and longer, as the concertation of the host $^{F/F}$Ir•L$^{bi\text{-}ph}$•PF$_6$ remained constant during the titration experiment. The wavelength 360 nm was used as excitation wavelength for luminescence measurements. There is an increase in the absorption of the bands in the high energy region, below 350 nm, upon incremental addition of Eu(hfac)$_3$•2H$_2$O to the solution. These new bands can be assigned to the spin allowed ^{1}LC(π-π) transition of $(hfac)_3$ ligand. Another evidence is that this new absorbance is attributed to the hfac ligands and not to the Eu(III) metal centre is that absorption titration of Ir(III) with Gd(III) unit gave the same changes, as shown in **Figure** 6-18 and **Figure** 6-19**.**

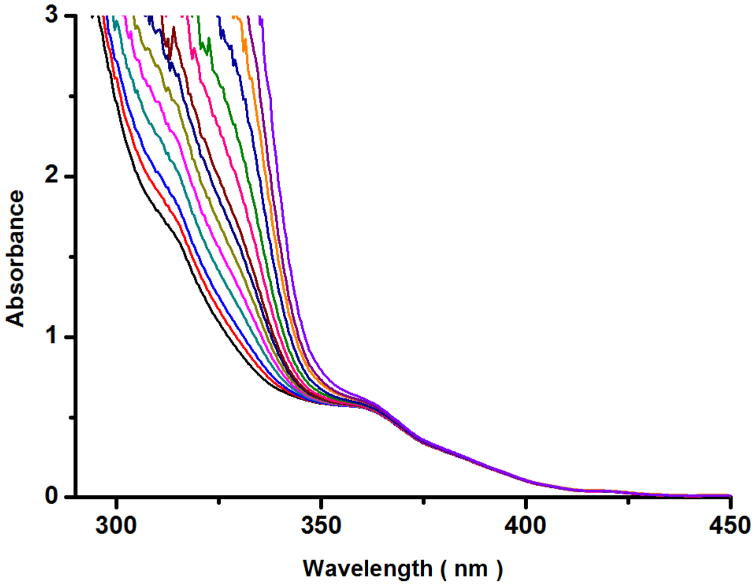

Figure 6-18. UV-Vis absorption spectra during the titration $^{F/F}$Ir•L$^{bi\text{-}ph}$•PF_6 [~10^{-4}M] with $Eu(hfac)_3$•$2H_2O$ [1.55×10^{-3}M] in MeCN at 293K.

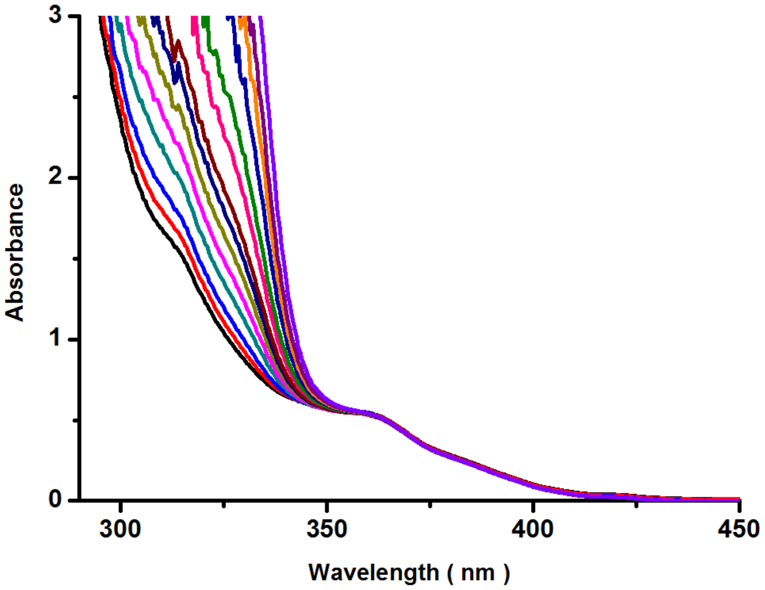

Figure 6-19. UV-Vis absorption spectra during the titration $^{F/F}$Ir•L$^{bi\text{-}ph}$•PF_6 [5.29×10^{-5} M] with [$Gd(hfac)_3$•$2H_2O$] up to [4.83×10^{-4} M] in MeCN at 298K.

6.8 Luminescence properties of $^{F/F}Ir{\bullet}L^{bi\text{-}ph}{\bullet}PF_6$ in the presence of $Eu(hfac)_3{\bullet}2H_2O$ and $Gd(hfac)_3{\bullet}2H_2O$.

The purpose of designing Ir(III)/Eu(III) dyad is to make a ratiometric sensor whose emission properties are modulated through binding between Eu(III) unit and the anion of interest. Binding Eu(III) with anions can be detected through changes in the Eu(III) emission, which was assumed to will occur due to changes in the coordination sphere around the Eu(III) ion when the anion is bound. The Ir(III) → Eu(III) energy transfer was investigated by titration of red emitting $Eu(hfac)_3{\bullet}2H_2O$ (5.07×10^{-3} M) into the solution of $^{F/F}Ir{\bullet}L^{bi\text{-}ph}{\bullet}PF_6$ (5.55×10^{-5} M) complex in air equilibrated MeCN at room temperature. During the titration, the Ir-based intensity emission was gradually quenched by coordination of the $Eu(hfac)_3$ unit to the secondary pypz coordinate site of $^{F/F}Ir{\bullet}L^{bi\text{-}ph}{\bullet}PF_6$. As it binds the intensity of sensitised Eu(III) emission gradually increases, since Ir(III)-Eu(III) PEnT occurs. The titration was continued until there is no further observed decrease in the Ir(III) luminescent emission intensity, upon which the formation of Ir(III)/Eu(III) dyad was considered complete. The overall luminescence color is changing from blue emission, which is from $^{F/F}Ir{\bullet}L^{bi\text{-}ph}{\bullet}PF_6$, to the red emission, which is from the Eu(III) centre of the Ir/Eu dyad at the end of the titration. Part way through the process, a balance between blue emission from $^{F/F}Ir{\bullet}L^{bi\text{-}ph}{\bullet}PF_6$ and mostly red emission from $^{F/F}Ir{\bullet}L^{bi\text{-}ph}{\bullet}Eu$ gives white luminescence emission. The changing of colour was observed under the UV-lamp. **Figure** 6-20 shows luminescence emission spectra through the titration process.[20]

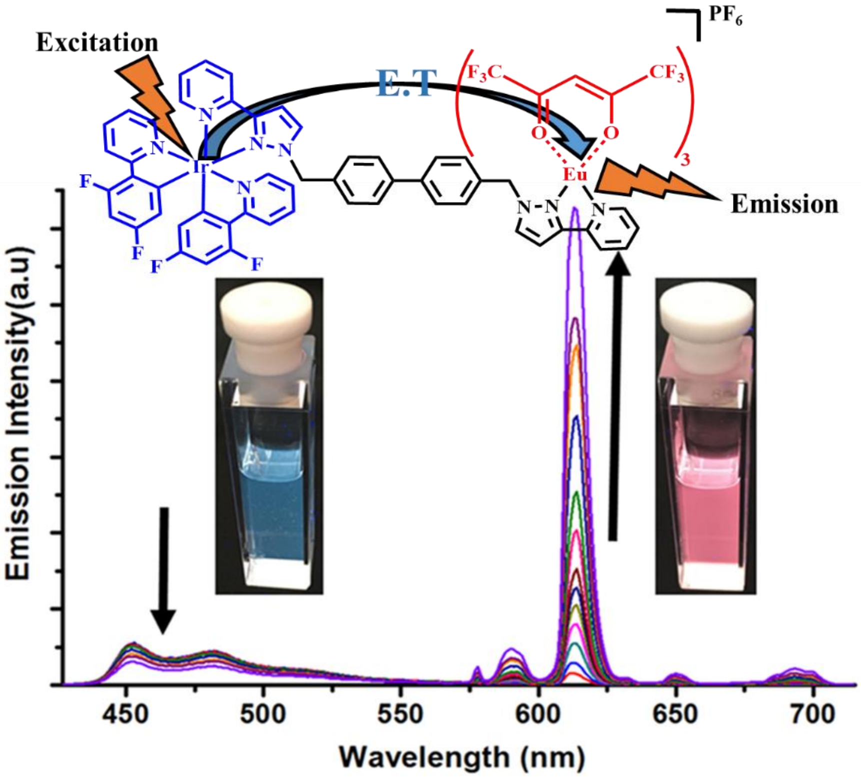

Figure 6-20. Quenching in the Ir(III) unit emission in $^{F/F}Ir{\bullet}L^{bi\text{-}ph}{\bullet}PF_6$ complex with energy transfer upon addition $Eu(hfac)_3(H_2O)_2$ in MeCN at 298 K. $\lambda_{exc.}$=360 nm.

The triplet energy level of $^{F/F}Ir{\bullet}L^{bi\text{-}ph}{\bullet}PF_6$ lies at 22,000 cm^{-1}, which acts as the energy donor, while the $^5D_0$ state of the $Eu(hfac)_3$ unit lies at 17,300 cm^{-1}, which acts as energy acceptor. This results in an energy gap between the two excited states of about 4,700 cm^{-1}, where minimally about 1700 cm^{-1} is needed to prevent back energy transfer.[19] The suitable excitation wavelength was used, 360 nm, in order to excite the Ir(III) unit, and prevent direct excitation of the Eu(III) unit. The manifold of Eu(III) emission peaks of (578, 590, 612, 650 and 690) nm,[25] attributed to ($^5D_0 \rightarrow {}^7F_0$, $^5D_0 \rightarrow {}^7F_1$, $^5D_0 \rightarrow {}^7F_2$, $^5D_0 \rightarrow {}^7F_3$ and $^5D_0 \rightarrow {}^7F_4$), was observed following addition of $Eu(hfac)_3.2H_2O$ to solution of $^{F/F}Ir{\bullet}L^{bi\text{-}ph}{\bullet}PF_6$, changing colour essentially from blue to red, when emission of $^{F/F}Ir{\bullet}L^{bi\text{-}ph}{\bullet}PF_6$ complex is partialy quenched, and luminescence of Eu(III) unit dominates. The limiting amount of Ir→Eu photoinduced energy transfer was achieved after addition of 1020 µL (3 equiv.) of $Eu(hfac)_3{\bullet}2H_2O$.

Also, $[Gd(hfac)_3{\bullet}2H_2O]$ was titrated to $^{F/F}Ir{\bullet}L^{bi\text{-}ph}{\bullet}PF_6$ complex solution in the same way described for $Eu(hfac)_3{\bullet}2H_2O$ complex. No PEnT process occurs from Ir(III) unit to Gd(III) unit as the lowest excited state of Gd(III) is too high in energy, so the emission colour of the Ir/Gd dyad was still blue which represents the Ir(III) based emission (**Figure** 6-21).

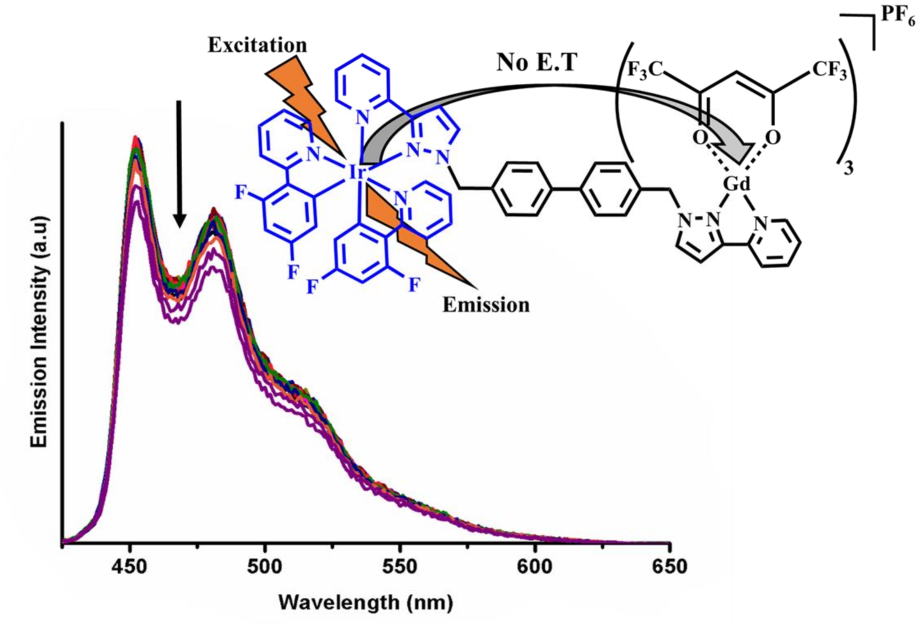

Figure 6-21. Quenching in the Ir(III) unit emission in $^{F/F}$Ir•L$^{bi\text{-}ph}$•PF$_6$ complex with no energy transfer on addition Gd(hfac)$_3$(H$_2$O)$_2$ in MeCN at 298 K. $\lambda_{exc.}$=360 nm.

The luminescence emission spectra were recorded during the titration as shown in the **Figure** 6-21. The emission spectrum shows vibrational resolved Ir(III) emission only, in the region 450-500 nm, which is an indicator there is no energy transfer to the Gd(III) unit. Interestingly, a partial small quenching of Ir(III) unit emission was observed in spite of a PEnT process being thermodynamically impossible. Therefore, the quenching process could be explained through PET mechanism[26, 27] rather than PEnT mechanism, and the electrostatic connection of [Gd(hfac)$_3$] with a vacant pendant pypz group facilitates PET mechanism for luminescence emission quenching of Ir(III)-based complex. Due to the Gd(III) unit not being able to act as an energy acceptor from Ir(III) unit, the Ir(III)/Gd(III) dyad was used in control experiments.

The Ir-based emission decay of Ir(III)/Eu(III) dyad is fitted to two exponential decay components with long and short lifetimes, for a satisfactory χ^2 equal to unity. The long lifetime component is 203 ns, corresponding to the free Ir(III) unit during the titration, while the short lifetime of *ca.* 27 ns corresponds to *ca.* 90% quenching of the Ir(III) unit emission in the Ir/Eu dyad by the subsequent Ir(III) →Eu(III) energy transfer process. The same scenario lifetime fitting was occurred with Ir(III)/Gd(III) dyad in two long- and short lifetime *ca.* 213 and 27 ns respectively, with the 27 ns component presumably corresponding to the small amount of PET which leads to slight quenching of Ir-based emission. These recorded lifetimes of Ir(III)/Eu(III)

and Ir(III)/Gd(III) dyads were used to calculate the rate constant energy transfer ca. 2.3×10^5 s^{-1}, which is taken from the **eq. (4-1).**[28]

6.9 Luminescence quenching studies with anions.

6.9.1 Quenching of Luminescence.

6.9.1.1 Principle of luminescence quenching by anion sensing.

Quenching of luminescence results in a decrease of the luminescence intensity of a substance. An Ir(III)/Eu(III) dyad is used as the basis of a ratiometric sensor for anions. A PEnT process occurs in Ir(III)→ Eu(III) dyad (as mentioned in previous section) by partial quenching (~90%) of the Ir(III) emission with concomitant sensitisation of Eu(III) emission in the visible region. Interestingly, binding the Eu(III) unit with anions, such as acetate, benzoate, dihydrogen phosphate and hydrogen sulfate, leads to release of Eu(III) from the pypz binding site connected to the ${}^{F/F}Ir{\bullet}L^{bi\text{-}ph}{\bullet}PF_6$ unit, at which point PEnT process does not happen and the sensitised emission from the Eu(III) unit disappears, as shown briefly in the **Figure** 6-22. This results in a progressive colour change from red to blue as the red emission component is not sensitised and the blue emission component increases in intensity.

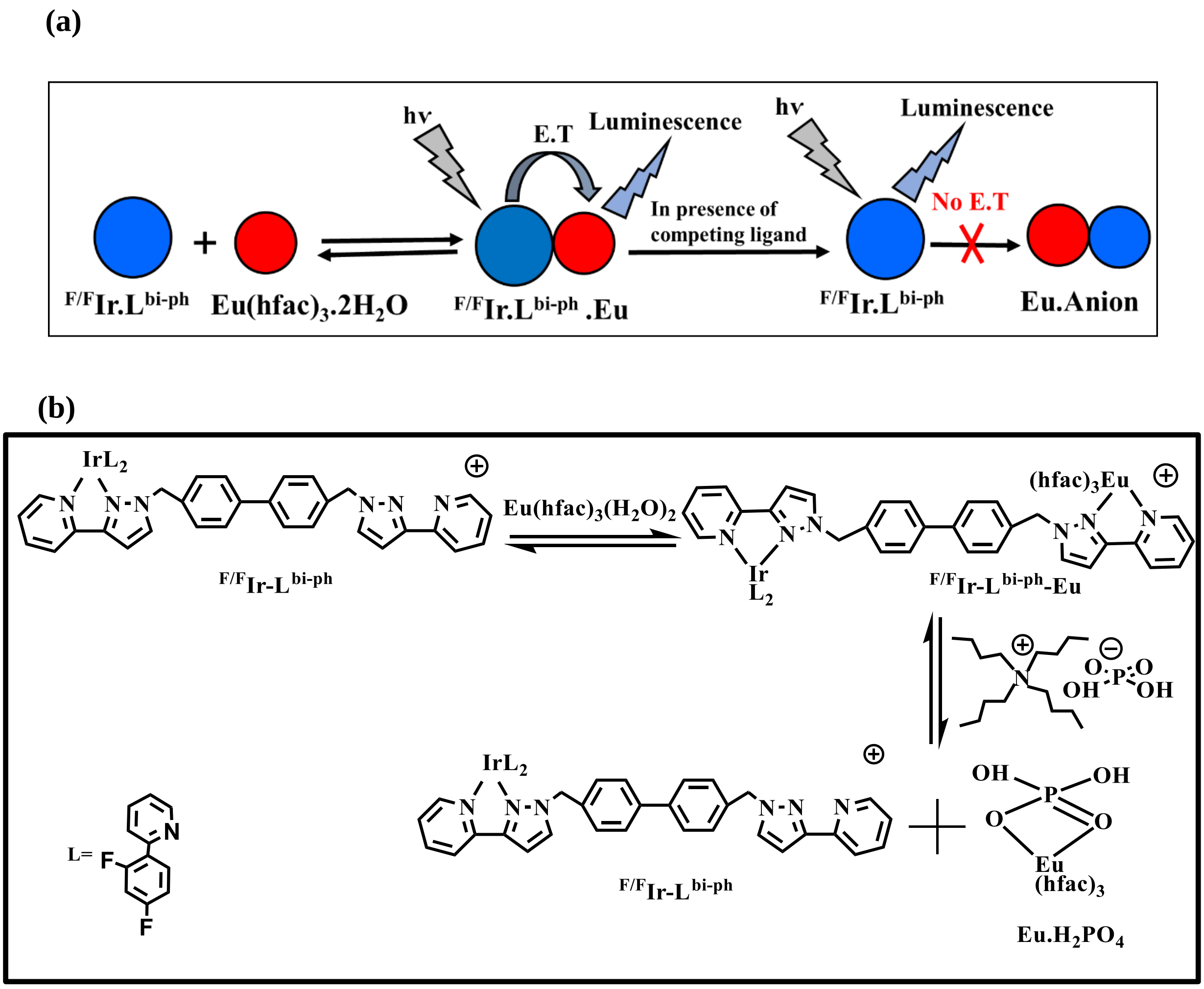

Figure 6-22 (a) Schematic illustration of $^{F/F}$Ir•L$^{bi\text{-}ph}$•Eu(hfac)$_3$ luminescence ‘‘ON-OFF’’ switch (quenching) process by anions. (b) Chemical equilibrium formation of $^{F/F}$Ir•L$^{bi\text{-}ph}$•Eu(hfac)$_3$ and H_2PO_4 interaction with $^{F/F}$Ir•L$^{bi\text{-}ph}$•Eu(hfac)$_3$.

6.10 Anions probes.

6.10.1 Use of a luminescent Ir(III)/Eu(III) dyad for ratiometric anion sensing.

The sensitised luminescence from the Eu(III) excited state in the Ir/Eu dyay emission can be controlled by the addition of anions (acetate, benzoate, dihydrogen phosphate and hydrogen sulfate). These anions act as competing ligands for the Eu(III) centre and remove it from the dyad as shown in **Figure** 6-22, therefore, excitation of Ir(III) unit only results in blue Ir(III) luminescence. In our study, all the anions act in similar way, by reducing the Eu(III) luminescence at λ_{max} 612nm and increasing Ir(III) emission intensity at λ_{max} 455 nm, with only very small differences in the individual emission spectra but a large difference in the balance between them.

The main principle of interaction of Eu(III) unit with the analyte anions is that O-donors are "harder" donors than the N-donors of the pypz group, which means that they will bind to the {Eu(hfac)$_3$} unit and displace it from the pypz donor.[29] In contrast, the Ir(III) unit is not affected by the added anions as the Ir(III) is kinetically inert and strongly bonded to its ligand set. Also, Eu(III) unit possess a positive charge most likely to bind with anions.[30]

All added anions can in principle coordinate to the Eu(III) unit as bidentate O-donor chelating ligands. In order to investigate the effect of the anions on Ir/Eu(III) emission, the following parameters were kept the same. There are some parameters to control the interact anions with Eu(hfac)$_3$ unit:

1- O-anion donor atom, which is coordinated easily with Eu(III) unit.

2- All anions were used as salts.

3- Titrated with the same lanthanide, Eu(hfac)$_3$.

4- The same Ir-based antenna group was used, $^{F/F}$Ir•L$^{bi\text{-}ph}$.

5- MeCN is used as a solvent.

The effect of anions on quenching Eu(III) emission probably depends upon structure, geometry and electron density of the anions. Results with different anions are discussed in the next section.

6.11 Results and Discussion.

6.11.1 The anions set

At the beginning of this study, we had accumulated luminescence titration data using 4 salts, (Tetrabutyl ammonium dihydrogen phosphate, tetrabutyl ammonium hydrogen sulfate, tetrabutyl ammonium acetate, and tetrabutyl ammonium benzoate) respectively as in **Figure** 6-23, with the $^{F/F}$Ir•L$^{bi\text{-}ph}$•Eu(hfac)$_3$ dyad complex in MeCN at room temperature being used as the luminescent sensor. These anions had provided the basis for ratiometric sensing and how coordination of anions to Eu(III) metal centre in a bidentate chelating way allow gradually changing in relative intensities of Eu(III) emission spectrum.

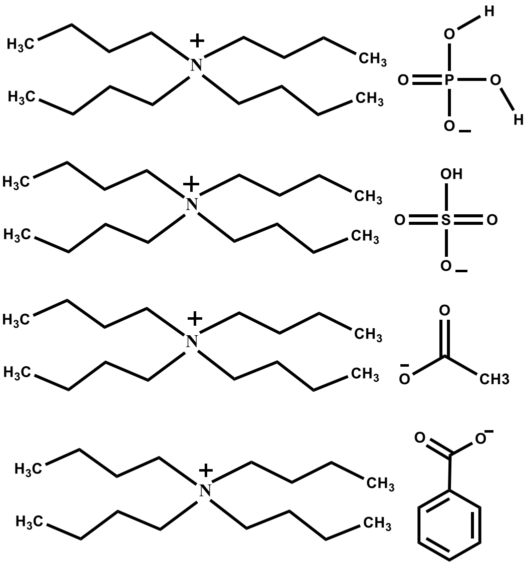

Figure 6-23. The anions set dihydrogen phosphate, hydrogen sulfate, acetate, and benzoate structures used in titration with $^{F/F}$Ir•L$^{bi\text{-}ph}$•Eu(hfac)$_3$ complex.

6.11.2 Absorption titration spectra for [$^{F/F}$Ir•L$^{bi\text{-}ph}$• Eu]PF$_6$ with various anions.

All the absorption data during the titration of $^{F/F}$Ir•L$^{bi\text{-}ph}$•Eu(hfac)$_3$ with anions (acetate, dihydrogen phosphate, benzoate, and hydrogen sulphate) were made in MeCN at room temperature; result of acetate absorption as example is shown in **Figure** 6-24. All absorption spectra show the same behaviour mentioned previously in this chapter, there is no change at 360 nm which is the wavelength used for excitation. However, in the high energy UV region there is a gradual increase in absorbance during the titrations which must be associated with the anions that are being added to the mixture. The equilibrium arising from the additional anions is shown in **Figure** 6-22-**b**.

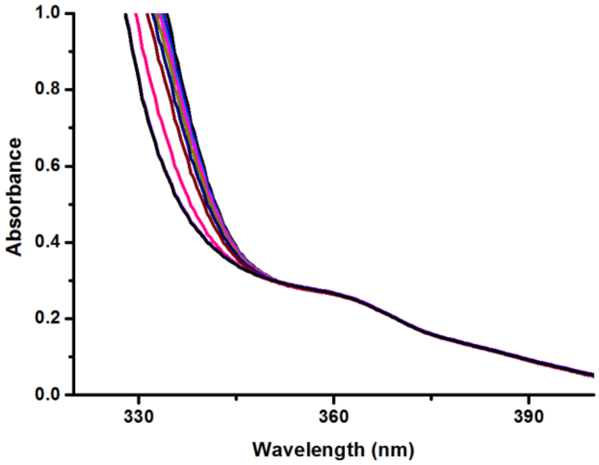

Figure 6-24. UV-Vis. absorption spectrum of $^{F/F}$Ir•L$^{bi\text{-}ph}$•Eu(hfac)$_3$ complex (~10^{-4}M) titrated with acetate up to (1.4×10^{-3}M) in MeCN at 293K.

6.11.3 General procedure of titration $^{F/F}$Ir•L$^{bi\text{-}ph}$•Eu(hfac)$_3$ with anion.

The equilibrium process that occurs on titration of a salt of an anion into a solution of the Ir/Eu dyad in MeCN using dihydrogen phosphate as an example is shown in **Figure** 6-25.

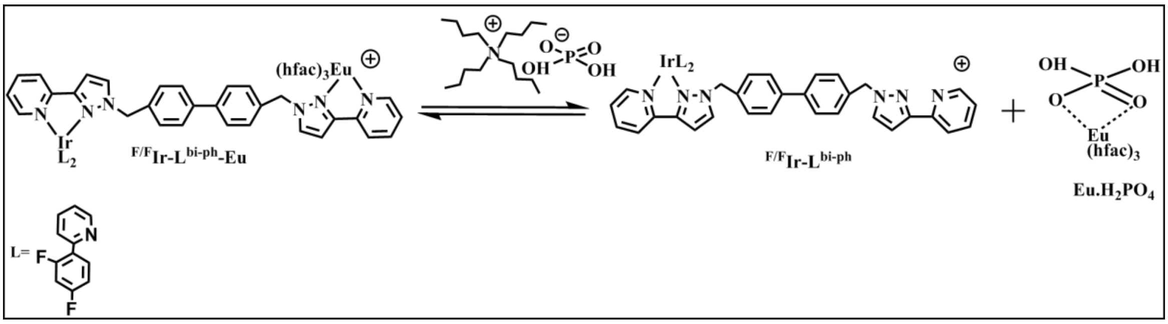

Figure 6-25 Shows titration steps of [$^{F/F}$Ir•L$^{bi\text{-}ph}$•Eu(hfac)$_3$]$^+$ with the anion dihydrogen phosphate.

During the titration the excitation wavelength was 360 nm (into the Ir-based MLCT/LC absorption manifold). The emission spectra were measured in the region between 400 – 700 nm to observe changes in Ir-based and Eu-based emission intensities, and the luminescence spectra were analysed by using the Origin program. The intensities of the integrated emission between 600 – 625 nm (for the main Eu-based emission maximum) were plotted against concentration of added anion and fitted to a 1:1 binding isotherm to obtain the corresponding binding constant.

6.11.3.1 Titration $^{F/F}Ir \bullet L^{bi\text{-}ph} \bullet Eu(hfac)_3$ with hydrogen sulfate anion.

Titration of $^{F/F}Ir \bullet L^{bi\text{-}ph} \bullet Eu(hfac)_3$ [6.95×10^{-4} M] with tetrabutylammonium hydrogen sulfate salt [2.24×10^{-3}M] in MeCN at room temperature resulted in steady decrease in the intensity of the Eu(III) emission (**Figure** 6-26-**a)** as the Eu(III) centre is separated from the dyad, and an increase in the $^{F/F}Ir \bullet L^{bi\text{-}ph} \bullet PF_6$ intensity emission as the Ir/Eu energy transfer decreases. The Eu-based emission intensity was quenched by > 90% after addition of 500 µL (~1 eq.) of hydrogen sulfate, and the final concentration of the hydrogen sulfate in this titration was 8.07×10^{-2} M. A gradual shift in the overall luminescence emission colour from red → white → blue, was observed, as the balance in the equilibrium mixture changed from $^{F/F}Ir \bullet L^{bi\text{-}ph} \bullet Eu(hfac)_3$ (predominantly red) → $^{F/F}Ir \bullet L^{bi\text{-}ph} \bullet PF_6$ (blue) as shown in **Figure** 6-26-**b**. Fitting the quenching data to a 1:1 binding isotherm gave an equilibrium binding constant of K= 69 M^{-1} for the same equilibrium as in **Figure** 6-25.

A Stern-Volmer plot shows that the emission quenching of the Eu(III) involves a combination of both static and dynamic processes. Direct binding of the $Eu(hfac)_3$ unit to the added anion by dative bond formation will provide the static quenching process, and possibly collision with the excess of hydrogen sulfate is responsible for the dynamic quenching (**Figure** 6-27).

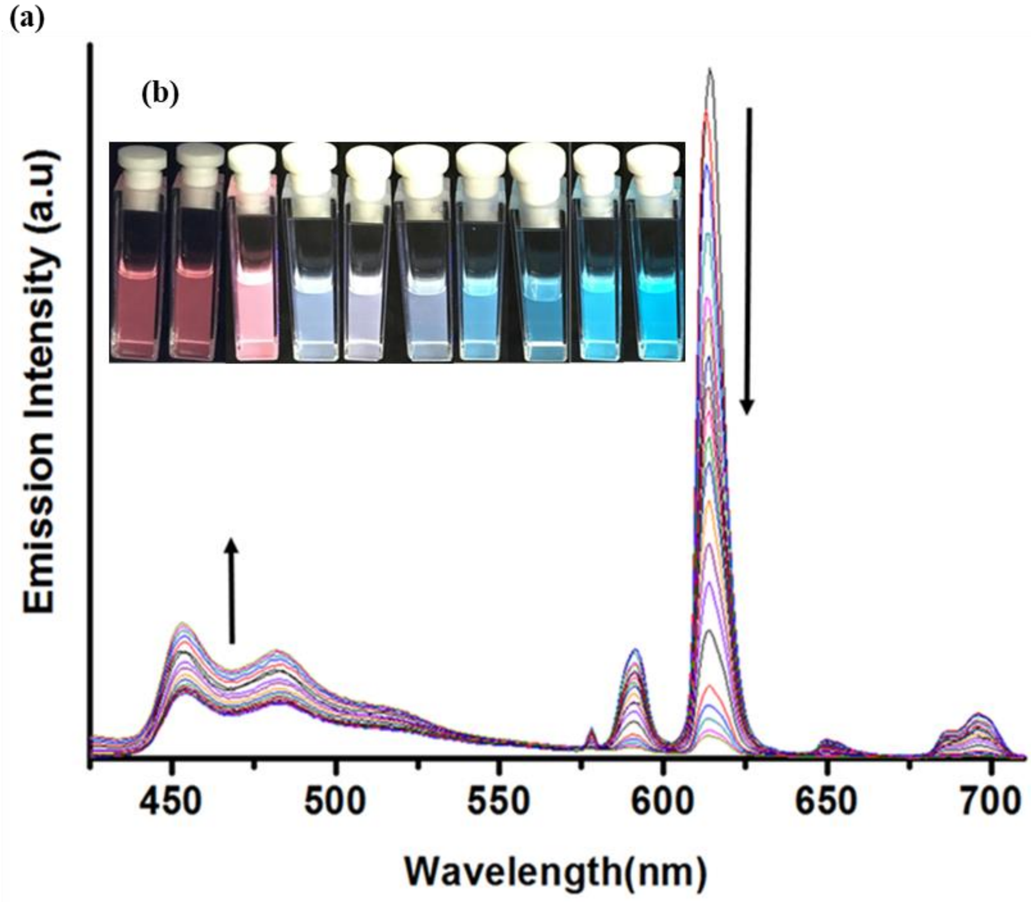

Figure 6-26. (a) Quenching of the Eu(III) unit emission in $^{F/F}$Ir•L$^{bi\text{-}ph}$•Eu(hfac)$_3$ complex upon addition of hydrogen sulfate in MeCN at 298 K. $\lambda_{exc.}$=360 nm. (b) Changing in the colour from red to blue via white during the titration.

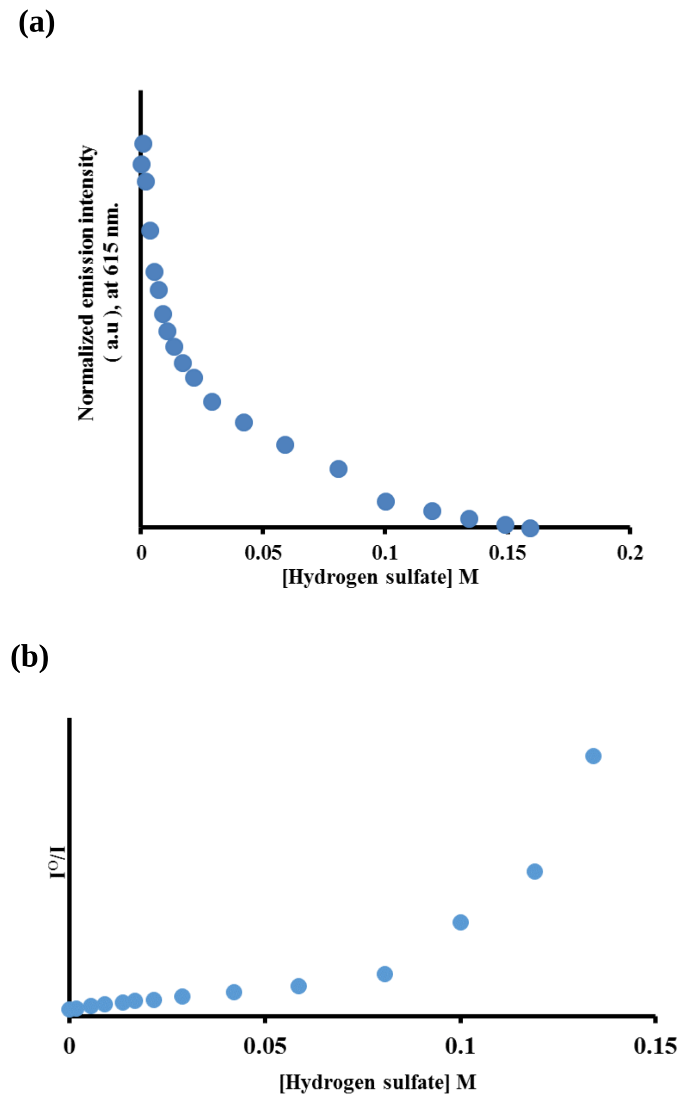

Figure 6-27. (a) Integration of luminescence emission intensity at 615 nm emission intensity of $^{F/F}$Ir•L$^{bi\text{-}ph}$•Eu(hfac)$_3$ [6.95×10^{-5} M] titrated with hydrogen sulfate in MeCN at room temperature. (b) Upward curvature Stern-Volmer plot of the integration luminescence emission.

6.11.3.2 Titration $^{F/F}$Ir•L$^{bi\text{-}ph}$•Eu(hfac)$_3$ with dihydrogen phosphate anion.

Titrations of $^{F/F}$Ir•L$^{bi\text{-}ph}$•Eu(hfac)$_3$ [6.95×10^{-4} M] were likewise performed with tetrabutylammonium dihydrogenphosphate salt [3.95 × 10^{-3} M] in MeCN at room temperature. The same general results are observed as that seen in the titration with hydrogen sulfate, with quenching of the Eu(III) emission intensity and an associated gradual increase in the Ir(III) emission as the Ir/Eu dyad is broken up by the added anion. The colour of the luminescence was changing from red to white (after *ca.* 3 equiv. of the anion), then to blue (after *ca.* 5 equiv.), that was tested by hand-held UV lamp, as shown in **Figure** 6-28.

Interestingly, early in the titration (after *ca.* 0.5 equiv. addition of dihydrogen phosphate) a small increase in the Eu(III) intensity emission at 615 nm, coupled to a slight shift in the emission maximum was observed. This small change might result from a change in the coordination sphere around Eu(III) without it being separated from the Ir/Eu dyad. One possibility is formation of a Eu(III)---dihydrogen phosphate---Eu(III) bridged structure and associated change in coordination environment of Eu(III), arising from monodentate bridging coordination of the anions (0.5 equivalents per Eu centre) as shown in **Figure** 6-29. Upon addition excess of dihydrogen phosphate, the intensity of luminescence of the Eu(III) unit continues to decrease as bidentate chelation of the anion separates the Eu(III) unit from the dyad at which point the $^{F/F}$Ir•L$^{bi\text{-}ph}$•PF_6 emission also increases (**Figure** 6-28). The data could be fitted to 1:1 binding isotherm and given an equilibrium constant K = 1900 M^{-1} for the formation of the {Eu(hfac)$_3$}(H_2PO_4) complex.

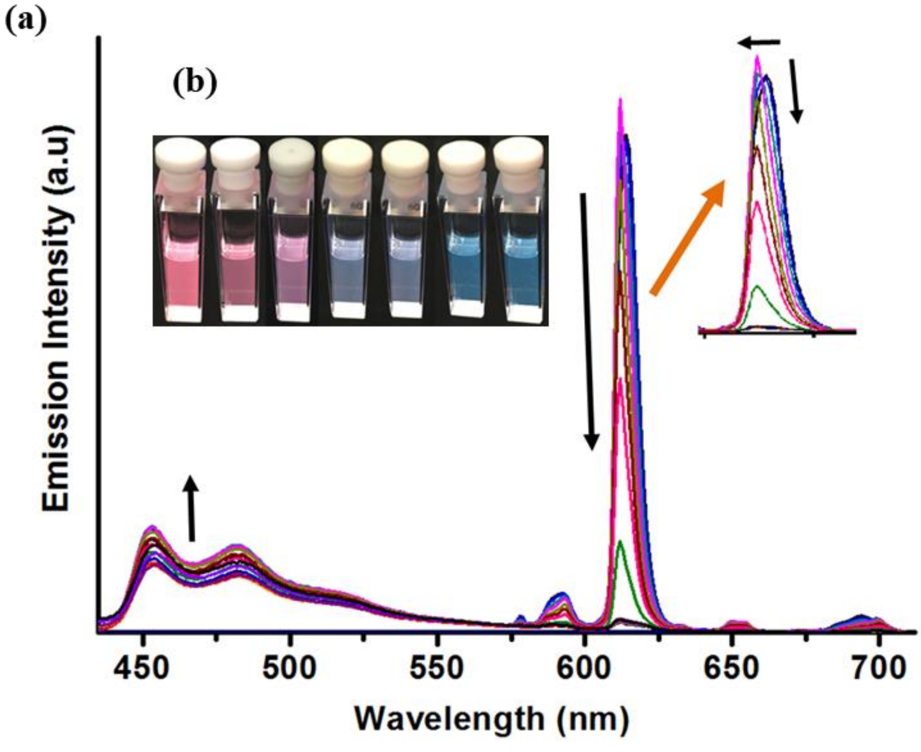

Figure 6-28. (a) Quenching in the Eu(III) unit emission peak upon addition of dihydrogen phosphate to $^{F/F}$Ir•L$^{bi\text{-}ph}$•Eu(hfac)$_3$ in MeCN at 298 K. $\lambda_{exc.}$=360 nm. Inset: zoom-in to show shifting and changing of the shape of Eu(III) emission at λ_{max} 615nm. (b) Changing in the colour from red to blue via white during the titration.

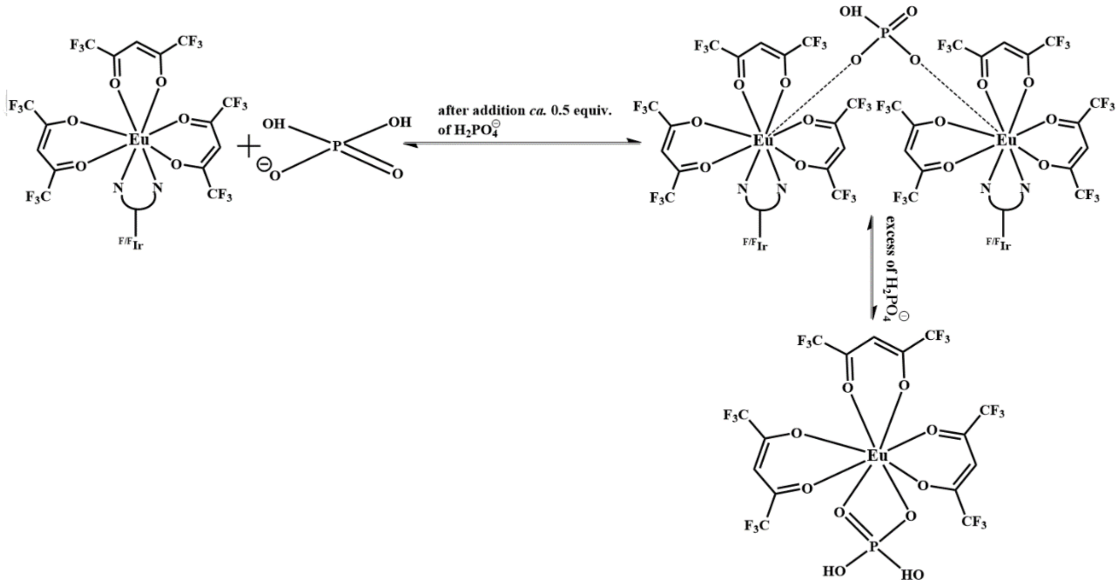

Figure 6-29. Suggested mechanism of binding dihydrogen phosphate at Eu(III) unit after 0.5 equiv. addition of dihydrogen phosphate to $^{F/F}$Ir•L$^{bi\text{-}ph}$•Eu(hfac)$_3$ complex in MeCN at room temperature.

A Stern-Volmer plot shows an upward curve revealing the combination of both static and dynamic quenching. Static quenching is generated by complex formation between dihydrogen phosphate and Eu(hfac)$_3$. Additional dynamic quenching may be generated from collisions between excess (free) of dihydrogen phosphate and $^{F/F}$Ir•L$^{bi\text{-}ph}$•PF$_6$ in the excited state (**Figure** 6-30).

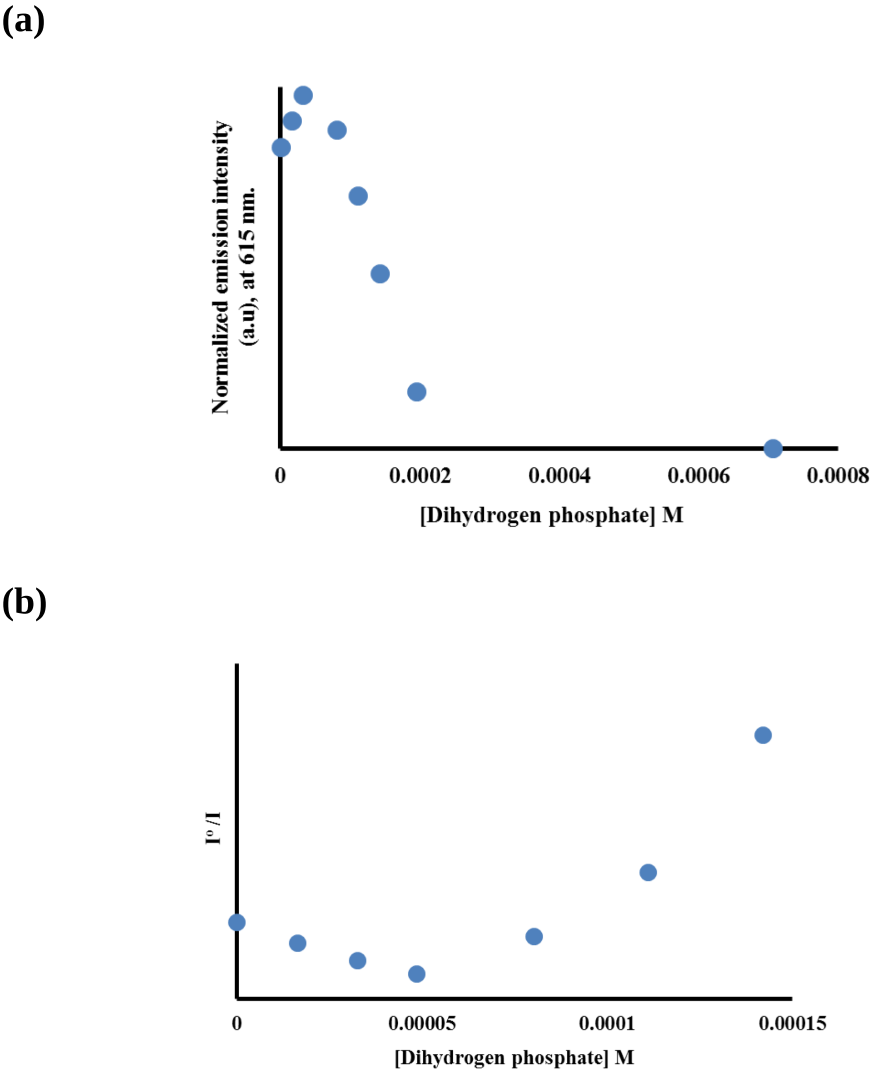

Figure 6-30. **(a) Changing in the luminescence emission intensity of Eu(III) unit on titration the dihydrogen phosphate with $^{F/F}$Ir•L$^{bi\text{-}ph}$•Eu(hfac)$_3$ in MeCN at room temperature ($\lambda_{exc.}$ 360 nm and. $\lambda_{max.}$ 615 nm). Interestingly, first three points shows the initial rise and then gradually decay. (b) A Stern-Volmer upward curvature represents the combination between static and dynamic quenching, that draws for the same data in (a).**

6.11.3.3 Titration $^{F/F}$Ir•L$^{bi\text{-}ph}$•Eu(hfac)$_3$ with benzoate anion.

Similar behvaiour was observed during the titration of $^{F/F}$Ir•L$^{bi\text{-}ph}$•Eu(hfac)$_3$ [6.95 × 10^{-5} M] with benzoate anion [3.95 × 10^{-3} M] in MeCN, with quenching of the Eu(III) unit emission as the benzoate anion displaces the [Eu(hfac)$_3$] unit from the dyad, and an associated gradual increase in the intensity emission of Ir(III) unit, as depicted in **Figure** 6-31. The rise in Eu-based emission intensity in the early stages of the titration, and then the main decay of luminescence (as also observed with hydrogen phosphate above) was detected. The rise happened after 1 equiv. also the colour changed gradually from red to white (after *ca.* 4 equiv.) then to blue emission (after *ca.* 5 equiv.) under UV lamp.

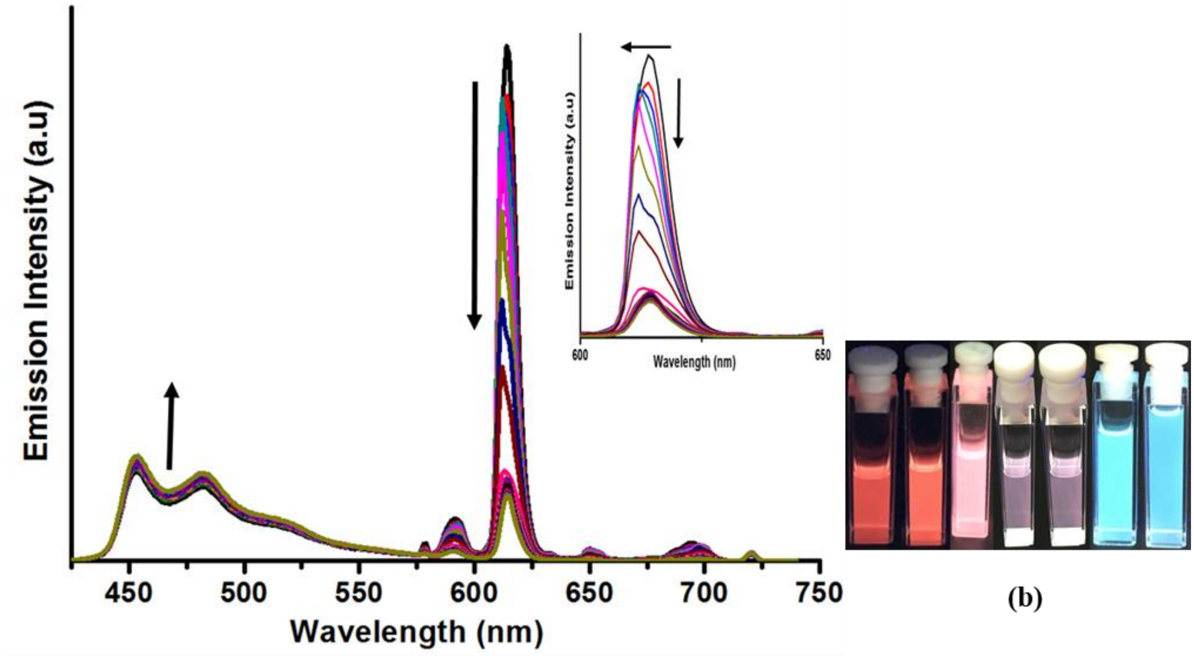

(a)

(b)

Figure 6-31. (a) Quenching in the Eu(III) unit emission peak upon addition of benzoate in MeCN at 298 K. $\lambda_{exc.}$=360 nm for Ir•L^{bi-ph}•Eu(hfac)$_3$ complex. Inset: zoom-in to show shifting and changing of the shape of Eu-bassed emission at λmax 615nm. (b) Changing in the colour from red to blue via white during the titration.

The reason for the rise in Eu-based emission in the early stages of the titration was the same reason mentioned in titration with dihydrogen phosphate anion, i.e. initial monodentate coordination of the benzoate anion without it being displaced from the dyad. The data could be fitted to 1:1 binding isotherm which afforded an equilibrium constant K=10900 M^{-1} for the formation of the Eu/benzoate complex. A Stern-Volmer plot is given in **Figure** 6-32 and again shows a mixture of static and dynamic quenching components.

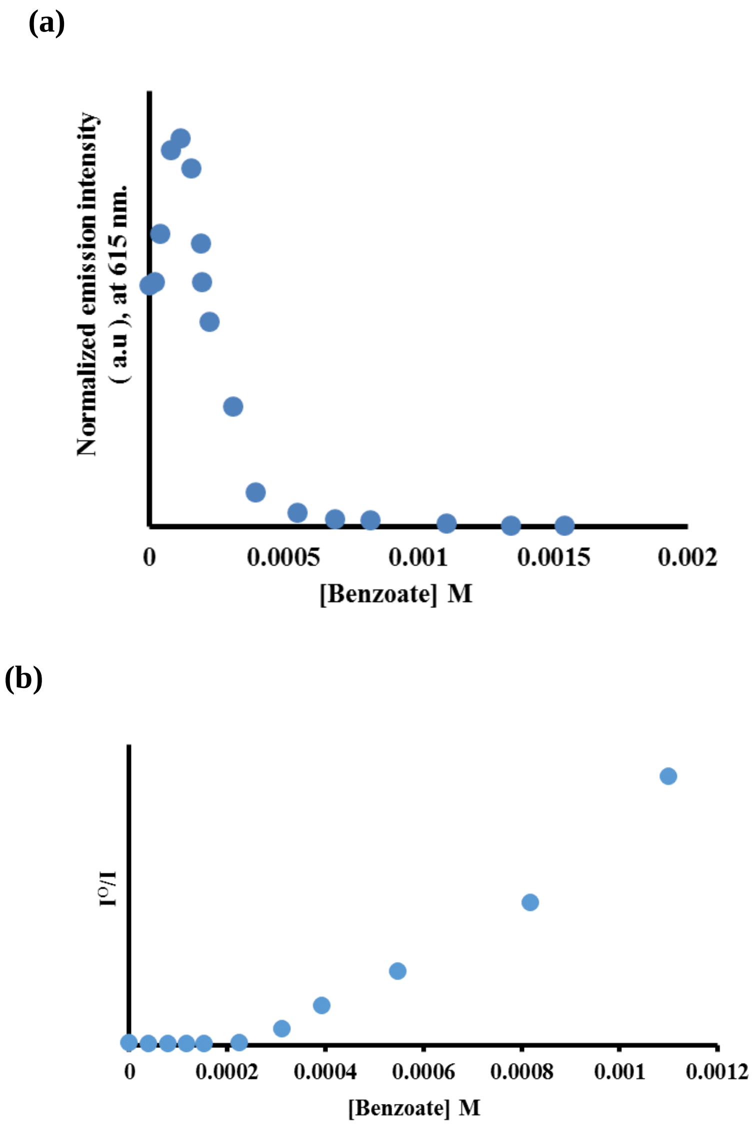

Figure 6-32. (a) Changing in the luminescence emission intensity of Eu(III) unit on titration benzoate with $^{F/F}$Ir•L$^{bi\text{-}ph}$•Eu(hfac)$_3$ in MeCN at room temperature ($\lambda_{exc.}$ 360 nm and. $\lambda_{max.}$ 615 nm). Interestingly, first three points shows the initial rise and then gradually decay. (b) A Stern-Volmer upward curvature represents the combination between static and dynamic quenching, that draws for the same data in (a).

6.11.3.4 Titration of $^{F/F}$Ir•L$^{bi\text{-}ph}$•Eu(hfac)$_3$ with acetate anion.

Titration of $^{F/F}$Ir•L$^{bi\text{-}ph}$•Eu(hfac)$_3$ [8.3×10^{-5} M] with tetrabutylammonium acetate [3.9×10^{-3} M] showed the same basic pattern of changes in luminescence behaviour (**Figure** 6-33**)** as observed with other anions, in MeCN at room temperature. Also the same early-stage rise, and shifting of the most intense Eu-based emission line was observed before the decay. The early-stage rise happened after addition of 1 equiv. of acetate and may be associated with monodentate coordination before displacement of the Eu(III) centre from the dyad occurs. Also the overall colour changed gradually from red to white (after ca. 0.7 equiv.) then to blue emission (after ca. 1 equiv.). The data could be fitted to a 1:1 binding isotherm which gave an equilibrium constant of K=16000 M^{-1} for the formation Eu/acetate complex. A Stern-Volmer plot is given in **Figure** 6-34 and shows the usual combination of static and dynamic quenching for the same reasons as suggested before.

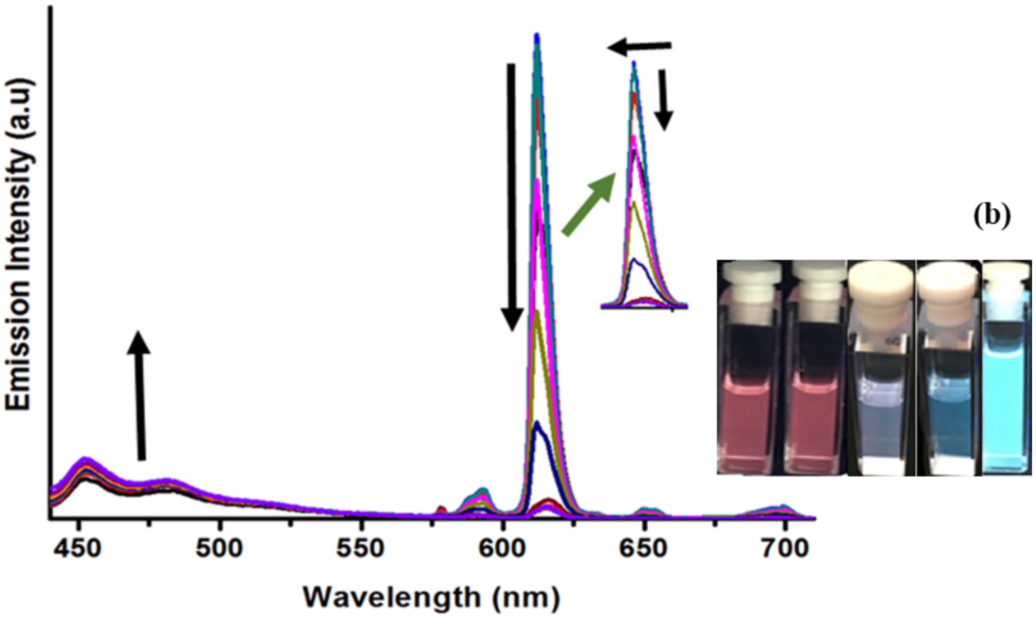

(a)

Figure 6-33. (a) Quenching in the Eu(III) unit emission peak upon addition of acetate in MeCN at 298 K. λ$_{exc.}$=360 nm for Ir•L$^{bi\text{-}ph}$•Eu(hfac)$_3$ complex. Inset: zoom-in to show shifting and changing of the shape of Eu-bassed emission at λ$_{max}$. 615nm. (b) Changing in the colour from red to blue via white during the titration.

(a)

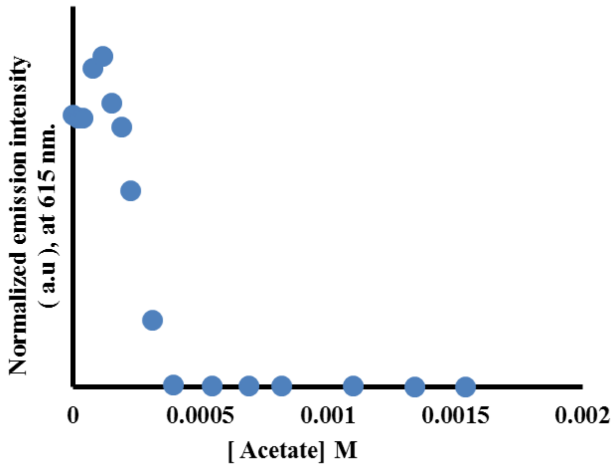

(b)

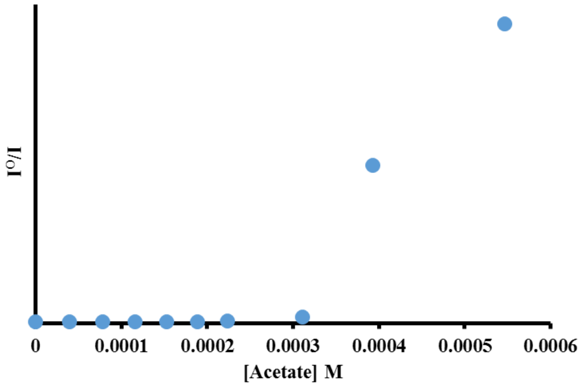

Figure 6-34. (a) Changing in the luminescence emission intensity of Eu(III) unit in $^{F/F}$Ir•L^{bi-ph}•Eu(hfac)$_3$ on titration with acetate in MeCN at room temperature ($\lambda_{exc.}$ 360 nm and. $\lambda_{max.}$ 615 nm). Interestingly, first three points show the initial rise and then gradually decay. (b) A Stern-Volmer upward curvature represents the combination between static and dynamic quenching, that draws for the same data in (a).

6.13 Comparison between different anions.

To compare between different anions binding to the Eu(III) unit, we compared their emission luminescence spectra during the titrations. **Figure** 6-35 shows that Ir(III)/Eu(III) dyad shows a different luminescence response to different anions based on differences in binding affinity that must arise from differences in structure, electron density and size. On the basis of binding constants data, which are summarised in **Table 6-1**, acetate binds best to Eu(III) and therefore causes the most quenching, and hydrogen sulfate binds poorest and causes least quenching.

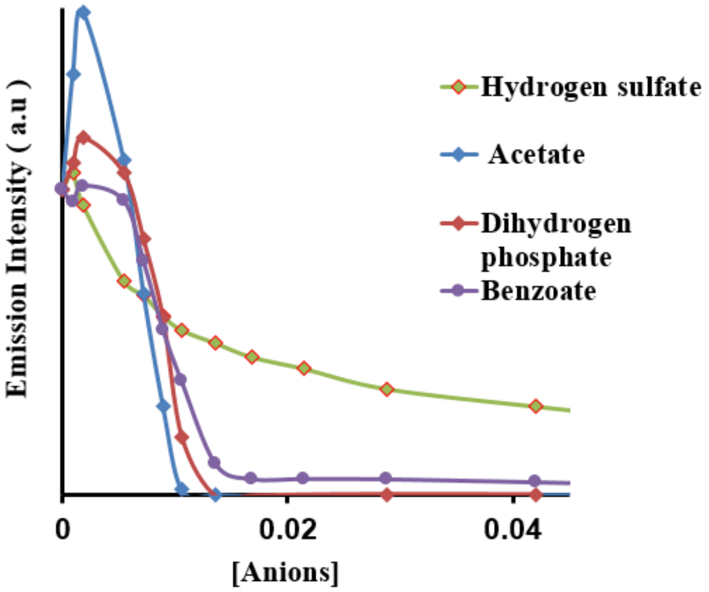

Figure 6-35. Comparison quenching luminescence emission intensity of different anions titrated with $^{F/F}$Ir•L$^{bi\text{-}ph}$•Eu(hfac)$_3$ at 615 nm emission line in MeCN.

Table 6-1 Binding constant data

Anions	Binding constant of anion with $^{F/F}$Ir•L$^{bi\text{-}ph}$•Eu (M^{-1})
Dihydrogen phosphate	1900
Hydrogen sulfate	69
Acetate	16000
Benzoate	10900

6.14 Conclusion.

A fruitful approach based on the design of Ir(III)/Eu(III) dyad as a probe for anions, based on combination of Eu(III) unit with Ir(III) unit in a single molecule, have been successfully utilised. These two units have luminescence intensity output in different regions. These photophysical properties allowed easily detectable changes in the luminescence intensity of Eu(III) unit in the visible region when an anion binds as a bidentate chelating ligand. An Ir(III)/Eu(III) dual luminescent system has accordingly been utilized for ratiometric sensing for anions. Binding of anions with the Eu(III) unit led to separation of the Eu(III) unit from the Ir(III) chromophore complex and a change in overall luminescence colour from red to blue. The hydrogen sulfate anion shows less effect on quenching the luminescence emission of Eu-based component compare to the acetate, dihydrogen phosphate and benzoate anions which show stronger quenching of Eu(III) based luminescence. Stern-Volmer plots showed that a mixture of static and dynamic quenching occurred in solution for each of the anions.

6.15 References

1 J. C. G. Bünzli, *J. Lumin.*, 2016, **170**, 866–878.

2 E. G. Moore, A. P. S. Samuel and K. N. Raymond, *Acc. Chem. Res.*, 2009, **42**, 542–552.

3 R. C. Evans, P. Douglas and C. J. Winscom, *Coord. Chem. Rev.*, 2006, **250**, 2093–2126.

4 X. Wang, H. Chang, J. Xie, B. Zhao, B. Liu, S. Xu, W. Pei, N. Ren, L. Huang and W. Huang, *Coord. Chem. Rev.*, 2014, **273–274**, 201–212.

5 J.-C. G. Bünzli and C. Piguet, *Chem. Soc. Rev.*, 2005, **34**, 1048–77.

6 G. Muller, *Dalton. Trans.*, 2009, 9692.

7 S. J. Butler, *Chem. Commun.*, 2015, **51**, 10879–10882.

8 D. F. Caffrey and T. Gunnlaugsson, *Dalton. Trans.*, 2014, **43**, 17964–17970.

9 X. Liu, J. Xu, Y. Lv, W. Wu, W. Liu and Y. Tang, *Dalton. Trans.*, 2013, **42**, 9840.

10 Y. Hu, Y. Li, J. F. Joung, J. Yin, S. Park, J. Yoon and M. H. Hyun, *Sensors Actuators, B Chem.*, 2017, **241**, 224–229.

11 J. A. Kitchen, E. M. Boyle and T. Gunnlaugsson, *Inorganica Chim. Acta*, 2012, **381**, 236–242.

12 R. B. P. Elmes and T. Gunnlaugsson, *Tetrahedron Lett.*, 2010, **51**, 4082–4087.

13 S. Li, C. Zhang, S. Huang, F. Hu, J. Yin and S. H. Liu, *RSC Adv.*, 2012, **2**, 4215.

14 A. Dorazco-Gonzalez, *Organometallics*, 2014, **33**, 868–875.

15 L. R. Joseph, *Principles of Fluorescence Spectroscopy*, Springer Science+Business Media, LLC, USA, University of Maryland School of Medicine, Baitimore, Maryland, USA, Third., 2010.

16 S. V. Eliseeva and J.-C. G. Bünzli, *Chem. Soc. Rev.*, 2010, **39**, 189–227.

17 A. Thibon and V. C. Pierre, *Anal. Bioanal. Chem.*, 2009, **394**, 107–120.

18 D. P. Andrew Beeby, Ian M. Clarkson, Rachel S. Dickins, Stephen Faulkner and J. A. G. W. and M. W. Louise Royle, Alvaro S. de Sousa, *J. Chem. Soc., Perkin Trans.*, 1999, **2**, 493–504.

19 D. Sykes and M. D. Ward, *Chem. Commun.*, 2011, **47**, 2279–2281.

20 D. Sykes, S. C. Parker, I. V Sazanovich, A. Stephenson, J. A. Weinstein and M. D. Ward, *Inorg. Chem.*, 2013, **52**, 10500–10511.

21 T. Sajoto, P. I. Djurovich, A. B. Tamayo, J. Oxgaard, W. A. Goddard and M. E. Thompson, *J. Am. Chem. Soc.*, 2009, **131**, 9813–9822.

22 M. D. Ward, *Coord. Chem. Rev.*, 2007, **251**, 1663–1677.

23 M. G. Colombo, T. C. Brunold, T. Riedener, H. U. Guedel, M. Fortsch and H.-B. Buergi, *Inorg. Chem.*, 1994, **33**, 545–550.

24 R. Ragni, E. a. Plummer, K. Brunner, J. W. Hofstraat, F. Babudri, G. M. Farinola, F. Naso and L. De Cola, *J. Mater. Chem.*, 2006, **16**, 1161.

25 D. Sykes, A. J. Cankut, N. M. Ali, A. Stephenson, S. J. P. Spall, S. C. Parker, J. a Weinstein and M. D. Ward, *Dalton Trans.*, 2014, **43**, 6414–28.

26 L. N. Puntus, K. A. Lyssenko, I. S. Pekareva and J. C. G. Bünzli, *J. Phys. Chem. B*, 2009, **113**, 9265–9277.

27 J.-C. G. Bunzli, in *Handbook on the Physics and Chemistry of Rare Earths. Chapter 287, Lanthanide Luminescence: From a Mystery to Rationalization, Understanding, and Applications*, Elsevier, Amsterdam, 2016, pp. 141–176.

28 A. Jana, S. J. A. Pope and M. D. Ward, *Polyhedron*, 2017, **127**, 390–395.

29 S. V Eliseeva, D. N. Pleshkov, K. A. Lyssenko, L. S. Lepnev, J.-C. G. Bünzli and N. P. Kuzmina, *Inorg. Chem.*, 2010, **49**, 9300–9311.

30 D. Parker, *Coord. Chem. Rev.*, 2000, **205**, 109–130.

CHAPTER SEVEN

Experimental Part

7 Experimental

7.1 Solvents and Chemicals

All starting solvents and chemicals organic reagents, which were used in synthesis, were purchased from commercial suppliers (Aldrich and VWR international, Fluorochem, SLS and Alfa Aesar). Also, all of them were bought stable under absolute conditions and used as received without purification with the exception of the metal salts $IrCl_2.xH_2O$ which were obtained from precious metals online (http://www.precmet.com.au/) and used as received, while the majority of dry solvent THF was obtained from a Grubbs dry solvent system of University of Sheffield.

7.2 Chromatography.

Glass columns with various lengths and widths were used in purification. Aldrich silica gel (Merck 70-230 STM) or alumina (Brockman grad III), which was earily converted to zero oxidation state by adding water (60 mL) for each 1Kg alumina, were used as a stationary phase. A thin layer chromatography (TLC) was used as a tester to know which condition is good to separate compounds from impurities. All TLC were carried out on Merck aluminium sheets which is coated with either silica or alumina gel in a thickness 0.2 mm.

7.3 Instrumentation.

All the instruments services were used in the Chemistry department, whereas cell imaging tests have been done in the Medical School at the University of Sheffield.

7.3.1 Nuclear Magnetic Resonance (^1H NMR) Spectroscopy.

NMR spectra were recorded using a Bruker AVANCE 400 spectrometer operating at 400.13MHz or a Bruker AVANCE III HD 400 spectrometer operating at 400.23MHz at 298K. ^1H NMR spectra were calibrated using tetramethylsilane as the internal standard if present or residual solvent peaks. Spectra were analysed using TopSpin 3.2. All chemical shifts are quoted in units of parts of million (ppm) shifts relative to tetramethylsilane (TMS) at 0ppm. The *J*-coupling constants are reported in Hertz (Hz) and are quoted to the nearest 0.1 Hz and are uncorrected. The multiplicity of the proton symbols are reported as s, d, t, m, dd, td and ddd which represent singlet, doublet, triplet, multiple, doublet of doublets, triplet of doublets and doublet of doublet of doublets respectively.

7.3.2 Mass Spectrometry.

Direct infusion electrospray mass (ES) were obtained on a waters LCT time of flight instrument. Liquid chromatography mass spectrometry (LMCT) were obtained on Agilent 6530 QTOF-LC/MS mass spectrometer instrument. Electron ionisation (EI) spectra were obtained on an Agilent Technologies 7200 Accurate-Mass Q-TOF GC/MS.

7.3.3 Infra-red Spectroscopy.

Infra-red spectra were obtained as solid on a Perkin Elmer, precisely spectrum 100, FTIR spectrometer.

7.3.4 Elemental Analysis.

All elemental carbon, hydrogen and nitrogen analyses were completed using a elemtar Vario Micro Cube Elemental Analyser.

7.3.5 X-ray crystallography.

All single crystal X-ray diffraction data were collected either on a Bruker Kappa or Smart APEX-II diffractometer at 100 K by using a seal-tube source Mo K_α radiation (λ= 0.71073 Å), or on a Bruker D8 Venture diffractometer equipped with a Photon 100 CMOS detector using microfocus seal-tube source of Cu-K_α radiation (λ= 1.54 Å). All absorption correction was measured by semi-empirical methods (SADABS), based on symmetry-equivalent and repeated reflections at different azimuthal angles. All crystals follow the same steps, a single crystal picked from the mother liquor to a slide and coated with fumble oil to examine under microscope. Then a single crystal was transferred quickly to the diffractometer into a stream of cold N_2, which kept the crystal from any decomposition resulting from solvent loss. Structures were solved using direct methods and refined against all F^2 values using program package SHELXTL[1, 2] or Olex2.[3] Non-hydrogen atoms are refined anisotropically. In the case where included solvent could not be refined satisfactory, a solvent mask (Olex2 implementation) was employed to account for the electron density. Hydrogen atoms were placed geometrically in calculated positions and refined using idealised geometries, riding model, including torsional freedom from CH_3 groups, and were assigned fixed isotropic displacement parameters.

7.4 Photophysical Measurements.

All solutions were measured using quartz cuvette cell with a path length 1 cm.

7.5 UV-Vis spectroscopy.

Absorption spectra were recorded on a Varian Cary 50 BIO UV-Visible Spectrometer at 298 K and baseline corrected.

7.6 Emission Spectroscopy.

Emission spectra were carried out using a Jobin Yvon Flouromax-4- spectrofluorometer and spectra data draw using origin program virgin 8. A de-aerated analyse solution was made using a quartz cuvette and bubbling argon through the solution for 20 minutes at 298 K.

7.7 Lifetime Measurements.

Time- resolved luminescence measurements were measured on Edinburgh Instruments Mini-τ instrument fitted with pulsed laser excitation source at wavelength 405 nm. Lifetime data was measured by using technique of single time correlated signal photon counting (TCSPC). All data fitted to single, double or triple an exponential decay curve depending on data set using mini-τ programme supplied by the same instruments.

7.8 Cell Imaging

EJ cells were cultured in DMEM /10% (v/v) Fetal calf serum (FCS) on coverslip. Next day, the cells were incubated with 10 μM of the complexes for 2 hours, then the media was removed. The cells were washed by PBS. A volume of 1% PFA in PBS solution was added and then left for 15 minutes at room temperature to fix the cells.

The fixative reagent was aspirated and the cells were washed again with PBS to remove any remaining PFA. The coverslip was mounted on a glass slide. Later, the coverslips were sealed by IMMU-Mount to be ready for imaging. The images were taken using Nikon eclipse TE200 microscope at 358/461nm Ex/Em. using irradiation with a Prior Lumen 200 at 50% light output (λ_{exc} 358 nm, unfiltered emission).

7.9 General Procedures for Luminesces Measurements.

7.9.1 UV-Vis, Luminescence and lifetime measurements.

Luminescence and lifetime of Ir-complexes were measured when absorption of complex was less than 0.1 using quarts cuvette cell with aerated MeCN as solvent.

7.9.2 Titration of Ir- complexes with [Ln(hfac)$_3$•2H$_2$O] complexes.

A stock solution of (2.5 mg) Ir- complex was prepared into 50 mL volumetric flask and filled with aerated solvent MeCN. Approximately (5 mg) of [Ln(hfac)$_3$•2H$_2$O] was prepared in (10 mL) volumetric flask and filled with the Ir- complex stock solution. A quartz cuvette cell was filled with (2mL) of stock solution and measurements were made by adding aliquots of the [Ln(hfac)$_3$.2H$_2$O] (0 µl – 500 µL) into the cuvette cell. In each addition, UV-Vis absorption, luminescence and lifetime measurements were recorded.

7.9.3 Quantum Yield Measurements.

Quantum yield (ϕ) values of aerated solution complexes were calculated using [Ru(bpy)$_3$][(PF$_6$)$_2$] in MeCN ($\phi = 0.018$)[4], [Pt(1,3-di(2-pyridyl)benzeneCl] ($\phi = 0.039$)[5] and [Ir•L^{naph}•Ir][(NO$_3$)$_2$] ($\phi = 0.09$)[6]. Quantum yield values were calculated using equation, which explained briefly in **chapter 2**.

7.9.4 Luminescence measurements at 77K.

Approximately (2.5 mg) of iridium complex was dissolved in aerated mixture of ethanol/methanol (4:1) solvent. A 1 mL of a solution was placed on the NMR tube and placed slowly in quartz nitrogen dewar, which filled with liquid nitrogen, until glass layer appear. This was then luminescence and lifetime were recorded.

7.10 Synthesis

7.10.1 Pypz

3-(2-pyridyl)pyrazole (pypz) compound was used as synthesised according to the literature method.[7]

7.10.2 Synthesis of $^{F/F}$Ir•L^{pyrene}•NO_3 complex

Both $^{F/H,H/H}$Ir•L^{pyrene}•NO_3 series follow the same synthesis procedure of the $^{F/F}$Ir•L^{pyrene}•NO_3. All data summarized on the **Table 7-1**.

A mixture of $^{F/F}$Ir•L^{pypz}•NO_3 (0.1 g, 0.13 mmole) and 1-(bromomethyl)pyrene (0.04 g, 0.13 mmole) in a ratio(1:1), Cs_2CO_3 (0.04 g, 0.13 mmol) and Bu_4NI as a catalyst were dissolved in MeCN (60 mL). The mixture was refluxed under the following conditions: temperature 90 ºC, 48hr., N_2 atmosher, and in dark. The yellow solution was cooled to room temperature and the solvent was evaporated to dryness then the yellow crude product was purified using silica gel column eluted with Toluene for 1000 mL then Toluene/MeOH in a ratio (95:5) until sure all unwanted bands got off then MeCN:H_2O:$KNO_{3(aq.)}$ in a ratio (100:10:5). To remove excess of KNO_3, the product was extracted with DCM/H_2O to remove excess of NO_3 salt.
^{1}H NMR (400MHz, CD_3CN): δ(ppm) 8.41 (1H, dt, *J* 1.0, 7.9); 8.32 (2H, d, *J* 7.6); 8.25 (1H, d, *J* 8.3); 8.22 (1H, d, *J* 2.7); 8.19-15 (1H, m); 8.14 (1H, d, *J* 1.5); 8.13-8.09 (1H, m); 8.06 (1H, d, *J* 9.2); 7.99-7.94 (2H, m); 7.94-7.89 (1H, m); 7.75 (1H, d, *J* 5.2); 7.64-7.57 (2H, m); 7.55 (1H, d, *J* 2.7); 7.44 (1H, d, *J* 9.2); 7.41-7.35 (2H, m); 7.30 (1H, ddd, *J* 1.3, 5.8, 7.4); 7.12 (1H, ddd, *J* 1.3, 5.9, 7.1); 6.79 (1H, dd, *J* 1.2, 7.9); 6.59 (1H, ddd, *J* 2.2, 9.3, 12.2; 6.10 (1H, d, *J* 17.4); 5.96 (1H, d, *J* 7.9); 5.88 (1H, dd, *J* 17.1); 5.68 (1H, dd, *J* 2.3, 8.5, 5.5); (1H, ddd, *J* 2.3, 9.4, 12.5); 5.28 (1H, dd, *J* 2.3, 8.6).

Table 7-1 Summary of mono-$^{F/F,\ F/H\ and\ H/H}$Ir•L^{pyrene}•NO_3 data.

Complex	Starting material / Scale	Scale (g, mmol) of 2-(bromomethyl) pyrene	scale of Cs_2CO_3	R_f.	Yield (%)	ESMS: *m/z*
$^{F/F}$Ir•L^{pyrene}•NO_3	$^{F/F}$Ir•pypz•NO_3 / (0.10 g, 0.13 mmol)	(0.04 g / 0.13 mmol)	0.04 g, 0.13 mmol	0.25	0.09g, 69%	931.99 $(M\text{-}NO_3)^+$
$^{F/H}$Ir•L^{pyrene}•NO_3	$^{F/H}$Ir•pypz•NO_3 / (0.10 g, 0.13 mmol)	(0.04 g / 0.13 mmol)	0.04 g, 0.13 mmol	0.24	0.08g, 67%	895.99 $(M\text{-}NO_3)^+$
$^{H/H}$Ir•L^{pyrene}•NO_3	$^{H/H}$Ir•pypz•NO_3 / (0.10 g, 0.14 mmol)	(0.04 g / 0.14 mmol)	0.04 g, 0.14 mmol	0.24	0.08 g, 62%	860.23 $(M\text{-}NO_3)^+$

7.10.2.1 Crystallographic data and structure refinement for $^{F/F}$Ir•L^{pyrene}•NO_3

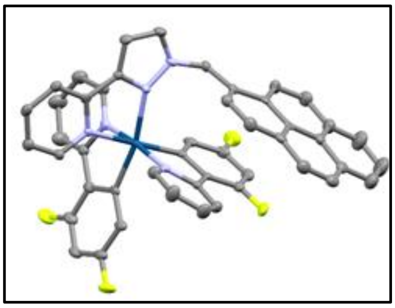

Formula	$C_{48}\,H_{31}Cl_2F_4IrN_6O_3$
Molecular weight	1078.89
T	100(2) K
Crystal system	Monoclinic
Space group	$P2_1/c$
α= 15.517(15) Å	α= 90°
b= 10.676(10) Å	β= 95.83(2)°
c= 23.21(2) Å	γ= 90°
V	3825(6) Å^3
Z	4
ρ	1.873 g/m^3
Crystal size	0.410 x 0.400 x 0.100 mm^3
μ	3.707 mm^{-1}
Data / restraints / parameters	5938 / 579 / 577
Final R1, $wR2^a$	0.0454, 0.1291

α The value of R1 is based on 'observed' data with I >2σ (I); the value of wR2 is based on all data.

7.10.2.2 ^{1}H NMR $^{F/H}$Ir•L^{pyrene}•NO_3 complex.

^{1}H NMR (400MHz, CD_3CN): δ(ppm) 8.34 (1H, dt, *J* 1.0, 7.9); 8.30 (2H, t, *J* 8.1); 8.15 (1H, d, *J* 9.0); 8.10 (2H, td, *J* 1.8, 7.6); 8.06 (1H, d, *J* 2.7); 8.01-7.95 (2H, m); 7.94 (1H, d, *J* 1.4); 7.92-7.85 (2H, m); 7.77-7.68 (2H, m); 7.62 (1H, ddd, *J* 1.4, 8.5); 7.57 (1H, d, *J* 5.7); 7.47 (1H, d, *J* 2.7); 7.42 (1H, d, *J* 7.4); 7.38-7.31 (2H, m); 7.24 (1H, ddd, *J* 1.4, 5.9, 7.6); 7.09 (1H, ddd, *J* 1.3, 5.8, 7.2); 6.71 (1H, dd, *J* 2.6, 8.8); 6.69-6.64(1H, m); 6.09 (1H, d, *J* 7.9); 6.00 (1H, d, *J* 17.0); 5.94 (1H, dd, *J* 5.6, 8.5); 5.86 (1H, s); 5.80 (1H, dd, *J* 2.5, 9.6,); 5.63 (1H, td, *J* 2.5, 8.9); 5.45 (1H, dd, *J* 2.56, 9.6).

7.10.2.3 ^{1}H NMR $^{H/H}$Ir•L^{pyrene}•NO_3 complex.

^{1}H NMR (400MHz, CD_3CN): δ(ppm) 8.35-8.33 (1H, m); 8.33-8.31 (1H, m); 8.30 (1H, d, *J* 7.8); 8.18 (1H, d, *J* 8.9); 8.14-8.10 (1H, m); 8.10-8.06 (1H, m); 8.05-7.99 (2H, m); 7.95 (1H, d, *J* 4.5); 7.94-7.91 (2H, m); 7.89 (1H, dd, *J* 1.5, 7.8); 7.79-7.73 (1H, m); 7.73-7.66 (2H, m); 7.63 (1H, ddd, *J* 1.5, 7.6, 8.1); 7.54 (1H, d, *J* 7.9) ; 7.43 (1H, d, *J* 2.8); 7.35 (1H, ddd, *J* 1.3, 5.5, 6.9); 7.26-7.21 (2H, m); 7.11(1H, ddd, *J* 1.3, 5.7, 7.3); 6.97 (1H, td, *J* 1.1, 7.5); 6.85-6.81 (1H, m); 6.79 (1H, dd, *J* 1.2, 7.3); 6.63 (1H, ddd, *J* 2.2, 6.3, 7.6); 6.28 (1H, d, *J* 3.6); 6.26 (1H, d, *J* 4.0); 6.21-6.14 (2H, m); 5.97-5.94 (1H, m); 5.91 (1H, s); 5.78 (1H, d, *J* 16.6).

7.10.3 Synthesis of $^{H/H}$Ir•CH$_3$•NO$_3$ complex.

Both $^{F/H,H/H}$Ir•CH$_3$•NO$_3$ series were synthesised by following the same synthesis procedure of the $^{F/F}$Ir• CH$_3$•NO$_3$. All data are summarized on the **Table 7-2**.

A mixture of $^{H/H}$Ir•pypz•NO$_3$ (0.11 g, 0.15 mmole) and methyl iodide (0.06 g, 0.40 mmole) in a ratio(1:2.5) were dissolved in MeCN (60 mL) . In present Cs$_2$CO$_3$ (0.05 g, 0.15 mmole) as base and NBu$_4$I as a catalyst. The mixture was refluxed under the following conditions: temperature 88 ºC, overnight, N$_2$ atmosphere, and in dark. A yellowish-brown solution was cooled to room temperature and the solvent was evaporated to dryness. The yellow oil crude product was purified using column chromatography on (200-300 mesh) of silica gel eluted with MeCN/KNO$_{3(aq.)}$ in ratio (96:4) %. To remove the excess of KNO$_3$, the product was dissolved in (25 mL) DCM. The organic layer was extracted using (60 mL) deionized H$_2$O then dried over MgSO$_4$, and filtered. The solvent was evaporated. A yellow solid product was collected and characterized.

^{1}H NMR (400MHz, CD$_3$CN): δ(ppm) 8.24 (1H, d, *J* 7.9); 8.11 (1H, d, *J* 8.1); 8.07 (1H, d, *J* 8.1); 8.04 (1H, dd, *J* 1.4, 7.8); 7.91 (1H, dd, *J* 1.3, 8.4); 7.87 (1H, dd, *J* 1.4, 8.4,); 7.83-7.79 (2H, m); 7.79-7.75 (3H, m); 7.63 (1H, d, *J* 5.7); 7.33 (1H, ddd, *J* 1.3, 5.5, 7.1); 7.21 (1H, d, *J* 2.6); 7.13 (1H, ddd, *J* 1.3, 5.8, 7.3); 7.09 (1H, ddd, *J* 1.3, 5.8, 7.3); 7.05 (1H, dd, *J* 1.0, 7.7); 7.00 (1H, td, *J* 1.0, 7.6); 6.92 (1H, td, *J* 1.2, 7.5); 6.87 (1H, td, *J* 1.2, 7.4); 6.31 (1H, d, 7.6); 6.20 (1H, d, *J* 7.5); 3.26 (3H, s).

Table 7-2 Summary of mono-$^{F/F,\ F/H\ and\ H/H}$Ir•CH$_3$•NO$_3$ data.

Complex	Starting material / Scale (g, mmol)	CH$_3$I	scale of Cs$_2$CO$_3$	R$_f$.	Yield (%)	ESMS: *m/z*
$^{F/F}$Ir•CH$_3$•NO$_3$	$^{F/F}$Ir•pypz•NO$_3$ / (0.1g, 0.13 mmol)	(0.05 g / 0.34 mmol)	0.04 g, 0.13 mmol	0.42	0.09g, 82%	732.14 (M-NO$_{3)}^{+}$
$^{F/H}$Ir•CH$_3$•NO$_3$	$^{F/H}$Ir•pypz•NO$_3$ / (0.10 g, 0.13 mmol)	(0.05 g / 0.34 mmol)	0.04 g, 0.13 mmol	0.35	0.08g, 80%	696.16 (M-NO$_3$)$^+$
$^{H/H}$Ir•CH$_3$•NO$_3$	$^{H/H}$Ir•pypz•NO$_3$ / (0.11 g, 0.15 mmol)	(0.06 g / 0.40 mmol)	0.05 g, 0.15 mmol	0.32	0.08 g, 73%	660.17 (M-NO$_3$)$^+$

7.10.4 ^{1}H NMR $^{F/F}$Ir•CH_3•NO_3 complex.

^{1}H NMR (400MHz, CD_3CN): δ(ppm) 8.36 (1H, d, *J* 8.3); 8.31 (1H, d, *J* 8.3); 8.28 (1H, t, *J* 1.0, 7.9); 8.10 (1H, td, *J* 1.4, 7.8); 7.96 (2H, s); 8.00-7.91 (2H, m); 7.84 (1H, d, *J* 2.7); 7.81 (2H, t, *J* 5.3); 7.64 (1H, dd, *J* 1.0, 5.7); 7.39 (1H, ddd, *J* 1.3, 5.6, 7.0); 7.23 (1H, d, *J* 2.7); 7.20 (1H, ddd, *J* 1.2, 5.5, 7.3); 7.15 (1H, ddd, *J* 1.3, 5.8, 7.3); 6.74-6.69 (2H, m); 5.77 (1H, dd, *J* 2.3, 8.6); 5.65 (1H, dd, *J* 2.4, 8.7); 3.35 (3H, s).

7.10.4.1 Crystallographic data and structure refinement for $^{F/F}$Ir•CH_3•NO_3 in a formula $^{F/F}$Ir•CH_3•I•MeCN

Formula	$C_{32}H_{23.50}F_4IrN_{5.50}O_{0.50}I$
Molecular weight	888.16
T	100(2) K
Crystal system	Monoclinic
Space group	$P2_1/c$
a = 14.151(2) Å	α= 90°.
b = 24.346(4) Å	β= 109.5874(19)°.
c = 9.5930(15) Å	γ= 90°.
V	3113.7(9) Å^3
Z	4
ρ	1.895 g/m^3
Crystal size	0.486 x 0.135 x 0.120 mm^3
μ	5.337 mm^{-1}
Data / restraints / parameters	5499 / 9 / 416
Final R1, *wR*2^{a}	R1 = 0.0695, wR2 = 0.1766

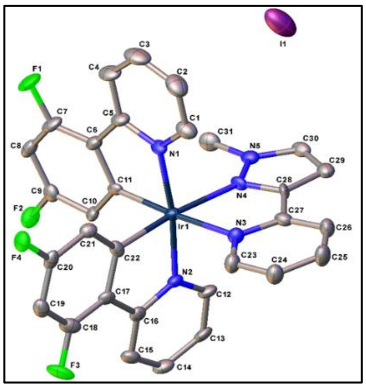

α The value of R1 is based on 'observed' data with I >2σ (I); the value of wR2 is based on all data.

7.10.4.2 ^{1}H NMR $^{F/H}$Ir•CH_3•NO_3 complex.

^{1}H NMR (400MHz, CD_3CN): δ(ppm) 8.24-8.22 (1H, m); 8.13-8.02 (3H, m); 7.97-7.83 (4H, m); 7.83-7.73 (3H, m); 7.61-7.55 (1H, m); 7.36 (1H, ddd, *J* 1.2, 5.5, 6.9); 7.20 (1H, d, *J* 2.8); 7.15 (1H, ddd, *J* 1.3, 5.8, 7.3); 7.11 (1H, ddd, *J* 1.3, 5.8, 7.3); 6.85-6.83 (1H, m); 6.18 (1H, dd, *J* 2.7, 6.2); 6.79-6.74 (1H, m); 5.90 (1H, dd, *J* 2.5, 9.5); 5.79 (1H, dd, *J* 2.5, 9.5).

7.10.5 Synthesis of $^{F/F}$ Ir•L^{Phenyl}•NO$_3$.

Both $^{F/H,\ H/H}$Ir•L^{Phenyl}•NO$_3$ series were prepared following the same synthesis procedure of the $^{F/F}$Ir•L^{Phenyl}•NO$_3$. All data are summarized on the **Table 7-3**.

A mixture of $^{F/F}$Ir•L^{pypz}•NO$_3$ (0.20 g, 0.25 mmole) and 2-(bromomethyl)phenyl (0.11 g, 0.64 mmole) in a ratio(1:2.5) were dissolved in MeCN (60 mL). The mixture was refluxed under the following conditions: temperature 88 ⁰C, overnight, N_2 atmosphere, and in dark. A yellowish-brown solution was cooled to room temperature and the solvent was evaporated to dryness. The yellow oil crude product was purified using column chromatography on (200-300 mesh) of silica gel eluted with MeCN/KNO$_{3(aq.)}$ in ratio (96:4)%. To remove the excess of KNO$_3$ the product was dissolved in (25 mL) DCM, then organic layer was extracted by using (60 mL) deionized H_2O then dried over MgSO$_4$ and filtered. The solvent was evaporated to give a yellow solid product.

Table 7-3 Summary of mono-$^{F/F,\ F/H\ and\ H/H}$Ir•L^{Phenyl}•NO$_3$ data.

Complex	**Starting material / Scale (g, mmol)**	**Scale (g, mmole) of 2-(bromomethyl)phenyl**	**R$_f$.**	**Yield (%)**	**ESMS: *m/z***
$^{F/F}$Ir•L^{Phenyl}•NO$_3$	$^{F/F}$Ir•pypz•NO$_3$ / (0.20 g, 0.25 mmol)	(0.11 g / 0.64 mmol)	0.26	0.12 g, 55%	808.87 (M-NO$_3$)$^+$
$^{F/H}$Ir•L^{Phenyl}•NO$_3$	$^{F/H}$Ir•pypz•NO$_3$ / (0.20 g, 0.26 mmol)	(0.11 g / 0.65 mmol)	0.24	0.18 g, 82%	772.18 (M-NO$_3$)$^+$
$^{H/H}$Ir•L^{Phenyl}•NO$_3$	$^{H/H}$Ir•pypz•NO$_3$ / (0.20 g, 0.26 mmol)	(0.11 g / 0.65 mmol)	0.24	0.15 g, 71%	736.91 (M-NO$_3$)$^+$

^{1}H NMR (400MHz, CD$_3$CN): δ(ppm) 7.21 (1H, d, *J* 7.8); 6.96 (1H, td, *J* 1.3, 1.3, 7.8); 8.82-7.92 (3H, m); 7.87 (1H, td, *J* 1.6, 7.6); 7.85-7.74 (3H, m); 7.74-7.70 (1H, m); 7.66 (1H, d, *J* 5.4); 7.59-7.52 (2H, m); 7.47 – 7.39 (2H, m); 7.35 (1H, td, *J* 1.2, 5.4, 7.3); 7.15-7.09 (2H, m); 7.07-7.01 (1H, m); 6.96 (1H, t, *J* 7.7); 6.80 (1H, td, *J* 2.6, 8.8); 6.67 (1H, td, *J* 8.9, 10.0); 6.08 (2H, d, *J* 7.4); 5.82 (1H, dd, *J* 2.5, *J* 9.7); 5.68 (1H, d, *J* 2.7); 5.66 (1H, d, *J* 2.5).

7.10.5.1 Crystallographic data and structure refinement for $^{F/F}\mathrm{Ir{\bullet}L}^{phenyl}{\bullet}\mathrm{NO_3}$

Formula	$C_{74}H_{54}F_8Ir_2N_{12}O_8$
Molecular weight	1775.69
T	100(2) K
Crystal system	Triclinic
Space group	P-1
a = 10.3553(4) Å	α= 89.079(2)°.
b = 12.1585(5) Å	β= 74.480(2)°.
c = 13.9382(6) Å	γ= 75.437(2)°.
V	1634.11(12) Å^3
Z	1
ρ	1.804 g/cm^3
Crystal size	0.430 × 0.340 × 0.300 mm^3
μ	4.161 mm^{-1}
Data / restraints / parameters	5776 / 110 / 518
Final R1, *wR*2^a	0.0199, 0.0561

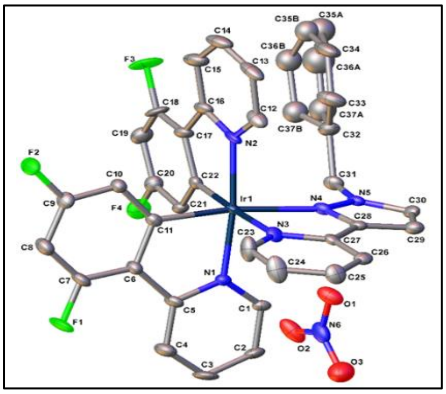

α The value of R1 is based on ‘observed’ data with I >2σ (I); the value of wR2 is based on all data.

7.10.5.2 ^{1}H NMR $^{F/H}\mathrm{Ir{\bullet}L}^{Phenyl}{\bullet}\mathrm{NO_3}$ complex

^{1}H NMR (400MHz, CD_3CN): δ(ppm) 8.32 (1H, d, *J* 7.8); 8.11-7.98 (2H, m); 7.94 (1H, s); 7.86 (1H, t, *J* 7.8, 15.0); 7.78-7.67 (4H, m); 7.61 (2H, d, *J* 7.2); 7.43-7.36 (2H, m); 7.33 (1H, t, *J* 6.5); 7.01-7.07 (2H, m); 7.07-6.92 (4H, m); 6.92-6.80 (3H, m); 6.27 (1H, d, *J* 7.0); 6.10 (3H, d, *J* 7.3); 5.16 (1H, d, *J* 16.2); 5.04 (1H, d, *J* 16.30).

7.10.5.3 ^{1}H NMR $^{H/H}\mathrm{Ir{\bullet}L}^{Phenyl}{\bullet}\mathrm{NO_3}$ complex

^{1}H NMR (400MHz, CD_3CN): δ(ppm) 8.32 (1H, d, *J* 7.8); 8.11-7.98 (2H, m); 7.94 (1H, s); 7.86 (2H, t, *J* 7.83, 15.2); 7.79-7.66 (4H, m); 7.61 (2H, d, *J* 7.0); 7.44-7.36 (2H, m); 7.33 (2H, t, *J* 6.4, 13.1); 7.17-7.07 (2H, m); 7.07-6.92 (4H, m); 6.92-6.79 (3H, m); 6.26 (1H, d, *J* 7.2); 6.10 (3H, d, *J* 7.4); 5.10 (1H, d, *J* 16.4); 5.04 (1H, d, *J* 16.4).

7.10.5.4 Crystallographic data and structure refinement for $^{H/H}$Ir•L^{phenyl}•NO$_3$. in a formula $^{H/H}$Ir•L^{phenyl}•Cl•H$_2$O•0.5MeCN

Formula	$C_{38}H_{32.50}ClIrN_{5.50}O$
Molecular weight	809.84
T	100(2) K
Crystal system	Monoclinic
Space group	$P2_1/c$
ɑ = 8.8735(9) Å	α= 90°.
b = 20.977(2) Å	β= 96.804(3)°.
c = 34.954(4) Å	γ= 90°.
V	6460.5(12) $Å^3$
Z	8
ρ	1.665 Mg/m^3
Crystal size	0.320 × 0.210 × 0.210 mm^3
μ	4.257 mm^{-1}
Data / restraints / parameters	14149 / 0 / 839
Final R1, $wR2^a$	R1 = 0.0499, wR2 = 0.1411

ɑ The value of R1 is based on 'observed' data with I >2σ (I); the value of wR2 is based on all data.

7.10.6 Synthesis of a new $^{F\ F/}$Ir•L^{2naph}•NO$_3$ complex

Both $^{F/H,\ H/H}$Ir•L^{2naph}•NO$_3$ series were prepared following the same synthesis procedure of the $^{F/F}$Ir•L^{2naph}•NO$_3$. All data are summarized on the **Table 7-4**.

A mixture of $^{F/F}$ Ir•pypz•NO$_3$ (0.13 g, 0.17 mmole) and 2-(bromomethyl)naphthalene (0.04 g, 0.18 mmole) in a ratio (1:1), cesium carbonate Cs_2CO_3 (0.04 g, 0.13 mmole) and Bu_4NI as a catalyst were dissolved in MeCN (60 mL). The mixture was refluxed under the following conditions: temperature 90 ºC, 48hr., under N_2 atmospher, and in dark. A yellow solution was cooled to room temperature and the solvent was evaporated to dryness then the yellow crude product was purified using silica gel column eluted with MeCN for 1000 mL then DCM/MeOH in a ratio (95:5 v/v).

^{1}H NMR: (CD_3CN) : δ(ppm) 8.39 (1H, d, *J* 8.1); 8.25 (1H, d, *J* 8.4); 8.18-8.14 (1H, m); 8.18-8.14 (1H, m); 8.12 (1H, dd, *J* 1.5, 7.8); 7.91 (2H, td, *J* 1.2, 7.8); 7.82 (1H, d, *J* 8.1); 7.76 (1H, d, *J* 5.2); 7.60-7.55 (2H, m); 7.52-7.47 (2H, m); 7.43-7.35 (2H, m); 7.27 (2H, d, *J* 8.1); 7.19 (1H, ddd, *J* 1.3, 5.8, 7.3); 7.13 (1H, td, *J* 1.0, 8.3); 7.07 (1H, dt, *J* 1.91, 8.39); 6.89 (1H, ddd, *J* 1.5, 5.8, 7.3); 6.64 (1H, ddd, *J* 2.3, 9.31, 12.1,); 6.54 (1H, ddd, *J* 2.3, 9.5, 12.1); 6.40 (1H, dd, *J* 1.8, 8.5); 6.14 (1H, s); 5.71 (1H, dd, *J* 2.3, 8.5); 5.51 (1H, d, *J* 17.3); 5.38 (1H, dd, *J* 2.2, 8.5); 5.22 (1H, d, *J* 17.3).

Table 7-4 Summary of mono-${}^{F/F,\ F/H\ and\ H/H}$Ir•L^{2naph}•NO$_3$ data.

Complex	**Starting material / scale (g, mmol)**	**Scale (g, mmol) of 2-(bromomethyl)naphthalene**	**scale of Cs$_2$CO$_3$**	**R$_f$.**	**Yield (%)**	**ESMS: *m/z***
${}^{F/F}$Ir•L^{2naph}•NO$_3$	${}^{F/F}$Ir•pypz•NO$_3$ / (0.13 g, 0.17 mmol)	(0.04 g / 0.18 mmol)	0.04 g, 0.13 mmol	0.3	0.11 g, 73%	858.2 [MNO$_3$+H]$^+$
${}^{F/H}$Ir•L^{2naph}•NO$_3$	${}^{F/H}$Ir•pypz•NO$_3$ / (0.1g, 0.13 mmol)	(0.03 g / 0.13 mmol)	0.05 g, 0.13 mmol	0.3	0.09 g, 82%	822.2 [MNO$_3$+H]$^+$
${}^{H/H}$Ir•L^{2naph}•NO$_3$	${}^{H/H}$Ir•pypz•NO$_3$ / (0.1g, 0.14 mmol)	(0.03 g / 0.14 mmol)	0.05 g, 0.14 mmol	0.25	0.09 g, 75%	786.2 [MNO$_3$+H]$^+$

7.10.6.1 ^{1}H NMR of a new ${}^{F/H}$Ir•L^{2naph}•NO$_3$ complex

^{1}H NMR (400MHz, CD$_3$CN) : δ(ppm) 8.42 (1H, d, *J* 8.0); 8.16 (1H, dd, *J* 1.5, 2.80); 8.10 (1H, tt, *J* 1.4, 7.8); 7.97 (1H, d, *J* 8.1); 7.86 (1H, td, *J* 1.4, 7.7); 7.84 – 7.76 (2H, m); 7.75 (1H, dt, *J* 6.45, *J* 1.4); 7.68 (1H, d, *J* 5.7); 7.55- 7.47 (4H, m); 7.41 (1H, tt, *J* 1.2, 8.2); 7.36-7.29 (2H, m); 7.20 (1H, ddd, *J* 1.3, 5.7, 7.0); 7.16-7.13 (1H, m); 7.13-7.08 (1H, m); 6.89-6.87 (1H, m); 6.85 (1H, dt, *J* 1.3, 7.3); 6.79-6.72 (1H, m); 6.70-6.63 (1H, m); 6.32 (1H, dt, *J* 1.6, 8.5); 6.19 (1H, s); 5.85 (1H, d, *J* 2.2); 5.82 (1H, d, *J* 2.4); 5.57 (1H, d, *J* 2.4); 5.55(1H, d, *J* 2.3); 5.45 (1H, d, *J* 16.9); 5.21 (1H, d, *J* 16.9).

7.10.6.2 ^{1}H NMR of a new ${}^{H/H}$Ir•L^{2naph}•NO$_3$ complex

^{1}H NMR (400MHz, CD$_3$CN): δ(ppm) 8.41 (1H, dt, *J* 7.9, *J* 1.0); 8.13 (1H, d, *J* 2.6); 8.05 (1H, td, *J* 1.5, 7.7); 8.00 (1H, d, *J* 8.1); 7.85-7.78 (2H, m); 7.74-7.68 (3H, m); 7.59-7.55 (1H, m); 7.53 (1H, d, *J* 2.7); 7.52-7.47 (2H, m); 7.41 (1H, ddd, *J* 1.2, 6.9, 8.1); 7.33 (1H, s); 7.32-7.26 (1H, m); 7.18 – 7.11 (2H, m); 7.08 (1H, ddd, *J* 1.3, 5.8, 7.3); 6.99 – 6.92 (2H, m); 6.90-6.82 (3H, m); 6.82-6.77 (2H, m); 6.28-6.26 (2H, m); 6.25 (1H, t, *J* 1.6); 6.20 (1H, s); 5.98 (1H, dd, *J* 1.0, 7.6); 5.40 (1H, d, *J* 16.7); 5.20 (1H, d, *J* 16.7).

7.10.7 Synthesis of a new $^{F/F}$Ir•L^{quinoline}•NO_3 complex

Both $^{F/H,H/H}$Ir•L^{quinoline}•NO_3 series follow the same synthesis procedure of the $^{F/F}$Ir•L^{quinoline}•NO_3. All data summarized on the

Table 7-5.

A mixture of $^{F/F}$Ir•pypz•NO_3 (0.10 g, 0.128 mmole) and 8-(bromomethyl)qunoline (0.029 g, 0.13 mmole) in a ratio(1:1), Cs_2CO_3 (0.04 g, 0.128 mmole) and Bu_4NI as a catalyst were dissolved in MeCN (60 mL). The mixture was refluxed under the following conditions: temperature 90 ^{o}C, 48 hr., in the N_2 gas, and in dark. A yellow solution was cooled to room temperature and the solvent was evaporated to dryness then the yellow crude product was purified using silica gel column eluted with MeCN for 1000 mL then MeCN:$KNO_{3(aq.)}$:H_2O (100:5:10) %. To remove excess of $KNO_{3,}$ the ppt. was dissolved in a minimum of DCM and water, extracted and evaporated to dryness.

Yield: (0.09 g, 75٪)

R_f:0.37

ESMS: *m/z* 859.2 $(M\text{-}NO_3)^+$, 430 $(M\text{-}NO_3\text{+}H)^{+2}$

^{1}H NMR (400MHz, CD_3CN): δ(ppm) 8.68 (1H, dd, *J* 1.7, 4.2); 8.38(1H, d, *J* 7.9); 8.29-8.22 (2H, m); 8.13 (2H, td, *J* 1.4, 7.5); 7.96-7.90 (2H, m); 7.79-7.72 (2H, m); 7.67 (1H, d, *J* 8.0) ; 7.61 (1H, dd, *J* 1.0, 5.7); 7.53 (1H, dd, *J* 4.2, 8.3); 7.51-7.47 (2H, m); 7.38 (1H, ddd, *J* 1.2, 5.5, 7.2); 7.27 (1H, ddd, *J* 1.3, 5.9, 7.3); 7.11 (1H, ddd, *J* 1.3, 5.8, 7.2); 6.79 (1H, t, *J* 7.5); 6.62 (1H, ddd, *J* 2.3, 9.3, 11.8); 5.91 (1H, d, *J* 17.9); 5.81 (1H, d, *J* 2.6); 5.79-5.73 (2H, m); 5.62 (1H, dd, *J* 2.3, 8.6); 5.38 (1H, dd, *J* 2.3, 8.7).

7.10.7.1 Crystallographic data and structure refinement for $^{F/F}$Ir•L^{quinoline}•NO_3 in a formula $^{F/F}$Ir•L^{quinoline}•NO_3•$0.5H_2O$.

Formula	$C_{40}H_{27}F_4IrN_7O_{3.5}$
Molecular weight	929.88
T	100 K
Crystal system	Monoclinic
Space group	C2/c
α= 35.035(5) Å	α=90^{o}
b= 14.0012 (8) Å	β= 107.247(3) ^{o}
c= 14.8491(19) Å	ϒ=90^{o}
V	6956.5(15) Å^3
Z	8
ρ	1.776 g/cm^3
Crystal size	0.3 × 0.2 × 0.12 mm^3
μ	3.914 mm^{-1}

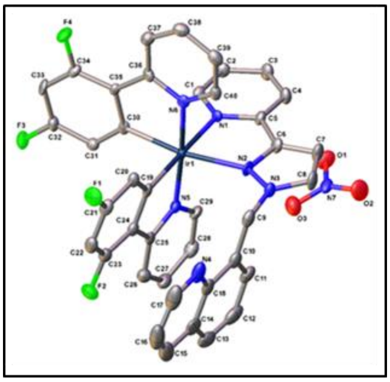

Data, restraints, parameters	8162 / 0 / 504
Final R1, $wR2^{a}$	0.0399, 0.0788

ɑ The value of R1 is based on 'observed' data with I >2σ (I); the value of wR2 is based on all data.

Table 7-5 Summary of mono-$^{F/F,\ F/H\ and\ H/H}$Ir•L^{quinoline}•NO_3 data.

Complex	**Starting material / Scale (g, mmol)**	**Scale (g, mmol) of 2-(bromomethyl)quinoline**	**Scale of Cs_2CO_3**	**R$_f$.**	**Yield (%)**	**ESMS: *m/z***
$^{F/F}$Ir•L^{quinoline}•NO_3	$^{F/F}$Ir•pypz•NO_3 / (0.10 g, 0.13 mmol)	(0.03 g / 0.13 mmol)	0.04 g, 0.13 mmol	0.37	0.09 g, 75%	859.2 $(M-NO_3)^+$, 430 $[M-NO_3+H]^+$
$^{F/H}$Ir•L^{quinoline}•NO_3	$^{F/H}$Ir•pypz•NO_3 / (0.10 g, 0.13 mmol)	(0.03 g / 0.13 mmol)	0.04 g, 0.13 mmol	0.28	0.08 g, 67%	823.2 $(M-NO_3)^+$, 411.6 $[M-NO_3+H]^+$
$^{H/H}$Ir•L^{quinoline}•NO_3	$^{H/H}$Ir•pypz•NO_3 / (0.10 g, 0.14 mmol)	(0.03 g / 0.14 mmol)	0.04 g, 0.14 mmol	0.25	0.08 g, 67%	787.2 $(M-NO_3)^+$, 394 $[M-NO_3+H]^+$

7.10.7.2 ^{1}H NMR $^{F/H}$Ir•L^{quinoline}•NO_3 complex

^{1}H NMR (400MHz, CD_3CN): δ(ppm) 8.64 (1H, dd, *J* 1.6, 4.2); 8.34 (1H, d, 8.0); 8.24 (1H, dd, *J* 1.6, 8.3); 8.10 (1H, td, *J* 1.4, 7.8); 8.06 (1H, d, *J* 2.7); 7.99 (1H, d, *J* 7.9); 7.94-7.87 (2H, m); 7.80-7.71 (3H, m); 7.68 (1H, d, *J* 8.3); 7.54 (1H, d, *J* 2.7); 7.50 (1H, ddd, *J* 1.2, 5.6, 6.9); 7.44 (1H, d, *J* 8.1); 7.38-7.33 (1H, m); 7.27 (1H, d, *J* 8.2); 7.25-7.19 (1H, m); 7.07 (1H, ddd, *J* 1.2, 5.8, 7.2); 6.80 (1H, d, *J* 7.6); 6.78 – 6.71(1H, m); 6.53 (1H, dd, *J* 5.6, 8.6); 5.92 (1H, d, *J* 18.1); 5.85 (1H, td, *J* 2.6, 8.9); 5.78 (1H, s); 5.74 (2H, dd, *J* 2.5, 9.5); 5.53 (1H, dd, *J* 2.5, 9.5).

7.10.7.3 Crystallographic data and structure refinement for $^{F/H}$Ir•L^{quinoline}•NO_3

Formula	$C_{40}H_{28}F_2IrN_7O_3$
Molecular weight	884.89
T	99.99 K
Crystal system	Monoclinic
Space group	$P2_1/c$
ɑ= 12.6733(10) Å	α=90^o
b= 26.469(2) Å	β= 102.930(4) ^{o}
c= 10.2335(8) Å	ϒ=90^o
V	3345.8(5) Å^3
Z	4

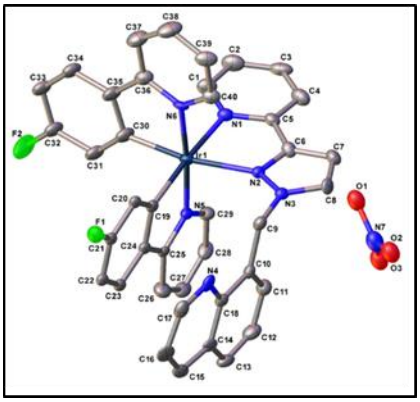

ρ	1.757 g/cm^3
Crystal size	0.3 × 0.2 × 0.2 mm^3
μ	8.265 mm^{-1}
Data, restraints, parameters	5895 / 490 / 400
Final R1, *wR*2[a]	0.0792, 0.1762

α The value of R1 is based on 'observed' data with I >2σ (I); the value of wR2 is based on all data.

7.10.7.4 ^{1}H NMR $^{H/H}$Ir•L^{quinoline}•NO$_3$ complex

^{1}H MR (400MHz, CD$_3$CN): δ(ppm) 8.60 (1H, dd, *J* 4.1, 1.5); 8.31 (1H, d, *J* 7.9); 8.23 (1H, dd, *J* 1.4, 8.2); 8.06 (1H, td, *J* 1.3, 7.8); 8.04-8.01 (1H, m); 7.99 (2H, t, *J* 7.9); 7.95 (1H, d, *J* 2.7); 7.87 (1H, td, *J* 1.3, 8.1); 7.75-7.66 (4H, m); 7.61 (1H, d, *J* 5.6); 7.40 (1H, d, *J* 2.6); 7.37 -7.27 (2H, m); 7.21 (1H, ddd, *J* 1.2, 5.8, 7.3); 7.06 (1H, ddd, *J* 1.1, 5.7, 7.1); 6.97 (1H, t, *J* 7.5); 6.87-6.76 (2H, m); 6.56 (1H, d, *J* 7.7); 6.50 (1H, t, *J* 7.5); 6.22-6.15 (2H, m); 5.99 (1H, d, *J* 7.5); 5.91-5.82 (2H, m); 5.65 (1H, d, *J* 17.4).

7.10.7.5 Crystallographic data and structure refinement for $^{H/H}Ir{\bullet}L^{quinoline}{\bullet}NO_3$ in a formula $^{H/H}Ir{\bullet}L^{quinoline}{\bullet}NO_3{\bullet}MeCN$

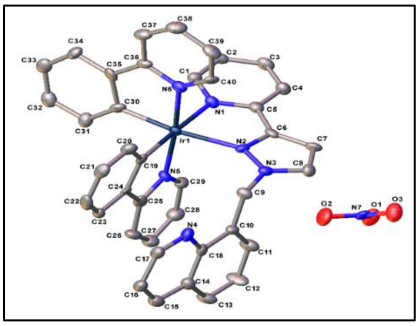

Formula	$C_{42}H_{33}IrN_8O_3$
Formula weight	889.96
T	100 K
Crystal system	Triclinic
Space group	*P*-1
α= 9.9062(13) Å	α= 101.203(5)°
b= 13.1377(17) Å	β= 92.169(5)°
c= 13.8554(18) Å	γ= 92.417(5)°
V	1765.3(4) Å^3
Z	2
ρ	1.674 g/cm^3
Crystal size	0.35 × 0.23 × 0.15 mm^3
μ	3.836 mm^{-1}
Data/restraints/parameters	8102 / 0 / 488
Final R1, *wR*2[*a*]	0.0792, 0.1762

α The value of R1 is based on ‘observed’ data with I >2σ (I); the value of wR2 is based on all data.

7.10.8 Synthesis of 1-Methyl-4-(2’-pyridyl)pyridinium iodide.

The synthesis of 1-Methyl-2-(2’-pyridyl)pyridinium iodide was accomplished following a procedure described by Ben Coe *et.al.*with some modification.[10] A solution of 4-(2’-pyridyl)pyridine (2.00 g, 12.8 mmole) in MeCN (50 mL) was bubbled and stirred under argon for 30 mins. Methyl iodide (2.4 mL, 38.6 mmole) was added slowly. The mixture was heated at 45 C for 48 h. A yellow precipitate was filtered and the filtrate was poured into stirring diethyl ether (200 mL). An off white precipitate was formed, filtrated and washed by (10 mL) diethylether.

ESMS: m/z =$[M-I]^+$:171

^{1}H NMR (400MHz, CD_3CN): δ(ppm) 9.67 (1H, s); 9.22 (1H, d, *J* 8.0); 8.96 (1H, dd, *J* 5.8); 8.81 (1H, d, *J* 4.4); 8.26-8.17 (2H, m); 8.06 (1H, td, *J* 1.6, 7.7); 7.61-7.54 (1H, m); 4.55 (3H, s)

7.10.8.1 Synthesis of $^{24}IrCl_2•PF_6$

A solution (1) of a 1-Methyl-2-(4'-pyridyl)pyridinium hexafluorophosphate (0.03 g, 1.2 mmole in 2-methoxyethanol (22 mL) was charged by argon. And a solution (2) of an $IrCl_3.3H_2O$ (0.2 g, 0.57 mmole) in water (8 mL) was also charged by argon. A solution (1) and (2) were mixed and refluxed at 120 °C for 48 hr under argon in dark by covering the round round bottom flask in foil. After cooling to room temperature, excess of NH_4PF_6 was added, the mixture was filtered and solvent evaporated. The precipetate was suspended with ice-cold water, filtered, rinsed with (4 mL) ice-cold water and washed rinsed with aceton/diethylether in aratio (1:3 mL) three times.

^{1}H NMR (400MHz, CD_3CN): δ(ppm) 8.86 (1H, d, *J* 2.8); 8.67 (3H, dd, *J* 2.1, 5.6); 8.48-8.39 (1H, m); 8.38-8.19 (3H, m); 8.19-7.97 (3H, m); 7.96-7.69 (2H, m); 7.62 (1H, td, *J* 4.8, 4.9); 7.36-7.26 (1H, t, *J* 9.1); 7.23-7.05 (3H, m).

7.10.8.2 Synthesis of $^{22}Ir•pypz•3PF_6$

Argon sparged a solution of 2-methoxy ethanol/water (4:1, 7.5 mL) for 20 mins. A mixture of $^{22}IrCl_2•PF_6$ (50.0 mg, 0.07 mmole) and $AgPF_6$ (35.4 mg, 0.14 mmole) was added and heated to 100 °C for 10 mins. Then, pypz (10.1 mg, 0.07 mmole) was added and the solution refluxed under argon for 36 h in dark. After cooling to room temperature, a yellow solution was obtained, filtered through celite to remove AgCl precipitate and the solvents were evaporated. The crud complex was purified by column chromatography on (200-300 mesh) silica gel eluted with $MeCN/KNO_{3(aq.)}/H_2O$ in a ratio (80:10:10), then sephedax LH20 eluting with MeOH. The main yellow band was collected and the solvent evaporated to dryness to give a bright yellow powder.

R_f: 0.45.

Yield (0.06, 75%).

ESMS: m/z 676.18 (M+H).

^{1}H NMR (400MHz, CD_3CN): δ(ppm) δ(ppm) 8.85 (2H, d, *J* 2.2, 7.3); 8.36 (2H, dd, *J* 2.6, 7.5); 8.13 (2H, td, *J* 1.0, 7.5, 15.3); 8.05-7.89 (2H, m); 7.88 (1H, d, *J* 5.3); 7.73 (1H, d, *J* 5.8); 7.65 (2H, t, *J* 5.6); 7.58 (1H, d, *J* 2.1); 7.48 (1H, d, *J* 5.1); 7.48-7.38 (2H, m); 7.20 (1H, ddd, *J* 2.2, 5.5, 6.7); 7.01 (1H, d, *J* 5.9); 6.92 (1H, d, *J* 1.7); 6.89 (1H, d, *J* 6.1); 4.10 (3H, s); 4.05 (3H, s).

7.10.8.3 Crystallographic data and structure refinement for ^{22}Ir•pypz•3PF$_6$.

Formula	$C_{30}H_{26}Cl_2IrN_7$
Molecular weight	747.68
T	100 K
Crystal system	Monoclinic
Space group	$P2_1/c$
a= 18.133(6) Å	α= 90°
b= 43.016(13) Å	β= 90.931(9)°
c= 8.506(3) Å	ϒ= 90°
V	663(45) Å^3
Z	8
μ	9.503 mm^{-1}
Crystal size	0.158 × 0.075 × 0.027
Final R1, *wR*2^a	0.0897, 0.1776

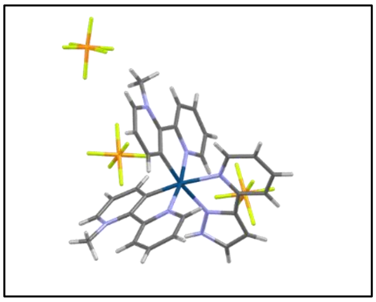

ɑ The value of R1 is based on ‘observed’ data with $I > 2\sigma(I)$; the value of wR2 is based on all data.

The synthesis method of ^{23}Ir•pypz•3PF$_6$ and ^{24}Ir•pypz•3PF$_6$ complexes were identical to ^{22}Ir•pypz•3PF$_6$ by using ^{23}IrCl$_2$•PF$_6$ and ^{24}IrCl$_2$•PF$_6$ in place to give a yellow precipitate.

7.10.8.4 ^{23}Ir•pypz•3PF$_6$

R$_f$: 0.40.

Yield (0.05, 63%).

^{1}H NMR (400MHz, CD$_3$CN): δ(ppm) 8.82 (2H, d); 8.26 (2H, dd, *J* 2.4, 7.6); 8.13 (2H, td, *J* 1.2, 7.9, 15.7); 8.07-7.92 (2H, m); 7.89 (1H, d, *J* 5.6); 7.76 (1H, d, *J* 6.2); 7.68 (2H, t, *J* 5.3); 7.61 (1H, d, *J* 1.9); 7.52 (1H, d, *J* 5.4); 7.48-7.38 (2H, m); 7.21 (1H, ddd, *J* 2.1, 5.8, 6.6); 7.03 (1H, d, *J* 6.1); 6.95 (1H, d, *J* 1.9); 6.89 (1H, d, *J* 6.3); 4.12 (3H, s); 4.08 (3H, s).

7.10.8.5 ^{24}Ir•pypz•3PF$_6$

R$_f$: 0.32.

Yield (0.06, 75%).

^{1}H NMR (400MHz, CD$_3$CN): δ(ppm) 8.45 (1H, dd, *J* 4.4, 7.8); 8.37-8.31 (1H, m); 8.32-8.25 (1H, m); 8.22 (1H, d, *J* 6.0); 8.18-8.00 (2H, m); 7.86 (1H, d, *J* 5.3); 7.75-7.66 (1H, m); 7.65-7.58 (1H, m); 7.51-7.41 (1H, m); 7.33-7.21 (1H, m); 7.02 (1H, s).

7.10.9 Synthesis of $L^{bi\text{-}ph}$

The method for the synthesis of $L^{bi\text{-}ph}$ was followed and modified from a literature procedure by Hall [8]. A mixture of and pypz (1.26 g, 8.73 mmole), aqueous NaOH (7.9×10^{-2}M, 3.16 cm^3) and Bu_4NI as a catalyst was refluxed in THF (65 mL) in 75 ºC for 10 min. To the mixture a 4,4´- bis(bromomethyl)biphenyl (1.00 g, 3.97 mmole) was added in 1:2 (4,4´-bis(bromomethyl)biphenyl:pypz) ratios and refluxed for 72 hrs. then cooled to room temperature. In a separating funnel aqueous layer and organic layer was suspension by using (25 mL) for each DCM and water. The organic extracts were dried over $MgSO_4$ and solution was evaporated in vacuo. A yellow product was sonicated in diethyl ether to obtain a white solid.

R_f: 0.6.

Yield (1.75g, 82 %).

ESMS: *m*/*z* 469.2.

^{1}H NMR (400MHz, $CDCl_3$): δ(ppm) 8.52 (1H, d, *J* 4.2); 7.86 (1H, d, *J* 7.3); 7.51 (1H, t, *J* 7.2); 7.38 (2H, d, *J* 7.8); 7.34 – 7.25(2H, m); 7.15(1H, d, *J* 8.0); 7.01 (1H, t, *J* 5.6); 6.86 (1H, d, *J* 1.8); 5.24 (2H, s).

7.10.10 Synthesis of $^{22}Ir•L^{bi\text{-}ph}•3PF_6$ complex.

Argon sparated a solution of 2-methoxy ethanol/water (4:1, 7.5 mL) for 30 mins. A mixture of $^{22}IrCl_2•PF_6$ (50.0 mg, 0.07 mmole) and $AgPF_6$ (35.4 mg, 0.014 mmole) was added and heated to 120 ºC for 10 mins. Then, $L^{bi\text{-}ph}$ (65.7 mg, 0.14 mmole) was added. The solution was refluxed under argon for 48 h. in dark. The mixture was cooled to room temperature and filtered through celit to remove AgCl precipitate and the solvents were evaporated. The filtrate was purified by column chromatography on (200-300 mesh) silica gel eluated by $MeCN/KNO_{3(aq)}/H_2O$ in a ratio (80:10:10), then for more purification sephedex LH20 was used and eluated with MeOH. The main yellow band was collected and dried to give a bright yellow powder.

Data for $^{22}Ir•L^{bi\text{-}ph}•3PF_6$.

R_f: 0.50.

Yield (0.08 g, 80 %).

ESMS: m/z 1007.59 (M+H).

^{1}H NMR (400MHz, CD_3CN): δ(ppm) 8.78 (1H, dd, *J* 2.3,7.8); 8.59 (1H, d, *J* 7.1); 8.63-8.55 (2H, m); 8.50 (1H, dd, *J* 2.3, 7.7); 8.35-8.12 (3H, m); 8.09 (1H, d, *J* 3.4); 8.06-8.04 (2H, m); 7.95 (1H, td, *J* 1.8, 7.2); 7.89 (1H, dd, *J* 2.2, 7.4); 7.82-7.75 (3H, m); 7.65 (3H, ddd, *J* 2.3, 5.2, 6.8); 7.60 (1H, ddd, *J* 1.3, 4.2, 7.3); 7.51-7.38 (4H, m); 7.38-7.45 (3H, m); 7.28 (3H, dd, *J* 2.0, 7.1); 7.05 (1H, ddd, *J* 2.3, 5.1, 7.3); 6.9 (1H, m); 6.01 (2H, dd, *J* 2.3, 7.2); 5.60 (1H, d, *J* 17.7); 5.47 (2H, s); 4.94 (1H, d, *J* 17.7); 4.57 (3H, s); 4.25 (3H, s).

7.10.10.1 Synthesis of ^{23}Ir•L$^{bi\text{-}ph}$•3PF_6 and ^{24}Ir•L$^{bi\text{-}ph}$•3PF_6

These complexes were synthesised and purified in a manner identical to ^{22}Ir•L$^{bi\text{-}ph}$•3PF_6 by using ^{23}IrCl_2•PF_6 and ^{24}IrCl_2•PF_6 in place of ^{22}IrCl_2•PF_6. A yellow precipitate was obtained. The characterisation data are as follow.

Data for ^{23}Ir•L$^{bi\text{-}ph}$•PF_6

R_f: 0.35.

Yield (0.06 g, 60 %).

^{1}H NMR (400MHz, CD_3CN): δ (ppm) 8.76 (1H, s); 8.53 (1H, d, *J* 4.8); 8.40 (1H, d, *J* 8.1); 8.26 (2H, d, *J* 9.8); 8.22 (2H, td, *J* 1.3, 7.8); 8.15(1H, d, *J* 2.8), 8.00-7.93 (2H, m); 7.91-7.85 (2H, m); 7.84 (1H, d, *J* 2.3); 7.74- 7.65 (4H, m), 7.61-7.52 (4H, m); 7.49 (1H, d, *J* 2.8); 7.47-7.39 (4H, m); 7.34 (1H, ddd, *J* 1.1, 4.9, 6.1); 7.71 (2H, d, *J* 8.1); 6.96 (1H, d, *J* 2.3); 6.91 (1H, d, *J* 6.2); 6.53 (1H, d, *J* 6.2); 6.04 (2H, d, *J* 8.1); 5.51-5.42 (3H, m); 4.48 (1H, d, *J* 17.7); 4.10 (3H, s); 4.05 (3H, s).

Data for ^{24}Ir•L$^{bi\text{-}ph}$•PF_6

R_f: 0.30.

Yield (0.07 g, 70 %).

^{1}H NMR (400MHz, CD_3CN): δ(ppm) 8.6 (1H, d, *J* 7.8); 8.56-8.50 (3H, m); 8.45-8.36 (3H, m); 8.27-8.19 (2H,m); 8.02 (1H, d, *J* 7.9); 7.98 (1H, d, *J* 6.4); 7.94 (1H, d, *J* 5.5); 7.91-7.85 (4H, m); 7.85-7.81 (2H, m); 7.68-7.61 (5H, m); 7.53-7.44 (4H, m); 7.37-7.32(1H, m); 7.23 (1H, s); 7.19 (2H, d, *J* 8.2); 6.96 (1H, d, *J* 2.2), 6.00 (2H, d, *J* 8.0); 5.60 (1H, d, *J* 17.7); 5.51 (2H, s); 5.11 (1H, d, *J* 17.8); 4.18 (3H, s); 4.08 (3H, s).

7.10.11 Synthesis of L^{naph}

Synthesis of L^{naph} was accomplished following the procedure described by Hall.[8] In this study a mixture of pypz (0.92 g, 6.36 mmole), aqueous sodium hydride NaH [60% dispersion in mineral oil] (1.58 g, 66.00 mmole) and Bu_4NI (20 mg) as a catalyst in dry THF (100 mL) was refluxed at 75 ºC with stirring for 10 min under N_2. Then 2,7′- bis(bromomethyl)naphthalene (Br-nap) (1.00 g, 3.18 mmole) in a 1:2 (Br-nap:pypz) ratios was added and the mixture was refluxed for 24hr. Then, this mixture was allowed to cool to room temperature, filtered, dried over $MgSO_4$ and a solution was evaporated by rotary evaporation. A yellow oil product was purified by silica column in elute DCM/MeOH (95:5 v/v) ratio.

Analysis found: C, 74.6; H, 5.5; N, 18.7%. for $C_{28}H_{22}N_6.0.5H_2O$

required: C, 74.5; H, 5.1; N, 18.6%.

R_f: 0.50.

Yield (0.89g, 69 %).

ESMS: *m/z* 443$(M+H)^+$.

^1H NMR (400 MHz, $CDCl_3$): δ(ppm) 8.46(1H, d, *J* 4.8); 7.81 (1H, d, *J* 7.9); 7.51(1H, d, *J* 8.3); 7.42 (1H, td, *J* 1.6, 7.8,); 7.35(1H, s); 7.24(1H, d, *J* 2.2); 7.12 (1H, d, *J* 8.5); 6.92-6.91 (1H, m); 6.82 (1H, d, *J* 2.2); 5.23 (2H, s).

7.10.11.1 Crystallographic data and structure refinement for L^{naph}.

Formula	$C_{28}H_{22}N_6$
Molecular weight	442.51
T	100(2) K
Crystal system	Orthorhombic
a= 4.9279(14) Å	α= 90°
b= 11.578(4) Å	β= 90°
c= 38.138(12) Å	γ= 90°
V	2176.0(12) Å^3
Z	4
ρ	1.351 g/cm^{-3}
Crystal size	0.25 × 0.16 × 0.11 mm^3
μ	0.083 mm^{-1}
Data, restraints, parameters	2763 / 0 / 309
Final *R*1, *wR*2[a]	0.079, 0.167

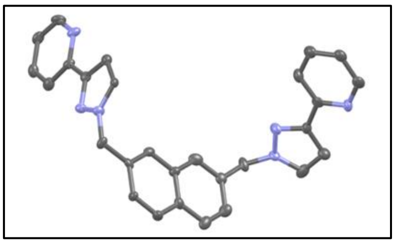

[a] The value of R1 is based on ‘observed’ data with I >2σ (I); the value of wR2 is based on all data.

7.10.12 The synthesis of the Ir-dimers

$^{F/F}$Ir-dimer, $^{F/H}$Ir-dimer and $^{H/H}$Ir-dimer synthesis were based on literature procedure.[9] To synthesis $^{F/F}$Ir-dimer, a mixture of $IrCl_3.XH_2O$ (1.80 g, 6.20 mmole) with ligand 2-(2, 4-difluorophenyl)pyridine (2.5 g, 14.90 mmole) was refluxed in a mixture of solvents 2-ethoxyethanol:H_2O (100:10 cm^3) in dark for 20 hr. The mixture was cooled to room temperature and a yellow precipitate was formed after adding 500 cm^3 of H_2O. The precipitate was filtered, washed with hexane and deionized water. In case of synthesis $^{F/H}$Ir-dimer and $^{H/H}$Ir-dimer a 2-(4-Fluorophenyl)pyridine and phenyl pyridine ligand were used respectively instead of 2-(2, 4-difluorophenyl)pyridine ligand. In all cases the dimer was used as starting materials without further purification.

ESMS for $^{F/F}$Ir-dimer: *m/z* 1216 (*M*)$^+$.

ESMS for $^{F/H}$Ir-dimer: *m/z* 1144 (*M*)+.

ESMS for $^{H/H}$Ir-dimer: *m/z* 1072 (*M*)+.

7.10.13 Synthesis of $^{F/F}$Ir•L^{naph}•NO_3 and $^{F/F}$Ir•L^{naph}•Ir•2PF_6 complexes.

A mixture of $^{F/F}$Ir-dimer (0.11 g, 8.81 mmol) and L^{naph} (0.10 g, 2.26 mmol) was dissolved in degassed solvents DCM /MeOH (3:1, v/v). The mixture was refluxed for 18 hr. under N_2 in the dark. Bright yellow solution was cooled to room temperature and the solvent was evaporated by rotary evaporation. DCM (25 cm^3) and $KPF_{6(aq.)}$ solution (20cm^3) were added and then the organic layer was extracted. The organic layer was dried over $MgSO_4$, filtered and removed the solvent to afford a yellow oil crude product. The crude was purified by silica gel chromatography through eluting with MeCN/ KNO_{3}(aq.) in ratio (96:4, v/v). The first major fraction to collect was $^{F/F}$Ir•L^{naph}•NO_3.

R_f: 0.55.

Yield: (0.15 g, 63%).

ESMS: *m/z* 1015.24 (*M* – NO_3)$^+$.

^{1}H NMR (400 MHz, CD_3CN): δ(ppm) 8.56 (1H, d, *J* 4.5); 8.34 (1H, d, *J* 7.9); 8.24 (1H, d, *J* 8.6); 8.15-8.06 (2H, m); 7.95 (1H, d, *J* 8.0); 7.89 (1H, t, *J* 7.8); 7.85-7.79 (2H, m); 7.78-7.67

(3H, m); 7.59 (1H, d, *J* 8.5); 7.51-7.42 (3H, m); 7.36 (1H, td, *J* 1.3, 6.6); 7.24 (1H, dd, *J* 4.8, 6.4); 7.18 (1H, td, *J* 1.2, 6.6); 6.98 (1H, s); 6.95 (1H, d, *J* 2.2); 6.92 (2H, d, *J* 4.0); 6.70-6.68 (1H, m); 6.62 (1H, td, *J* 2.3, 11.1); 6.55-6.41 (2H, m); 5.87 (1H, s); 5.68 (1H, dd, *J* 2.2, 8.4); 5.51-5.47 (3H, m); 5.30 (1H, dd, *J* 2.2, 8.5); 5.19 (1H, d, *J* 17.6).

For the elemental analysis, the sample was analysed as the hexafluorophosphate salt.

Elemental analysis: found C, 52.7; H, 3.4; N, 11.2%. $C_{50}H_{34}F_4IrN_8PF_6$•2MeCN

required: C, 52.2; H, 3.3; N, 11.3%.

7.10.13.1 Crystallographic data and structure refinement for $^{F/F}$Ir•L^{naph}•NO_3 in a formula [Ir(F_2ppy)$_2$(L^{naph})](NO_3)•2MeCN•H_2O.

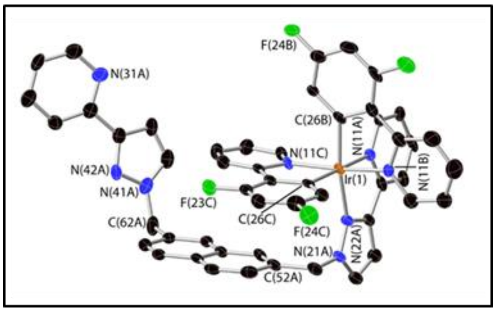

Formula	$C_{54}H_{42}F_4IrN_{11}O_4$
Molecular weight	1177.18
T	100(2) K
Crystal system	Monoclinic
Space group	*C*2/c
a= 41.4653(17)	α= 90^o
b= 15.8612(6)	β= 1100.806(2)^o
c= 15.7425(6)	γ= 90^o
V	10170.1(7)
Z	8
ρ	1.538 g/cm^{-3}
Crystal size	0.25 × 0.24 × 0.21
μ	2.698 mm^{-1}
Data, restraints, parameters	8977 / 84 / 690
Final *R*1, *wR*2^{a}	0.065, 0.183

ɑ The value of R1 is based on ‘observed’ data with I >2σ (I); the value of wR2 is based on all data.

The second yellow fraction to elute was dinuclear $^{F/F}$Ir•L^{naph}•Ir•2NO_3. Then solvents were evaporated and anion convert to PF_6 through metathesis with $KPF_{6(aq.)}$. Complex was collected as $^{F/F}$Ir•L^{naph}•Ir•2PF_6 as a yellow solid.

R_f: 0.30

Yield: (0.70 g, 17%).

ESMS: *m/z* 1587.2 $(M - PF_6)^+$.

^{1}H NMR (400 MHz, CD_3CN): δ(ppm) 8.35 (1H, t, *J* 8.9) ; 8.27-8.19 (2H, m) ; 8.17-8.06 (1H, m); 7.97-7.86 (1H, m); 7.77-7.65 (2H, m); 7.62-7.48 (1.5H, m); 7.48-7.33 (2.5H, m); 7.30-7.00 (2.5H, m); 6.92-6.90 (0.5H, m); 6.87-6.75 (1H, m); 6.70-6.57 (1H, m); 6.54-6.41 (1.5H, m); 6.28 (0.5H, d, *J* 8.6); 5.88 (0.5H, s); 5.68-5.65 (0.5H, m); 5.63-5.50 (1H, m); 5.44 (0.5H, d, *J* 17.3); 5.35-5.30 (0.5H, m); 5.28-5.26 (0.5H, m); 5.22-5.10 (1.5H, m).

Elemental analysis: found C, 46.4; H, 3.1; N, 8.5%. $C_{72}H_{46}F_8Ir_2N_{10}$•$2PF_6$•2MeCN

required: C, 46.6; H, 2.7; N, 8.6%.

7.10.13.2 Crystallographic data and structure refinement for $^{F/F}$Ir•L^{naph}•Ir•$2PF_6$ in a formula [{Ir(F_2ppy)$_2$)}$_2$(μ–L^{naph})](PF_6)$_2$•6MeCN.

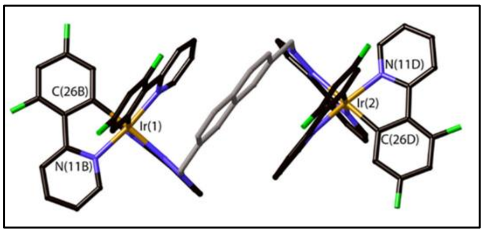

Formula	$C_{84}H_{64}F_{20}Ir_2N_{16}P_2$
Molecular weight	2123.85
T	110(2) K
Crystal system	Triclinic
Space group	*P*-1
a= 13.6101(9) Å	α= 103.115(3)°
b=17.2667(11) Å	β= 91.695(3)°
c=18.3547(13) Å	γ= 99.224(3)°
V	4136.8(5) Å^3
Z	2
ρ	1.705 g/cm^3
Crystal size	0.41 × 0.39 × 0.38 mm^3
μ	3.354 mm^{-1}
Data, restraints, parameters	18878/ 67 / 1101
Final *R*1, *wR*2^a	0.038, 0.123

ɑ The value of R1 is based on 'observed' data with I >2σ (I); the value of wR2 is based on all data.

Both $^{F/H,\ H/H}$Ir•L^{naph}•NO_3 series follow the same synthesis procedure of the $^{F/F}$Ir•L^{naph}•NO_3. All data summarized on the **Table 7-6**.

Table 7-6 Summary of mono-$^{F/F,\ F/H\ and\ H/H}$Ir•L^{naph}•NO_3 data.

Complex	Starting material / Scale (g, mmol)	Scale (g, mmole) of L^{naph}	R$_f$.	Yield (%)	ESMS: *m/z*
$^{F/F}$Ir•L^{naph}•NO_3	$^{F/F}$Ir•dimer/ (0.10 g, 8.81 mmol)	(0.10 g / 2.26 mmol)	0.55	0.15 g, 63%	1015.24 (M-NO_3)$^+$
$^{F/H}$Ir•L^{naph}•NO_3	$^{F/H}$Ir•dimer/ (0.20 g, 6.20 mmol)	(0.10 g / 3.10 mmol)	0.45	0.18 g, 70%	1041.26 (M-NO_3)$^+$
$^{H/H}$Ir•L^{naph}•NO_3	$^{H/H}$Ir•dimer / (0.20 g, 8.20 mmol)	(0.10 g / 2.50 mmol)	0.43	0.15 g, 68%	1005.27 (M-NO_3)$^+$

7.10.13.3 ^{1}H NMR of $^{F/H}$Ir•L^{naph}•NO$_3$ complex

^{1}H NMR (400 MHz, CD$_3$CN): δ(ppm) 8.52 (1H, d, *J* 4.1); 8.29 (1H, d, *J* 7.9); 8.08-8.01 (2H, m); 7.95 (1H, d, *J* 7.9); 7.90 (1H, d, *J* 7.9); 7.84 (1H, d, *J* 2.2); 7.82- 7.75 (2H, m); 7.75-7.67 (3H, m); 7.64 (1H, d, *J* 5.4); 7.50-7.40 (3.6H, m); 7.31-7.25 (1H, m); 7.25-7.20 (1H, m); 7.12-7.04 (2H, m); 7.03 (1H, s); 6.97 (1H, d, *J* 2.3); 6.91 (1H, t, *J* 7.3); 6.74-6.70 (3H, m); 6.58 (1H, td, *J* 2.2, 8.7); 6.30 (1H, dd, *J* 1.0, 8.3); 5.93 (1H, s); 5.81 (1H, dd, *J* 2.03, *J* 9.6); 5.5-5.36 (3H, m); 5.41 (1H, d, *J* 17.0); 5.17 (1H, d, *J* 17.0).

7.10.13.4 ^{1}H NMR of $^{H/H}$Ir•L^{naph}•NO$_3$ complex

^{1}H NMR (400 MHz, CD$_3$CN): δ(ppm) 8.57 (1H, d, *J* 4.4); 8.29 (1H, d, *J* 7.9); 8.08-8.02 (2H, m); 7.97 (2H, t, *J* 7.5); 7.85-7.78 (3H, m); 7.76 (1H, t, *J* 1.7, 7.6, 9.4); 7.71-7.66 (3H, m); 7.52-7.45 (3H, m); 7.41 (1H, d, *J* 2.5); 7.30 (1H, ddd, *J* 1.35, 5.6, 7.1); 7.28-7.23 (1H, m); 7.11-7.05 (3H, m); 7.00-6.90 (3H, m); 6.81-6.80 (2H, m); 6.80-6.15 (2H, m); 6.69 (1H, ddd, *J* 1.3, 5.6, 7.2); 6.10 (1H, ddd, *J* 1.6, 8.4); 6.36-6.16 (1H, m); 5.05 (1H, s); 5.03-5.88 (1H, ddd, *J* 0.8, 7.8); 5.52 (2H, s); 5.16 (1H, d, *J* 17.2); 5.10 (1H, d, *J* 17.0).

7.10.14 Synthesis of $^{F/F}$Ir•L^{naph}•Re(CO)$_3$Cl•NO$_3$ complex

A (22 mg, 0.20 mmol) of a mono-$^{F/F}$Ir•L^{naph}•NO$_3$ complex was added to (8 mg, 0.24 mmol) Re(CO)$_5$Cl complex, the mixture was refluxed under N$_2$ for 24 hr. in MeCN solvent. A yellow solution was formed and cooled to room temperature. The solvent was evaporated and KPF$_{6(aq.)}$ solution (25cm^3) and DCM (25cm^3) were added. The mixture was shacked to extract the organic layer. The organic layer was dried over MgSO$_4$, filtered and solvent was removed to dryness. To purify the crude product, a silica gel column chromatography was used and eluting with MeCN:KNO$_{3(aq.)}$ in a ratio (98:2, v/v). A pure yellow solid complex was obtained and characterised.

R$_f$: 0.50

Yield: (0.10 g ,26%).

ESMS: *m/z* 1321.2 (*M* – PF$_6$)$^+$.

IR: unresolved shoulder ν_{CO} signal at 1877 cm^{-1}

^{1}H NMR (400 MHz, CD$_3$CN): δ(ppm) 8.93-8.92 (1H, m); 8.31-8.30 (1H, m); 8.25-8.20 (1H, m); 8.17-8.13-8.12 (2 H, m); 8.12-8.04 (3H, m); 7.94-7.83 (2H, m); 7.75-7.66 (2H, m); 7.60-

7.58 (1H, m); 7.56-7.42 (3.5H, m); 7.41-7.32 (1.5H, m); 7.27-7.20 (1.5H, m); 7.20-7.09 (1.5H, m); 7.09-7.02 (1.5H, m); 6.97 (0.5H, s); 6.81-6.69 (1H, m); 6.65 (1H, ddd, *J* 2.3, 9.4, 12.5); 6.57-6.47 (1H, m); 6.43-6.40 (1H, m); 6.0. (1H, d, *J* 15.0); 5.93-5.84 (1H, m); 5.82-5.71 (1H, m); 5.71-5.64 (1H, m); 5.50-5.42 (1H, m); 5.34 (1H, dd, *J* 2.3, 8.6); 5.20 (1H, d, *J* 17.3).

Elemental analysis:found: C, 43.3; H, 2.8; N, 7.5%. $C_{53}H_{34}F_4IrN_8O_3ReCl•PF_6•H_2O$

required: C, 42.9; H, 2.4; N, 7.5%.

7.10.14.1 Crystallographic data and structure refinement for $^{F/F}$Ir•L^{naph}•Re•NO_3 in a formula [{$(F_2ppy)_2$Ir}(L^{naph}) {Re$(CO)_3$Cl}](NO_3)•MeCN•0.64H_2O.

Formula	$C_{55}H_{38.28}ClF_4IrN_{10}O_{6.64}Re$
Molecular weight	1435.32
T	110(2) K
Crystal system	Triclinic
Space group	*P*-1
a= 12.0080(4) Å	α= 64.392(2)°
b= 15.1430(5) Å	β= 77.127(2)°
c= 15.9523(5) Å	γ= 89.872(2)°
V	2535.41(15) Å^3
Z	2
ρ	1.880 g/cm^3
Crystal size	0.42 × 0.26 × 0.19 mm^3
μ	5.139 mm^{-1}
Data, restraints, parameters	11413 / 38 / 741
Final R1, *wR*2^a	0.0372, 0.121

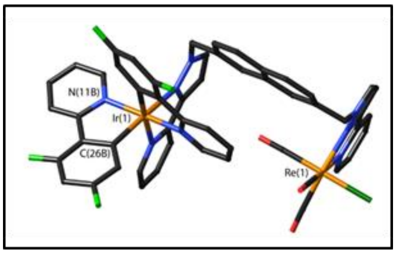

α The value of R1 is based on 'observed' data with I >2σ (I); the value of wR2 is based on all data.

7.11 References

1 G. M. Sheldrick, *Acta Crystallogr. Sect.*, 2008, **A64**, 112–122.

2 G. M. Sheldrick, *Acta Crystallogr.*, 2015, **71**, 3–8.

3 O. V. Dolomanov, L. J. Bourhis, R. J. Gildea, J. A. K. Howard and H. Puschmann, *J. Appl. Crystallogr.*, 2009, **42**, 339–341.

4 K. Suzuki, A. Kobayashi, S. Kaneko, K. Takehira, T. Yoshihara, H. Ishida, Y. Shiina, S. Oishi and S. Tobita, *Phys. Chem. Chem. Phys.*, 2009, **11**, 9850–9860.

5 J. A. G. Williams, E. S. Davies, J. A. Weinstein and C. Wilson, *Inorg. Chem.*, 2003, **42**, 8609–8611.

6 Z. N. Zubaidi, A. J. Metherell, E. Baggaley and M. D. Ward, *Polyhedron*, 2017, **133**, 68–74.

7 A. J. Amoroso, A. M. C. Thompson, J. C. Jeffery, P. L. Jones, M. J. A and M. D. Ward, *J. Chem. Soc.-Chem. Commun.*, 1994, **0**, 2751–2752.

8 B. R. Hall, PhD Thesis, University of Sheffield, 2011

9 S. Sprouse, K. A. King, P. J. Spellane and R. J. Watts, *J. Am. Chem. Soc.*, 1984, **106**, 6647–6653.

10 B. J. Coe, M. Helliwell, S. Sánchez, M. K. Peers and N. S. Scrutton, *Dalton. Trans.*, 2015, **44**, 15420–15423.

APPENDIX

Appendix A

Chapter Four

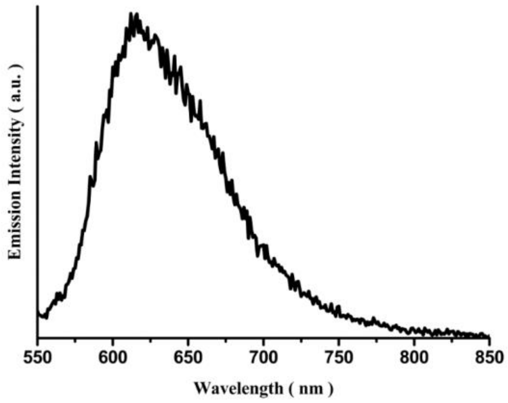

^{22}IrCl$_2$•PF$_6$ in EtOH-MeOH in air

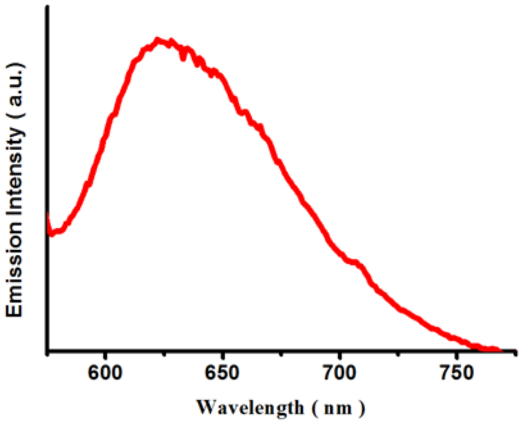

^{22}IrCl$_2$•PF$_6$ in EtOH-MeOH at 77K

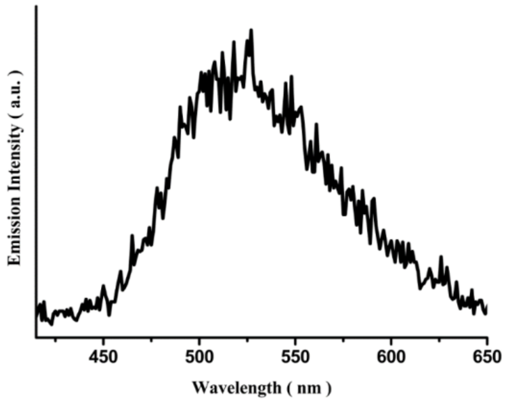

^{23}IrCl$_2$•PF$_6$ in EtOH-MeOH in air

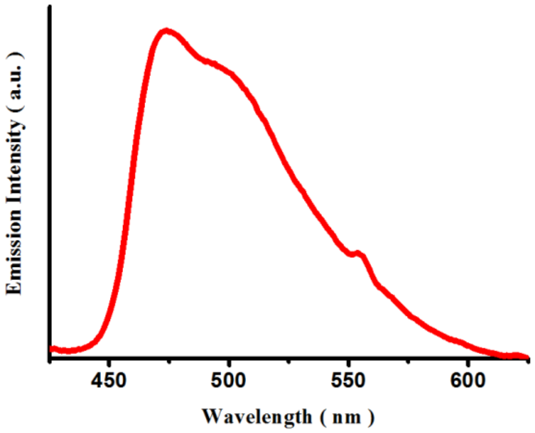

^{23}IrCl$_2$•PF$_6$ in EtOH-MeOH at 77K

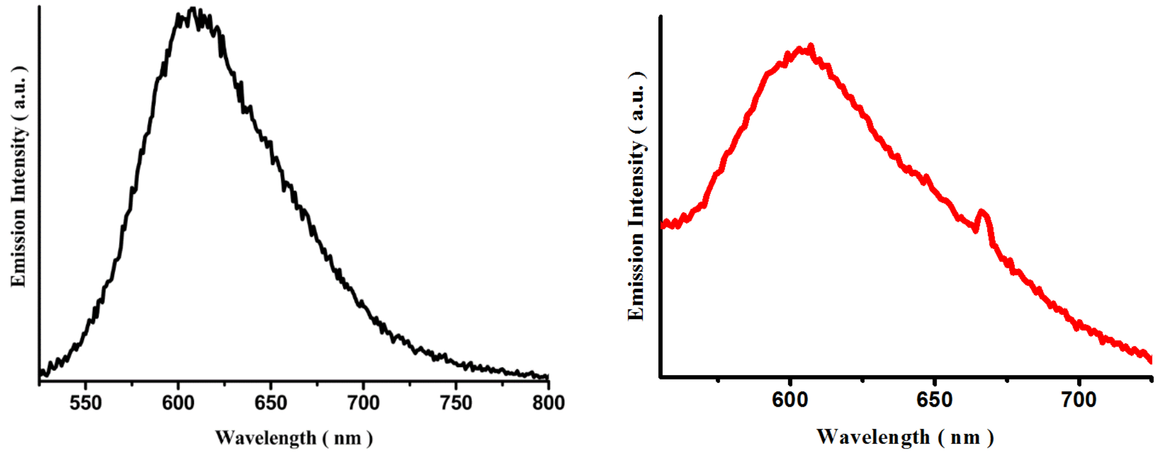

^{24}IrCl$_2$•PF$_6$ in EtOH-MeOH in air **^{24}IrCl$_2$•PF$_6$ in EtOH-MeOH at 77K**

Figure A-1 Emission spectrum of ^{22}Ir.Cl$_2$.PF$_6$, ^{22}Ir.Cl$_2$.PF$_6$ and ^{22}Ir.Cl$_2$.PF$_6$ in EtOH-MeOH at 298K and 77K.

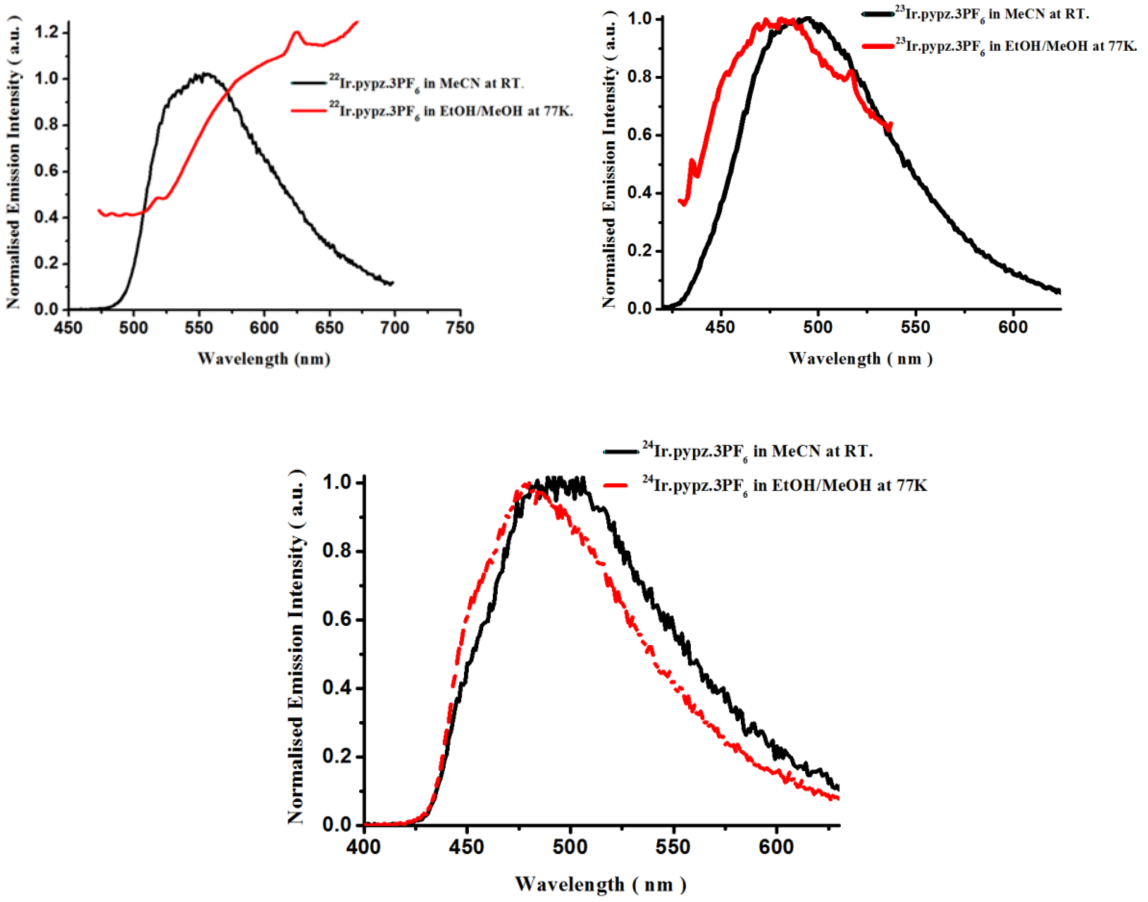

Figure A-2 Normalised emission spectra of $^{N/N}$Ir•pypz•.3PF$_6$ in MeCN at 298 K and 77K for $^{N/N}$Ir•pypz•3PF$_6$.